



HAL
open science

Modelling past and future sandy shoreline change and the respective uncertainties: toward a holistic approach

Maurizio d'Anna

► **To cite this version:**

Maurizio d'Anna. Modelling past and future sandy shoreline change and the respective uncertainties: toward a holistic approach. Geomorphology. Université de Bordeaux, 2022. English. NNT: 2022BORD0034 . tel-03615236

HAL Id: tel-03615236

<https://theses.hal.science/tel-03615236>

Submitted on 21 Mar 2022

HAL is a multi-disciplinary open access archive for the deposit and dissemination of scientific research documents, whether they are published or not. The documents may come from teaching and research institutions in France or abroad, or from public or private research centers.

L'archive ouverte pluridisciplinaire **HAL**, est destinée au dépôt et à la diffusion de documents scientifiques de niveau recherche, publiés ou non, émanant des établissements d'enseignement et de recherche français ou étrangers, des laboratoires publics ou privés.

THÈSE PRÉSENTÉE
POUR OBTENIR LE GRADE DE

DOCTEUR DE

L'UNIVERSITÉ DE BORDEAUX

ÉCOLE DOCTORALE: Sciences et Environnements (EDSE 304)

SPÉCIALITÉ: Physique de l'environnement

Par: Maurizio D'ANNA

**Modélisation de l'évolution passée et future du
trait de côte sableux et de ses incertitudes: vers
une approche holistique**

Sous la direction de: Bruno CASTELLE et Déborah IDIER

Soutenue le 10 Février 2022

Membres du jury :

BARTHELEMY, Eric	Professeur	Université Grenoble Alpes	Président/Rapporteur
FALQUES, Albert	Professeur	Universitat Politècnica de Catalunya	Rapporteur
SPLINTER, Kristen D.	Professeure Associée	University of New South Wales	Examineur
YATES, Marissa	Chargée de recherche	Saint Venant Hydraulics Laboratory	Examineur
COCO, Giovanni	Professeur Associé	University of Auckland	Examineur
MENDEZ, Fernando J.	Professeur Associé	Universidad de Cantabria	Examineur
CASTELLE, Bruno	DR CNRS	Université de Bordeaux	Directeur
IDIER, Déborah	Docteur BRGM	BRGM	Directeur
LE COZANNET, Goneri	Docteur BRGM	BRGM	Invité
ROHMER, Jeremy	Docteur BRGM	BRGM	Invité

Titre: Modélisation de l'évolution passée et future du trait de côte sableux et de ses incertitudes: vers une approche holistique

Résumé : L'évolution du trait de côte le long des littoraux sableux répond à une multitude de processus qui interagissent entre eux sur différents échelles spatiales et temporelles, compliquant considérablement sa prédiction. La modélisation de l'évolution du trait de côte est dépendante des incertitudes associées aux conditions de forçage (*e.g.* niveau de la mer et régime de vagues) ainsi que par des incertitudes liées aux hypothèses des modèles utilisés. Malgré les progrès récents réalisés dans la quantification des effets des incertitudes liées de la remontée du niveau marin, la compréhension des incertitudes de prédiction d'évolution du trait de côte sous l'action combinée des vagues et du niveau marin est encore limitée. Afin d'examiner l'influence de ces différentes sources d'incertitude sur les évolutions du trait de côte modélisées, cette thèse propose un cadre probabiliste qui combine des modèles d'équilibre en réponse à l'action des vagues, un modèle de réponse à la remontée du niveau marin, et des méthodes de décomposition de la variance. Cette approche est utilisée pour analyser les incertitudes associées à l'évolution pluri-décennale passée et future sur la plage du Truc Vert (France), dominée par processus transversaux. Les interactions des effets de la remontée du niveau marin et de l'action des vagues n'ayant pas fait l'objet d'analyse conceptuelle détaillée, ce travail présente aussi une nouvelle interprétation physique de la réponse de plage à la remontée du niveau marin pour soutenir l'intégration de ce processus dans les modèles d'équilibre du trait de côte. L'évolution du trait de côte sous les effets combinés des vagues et de l'augmentation du niveau marin révèle des interactions complexes entre les différents facteurs, contribuant aux incertitudes sur les prévisions de trait de côte. Les incertitudes sur les prédictions du trait de côte au Truc Vert pendant le 21^{ème} siècle sont contrôlées par les incertitudes sur les conditions futures de vagues et les paramètres des modèles pendant la première moitié du siècle. Puis, dans un deuxième temps, les incertitudes sur la remontée du niveau marin deviennent dominantes dans les dernières décennies du siècle. Quand les incertitudes de la remontée du niveau marin sont négligeables, les incertitudes sur la variabilité des conditions de vagues deviennent dominantes, représentant jusqu'au 83% des incertitudes associée au trait de côte simulé. Les résultats montrent aussi que les incertitudes sur les projections du trait de côte sont influencées par les hypothèses des différents modèles d'équilibre ainsi que le scénario de climat futur.

Mots clés: modèles d'équilibre de trait de côte; incertitudes; remonté du niveau de mer; analyse de sensibilité globale; Truc Vert.

Title: Modelling past and future sandy shoreline change and the respective uncertainties: towards a holistic approach

Abstract: Shoreline change along sandy coasts responds to a myriad of processes interacting at different spatial and temporal scales, making shoreline predictions challenging. Shoreline modelling inherits uncertainties from the primary driver boundary conditions (*e.g.* sea-level rise and wave forcing) as well as uncertainties related to model assumptions and/or misspecifications of the physics. Despite the recent progresses in addressing uncertainties related to sea-level rise (SLR), the uncertainties related to wave-driven shoreline response are still poorly understood. This thesis gathers wave-driven equilibrium shoreline models, SLR-driven recession models, and variance decomposition methods into a probabilistic framework to investigate the roles of several sources of uncertainty in modelled shoreline change. The framework is applied to analyse the uncertainties associated with past and future multi-decadal shoreline evolution at the cross-shore transport dominated sandy beach of Truc Vert (France). As the physics of the combined action of waves and sea-level rise has not yet been described in detail, the thesis also presents a novel physical interpretation of the beach response to sea-level rise to support the integration of SLR-driven recession into equilibrium shoreline models. Shoreline response under the coupled effects of waves and SLR reveals complex patterns and interplays of the several contributions of uncertainties to shoreline predictions. Overall, uncertainties on Truc Vert shoreline predictions across the 21st century are driven by the uncertain model free parameters and wave conditions over the first half of the century. Then, the uncertainties on SLR become the dominant driver over the last decades. When uncertainties on SLR are negligible, the uncertainties of wave conditions variability are responsible for up to 83% of the uncertainties in modelled shoreline. It is also observed that the uncertainties in modelled shoreline trajectories depend on the underlying physical assumptions of different equilibrium shoreline models and future climate scenario.

Keywords: equilibrium shoreline models; uncertainties; sea-level rise; global sensitivity analysis; Truc Vert.

*“If I have been able to see this far,
it was only because I stood on the shoulders of giants.”*

Isaac Newton

Acknowledgements

This section of the manuscript is probably the hardest thing I had to redact over the last 3 years and 3 months of PhD. It is always hard to accept the end of such good experiences, but also to emphasize how important are the the people that I crossed along the way and/or shared bits of it with me. Many people were involved in this work, either with scientific contributions or with their emotional and psychological support, and if despite my efforts I left someone out of this acknowledgements I would like to thank them in the first place and blame my old age with its memory decay!

I dedicate my first thoughts to Bruno and Déborah, who gave me the chance to take on this research and backed me up all along this journey. I will always appreciate how lucky I've been to be mentored by you. You eased me into the world of research (which was completely new for me) and made me feel so comfortable in it that I don't want to leave it anymore! You two have been wonderful role models, as scientists and as humans, and treated me more like a colleague than a student allowing me to develop and explore while keeping me on the right track (or near it!).

I also thank Jérémy and Gonéri, who I thank so much for patiently teaching so many things to me, for the technical (and not) advises, and for encouraging me until the end.

I greatly appreciate all the colleagues who welcomed me to the R3C team of the BRGM in Orléans, and had to deal with my poor French (sorry!). In particular, I would like to thank Arthur R. for the patience with my endless Matlab and LX-Shore questions and all the support for settling in Orléans, and Rémi for all the talks and good 'office mate' vibes.

Thanks Wagner for keeping the mood permanently alive and good, I will (I already do) miss 'coffee' talks and the *Shakira* nights.

Great part of my appreciation goes to the members METHYS team of the EPOC lab, who received me nicely in Bordeaux and immediately made me feel part of the team (Aldo, Isabel, Vincent, Nadia, Bertrand, Berengère, Philippe and Natalie), despite the troubling times of the COVID-19 pandemic and a fire in the laboratory building.

I am grateful I had the chance to share the friendly and social ambience with the PhD students and post-docs that I met: Jack, Arthur M., Mélanie, Marion, Olivier, Junli, Carla, les jumelles infernales (Marine & Emilie), I will miss all the beers, talks and loughs! A real bunch of fantastic people. Thank you Kévin and Marika for all the advises and for motivating me to go out more often. Although it was unfortunate that you didn't manage to go to Australia during the year that I was in Bordeaux, it worked pretty well for me!

Thanks Isaac, Abril and Sophie for being such good friends, the shared addiction to coffee and the tik-tak videos of cats. I trust you will visit this page every Monday:

<https://www.youtube.com/watch?reload=9&v=bmfudW7rbG0>

I also appreciate having met Carlos, Natan, Monique and Elsa even if we crossed only for a few weeks it is already obvious that you're wonderful persons.

Despite the limits imposed by the pandemic, I'm very grateful I had the chance to (virtually) meet and work with many great people. In particular, I would like to thank Sean Vitousek, Laura Cagigal, José Antolinez and Raimundo Ibaceta for the nice and constructive exchanges. I also take the chance to thank again Eric Barthélémy, Albert Falqués, Marissa Yates, Kristen Splinter, Fernando Mendez and Giovanni Coco for taking part to the committee of my PhD defence.

Last but not least, I thank Dorine for supporting and tolerating me all along the PhD, my friends Bruna, Corinna, Chiara, Kasia, Gabriella and my family who always believed in me. Special thanks go to Sabine and Gio Cozzuto for sharing, understanding and being there for me all the time, and Domenico for helping me spreading *ingenuity* everywhere.

Finally, I would like to acknowledge the BRGM, the University of Bordeaux, and the Make-Our-Planet-Great-Again program that funded this work and allowed me to realize this PhD in the best conditions.

To all of you, Grazie, Merci, Thank you, Gracias, Dziękuję.
Hasta plus!



Table of Contents

- 1. Introduction 13**
 - 1.1. Context..... 13
 - 1.2. Objectives and approach..... 17
 - 1.3. Thesis outline..... 18
- 2. Study site, material and method 21**
 - 2.1. Truc Vert beach, past and future environmental conditions..... 21
 - 2.2. Shoreline change models 28
 - 2.3. Method..... 33
- 3. Integrating SLR-driven recession into equilibrium shoreline models 37**
 - 3.1. Introduction 37
 - 3.2. Sea-Level-Driven Recession and Equilibrium Shoreline Models..... 40
 - 3.3. Integrating Sea-Level Rise in Equilibrium Shoreline Models..... 46
 - 3.4. Model Application..... 50
 - 3.5. Discussion..... 54
 - 3.6. Conclusions 58
- 4. Impact of model free parameters and sea-level rise uncertainties on a 20-year shoreline hindcast 61**
 - 4.1. Introduction 61
 - 4.2. Data, models and method 63
 - 4.3. Input probability distributions 66
 - 4.4. Results 68
 - 4.5. Discussion and conclusions 73
 - 4.6. Conclusions 77
- 5. Uncertainties on future shoreline projections to 2100 79**
 - 5.1. Introduction 79
 - 5.2. Material and method..... 82
 - 5.3. Input probability distributions for future projections 85
 - 5.4. Results 90
 - 5.5. Discussion..... 96
 - 5.6. Conclusions 104

6. Effects of stochastic wave forcing on equilibrium shoreline modelling across the 21st century	105
6.1. Introduction	105
6.2. Material and Methods	109
6.3. Input Uncertainties	114
6.4. Results	120
6.5. Discussion.....	126
6.6. Conclusions	134
7. Conclusions and perspectives	137
7.1. Conclusions	137
7.2. Research perspectives.....	139
Publications and presentations	143
Research articles	143
Conference presentations.....	143
References	145
Appendix A Methodology	155
A1. Direct formulation for wave refraction and breaking.....	155
A2. Global Sensitivity Analysis	155
Appendix B Supporting information for Chapter 3	160
B1. Passive Flooding, Wave Reshaping and the Bruun Rule	160
B2. Integrating SLR-Driven Disequilibrium into ESMs with Feedback	160
Appendix C Supporting information for Chapter 5	166
C1. Wave projections correction.....	166
C2. Construction of the high-end sea level scenario	169
C3. Model free parameters probability distribution.....	169
C4. Ensemble waves test with ShoreFor.....	171
Appendix D Supporting information for Chapter 6	174
D1. Wave ensemble and hindcast wave data comparison.....	174
D2. Sea-Level Rise.....	176
D3. Past scenario simulation with the Yates model	177

List of notations

Acronyms	Description
RCP	Representative Concentration Pathway
GSA	Global Sensitivity Analysis
SLR	Sea-level rise
B	Bruun model
ESM	Equilibrium shoreline model
MHW	Mean high water
MLW	Mean low water
MSL	Mean sea level
PF	Passive flooding model
WR	Wave reshaping
BW18	Bricheno and Wolf (2018) Wave projections
Y09	Yates et al. (2009) model
SF	Splinter et al. (2014b) model
Symbols	Description
μ	Median
a, b	Yates model disequilibrium condition parameters
D_m	Mean wave direction
dY_{PF}	Passive flooding shoreline change
$\overline{dY_{PF}}$	Time averaged shoreline change due to passive flooding
dY_{WR}	Shoreline change induced by wave reshaping induced by passive flooding
$\overline{dY_{WEC}}$	Time averaged shoreline change induced by wave reshaping
E	Wave energy
F	Hydrodynamic forcing
$H_{o,s}$	Deep water significant wave height
H_s	Significant wave height
k	Shoreline response rate parameter of equilibrium shoreline models
LT	Long-term shoreline change processes
ST	Short-term shoreline change processes
$\tan(\alpha)$	Average slope of the active beach profile
$\tan(\beta)$	Average slope of the beach forshore

T_p	Peak wave period
X_i	Uncertain input variable
Y	Shoreline position
ΔD	Disequilibrium beach state
ρ	Correlation coefficient
σ	Standard deviation
Φ	Beach memory parameter of the <i>ShoreFor</i> model

Chapter 1

1. Introduction

1.1.Context

Ongoing climate change is one of the largest concerns of our time, and its largest impacts on the environment are yet to come. Global mean sea-level rise is accelerating since 1870, and is expected to continue rising over the 21st century, although acceleration may be avoided if the Paris Agreement ‘below 2°C climate warming’ target is met (Magnan et al., 2019). In addition, depending on the region, climate change could drive variations in storminess, storm tracks and sea surface temperature, modifying the future wave conditions (Morim et al., 2020).

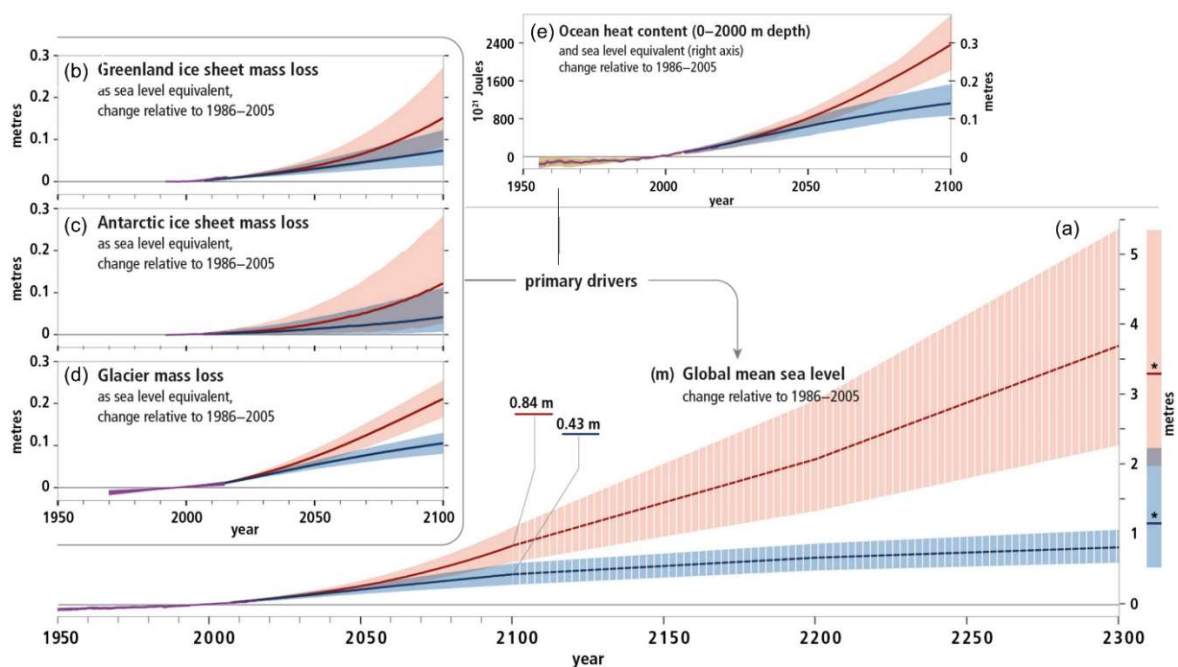


Figure 1.1. Observed and modelled historical changes in the ocean since 1950 and projected future changes under low (RCP2.6) and high (RCP8.5) greenhouse gas emissions scenarios. Changes are shown for (a) global mean sea level and the primary drivers of sea-level rise: (b) Greenland Ice sheet, (c) Antarctic ice sheet, and (d) Glacier mass losses, and (e) Global ocean heat content change (0–2000 m depth). Modified from Fig.SM1 of the Special Report on Oceans and Cryosphere (Oppenheimer et al., 2019).

Meanwhile, the expected growth of population density in low-lying coastal areas during the twenty-first century (Merkens et al., 2016) increases the need for efficient adaptation plans of coastal communities (Magnan et al., 2019). The spatial heterogeneity of sea-level rise (SLR), wave-climate change, and vulnerability of coastal communities raise the need for long-term (multi-decadal) shoreline projections with their related uncertainties. Such projections will support risk-informed decision making process (Hinkel et al., 2019; Wainwright et al., 2015).

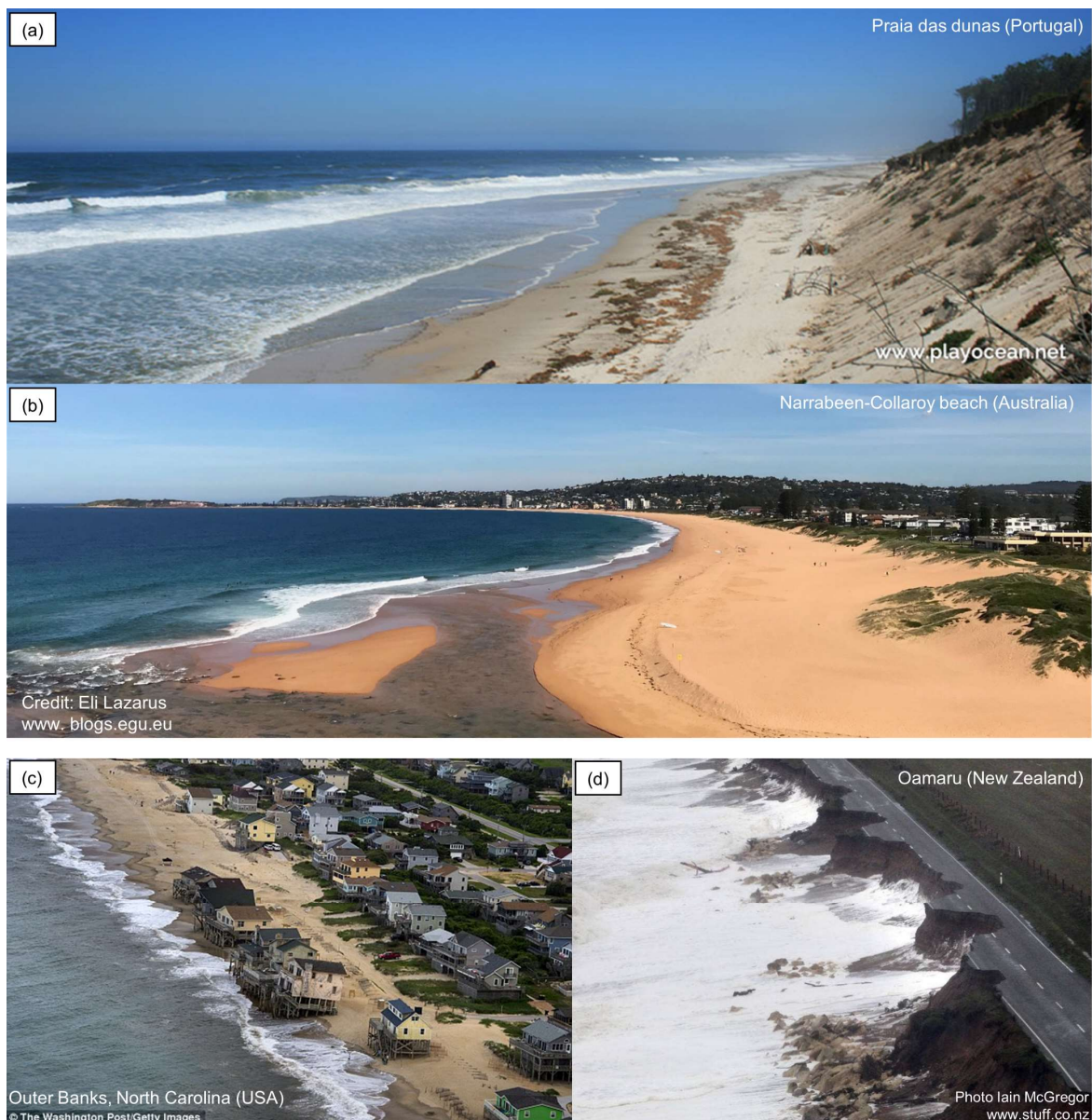


Figure 1.2. Photographs of the sandy beaches of (a) Praias das dunas (Portugal), and (b) Narrabeen-Collaroy (Australia); and examples of coastal risk associated to beach erosion at (c) Outer Banks (North-Carolina, USA) and (d) Oamaru (New Zealand).

The shoreline change is one of the main indicators of the beach variability, which is particularly important for human settlements on coastal zones and coastal ecosystems. Although the shoreline is generally intended as the boundary line between land and sea, its definition depends on the context and purpose of the analysis (Boak and Turner, 2005; Burningham and Fernandez-Nunez, 2020).

Sandy beaches cover about one-third of the Earth's ice-sheet free coasts (Luijendijk et al., 2018), and provide an important natural and socio-economical resource to coastal communities (Ghermandi and Nunes, 2013) as well as a buffer zone during storm events. They are one of the most naturally variable environments on earth and their shorelines respond to several natural and anthropogenic factors interacting on different time scales with the local geological settings (Stive et al., 2002). Natural agents include waves, sea level changes, winds and other climatic forcing, while human interventions can influence sediment supply and redistribution, and local ground motion.

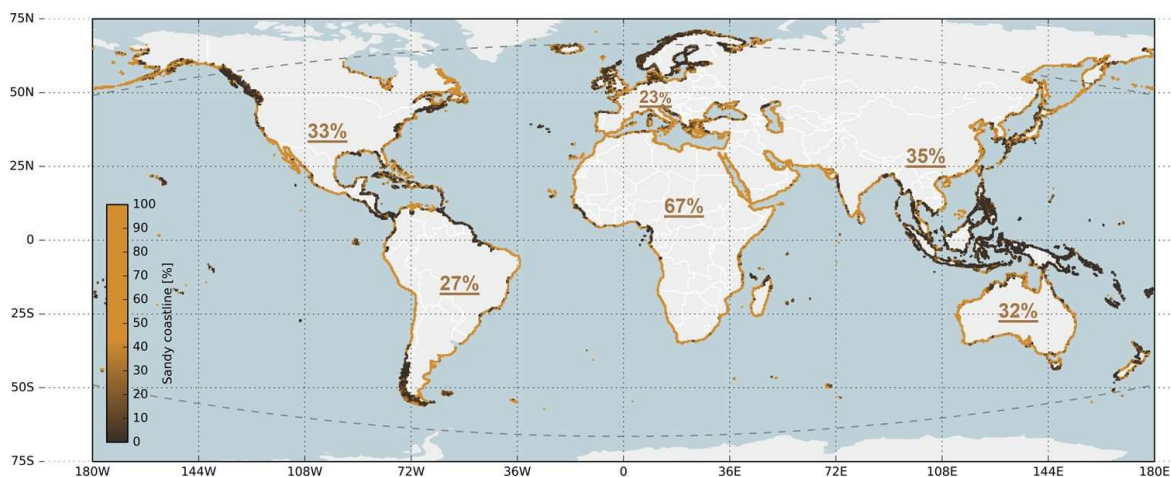


Figure 1.3. Global distribution of sandy shorelines; the coloured dots along the world's shoreline represent the local percentage of sandy shorelines (yellow is sand, dark brown is non-sand), with the underlined percentages indicate the percentages of sandy shorelines averaged per continent. Figure from Luijendijk et al. (2018).

On open sandy beaches, shoreline change is often dominated by wave energy variations on the time scales of storms to season and years due, among other factors, to interannual variability of winter wave energy (Dodet et al., 2019), while sea-level rise (SLR) affects shoreline trends over longer time scales (decades to centuries). On cross-shore dominated sites, during storms the upper portion of the beach profile erodes and the sediment is deposited offshore, while the sediment is moved back to the shore when wave height declines, driving the profile towards its original shape (Wright and Short, 1984; Yates et al., 2009). The effects of this mechanism are interconnected with the sea level changes, which

provides more or less access to the upper beach deposits (*e.g.* dunes). Hence, the co-action of waves and sea level change on different time scales is crucial to shoreline evolution.

The complex dynamics of sandy shorelines together with the limited predictability of the future climate make shoreline predictions challenging (Vitousek et al., 2017a), forcing coastal scientists, managers and engineers to embrace uncertainties and move towards probabilistic approaches (Ranasinghe, 2020; Toimil et al., 2020). ‘*Uncertainty analysis*’ is a practice that focuses on quantifying the uncertainties on the outputs of an estimation process (*e.g.* modelling), provided a set of recognized uncertain inputs. One way of doing this is through Monte Carlo-based approaches (*i.e.* ensemble modelling), where probability distributions associated with the uncertain input variables are used to generate a number of possible model input combinations. Then, each set of sampled input variables is used to produce an ensemble of model realizations, of which one can estimate the statistical information relevant to the purpose of the analysis (mean, variance, confidence bounds, etc.) (Saltelli et al., 2008).

In the last decade, many studies have focused on the effects of SLR uncertainties (Athanasίου et al., 2020; Le Cozannet et al., 2019, 2016; Thiéblemont et al., 2021; Vousdoukas et al., 2020) and changes in storminess based on data extrapolation and/or empirical models (Allenbach et al., 2015; Casas-Prat et al., 2016; Toimil et al., 2017; Vousdoukas et al., 2020) on future shoreline uncertainties. However, these studies do not explicitly resolve wave-driven shoreline change, and it is advocated that new methods have to be developed to predict the impacts of SLR on the coast (Cooper et al., 2020). For instance, short- and long-term variability in wave energy, as well as the storm sequencing, can have a significant influence on evolution shoreline patterns (Coco et al., 2014; Splinter et al., 2014a; Vitousek et al., 2021).

Resolving long-term wave-driven shoreline change in ensemble settings requires high computational efficiency. In this context, equilibrium shoreline models are particularly convenient tools (Montaño et al., 2020) as they simulate cross-shore shoreline response to wave-driven sediment transport processes on time scales from hours to decades with low computational demand (Alvarez-Cuesta et al., 2021a; Davidson et al., 2013; Davidson, 2021; Jaramillo et al., 2020; Lemos et al., 2018; Robinet et al., 2018; Splinter et al., 2014b; Toimil et al., 2017; Vitousek et al., 2017b; Yates et al., 2009).

The need for modelling shoreline change over long time scales, where SLR becomes important, motivated the integration of SLR-driven erosion models (*e.g.* the Bruun (1962) model) into wave-driven equilibrium models (*e.g.* Alvarez-Cuesta et al., 2021a; Antolínez

et al., 2019; Robinet et al., 2020; Vitousek, et al., 2017b). However, so far, the interplay among the different hydrodynamic drivers within equilibrium shoreline models has not yet been explored in detail, and applications coupling these processes disregarded the conceptual relationship between the two models.

In addition, uncertainties on long-term shoreline modelling obtained by explicitly resolving wave- and sea-level-driven shoreline change are far from being fully understood, and more holistic approaches are required to untangle model uncertainties and understand the role of its multiple drivers.

1.2. Objectives and approach

This research was performed both at BRGM (Bureau de Recherche Geologique et Minière) and UMR-EPOC (Environnements et Paléoenvironnements Océaniques et Continentaux) laboratory, including collaborations with the USGS (United States Geological Survey, USA) and the Universidad de Cantabria (Spain). The work relies on data collected at a labelled SNO Dynalit site and is co-funded by the Make Our Planet Great Again (MOPGA) program and BRGM.

The thesis aims to gain new understanding of how different sources of uncertainties influence multi-decadal shoreline modelling, while resolving wave-driven shoreline change on the time scale of hours and taking into account sea-level rise. With this purpose, an ensemble-based probabilistic framework is developed combining equilibrium shoreline models (Splinter et al., 2014b; Yates et al., 2009), and variance decomposition approaches building on the works of Le Cozannet et al. (2019, 2016). This approach is applied to the cross-shore transport dominated Truc Vert beach (France) combining several equilibrium shoreline models with the Bruun (1962) model. As a preliminary step, a re-examination of the underlying physical processes of wave- and SLR-driven equilibrium shoreline models is provided to verify their compatibility. Throughout this thesis, the following research questions are tackled:

Q1. *How can the effects of short- and long-term drivers (i.e. wave action and SLR) be combined in the context of equilibrium shoreline modelling?*

Q2. *On which time scale the uncertainties on SLR become the primary driver of the uncertainties on modelled shoreline?*

Q3. *How do the relative contributions of uncertain model parameters and physical forcing to modelled shoreline uncertainties evolve over time?*

Q4. How do the uncertainties on model parameters and equilibrium approaches relate to the wave climate forcing?

Q5. What is the role of uncertain wave climate variability on modelled shoreline?

1.3. Thesis outline

The remainder of the manuscript is structured as follows, with Chapters 3 to 6 tackling the research questions listed above and including the respective state-of-the-art:

- **Chapter 2: Study site, material and method.** This chapter provides an outline of Truc Vert beach, wave and sea level data used in the applications, and a description of the shoreline models and variance decomposition approach.
- **Chapter 3: Integrating SLR-driven recession into equilibrium shoreline models.** In this chapter, we present a novel physical interpretation of the beach response to sea-level rise that identifies two main contributing processes: passive flooding and increased wave-driven erosion efficiency. Based on this new concept, the integration of SLR-driven recession into equilibrium shoreline models is analysed and an idealized test case is used to show how the physical mechanisms underpinning the Bruun Rule can be described within the integrated models.
- **Chapter 4: Impact of model free parameters and sea-level rise uncertainties on a 20-year shoreline hindcast.** This chapter includes an uncertainty analysis of a 20-year shoreline reconstruction based on 3000 simulations obtained using wave- and SLR-driven cross-shore shoreline models while considering the uncertainties associated with sea-level rise, depth of closure and three model free parameters. The relative impact of each source of uncertainty on the model results is further addressed performing a Global Sensitivity Analysis.
- **Chapter 5: Uncertainties on future shoreline projections to 2100.** This chapter, analyses the uncertainties associated with future shoreline evolution at Truc Vert beach over the 21st century. Wave-driven shoreline change is resolved using two different equilibrium modelling approaches to provide new insight into the contributions of sea-level rise, and free model parameters uncertainties on future shoreline change in the frame of climate change. Global Sensitivity Analyses are performed for two future climate scenarios.
- **Chapter 6: Effects of stochastic wave forcing on equilibrium shoreline modelling across the 21st century.** This chapter focuses on the response of two different wave-

driven equilibrium shoreline models to wave-forcing ensembles. A Global Sensitivity Analysis is performed to assess the impact of stochastic wave chronology on the respective long-term shoreline predictions relative to other uncertain variables while accounting for possible interactions among them.

- **Chapter 7: Conclusions and perspectives.** In this chapter, we summarize the conclusions drawn from the present work and perspectives on future research developments.

It is noted that a large portion of the work presented here is described in published and submitted research articles (D'Anna et al., 2020; D'Anna et al., 2021a; 2021b; and D'Anna et al. (under review)).

Chapter 2

2. Study site, material and method

In this chapter, we describe the site of application with the respective shoreline position, wave and mean sea level data, as well as the shoreline models and the methods used for the analyses carried out throughout this manuscript.

2.1. Truc Vert beach, past and future environmental conditions

2.1.1. General description

The probabilistic framework adopted within this work is applied to the open sandy beach of Truc Vert, located within a straight section of the ~130 km long Gironde coast in southwest France (Figure 2.1a). Truc Vert is backed by a high (~20 m) and large (~250 m) aeolian dune (Robin et al., 2021) separating the beach from a large area of state-owned forest (Figure 2.1b-d). The beach is exposed to a highly energetic wave climate generated in the North Atlantic Ocean. Truc Vert is a meso-macro-tidal beach with a ~3.7 m annual mean spring tidal range and a maximum astronomical tide range reaching up to 5 m (Castelle et al., 2018a), with negligible tidal currents compared to wave-driven currents in the nearshore zone. The sediment consists of well-mixed fine to medium sand with a mean grain size of about 0.35–0.40 mm (Gallagher et al., 2011). The beach morphology is strongly variable alongshore, typically double barred with the inner intertidal sandbar classified as transverse bar and rip (Sénéchal et al., 2009), and the outer bar as crescentic (Castelle et al., 2007). The absence of coastal or inland structures nearby, together with the wealth of available data, make this site a worthy benchmark for modelling and interpreting shoreline response to natural processes. Starting from the early 2000s, Truc Vert beach has been intensively monitored (see Section 2.1.2.1).

On the long term (at least 70 years), this stretch of coast has been reasonably stable (Castelle et al., 2018b), although the strong interannual variability of winter wave energy can result in extreme winters causing severe beach and dune erosion (Castelle et al., 2015;

Masselink et al., 2016). Cross-shore processes driven by the temporal variability of incident wave energy have been recognized to be the main driver of shoreline changes at Truc Vert (Castelle et al., 2014; Robinet et al., 2018, 2016), in line with the negligible longshore drift gradients in this area (Idier et al., 2013).

Local shoreline variations observed over the past decades, as well as past and future projections of wave and sea level conditions are described in the upcoming subsections.

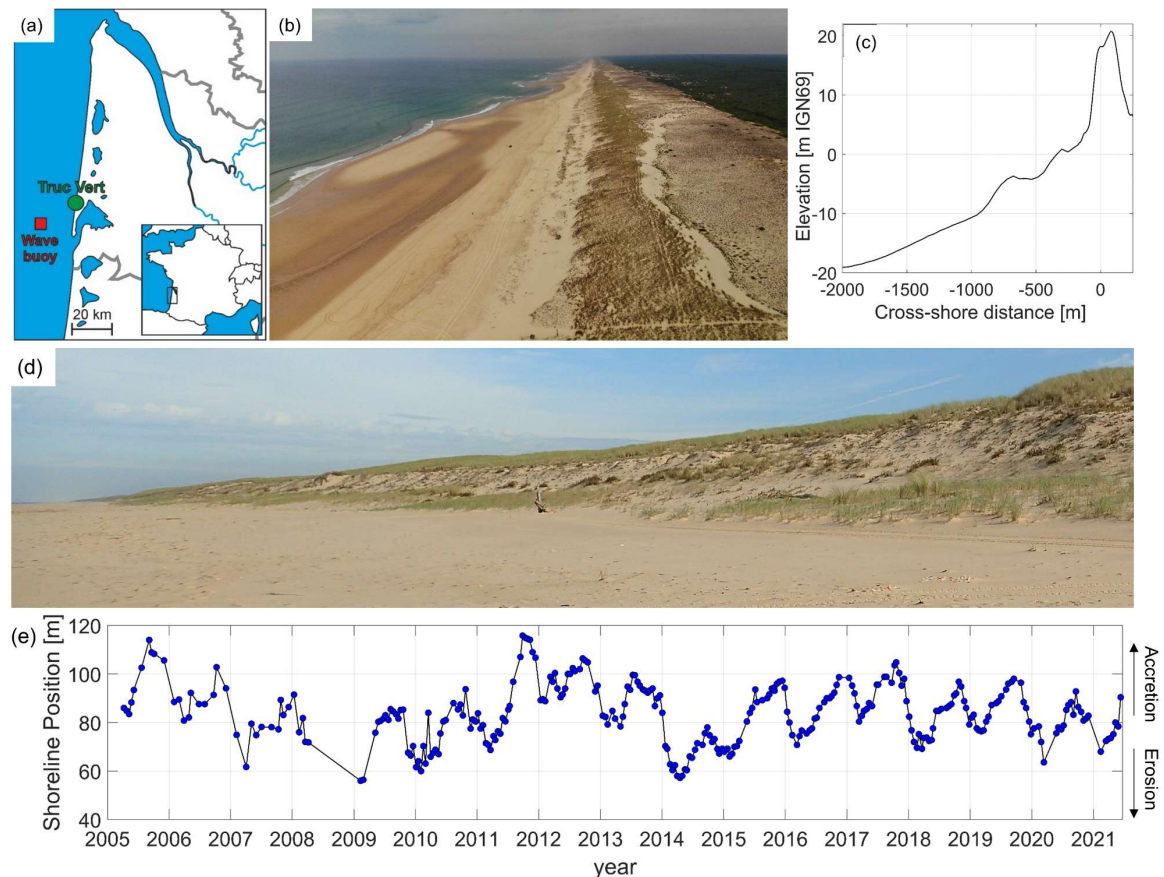


Figure 2.1. (a) Map of the southwest coast of France with the location of Truc Vert beach (green), and wave hindcast and projections grid points co-located with the CANDHIS *in situ* wave buoy (red and yellow, respectively); Photographs of Truc Vert beach and dune landscape from (b) UAV aerial view (photo by B. Castelle), and (d) foredune view (photo by S. Bujan); (c) 4 km alongshore-averaged beach-dune profile from merged 2008 topo-bathymetry (submerged beach) and 2018 UAV-photogrammetry digital elevation model (emerged beach and dune); (e) Time series of alongshore-averaged shoreline (1.5-m elevation proxy) position between April-2005 and June-2021 derived from the topographic surveys.

2.1.2. Past environmental conditions

2.1.2.1. Shoreline and topo-bathymetry

Monthly or bimonthly sampled topographic DGPS surveys have been performed at spring low tide from April 2005 to June 2021 with a 1-year gap between 2008 and 2009.

The alongshore coverage of the surveys increased over the years: from 350 m to 750 m in 2005-2008, from 750 m to 1200 m in 2008-2012 and from 1200 m to 1900 m starting from 2012 to present. Throughout this thesis, following Castelle et al. (2014) the shoreline was defined as the intersection of the beach profile with the 1.5 m level contour above mean sea level, which approximately corresponds to the mean-high water level at Truc Vert beach. This shoreline proxy is also the one that best correlates to variations in total beach-dune volume (Robinet et al., 2016). Figure 2.1e illustrates the strong modulation of the observed alongshore averaged shoreline position, with seasonal excursions (most eroded to most accreted position) of the order of ~ 27 m, occasionally exceeding 40 m (winter 2013-2014), and interannual fluctuations of the order of ~ 15 m amplitude (e.g. 2012-2017).

In order to compute the main characteristics of the active profile at Truc Vert (Figure 2.1c), which are critical in addressing the influence of SLR on shoreline response, we used a 2-m resolution topo-bathymetry collected in 2008 at Truc Vert during the ECORS'08 campaign (Parisot et al., 2009; Sénéchal et al., 2011). The data cover the nearshore area from the elevation of -10 m to roughly +2 m IGN69 (approximately the mean sea level). In addition, we used recent high-resolution digital elevation model inferred from UAV-photogrammetry between October 2017 and October 2018 covering 4 km of beach-dune system (Laporte-Fauret et al., 2019). For more details on the topo-bathymetric datasets the reader is referred to Castelle et al. (2020).

2.1.2.2. Hindcast wave data (1994-2021)

Historical wave data (H_s , T_p , and D_m), from January 1994 to June 2021, was extracted from the NORGAS-UG regional hindcast model (Michaud et al., 2016) at the grid point co-located with the *in situ* CANDHIS wave buoy (44°39'9" N; 1°26'48" W) moored in ~ 50 m depth offshore of Truc Vert beach (Figure 2.1a). The NORGAS-UG model covers the French Atlantic coastal area using an unstructured mesh grid with resolution of 10 km offshore, increasing to 200 m nearshore. The wave model has been validated against several French and international wave buoy data, and showed 0.96-0.99 correlations coefficients, 0.15-0.21 m RMSE, and -0.02 to 0.04 m bias (Michaud et al., 2016). The hindcasted wave time series (1994-2021) shows the typical seasonal and interannual modulation of the incident wave climate, with prevailing west-northwest incidence at Truc Vert beach (Figure 2.2).

Incident wave energy shows a strong seasonal modulation of significant wave height (H_s) and peak wave period (T_p) (Castelle et al., 2018a; Charles et al., 2012; Robinet et al., 2016) reaching monthly mean values of 1.1 m and 9 s in August, and 2.4 m and 12.8 s in

January, respectively. The local winter wave energy also shows interannual variations driven by natural large-scale patterns of atmospheric variability such as the West Europe Pressure Anomaly (Castelle et al., 2017), which affects the spatio-temporal distribution of storm events and clustering winters (Castelle et al., 2015; Masselink et al., 2016).

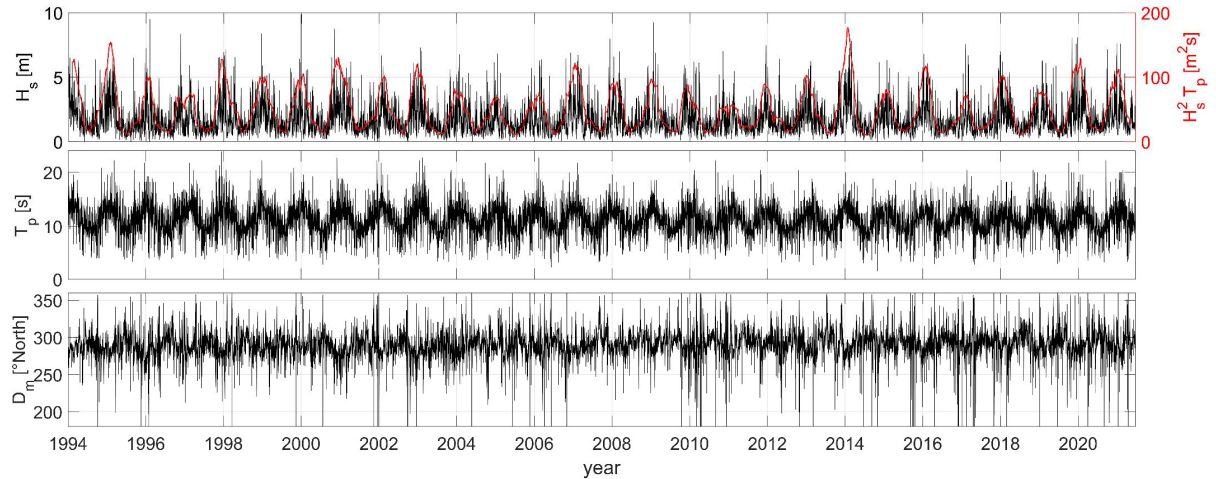


Figure 2.2. NORGAS-UG wave hindcast time series from 1994 to 2021 at (44°39'9" N; -1°26'48" W) offshore of Truc Vert beach (Figure 2.1a) including: (a) significant wave height, H_s (black line) and 3-month averaged $H_s^2 T_p$ (red line); (b) peak wave period T_p ; and (c) mean wave direction expressed in Nautical convention, D_m .

2.1.2.3. Past mean sea level reconstruction

The absolute mean sea level time series at the Bay of Biscay was reconstructed between 1998 and 2021 using a Kalman filter approach assimilating available tide gauge records in this region (Rohmer and Le Cozannet, 2019). The resulting SLR rates are roughly constant at 2.1 ± 0.1 mm/year (median $\pm \sigma$). Local relative MSL change at Truc Vert beach was calculated by adding the effect of vertical land motion to the relative regional sea level estimate. Vertical land motion in Truc Vert area was estimated using the near Cap-Ferret permanent GNSS station from the SONEL database (Santamaría-Gómez et al., 2017), which provides data from 2005 to 2016, when the station has been decommissioned. The GNSS station measures the effects of glacial isostatic adjustment and current gravitational, rotational and deformation changes associated to ongoing glaciers and ice-sheets melting (Frederikse et al., 2020). These effects were subtracted from the observed GNSS records over the observation period to assess residual vertical ground motions obtaining a subsidence rate of 1.2 ± 0.6 mm/yr. This resulted in a roughly constant SLR rate of 3.3 ± 0.7 mm/yr over the past decade (Figure 2.3). The observed lowering ground might be due to slow subsidence of the former Leyre riverbed (Klingebiel and Legigan, 1992). The

pointwise Cap-Ferret GNSS station information may not be exactly that of the surrounding area. This is part of the residual uncertainties of our study.

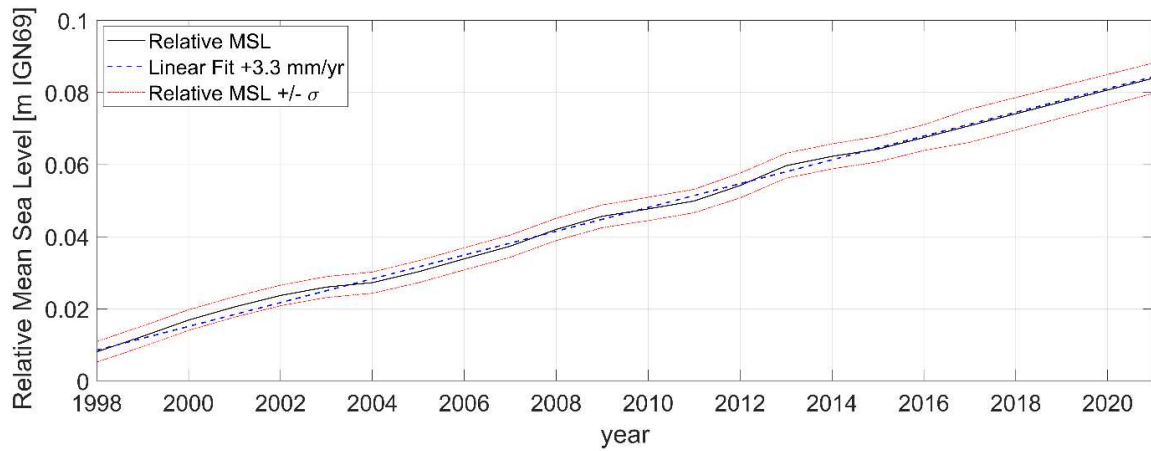


Figure 2.3. Relative Mean Sea Level time series (black line) relative to Cap-Ferret land elevation (m NGF IGN69), with uncertainty interval (red lines) and linear approximation (blue dashed line) over 1998-2021.

2.1.3. Sea level and waves projections

The applications on future shoreline projections illustrated in the following chapters considered different future climate scenarios based on Representative Concentration Pathways (RCP). RCPs have been introduced by the *Intergovernmental Panel on Climate Change* (IPCC) to synthesize several reference scenarios of plausible future climate, depending on greenhouse gas concentration and intensity of radiative forcing by 2100 (2.6, 4.5, 6, and 8.5 W/m², respectively). Throughout this work, we mainly assessed shoreline projections for the scenarios RCP4.5 and RCP8.5. The RCP4.5 corresponds to an ‘intermediate scenario’, where emissions decline after 2050 and global-mean-sea-level rise rate stabilize, while RCP8.5 depicts a fossil-fuel intensive ‘business-as-usual’ emission scenario associating a persistent acceleration of global-mean-sea-level rise throughout (and beyond) the 21st century.

2.1.3.1. Future mean sea level projections

Global mean sea level projections until 2100 are available from the *Special Report of Ocean and Cryosphere in a Changing Climate* (SROCC, Oppenheimer et al., 2019). SROCC estimates build on the *Fifth Assessment Report* (AR5, Wong et al., 2014) with a revised assessment of the Antarctic dynamics contribution based on new evidence on marine ice-sheets instabilities since the AR5. SROCC provides median values of each sea level change contribution with associated *likely range* for several RCP scenarios. Unlike other IPCC reports, the SROCC defines the ‘likely range’ as the 17th-83rd percentiles of the

distribution of sea-level rise (Oppenheimer et al., 2019). We reproduced the SROCC global MSL projections to Truc Vert beach following Thiéblemont et al. (2019) and considering the regional fingerprints of each mechanism contributing to sea-level changes, including the effect of glacial isostatic adjustment (Slangen et al., 2014). This results in regional relative 2020-2100 SLR estimate (median and likely range) of 0.63 ± 0.26 m and 0.37 ± 0.16 m for the RCP8.5 and RCP4.5 scenarios, respectively.

Residual vertical land motion, which is assumed to be due to slow-ongoing geological processes (see subsection 2.1.2.3 and Klingebiel & Legigan, 1992), is assumed to maintain the observed past rate (1.2 ± 0.6 mm/yr) over the 21st century. Due to the large uncertainty (0.6 mm/yr) of the subsidence rate, the stability of the area is not excluded, but associates a very low probability (2.1%). The inclusion of ground motion results in a local relative MSL rise of 0.73 ± 0.27 m and 0.47 ± 0.17 m from 2020 to 2100 for RCP8.5 and RCP4.5 scenarios, respectively (Figure 2.4). Further detail on future SLR is provided in Chapter 5.

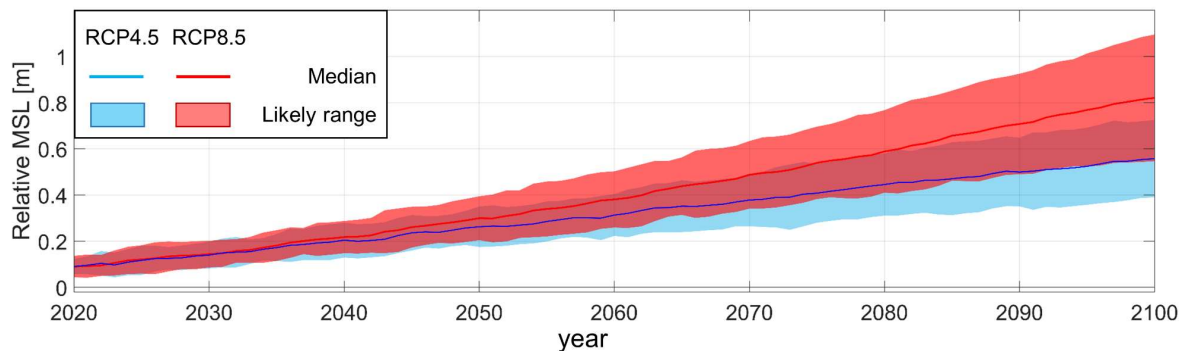


Figure 2.4. Relative mean sea level over the period 2020-2100, including median (solid lines) and likely range (shaded areas) for the RCP4.5 (blue) and RCP8.5 (red) scenarios.

2.1.3.2. Future wave projections (2020-2100)

The assessment of future shoreline evolution at Truc Vert requires a continuous, high frequency (*e.g.* a few hours), wave time series. Bricheno and Wolf (2018) (hereafter BW18) provide state-of-the-art wave projections throughout the 21st century in the Northeast Atlantic region for the RCP8.5 and RCP4.5 scenarios. As part of the *Coordinated Ocean Wave Climate Project (COWCLIP)*, BW18 wave data belong to an ensemble of global and regional wave climate projections, forced with several Global Climate Models and using different wave models. Within COWCLIP, changes were found to be robust in the North Atlantic region, suggesting a slight decrease of annual mean H_s and a clockwise rotation of waves off the Aquitanian coast that is more pronounced for high climate forcing (Morim et

al., 2019). However, amongst the COWCLIP ensemble, to our knowledge, only BW18 produced uninterrupted time series of wave data with sufficient spatial resolution to properly reproduce the wave climate offshore our study site. The continuous hourly time series of wave conditions was produced by BW18 using a dynamical downscaling approach and a nested setup of the WaveWatchIII® spectral wave model (Tolman, 2009). The wave model covers the Northwest European coastal area with a grid resolution of 0.083° (<9 km) and was forced with the downscaled EC-Earth global climate model (Hazeleger et al., 2012). For both RCP scenarios, BW18 model is run from 2006 to 2100 in a regional atmospheric model configuration ($\sim 0.11^\circ$ resolution), in the frame of the EURO-CORDEX project. BW18 also provide the results of a *historic* model run, forced with the EC-Earth model climate, for the period 1970-2004. Such simulation is needed to estimate relative change between past and future wave climate or for the correction of the potential biases between the modelling results and reference wave data (e.g. wave buoy data or modelled wave hindcast), which result from climate models bias (see e.g. Charles et al., 2012). From the BW18 modelling, we extracted wave data (H_s , T_p , and D_m) over 2020-2100 (for shoreline projections) from the nearest grid point to the CANDHIS wave buoy (~ 3 km North-East; Figure 2.1a), in ~ 50 m depth, for both RCP8.5 and RCP4.5 scenarios. To reduce the bias in modelled future waves, we analysed the seasonal quantiles of the 1994-2004 portion of BW18 *historic* wave time series (extracted at the same location as the 2020-2100 wave data) and the seasonal quantiles of the NORGAS-UG hindcast, and set-up a seasonal *quantile-quantile* correction that we applied to the 2020-2100 wave dataset (details in Appendix C1). The corrected BW18 wave time series for RCP8.5 and RCP4.5 scenarios are shown in Figure 2.5b and Figure 2.5c, respectively. Hereon, we refer to BW18 as the corrected wave time series.

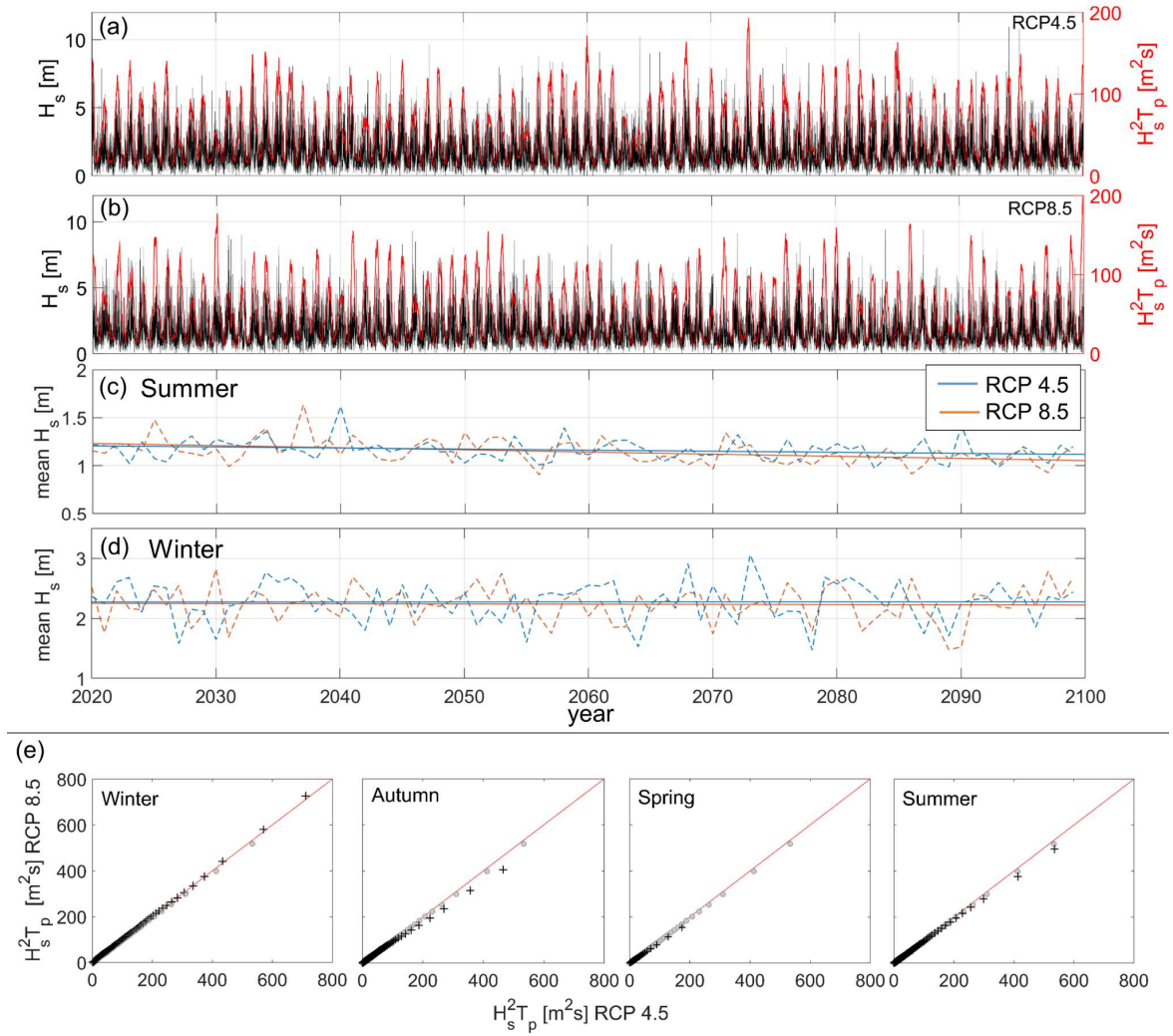


Figure 2.5. Wave data offshore of Truc Vert (44°39'9" N; -1°26'48" W), including: time series of corrected H_s (black lines) and 3-month averaged $H_s^2T_p$ (red lines) for (a) RCP4.5 and (b) RCP8.5 scenarios 2020-2100 Bricheno and Wolf (2018) wave projections; linear trends (solid lines) of annual (c) summer and (d) winter mean H_s (dashed lines) of 2020-2100 corrected Bricheno and Wolf (2018) wave projections, for RCP4.5 (blue) and RCP8.5 (orange) scenarios. For RCP8.5 (RCP4.5), the trend of summer and winter mean H_s are -2 mm/year (-1 mm/year) and -0.05 mm/year (-0.05 mm/year). The trends were tested to be statistically significant (more than 99% significance) using Student's t-tests. (e) Quantile-quantile comparison between RCP4.5 and RCP8.5's 3-month average of $H_s^2T_p$ projections for the four seasons (black crosses) and for the full datasets (grey circles).

2.2. Shoreline change models

The 'equilibrium beach' concept suggests that, when exposed to stationary forcing conditions, a beach develops a mean (equilibrium) profile shape and a respective shoreline position that remain stable over time. As real environmental conditions on time scales shorter than a year (and sometimes longer) are not stationary, the equilibrium condition (profile shape/shoreline position) is dynamic and depends on the mutual interaction between the nearshore hydrodynamics and beach profile shape over time (Wright and Short, 1984). Based on this concept, equilibrium shoreline models compute wave-driven cross-shore

shoreline response of on time scales as short as hours. On longer time scales (decades to centuries) the concept of stationary equilibrium can be used to address chronic beach recession due to SLR, *e.g.* the Bruun (1962) model.

Throughout this thesis, we assessed wave-driven shoreline response using two equilibrium-based models: the Yates et al. (2009) model (Chapters 5 and 6), and an adaptation of the *ShoreFor* model (Davidson et al., 2013; Splinter et al., 2014b) (Chapters 4, 5 and 6). Chronic shoreline retreat induced by SLR was estimated using the Bruun model. Given that the Truc Vert offshore bathymetric iso-contours are essentially shore-parallel, the breaking wave conditions, required to force the wave-driven shoreline models, were computed directly from offshore wave conditions using the Larson et al. (2010) formula. This formula derives from a simplified solution of the wave energy flux conservation equation combined with Snell's law (see Appendix A1). As shoreline change at Truc Vert is known to be dominated by cross-shore sediment transport with negligible gradients in longshore transport (Castelle et al., 2014; Splinter et al., 2014b), longshore sediment transport was not computed. Hereon throughout this thesis, the convention is assumed that a positive (negative) shoreline change rate $dY/dt > 0$ ($dY/dt < 0$) indicates shoreline accretion (erosion). The following subsections describe the two wave-driven shoreline models and the Bruun Rule.

2.2.1. Wave-driven shoreline models

Equilibrium shoreline models parameterize complex sediment transport processes and rely on shoreline data to calibrate empirical parameters. Such parametrization allows for the modelling of shoreline behaviour on time scales ranging from hours to decades at a low computational cost. These models are based on the principle that local wave climate drives the shoreline towards a time-varying equilibrium position at a rate that depends on the instantaneous wave thrust (*e.g.* wave power or energy) available to move the sediment, and the dynamic disequilibrium state of the beach (Wright and Short, 1984). The *ShoreFor* and Yates et al. (2009) models differ primarily in the respective formulations of the (dis)equilibrium state and how these respond to the time-variability of wave conditions.

2.2.1.1. *ShoreFor* model

The *ShoreFor* model (hereafter SF) adopts a disequilibrium condition based on the wave history, expressed as a disequilibrium of dimensionless fall velocity ($\Delta\Omega$) and its standard deviation ($\sigma_{\Delta\Omega}$). The governing equation for shoreline change rate reads:

$$\frac{dY}{dt} = k_s^{+/-} P^{0.5} \frac{\Delta\Omega}{\sigma_{\Delta\Omega}} + b \quad (2.1)$$

where, $k_s^{+/-}$ ($\text{m s}^{-1} \text{W}^{-0.5}$) is a response rate parameter, P (W) is the wave power at breaking, and b (m/s) is an empirical linear term trend. The disequilibrium state at a given time is defined as the normalized difference between the equilibrium and current dimensionless fall velocities ($\Delta\Omega = \Omega_{eq} - \Omega$), calculated from breaking wave conditions. Here we adapt the SF model by using offshore wave conditions rather than breaking ones, following Robinet et al. (2018):

$$\Omega = \frac{H_{s,o}}{T_p w} \quad (2.2)$$

$$\Omega_{eq} = \sum_{i=1}^{2\Phi} \Omega_i 10^{-1/\Phi} \left[\sum_{i=1}^{2\Phi} 10^{-1/\Phi} \right]^{-1} \quad (2.3)$$

where w (m/s) is the sediment fall velocity, and Φ (days) is a beach memory parameter. The equilibrium term (Ω_{eq} , Equation 2.3) is defined by the weighted average of Ω over the past 2Φ days, attributing to Φ the role of ‘memory’ of the beach. As w is assumed constant over time and Φ is a stationary parameter, the dynamic equilibrium state fully relies on the variability of wave conditions, providing SF with the ability to respond to long-term variations of wave regime. The $k_s^{+/-}$ parameter (Equation 2.1) is the shoreline response rate, and assumes different values for accretion (k_s^+ , $\Delta\Omega > 0$) and erosion (k_s^- , $\Delta\Omega < 0$) events, which are driven by different processes associating different time scales. The values of the $k_s^{+/-}$ parameter for accretion and erosion conditions are considered proportional through an ‘erosion rate’ r ($k_s^- = r k_s^+$). The rate r is not a model free parameter but is defined by the wave forcing, and is such that an increasing (decreasing) trend the wave forcing over the simulated period produces an erosive (accreting) trend of shoreline change, and is estimated as follows:

$$r = \left| \frac{\sum_{i=1}^N \langle F^+ \rangle}{\sum_{i=1}^N \langle F^- \rangle} \right| \quad (2.4)$$

$$F = P^{0.5} \frac{\Delta\Omega}{\sigma_{\Delta\Omega}} \quad (2.5)$$

where N is the number of time-steps over the simulated period, F^+ and F^- refer to accretion ($\Delta\Omega > 0$) and erosion ($\Delta\Omega < 0$) events, respectively, and $\langle \cdot \rangle$ denotes an operation that removes the linear trend. Here, the sign of $\Delta\Omega$ does not change the absolute value of $F^{+/-}$. For an extended description of SF the reader is referred to Davidson et al. (2013) and

Splinter et al. (2014b). In SF, the model free parameters to be calibrated at a given site are k_s^+ , Φ and b . While in this work these parameters are calibrated with an optimization algorithm (see Chapters 4, 5 and 6), the SF formulation is such that the optimal values of the free parameters can be derived with simple regression methods (*e.g.* least square method, Davidson et al., 2013). Physically, the $k_s^{+/-}$ ($\text{m s}^{-1}\text{W}^{-0.5}$) is a measure of the efficiency of wave forcing to drive shoreline change (as described by Splinter et al., 2014b), which can also be interpreted as a time scale of shoreline response (Vitousek et al., 2021). Indeed, a low efficiency corresponds to a slow shoreline response and a longer time scale, and *vice versa*. Φ (days) is a time scale for the duration of the impact that past waves exerted on the beach, and provides the ability for the model equilibrium condition to evolve along with long-term wave energy trends. The parameter b (m/s) is a linear term that encapsulates the effect of slow processes, other than wave-driven equilibrium-based, which may drive chronic shoreline change (*e.g.* wind driven sediment transport) and that are not explicitly resolved in the model. The latter parameter is set to $b=0$ for the applications described in Chapters 3, 5 and 6, given the long time scale of the simulations and the absence of secondary processes (*e.g.* longshore gradients in sediment transport) that may drive long-term shoreline trends at Truc Vert.

2.2.1.2. Yates model

In Yates' model (hereafter Y09) the disequilibrium condition is defined as a function of the current shoreline position, and the cross-shore rate of shoreline change is calculated as follows:

$$\frac{dY}{dt} = k_y^{+/-} E^{0.5} (E_{eq}(Y) - E) \quad (2.6)$$

where $k_y^{+/-}$ ($\text{m}^2 \text{s}^{-1}/\text{m}$) is the response rate parameter, E (m^2) is the wave energy, Y (m) is the current shoreline position, and $E_{eq}(Y)$ is the wave energy that would cause no change to the current shoreline position Y . The $k_y^{+/-}$ parameter is analogous to $k_s^{+/-}$ of SF in that it represents the efficiency rate of the incident wave forcing to shoreline change, or a time scale parameter (see the analytical derivation of the Y09 time scale of shoreline response in Vitousek et al., 2021). However, contrary to SF, in Y09 k_y^+ , and k_y^- are independent free parameters. The equilibrium wave energy E_{eq} is related to the shoreline position through the empirical *equilibrium energy function*:

$$E_{eq}(Y) = a_1 Y + a_2 \quad (2.7)$$

where a_1 (m^2/m) and a_2 (m^2) are empirical coefficients. While a_1 and a_2 associate the dimensions of 'energy per meter' and 'energy', respectively, these are to be interpreted as

empirical parameters. In Y09, the values for a_1 , a_2 , k_y^+ , and k_y^- are specific to the site of application, and need calibration against available wave and shoreline observations. Contrarily to SF, the Y09 parameters cannot be calibrated with regression methods but require the implementation of an iterative optimization technique such as the one used herein (Chapters 5 and 6). Physically, $k_y^{+/-}$, once again is a measure of the shoreline reactivity to the incident wave forcing, and is expressed in (m s⁻¹/m). Contrary to SF, here the equilibrium state formulation does not include an explicit ‘beach memory’ term, but implicitly accounts for recent past events through Equation 2.7. As the coefficients of Equation 2.7 (a_1 , a_2) are estimated based on the wave conditions observed during the calibration period and remain stationary over time, the equilibrium wave energy (E_{eq}) is insensitive to wave-climate variability on timescales longer than the calibration period.

2.2.2. Sea-level-driven shoreline recession model

Herein, the chronic beach erosion due to SLR was estimated using the Bruun (1962) model (also known as ‘Bruun Rule’), which is based on the equilibrium beach concept and cross-shore balance of sediment volume. The Bruun model assumes that under rising sea level, on time scales larger than years, the average beach profile translates upwards and landwards, producing a shoreline retreat (dY_{SLR}/dt) given by:

$$\frac{dY_{SLR}}{dt} = \frac{SLR_{rate}}{\tan(\beta)} \quad (2.8)$$

where SLR_{rate} is the rate of SLR (m/time), and $\tan(\beta)$ is the average slope of the active beach profile defined between the landward and offshore limits of sediment exchange. While the reliability of this model is highly debated for its oversimplification of the reality (Cooper and Pilkey, 2004; Ranasinghe et al., 2012), its simple linear formulation has been extensively used worldwide. In addition, Truc Vert beach is a relatively undisturbed beach-dune environment with large accommodation space, which makes this site in line with most of the Bruun Rule underlying assumptions (see Chapter 3). Given the large seasonal and interannual variability of the berm shape and position and the occasional scarping of the foredune at Truc Vert, the dune crest is preferred to define the landward limit of the active profile (Bruun, 1988; Wolinsky and Murray, 2009). Therefore, the active profile is considered to extend between the dune crest and down to the depth of closure (DoC), defined as the depth beyond which morphological changes induced by wave on the beach profile are considered negligible. We estimated the DoC according to Hallermeier (1978), and the corresponding $\tan(\beta)=0.023$ using the beach profile reported in Figure 2.1c.

2.3. Method

2.3.1. Integrating Sea-level rise in equilibrium shoreline models

The wave-driven shoreline models and the Bruun Rule described in the previous section all rely on the equilibrium beach profile concept. Integrating these two models into a unified framework can improve our understanding and predictive skill of future shoreline behaviour. However, given that both models account for wave action, but in different ways and over different time scales, a critical re-examination of the SLR-driven recession process was required. Indeed, SLR-driven erosion (*e.g.* Bruun Rule) can be integrated with wave-driven equilibrium shoreline models in different ways. Chapter 3 provides a detailed analysis of possible approaches to combine wave-driven shoreline change with the effects of SLR based on the decomposition of short- and long-term drivers (*i.e.* wave action and SLR) in the frame of equilibrium shoreline modelling. The analysis includes an idealized application to Truc Vert shoreline change. The application showed that, when the Bruun model's assumptions are satisfied, the wave-driven models combined with the Bruun Rule with no feedbacks between them implicitly model the primary processes driving the sea-level-induced long-term shoreline retreat at this site. Therefore, in the applications illustrated throughout this thesis, the wave- and SLR-driven shoreline responses were computed separately and then combined linearly, so that no feedback mechanisms occur between the models, regardless of the wave-driven shoreline model (*i.e.* SF or Y09).

2.3.2. Global Sensitivity Analysis

Throughout this work, we address the sensibility of long-term shoreline predictions to several sources of uncertainties. The uncertainties associated to model assumptions (epistemic) and unpredictability of climate forcing (intrinsic) propagate through the model resulting in uncertain model results. For a given set of n uncertain input variables (X_1, \dots, X_n), uncertainties on each variable can be represented by a probability distribution covering the range of possible values associated to the variable (Figure 2.6). An ensemble of model results can be the distribution of modelled shoreline positions at a given time (Figure 2.6). While epistemic uncertainties can be reduced by acquiring new knowledge and/or removing simplifying assumptions, intrinsic uncertainties derive from the random nature of some physical processes and cannot be reduced. Regardless of their nature, the uncertainties affecting the input variables can have a different influence on the model outcome.

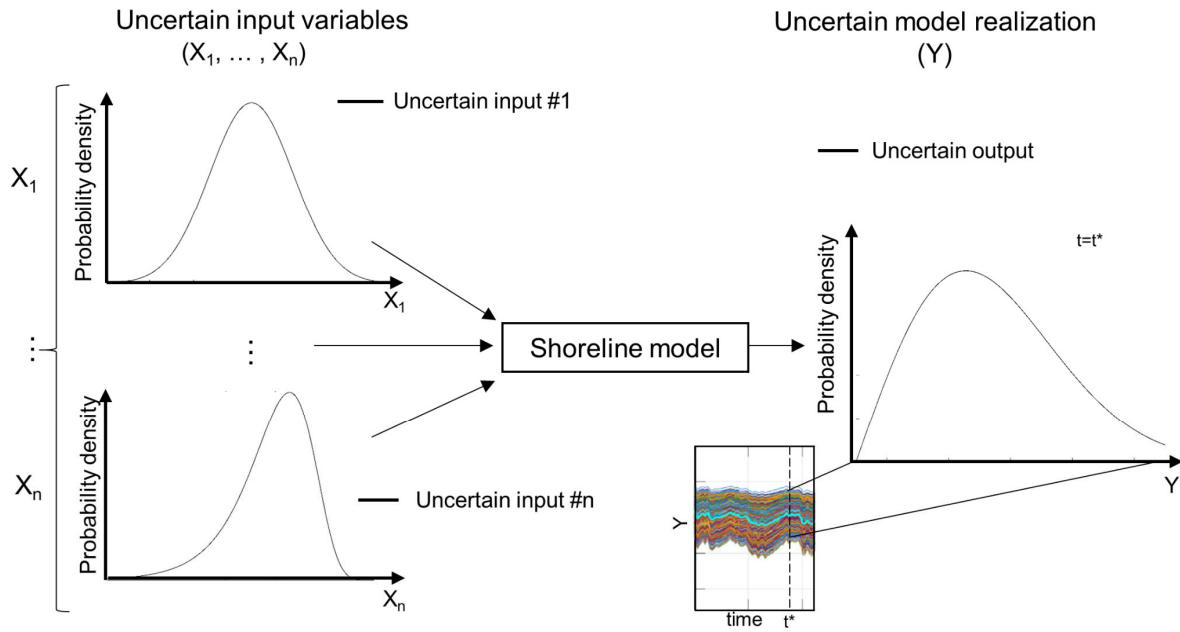


Figure 2.6 Schematic representation of the propagation of uncertainties on n input variables (X_1, \dots, X_n) through a model, producing uncertain outputs (Y), e.g. a distribution of modelled shoreline positions (coloured lines) at a time $t=t^*$. Uncertainties on each variable are represented through the respective probability density function (black curves) and their variance.

In variance-based approaches, the uncertainties associated with a variable X are represented by its variance (σ^2), defined as:

$$\sigma^2 = \frac{1}{N} \sum_{i=1}^N (x_i - \mu)^2 \quad (2.9)$$

where x_i is the i -th sampled value of X , N is the number of samples, and μ is X 's median.

We quantified the different contributions to the uncertainties of modelled shoreline change at Truc Vert beach by performing a variance-based GSA (Saltelli et al., 2008). The variance-based GSA explores the full range of realistic combinations of n uncertain model inputs (X_1, \dots, X_n) with the aim to divide the uncertainties (*i.e.* variance) of probabilistic model results into several portions, each one attributed to an uncertain model input (or a set of inputs). The resulting contribution that an uncertain input X_i provides to the uncertainties in model predictions (Y) is given by the main effect (first-order sensitivity), and by interaction terms (higher-order sensitivity). The main effect measures the sensitivity of model results to variations of the X_i value alone, while the higher-order components measure the additional effects that simultaneous variations of X_i with other uncertain inputs (X_j) have on the results' variance. The latter accounts for the fact these simultaneous variations may drive a larger contribution to the results variance than the cumulated main effects (individual variations) of X_i 's.

Figure 2.7 illustrates schematically the variance-based GSA framework for a set of uncertain input variables (X_1, \dots, X_n), represented by the respective probability density functions, producing an uncertain model output with its associated variance (σ^2). If an uncertain input is fixed to its true value (e.g. $X_1 = X_1^*$), the effects of the uncertainties on X_1 and interactions with other uncertain variables on the results variance (conditional to $X_1 = X_1^*$) are removed (see red lines in Figure 2.7).

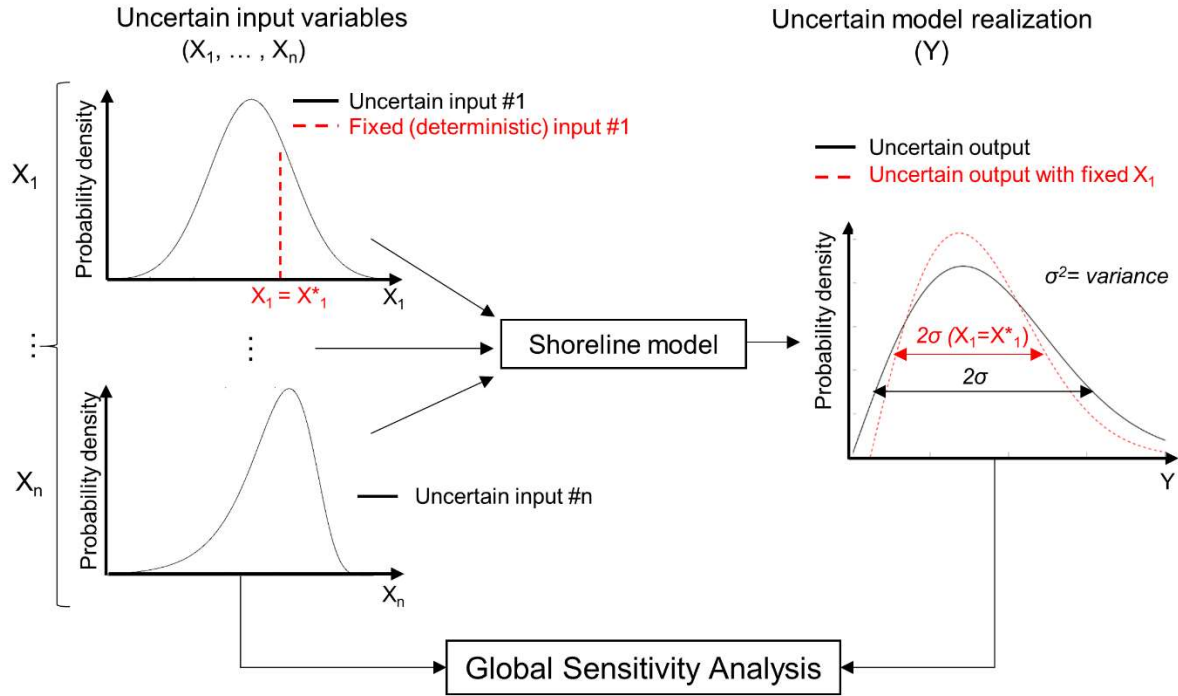


Figure 2.7. Schematic representation of the propagation of uncertainties on n input variables (X_1, \dots, X_n) through a model, producing uncertain outputs (Y). Uncertainties on each variable are represented through the respective probability density function (black curves) and their variance. The scheme shows that fixing the value of a given variable (e.g. X_1) alters the variance of the model outcome (red dashed lines).

Based on this concept, for each uncertain input X_i , the normalized main effect of X_i uncertainties on the model results can be synthesized by a sensitivity measure (S_i), also known as first-order Sobol' indices (Sobol', 2001), expressed as:

$$S_i = \frac{\text{Var}(E(Y|X_i))}{\text{Var}(Y)} \quad (2.10)$$

where Y is the model prediction, X_i is the i -th uncertain input variable, $E(Y|X_i)$ is the expected value of Y conditional to X_i , and $\text{Var}(E(Y|X_i))$ is the variance of the $E(Y|X_i)$ s obtained for all the possible values of X_i . S_i quantifies the percentage of the model results variance that can be attributed to the uncertainties on the variable X_i alone. When X_i interacts with other uncertain inputs (e.g. X_j) within the model, the uncertainties associated with X_j may amplify the impact of X_i on the results uncertainties (and those of X_i may amplify the impact of X_j)

compared to the first-order effects. In this case, the contribution of X_i and X_j to the variance of model results is larger than $S_i + S_j$. The latter contribution as well as higher-order effects can be estimated by calculating higher-order Sobol' indices with formulations analogous to Equation 2.10 (see Appendix A2).

The GSA described above builds on the assumption that all the uncertain input variables are statistically independent from one to another, and the presence of correlations among the uncertain input variables can influence the GSA (Do and Razavi, 2020; Iooss and Prieur, 2019). In the latter case, a more careful interpretation of Equation 2.10 should be given: part of the S_i of a given variable will also contribute to the S_j s ($j \neq i$) of the correlated variables. Therefore, while for statistically independent inputs the sum of S_i s is expected to be ≤ 1 , it may exceed 1 when using even slightly correlated variables. However, interpreting the index S_i as a measure for the reduction in the uncertainty of the output when fixing X_i remains valid in any situation, *i.e.* S_i can be used to identify the input variable that should be fixed to reduce the results variance. Whether dependencies are present or not, the index provides a measure of importance (*i.e.* a sensitivity measure) that is useful for the ranking of the different uncertainties (Da Veiga et al., 2009).

The GSA results are interpreted as the share of variance in modelled shoreline that is due to a given uncertain input variable (or combination of variables), expressed in percentage between 0 and 1. For instance, at a given time, $S_{i,SLR} = 0.3$ means that uncertainties in future SLR alone are responsible for 30% of the variance in shoreline projections. Comparing the values of S_i for all input variables allows ranking them in terms of importance and identify the main drivers of the shoreline prediction's uncertainty, regardless of their absolute magnitude. It is also noted that a direct confrontation of the results from different GSA applications is only possible when the GSAs are performed on the same sets of uncertain input variables. The method can be summarized in three steps:

- 1) Definition of probability distribution associated to each uncertain input variable;
- 2) Generation of ensemble modelled shoreline projections, by means of a Monte-Carlo-based procedure (with accounts for dependence among the input parameters);
- 3) Computation of sensitivity index (*e.g.* Sobol' index) time series for each uncertain input variable.

Chapter 3

3. Integrating SLR-driven recession into equilibrium shoreline models

This chapter provides a re-examination of interacting short- and long-term processes (*i.e.* wave- and SLR-driven) driving shoreline change in the context of equilibrium-based modelling with the aim to answer the methodological question *Q1* highlighted in Section 1.2.

“**Q1.** *How can the effects of short- and long-term drivers (i.e. wave action and SLR) be combined in the context of equilibrium shoreline modelling?*”

The chapter is based on the following conceptual study:

D’Anna, M., Idier, D., Castelle, B., Vitousek, S., & Le Cozannet, G. (2021). Reinterpreting the Bruun Rule in the context of equilibrium shoreline models. *Journal of Marine Science and Engineering*, 9(9). <https://doi.org/10.3390/jmse9090974>

3.1. Introduction

Sandy beaches are dynamic environments, responding to a variety of complex processes interacting on different temporal and spatial scales (Ranasinghe, 2016). As sea-level rise (SLR) is accelerating due to climate change (Oppenheimer et al., 2019), reliable projections of shoreline change on long (decadal to centennial) time scales are critical for coastal managers and decision makers (Toimil et al., 2020; Vitousek et al., 2017a). SLR-driven shoreline recession occurs on time scales from decades to centuries as a result of the interaction between short- and long-term processes (*e.g.* wave action and SLR). Accurately integrating the SLR-driven erosion into more comprehensive shoreline change models is therefore necessary to improve our understanding and the predictability of long-term shoreline evolution in the context of climate change.

For the past 60 years, the Bruun (1962) model has been the most widely used method to estimate long-term beach recession due to SLR, and its use in contemporary applications keeps growing (Figure 3.1). The core assumption of the Bruun Rule is that a beach maintains

a constant elevation profile and migrates upwards and landwards under the influence of SLR, based on the concept of equilibrium beach profile adjustment, under a number of assumptions (outlined in 3.2.1). The validity of the Bruun Rule has been recently demonstrated in laboratory settings under certain conditions (Atkinson et al., 2018; Bayle et al., 2020).

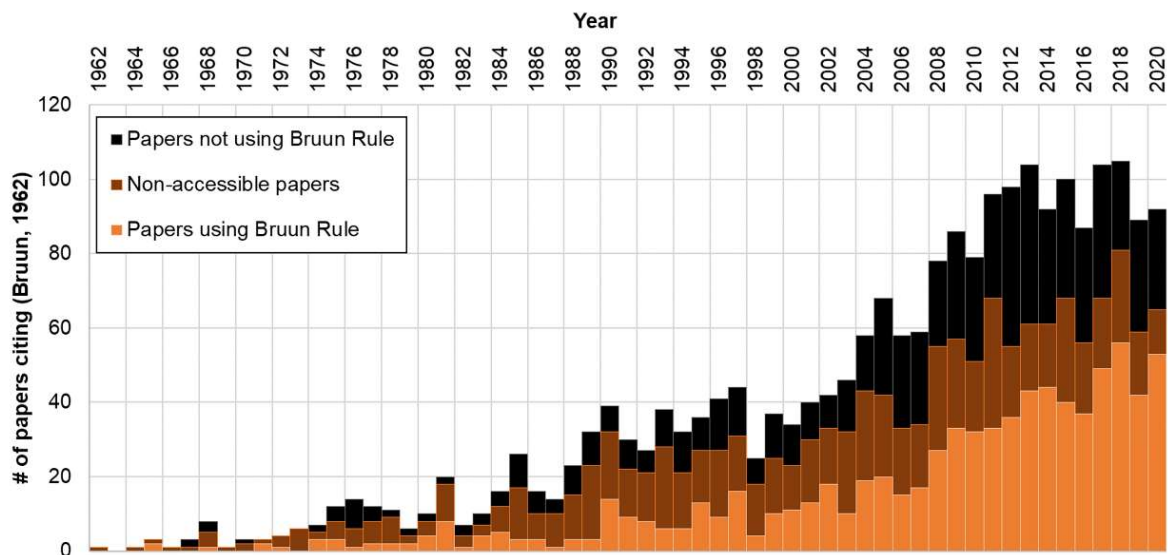


Figure 3.1. History of papers (per year) that cited Bruun (1962) from 1962 to 2020, divided by: papers in which the Bruun Rule is employed (bright orange); non-accessible papers where the use of the Bruun Rule is uncertain (dark shaded orange); and papers citing Bruun (1962) but not employing the Bruun Rule (black). Source: Google Scholar® search engine.

Bruun’s model calculates shoreline recession explicitly as a function of SLR, and implicitly from the long-term effect of combined hydrodynamic processes (*e.g.* waves, tides, currents, etc.). To the authors’ knowledge, the physical mechanisms of shoreline recession driven by the combination of waves and SLR has never been explicitly described.

In recent years, the development of equilibrium-based shoreline models (ESMs) enabled a skilful simulation of wave-driven shoreline change on cross-shore-transport-dominated coasts (Davidson et al., 2013; Jara et al., 2015; Miller & Dean, 2004; Splinter et al., 2014b; Yates et al., 2009). ESMs parameterize complex sediment transport processes and rely on shoreline data to calibrate free model parameters. Such parametrization allows for the modelling of shoreline behaviour on time scales ranging from hours to decades at a low computational cost. These models are conceptually similar to the Bruun Rule in that the equilibrium beach profile adjusts to the forcing conditions. ESMs model the short-term dynamic beach response to incident wave conditions rather than adjustments due to sea-level change. During storms, the upper portions of the beach profile erode, and the sediment is deposited offshore in response to increased incident wave energy (see, *e.g.* Yates et al.

2009). When wave height declines, the sediment is moved back to the shore, driving the profile to its original shape. ESMs show skill in predicting erosion/accretion cycles on hourly (single storm) to yearly/decadal time scales (e.g. Splinter et al. 2014b, Yates et al. 2009, Castelle et al. 2014, and Lemos et al., 2018).

Applying ESMs over long time scales, where sea-level rise becomes important, is a critical step toward more comprehensive long-term shoreline projections. The most widely used solution is to couple ESMs with the Bruun model (Banno et al., 2015; Dean & Houston, 2016; Vitousek et al., 2017b, and Chapters 4, 5 and 6). However, so far, the effects of hydrodynamic processes implicitly modelled by the Bruun Rule have never been explored in detail, and applications coupling these processes disregarded the conceptual relationship between the two models. Therefore, coupling ESMs with SLR-driven recession models requires a re-examination of the basic hypotheses and underlying physical processes of these models to verify their compatibility, modify them if necessary and lay the foundations for further developments. Such a re-examination is particularly warranted given the accelerating SLR trajectories and the increasing reliance on the Bruun Rule (see Figure 3.1).

In this chapter, we present a novel interpretation of the physical mechanism of SLR-driven erosion in the context of equilibrium beach theory, focusing on the interaction between short- and long-term drivers (*i.e.* wave action and SLR). We use the proposed concept (i) to provide a new perspective on the Bruun Rule's underlying physics and (ii) to analyse the integration of SLR-driven recession into ESMs. Finally, we identify and discuss potential future research avenues to extend the validity of integrated ESMs beyond the limited set of conditions where the stand-alone Bruun Rule is applicable. The remainder of the chapter includes a brief review of the Bruun model and the proposed interpretation of the generalized physical mechanism of SLR-driven shoreline recession, with an overview on ESMs and their potential role in quantifying SLR-driven shoreline change (Section 3.2); an analysis of the integrated SLR-driven recession and ESMs in a generalized case and under Bruun's assumptions (Section 3.3); and a model application to an idealized test case at the cross-shore-transport-dominated Truc Vert beach (Section 3.4). The results and implications for future improvements in shoreline modelling are discussed in Section 3.5. Conclusions are drawn in Section 3.6.

Complementary mathematical insights on how the Bruun Rule can be expressed using the proposed conceptualization are included in Appendix B1. Further details on integrating ESMs and SLR-driven recession models with the dynamic feedbacks, described in Section 3.3.2, are provided in Appendix B2.

3.2. Sea-Level-Driven Recession and Equilibrium Shoreline Models

3.2.1. The Bruun Model

The Bruun Rule (1962), introduced in Section 2.2.2, models the long-term (>decadal) shoreline adjustment to SLR. The model assumes that: (i) a theoretical equilibrium beach profile exists and is maintained over time; (ii) sediment volume is conserved cross-shore between the limits of the active beach profile (down to a so-called “depth of closure”); (iii) SLR always induces long-term shoreline retreat (as the beach profile migrates upward and landward with SLR in order to conserve sediment volume); and (iv) there is unlimited available sediment from the subaerial beach (Bruun, 1988, 1983).

The theoretical equilibrium profile shape is determined by the local sediment and wave climate characteristics (Dean, 1991). Therefore, the preservation of the equilibrium profile shape implies that the local wave climate characteristics remain roughly constant. According to the Bruun model, under the assumptions listed above, the long-term beach profile responds to SLR with a landward and upward translation (Figure 3.2), producing a total shoreline retreat (Y_{Bruun}) given by:

$$Y_{Bruun} = \frac{SLR}{\tan(\beta)} \quad (3.1)$$

where $\tan(\beta)$ is the mean slope of the active beach profile between the offshore limit of sediment exchange (*i.e.* the depth of closure) and the stable emerged beach location (*e.g.* emerged berm, dune toe or dune crest). The depth of closure is determined by the local sediment size and the frequency of extreme waves over a given period of time, and thus depends on the local wave climate (Hallermeier, 1978). This last point highlights another strong link between the Bruun model and the wave climate. As the depth of closure depends on the time window observed and the respective distribution of extreme wave events (Nicholls, 1998), the assumption of a constant depth of closure implies a long-term stationarity of the wave climate.

The derivation of the original Bruun model was essentially based on an intuitive unification of physical beach characteristics and nearshore processes (Bruun, 1988). An implicit assumption of the Bruun model is that, in response to SLR, the sediment is redistributed over the profile by the long-term integrated effects of wave action (Bruun, 1988). This mechanism can be interpreted as the sea level setting a new non-equilibrium beach profile state, and the incident wave action mobilizing or relaxing the beach back toward equilibrium.

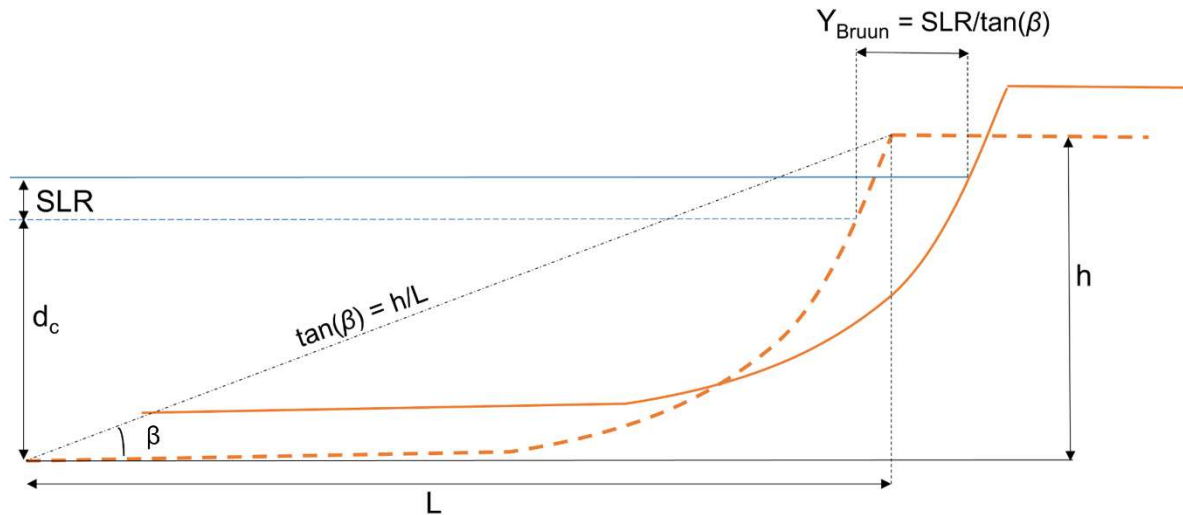


Figure 3.2. Schematic of the original Bruun model, where: SLR is the sea-level rise and Y_{Bruun} the respective shoreline recession over the considered time lap; h and L are, respectively, the vertical and cross-shore extent of the active beach, delimited seaward by the depth of closure (DoC) and landward by the berm, dune toe or dune crest; and $\tan(\beta)$ is the average slope of the active beach profile.

Intuitively, if SLR occurred in the absence of sediment suspension and redistribution processes (e.g. waves), the shoreline regression would only result from the inundation of the landward profile (i.e. passive flooding, see Anderson et al., 2018). This implies that the local wave climate must provide sufficient energy to mobilize sediment and reshape the profile quickly enough for the profile relaxation to keep pace with SLR (Davidson-Arnott, 2005). Therefore, the shoreline recession modelled by the Bruun Rule (Equation 3.1) could be decomposed in two contributions: an instantaneous geometric shoreline retreat due to the flooding of the beach, and a long-term profile relaxation resulting from the cumulated action of nearshore hydrodynamic processes such as wave breaking. While the first is a well understood process (known as passive flooding), there is no explicit description of the physical mechanism driving the second contribution of the Bruunian response to SLR.

Over the past two decades, several alternative interpretations of the model's underlying assumptions were provided to critically evaluate its validity as an independent predictive tool (Cooper and Pilkey, 2004; Ranasinghe et al., 2012; Rosati et al., 2013; Wolinsky and Murray, 2009). However, they did not investigate this second contribution. Instead, they highlighted processes omitted by the Bruun Rule, such as the influence of local geology and sediment supply (Cooper and Pilkey, 2004), landward sediment transport, dune erosion and aeolian sediment transport, and proposed modified versions of the model to include these processes with additional terms (Davidson-Arnott, 2005; Dean and Houston, 2016; Rosati et al., 2013). The Bruun model was developed to account only for the contribution of SLR to long-term coastal recession and does not consider other possible contributions to erosion,

such as the long-term variability of the wave climate (Bruun, 1988). Therefore, the applicability of the Bruun model alone is restricted to a limited range of coasts (Bruun, 1988).

3.2.2. A physical interpretation of the Beach response to Sea-Level Rise

Consider an idealized equilibrium beach profile, where the shoreline (Y) is defined as the instantaneous intersection of the beach profile and mean sea level (Figure 3.3a). Here, the foreshore is defined as the intertidal portion of beach between the mean high water (MHW) level and the mean low water (MLW) level (Figure 3.3). With a stable mean sea level, the local wave climate produces seasonal fluctuations in the cross-shore beach profile around its theoretical equilibrium position. A rise in sea level floods the foreshore (Figure 3.3b), leading to a shoreline recession (Passive Flooding, Y_{PF}) proportional to the average foreshore slope, as follows:

$$Y_{PF} = \frac{SLR}{\tan(\alpha)} \quad (3.2)$$

where $\tan(\alpha)$ is the mean foreshore slope. The shoreline recession due to passive flooding is purely geometric: it is the simple result of the change of the reference shoreline position (*e.g.* MSL), and occurs in the absence of sediment transport (Anderson et al., 2018). However, with respect to the new MSL (MSL' in Figure 3.3b), the beach slope across the profile is generally higher when the profile is concave (Figure 3.3b), as is the case for the majority of real beaches. A generally steeper (more accreted) profile is, on average, more balanced with low energy waves and less balanced with high energy waves (Wright and Short, 1984). Hence, the elevated mean sea-level position (MSL') brings the “beach–wave climate” system into a disequilibrium state where the current wave conditions are larger than in the equilibrium state. Consequently, continuous wave action tends to reshape the beach profile toward its equilibrium shape (Figure 3.3c), driving a further landward displacement of the shoreline position (Wave Reshaping, Y_{WR}). Recall that the beach profile in equilibrium with MSL' (Figure 3.3c) represents the mean position of the seasonal profile fluctuations. Therefore, depending on the energy provided by the incident wave conditions after a rise in sea level, the resulting, time-dependent effect of wave reshaping (here called dY_{WR}) may not immediately reach Y_{WR} (Figure 3.3c), but would be gradually achieved with the cumulative wave action. In this mechanism, Y_{PF} occurs simultaneously with SLR, while the associated Y_{WR} develops on the time scale of several wave events.

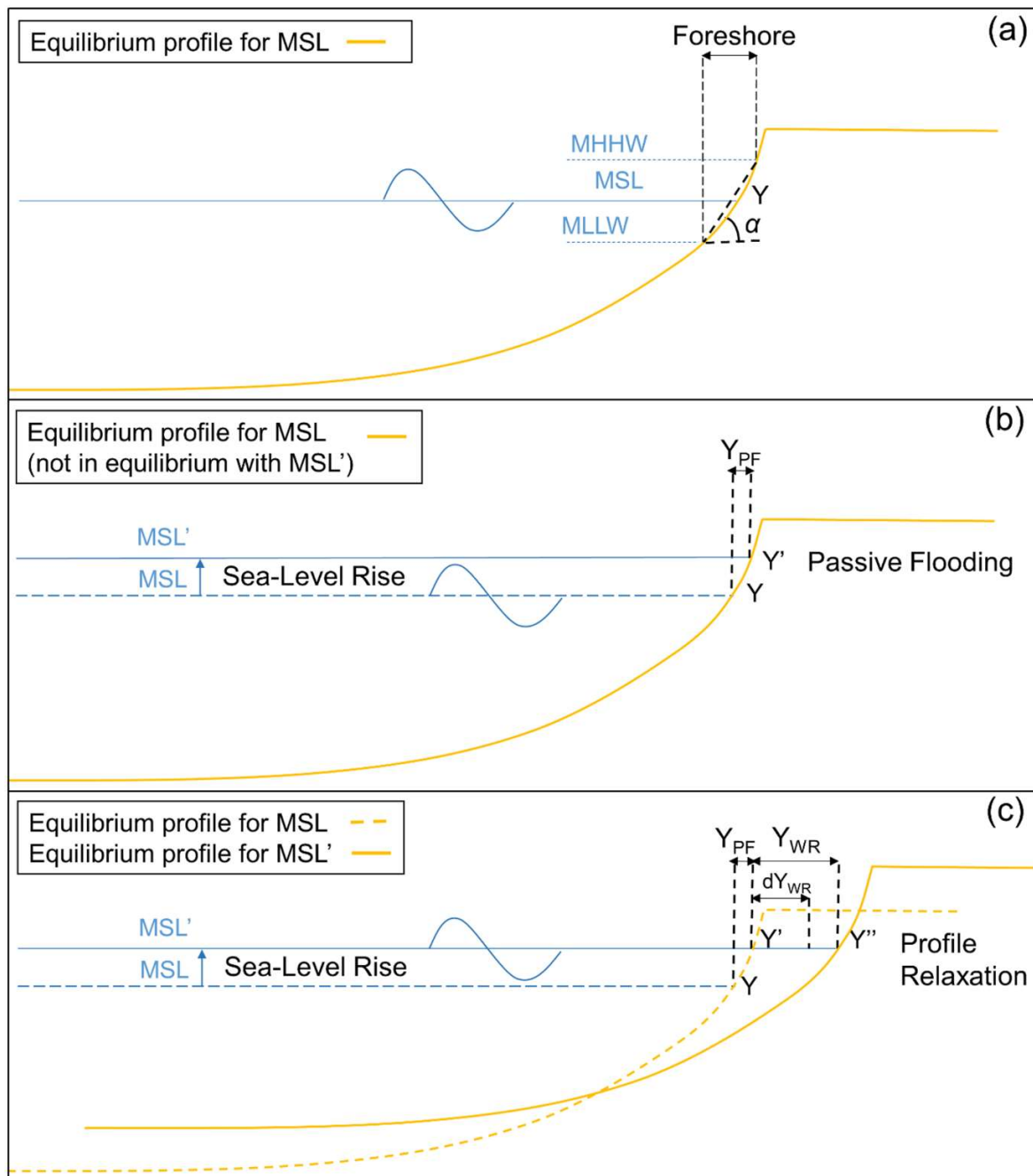


Figure 3.3. Scheme of the SLR-induced beach recession's physical conceptualization: (a) theoretical equilibrium profile for the given mean sea-level, tide and wave conditions; (b) passive flooding of the profile for a given rise in sea level; (c) profile relaxation driven by wave action in response to the disequilibrium between wave climate and the profile in panel (b) with the new mean sea level.

When the Bruun Rule assumptions (Section 3.2.1) are satisfied, namely the assumption of stationary long-term wave climate and constant SLR rate, over periods associating no trends in wave climate (*e.g.* $dT \geq O(\text{year})$), the mean rates of passive flooding and wave reshaping effects are constant (see Appendix B1 for more details). Therefore, under these

specific conditions, on the time scale of dT , the Bruun Rule can be expressed in terms of cumulated passive flooding and wave reshaping effects, as follows:

$$Y_{Bruun} = \frac{SLR}{\tan(\alpha)} = Y_{PF} + Y_{WR} \quad (3.3)$$

Differently from the passive-flooding component (Y_{PF}), the wave reshaping term (Y_{WR}) results from sediment transport processes. In fact, Y_{WR} is the result of the change in wave-energy efficiency on sediment transport over a fixed amount of time, dt , due to the disequilibrium introduced by the sea-level change. Thus, quantifying Y_{WR} requires the evaluation of the disequilibrium increase induced by SLR, and the functional correspondence between shoreline response and disequilibrium state. This is discussed in the next two subsections.

3.2.3. Disequilibrium and beach profile relaxation in equilibrium shoreline models

Equilibrium shoreline models (ESMs) assume the existence of an equilibrium beach profile and rely on the concept of disequilibrium between the current beach state and the current wave conditions (Wright and Short, 1984). A general ESM schematization is given by:

$$\frac{dY}{dt} = k^{+/-} F \Delta D \quad (3.4)$$

where F is the incident wave thrust function, ΔD the disequilibrium state, and $k^{+/-}$ a model free response rate parameter that has different values for accretion ($\Delta D > 0$) and erosion ($\Delta D < 0$) events, and can assume different physical meanings based on the formulation of F and ΔD (e.g. equilibrium time scale, or wave power efficiency). The time-varying disequilibrium condition ΔD can be defined in reference to the current beach profile position (Banno et al., 2015; Falqués et al., 2007; Jara et al., 2015; Miller & Dean, 2004; Toimil et al., 2017; Vitousek et al., 2017b; Yates et al., 2009) or to the wave history (Davidson et al., 2013; Robinet et al., 2018; Splinter et al., 2014b). Recalling Section 2.2.1, typical expressions of disequilibrium conditions based on shoreline position (ΔD_1) and wave history (ΔD_2) are shown in Equations (3.5) and (3.7), respectively:

$$\Delta D_1 = E_{eq}(Y) - E \quad (3.5)$$

where E is the incident wave energy, Y is the current shoreline position and E_{eq} is the wave energy in equilibrium with Y and the beach profile, *i.e.* the wave energy that would cause no change to the current shoreline position Y , defined, for instance, by a linear relationship:

$$E_{eq} = aY + b \quad (3.6)$$

with a and b being two empirical parameters, as in Yates et al.(2009):

$$\Delta D_2 = \left(\frac{H_s}{T_p} \right) - \left(\frac{H_s}{T_p} \right)_{eq} \quad (3.7)$$

where H_s is the incident significant wave height, T_p is the peak wave period and $(H_s/T_p)_{eq}$ is an equilibrium wave condition defined as function of the past wave conditions (*e.g.* a weighted average of the past H_s/T_p over a period Φ , calibrated for the site of application; see, *e.g.* Splinter et al. 2014b).

Depending on the approach, ΔD can thus be quantified in different ways, using either equilibrium wave energy or wave steepness, as in Equations (3.5) and (3.7), respectively. Each approach to evaluate ΔD (and F) is associated to a different physical interpretation to the k parameter (Vitousek et al., 2021). However, regardless of the way it is defined, the disequilibrium state ΔD at a given time expresses the direction of shoreline response as well as the efficiency of the incoming waves in shaping the profile toward its theoretical equilibrium state.

3.2.4. Sea-Level-Rise-Driven Disequilibrium within ESMs

In the context of SLR, the explicit relationship between the disequilibrium state of the beach (ΔD) and the wave-driven shoreline change provided by ESMs can be used to quantify the wave reshaping effect (dY_{WR}) responding to the sea-level-induced disequilibrium. For instance, consider an ESM based on the current shoreline position (Equation 3.5), where the equilibrium wave energy (E_{eq}) is expressed by Equation 3.6. An increase in MSL ($dMSL$) induces passive flooding (dY_{PF}), corresponding to a landward shift of the reference shoreline (Figure 3.3b), *i.e.* a smaller Y value. Recall that this shift represents only a translation of the reference system, with no morphologic change to the beach profile. The second consequence of SLR, observed in Figure 3.3b, is a general increase in the bottom slope relative to the local wave climate propagating over the new MSL. In morphologic terms, this steeper beach profile is no longer in equilibrium for the mean wave climate at the site of interest. In particular, the steeper beach profile is closer to the equilibrium profile for low energy wave conditions, and farther to the equilibrium profile for high energy wave conditions (Wright and Short, 1984). If the mean wave climate does not change, wave events are more likely to result in an overall (erosive) disequilibrium of the “beach–wave climate” system (Figure 3.3c). As the equilibrium condition is defined in terms of wave energy (E),

the SLR-induced disequilibrium can be expressed as a decrease in equilibrium wave energy ($dE_{eq,SLR} < 0$), and can be injected in Equation 3.6:

$$E_{eq} = aY + b + dE_{eq,SLR} \quad (3.8)$$

This indicates that, for a given shoreline position (Y), less wave energy is required to erode the beach and restore the equilibrium. Or, alternatively, for a given wave condition, the mean erosive efficiency of waves is increased, which likely results from an increased bottom slope across the beach profile due to SLR and wave breaking tending to occur closer to the shore. Further insights on $dE_{eq,SLR}$ are provided in Section 3.3.2 and Appendix B2.

3.3. Integrating Sea-Level Rise in Equilibrium Shoreline Models

SLR-driven erosion can be integrated with ESMs using different methods. In turn, the ESMs' response to SLR can be different depending on how sea-level change is implemented in the model and whether the applied disequilibrium condition is influenced by the sea level. Below, we analyse approaches where wave-driven shoreline change and the effects of SLR are evaluated separately and combined linearly (Section 3.3.1), and approaches where the ESM's disequilibrium condition interacts dynamically with the effects of SLR (Section 3.3.2).

3.3.1. Linear Combinations of SLR Effects and ESMs

If the ESM's equilibrium formulation is based on wave history (Equation 3.7), the impact of SLR can be integrated by linearly combining the ESM with passive flooding and wave reshaping models at each time step, and the differential equation for shoreline change reads:

$$dY = (k^{+/-} F \Delta D_2) dt + dY_{PF} + dY_{WR} \quad (3.9)$$

ESMs with disequilibrium conditions that are a function of shoreline position (*e.g.* based on Yates et al., 2009, as in Equation 3.5) can be sensitive to sea-level change or to the permanent flooding dY_{PF} that follows. For this type of ESMs, the shoreline changes caused by short-term (ST) and long-term (LT) processes can be treated as independent components to avoid spurious feedbacks between the ESM and the SLR impact model:

$$dY_{ST} = k^{+/-} F (E_{eq}(Y_{ST}) - E) dt \quad (3.10)$$

$$dY_{LT} = dY_{PF} + dY_{WR} \quad (3.11)$$

$$dY = dY_{ST} + dY_{LT} \quad (3.12)$$

so that the ESM and SLR effects ($Y_{PF} + Y_{WR}$) are computed independently over the simulated period and then simply added. In such approaches, the equilibrium energy term in Equation 3.5 is a function of the sole current shoreline position driven by the wave action in the absence of SLR ($E_{eq} = E_{eq}(Y)$).

For applications where Bruun's assumptions are satisfied, the SLR-driven shoreline retreat in Equation 3.9 and Equations 3.10–3.12 can be given by the Bruun model (Equation 3.3). Such linear combination between ESMs and the Bruun model has been done in several applications (*e.g.* Chapters 4, 5 and 6, Robinet et al., 2018, and Vitousek et al., 2017b). However, these studies did not explicitly acknowledge the physical mechanisms underlying the Bruun model (*i.e.* $Y_{PF} + Y_{WR}$).

3.3.2. SLR Effects and ESMs with Dynamic Interactions

Below, we illustrate an alternative to the approach described by Equations 3.10–3.12, in which short- and long-term shoreline change are resolved in the same equation system at each time step (dt) for ESMs with disequilibrium conditions that are a function of shoreline position (*e.g.* Equation 3.5), thereby enabling feedbacks between the modelled processes. Here, the wave reshaping (dY_{WR}) is explicitly computed at each time step within the ESM as a response to passive flooding (and thus to SLR). If SLR is applied at a given time step, the consequent dY_{PF} is added on the short-term to the ESM (Equation 3.4), accounting for the shoreline retreat induced by passive flooding. If the equilibrium condition is expressed as $E_{eq}(Y) = aY + b$ (as per Yates et al., 2009), then the first (geometric) effect of passive flooding results in a disequilibrium change $dE_{eq,SLR}$, which affects the wave-driven shoreline response and results in the wave reshaping (dY_{WR}) effect, as explained in Section 3.2.4. Quantifying $dE_{eq,SLR}$, *i.e.* the change in equilibrium wave energy due to SLR, is not straightforward. To our knowledge, the literature does not provide a physical expression of the increase in wave-driven erosion efficiency as a function of SLR. Therefore, to go one step further in the quantification of this complex interaction, we make the reasonable (though approximate) assumption that the increase in wave efficiency ($dE_{eq,SLR}$) has the same magnitude as the apparent increase in wave energy associated with the passive flooding shift (*i.e.* $dE_{eq,SLR} = -a dY_{PF}$, which is further explored in Appendix B2). Such assumption is realistic, as it translates that the steepening of the beach profile relative to the risen MSL is equivalent to the effect of an apparent accretion event that wave reshaping tends to reverse. Hence, for a given wave energy, additional erosion must occur (resulting from an elevated SLR), and, consequently, the magnitude of this wave-efficiency-driven

erosion (dY_{WR}) is the same as dY_{PF} . We further discuss the development of this assumption and its consistency with the Bruun Rule in Appendix B2. The assumption above is based on intuitive physical considerations and is used in the present chapter for demonstrational purposes in the following sections. We discuss alternative methods to estimate $dE_{eq,SLR}$ that do not rely on this assumption in Section 3.5. Here, where the disequilibrium condition is based on the shoreline position, the disequilibrium change caused by SLR ($dE_{eq,SLR}$), which produces dY_{WR} , can be expressed adopting the assumption above and injected into Equation 3.5, obtaining:

$$E^*_{eq}(Y, dE_{eq,SLR}) = aY + b + dE_{eq,SLR} \quad (3.13)$$

$$\Delta D^*_1 = E^*_{eq}(Y, dE_{eq,SLR}) - E \quad (3.14)$$

where the (*) symbol indicates that the disequilibrium condition responds to short-term changes in the shoreline position accounting for the geometric changes in the reference shoreline position due to passive flooding. Recall that although the additional SLR-induced disequilibrium is expressed as a function of dY_{PF} , the resulting dY_{WR} is of a different nature (Section 3.2.2). In response to the altered equilibrium owing to SLR, the model captures a time-dependent, wave-driven erosion process at each modelled time step to profile reshaping (dY_{WR}). In this approach, the instantaneous adjustment to SLR is included by adding the sole dY_{PF} term to the ESM and using the equilibrium condition in Equation 3.13:

$$dY = k^{+/-} F(E^*_{eq} - E) dt + dY_{PF} \quad (3.15)$$

Approaches that modified the equilibrium condition of ESMs to integrate additional physical processes have been previously proposed in the literature. For example, Jaramillo et al. (2020) introduced shoreline trends associated with long-term sources and sinks of sediment (*e.g.* gradients in longshore sediment transport or beach nourishments), using an empirical linear term. Other approaches that modified the ESM's disequilibrium condition were applied under the validity of Bruun's assumptions, although they were based on Bruun-like (Antolínez et al., 2019; Banno et al., 2015) or empirical terms (Miller and Dean, 2004; Toimil et al., 2017) and did not identify separate contributions to SLR-driven erosion, such as Y_{PF} and Y_{WR} .

Figure 3.4 illustrates the behaviour of a model using the approach proposed in Equation 3.15 in response to a perturbation of MSL, in a simple idealized setup. Equation 3.15 is forced with constant wave forcing F (where $F = E^{0.5}$ and $E = H_s^2/16$) and a stepwise increase in sea level of 30 cm (Figure 3.4a). In this example, we apply realistic values of the model parameters a , b , k^+ and k^- (see Table 3.1), and a mean wave height H_s of 2.5 m, which are

derived from the test case described in Section 3.4.1. Then, we repeated the application increasing and decreasing the mean wave height by 50% (*i.e.* 3.75 m and 1.25 m, respectively).

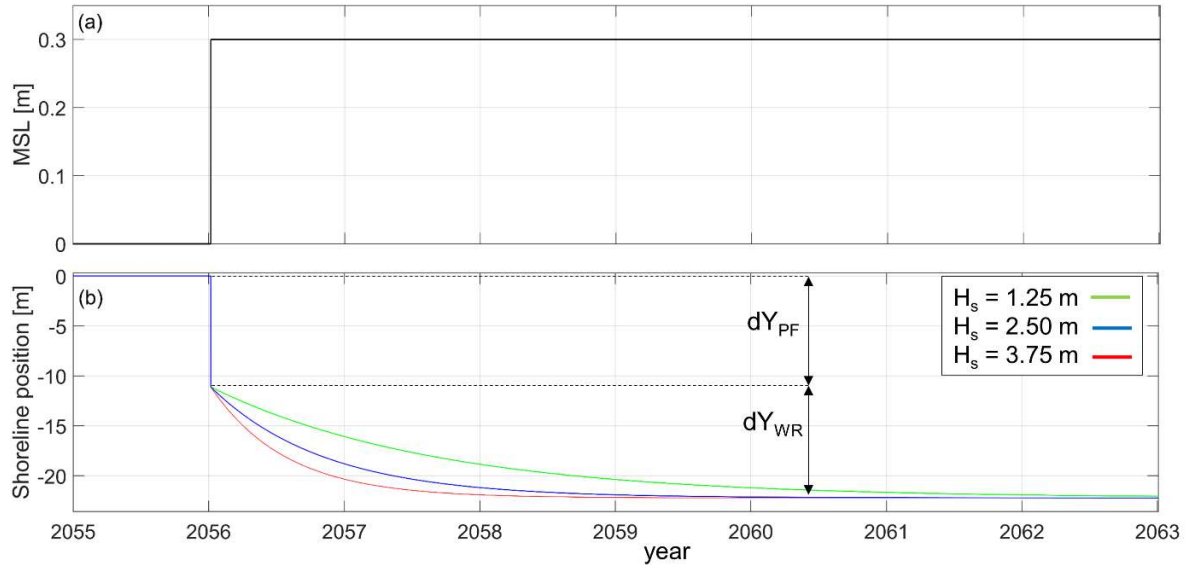


Figure 3.4. Application of the approach proposed in Equation 3.15, using constant wave energy and a 30 cm instantaneous sea-level rise. (a) Mean sea-level time series used in the application; (b) shoreline response showing the instantaneous passive flooding and the progressive effect of wave reshaping for a constant mean incident wave height of 1.25 m (green line), 2.50 m (blue line) and 3.75 m (red line).

Table 3.1. Simulation setup information including the governing equation, disequilibrium approach, SLR approach and calibrated model free parameters. The (*) symbol indicates that the feedback between the models is enabled.

Simulation	Model	ΔD	SLR-driven model	k^+	k^-	a	b	Φ
SF NoSLR	Equation 3.4	ΔD_2	-	1.01^{-8} [$\text{ms}^{-1}(\text{W}/\text{m})^{-0.5}$]	4.40^{-8} [$\text{ms}^{-\Phi}\text{W}/\text{m})^{-0.5}$]	-	-	1187 [days]
SF + B	Equation 3.9	ΔD_2	Bruun					
Y09 NoSLR	Equation 3.4	ΔD_1	-	0.54 [ms^{-1}/m]	0.68 [ms^{-1}/m]	-0.01 [m^2/m]	0.55 [m^2]	-
Y09 + B	Equations 3.10–3.12	ΔD_1	Bruun					
(Y09 + PF)*	Equation 3.15	ΔD_1^*	PF					

After a first period of stable shoreline position, in equilibrium with the applied constant wave energy, Figure 3.4b shows the two separate effects of passive flooding and wave reshaping, *i.e.* an instantaneous retreat corresponding to the immediate passive flooding induced by the stepwise SLR, followed by a gradual erosion produced by the wave action to relax the beach profile into a new equilibrium condition. Such modelled behaviour shows the same characteristics of shoreline response to step-wise SLR observed in laboratory settings under stationary wave conditions (Atkinson et al., 2018). In response to the change

in sea level, the relaxation time of the beach profile toward the equilibrium position associated with different constant wave conditions would have been shorter (longer) for more (less) energetic waves (Figure 3.4b). This means that for a fast-changing sea level and persistent low-energy wave conditions, the instantaneous passive flooding and the slow development of the wave reshaping effect can be more easily isolated. Moreover, such conditions may not allow the full relaxation of the beach profile (and therefore dY_{WR}) until the occurrence of a high-energy wave event (*e.g.* storm).

3.4. Model Application

3.4.1. Test Case

The following application aims at showing that when the assumptions underpinning the Bruun model (Section 3.2.1) are satisfied, the proposed mechanism explains the physics of the Bruun model shoreline retreat. We applied the variants of the combined SLR- and wave-driven shoreline change developed above, in Equations 3.9–3.15, to model 88 years of shoreline change at Truc Vert beach, in southwest France (Section 2.1), in an idealized setup that satisfies the main Bruun model’s assumptions (*i.e.* cross-shore transport only, conservation of a long-term trend in wave energy and constant SLR rate). The following test case is intended as a proof-of-concept study rather than a site-specific hazard assessment. Hence, the results are generalizable to cross-shore-dominated beaches around the world where Bruun’s conditions apply.

ESMs were found to reproduce the shoreline evolution over a decadal time scale at Truc Vert with very good results, using equilibrium based on wave history (Castelle et al., 2014; Splinter et al., 2014b), but also based on the shoreline position (Castelle et al., 2014), *i.e.* using Equations 3.6 and 3.5, respectively. Historical wave conditions over the period between 1st January 2012 and 31st December 2019, associated with no long-term shoreline trend on the same period, are extracted from the NORGAS-UG hindcast (Section 2.1.2.2). A synthetic wave time series, constructed by replicating the historical (2012–2019) time series end-to-end over 80 years, was then used to force the model from 1st January 2012 to 31st December 2099. Such a simplified approach is sufficient to compare different models under a periodic wave climate, which is required for the application of the Bruun model. Breaking wave conditions were computed using the formula of Larson et al. (2010) (Section 2.2). Relative SLR rates were evaluated at this site using the median of SROCC projections

(Oppenheimer et al., 2019) for the high emission RCP 8.5 scenario (Section 2.1.3.1), over the simulation period (Figure 3.5). This corresponds to a SLR rate of ~ 1 cm/year by the mid-21st century (Oppenheimer et al., 2019; Thiéblemont et al., 2019). The main characteristics of the active beach profile were estimated using the topo-bathymetry and a high-resolution digital elevation model described in Section 2.1. The mean profile slope ($\tan(\beta)$) required by the Bruun model was calculated using the beach profile (Figure 2.1c) between the dune toe and the depth of closure obtained from the Hallermeier formula (see Equation 3 of Hallermeier, 1978). The latter computes the yearly depth of closure as a function of the wave height exceeded for 12 hours in a year ($H_{0.137\%}$) and the corresponding wave period. Given that this calculation depends on the period of the wave time series over which extreme wave conditions are extracted, we applied the Hallermeier formula to each year of the available wave data and adopted the median of the resulting values (~ 14 m). The resulting mean profile slope is $\tan(\beta)=0.014$. The time average foreshore slope $\tan(\alpha)$ was estimated from the portion of beach profile between the MHW (+1.39 m Above Mean Sea Level) and MLW (-1.54 m Above Mean Sea Level) using 84 topographic surveys between 2016 and 2019, with $\tan(\alpha)=0.026$.

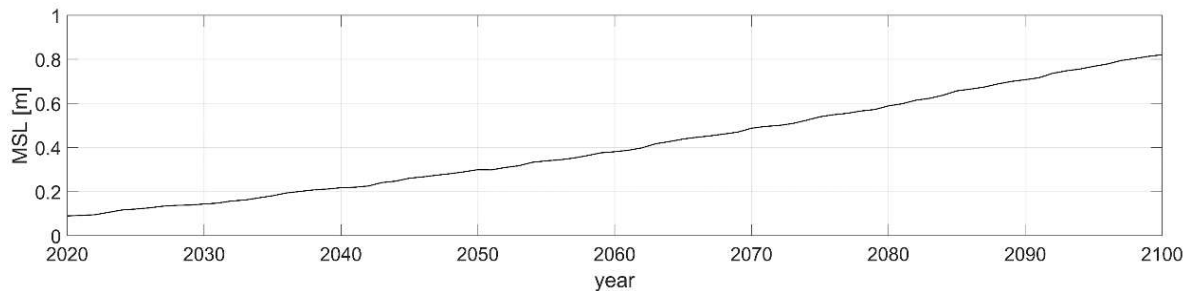


Figure 3.5. Future mean sea level time series estimated at Truc Vert using median SROCC sea-level rise projections in the RCP8.5 scenario.

ESMs were run at a 1-hour time step using the two different disequilibrium approaches described in Section 3.3. In the first approach (herein Y09, referring to the Yates et al. (2009)-like model) the disequilibrium condition is based on a prior shoreline position (Equation 3.5, with $E_{eq} = aY + b$, while the square root of wave energy at breaking is used as forcing (F), in line with models based on this type of disequilibrium condition (Jara et al., 2015; Lemos et al., 2018; Ludka et al., 2015; Yates et al., 2011, 2009). The second approach (herein SF, referring to the Splinter et al. (2014b)-like model) adopts a disequilibrium condition based on the offshore wave history (Equation 3.7), with $(H_{o,s}/T_p)_{eq}$ defined as the weighted average of $H_{o,s}/T_p$ over the previous Φ days, and the square root of wave power at breaking as forcing, similarly to models using this type of approach (Davidson et al., 2013; Robinet et al., 2020; Splinter et al., 2014b; and applications in

Chapters 4 and 5). For each approach, the ESM $k^{+/-}$ and respective parameters (a and b for Y09, and Φ for SF) were calibrated using the Simulated Annealing optimization technique (Bertsimas and Tsitsiklis, 1993) on Equation 3.4, and the Truc Vert mean shoreline position estimated with topographic surveys between 2012 and 2019 (Section 2.1.2.1). The calibration was performed from 1st January 2012 to 31st December 2019, which shows no long-term shoreline trend (Figure 3.6a). For the purpose of the present idealized case application, we assumed that no SLR occurs over the calibration period, so that the models reproduce the shoreline evolution as the only response to the wave climate, with no long-term trend. The optimized parameters are reported in Table 3.1. The resulting Y09 and SF models produced a Root-Mean-Square-Error of 4.68 m and 6.99 m, respectively, and a coefficient of determination R^2 of 0.83 and 0.62, respectively. Over the calibration period, Y09 captured the interannual shoreline variability better, producing a higher R^2 . However, both models visually demonstrated good skill and capture the overall shoreline behaviour (Figure 3.6a). A preliminary simulation over the period 2012–2099 with no SLR was performed for each model to verify that the ESM does not produce any long-term shoreline trend in the absence of SLR (‘Y09 NoSLR’ and ‘SF NoSLR’ in Figure 3.6b and Table 3.1).

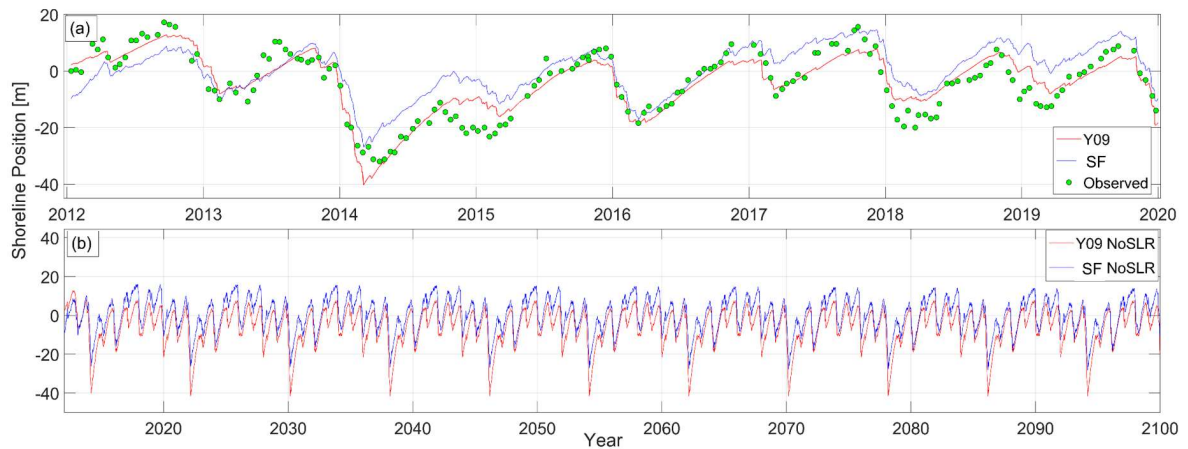


Figure 3.6. (a) Shoreline time series over the period 2012–2019. The red and blue lines represent the modelled shoreline obtained using Y09 and SF, respectively, and the green dots represent the mean shoreline position estimated from topographic surveys. (b) Modelled shoreline time series from 1st January 2012 to 31st December 2099 with no SLR.

3.4.2. Integration of SLR Impact Model into ESMs

Three simulations were run, coupling first SF and Y09 with the Bruun model (B) and no feedback (Equations 3.9 and 3.12, respectively), and then the Y09 with a “passive flooding” (PF) model feeding back into the equilibrium condition (Equation 3.15). As the configuration of the applications satisfies the main Bruun model assumptions (no long-term variability of the wave climate, absence of processes other than SLR inducing shoreline

trends, no short-term sea level fluctuations), the simulation results are expected to be consistent with the Bruun model and reproduce the cumulated effects of Y_{PF} and Y_{WR} .

3.4.3. Results

Figure 3.7a shows that the simulated shoreline positions produced with the model configurations (Y09 + B) and (SF + B) are consistent and in line with the trend estimated by the Bruun model alone (black line). These results show that, in the absence of feedback between the ESM and the SLR impact model (*i.e.* the disequilibrium approach is independent from the SLR-induced shoreline change), the ESM reproduces the short-term shoreline fluctuations and the Bruun model reproduces the long-term Y_{PF} and Y_{WR} contributions.

The combined (Y09 + PF)* models reproduce the effects of SLR on the shoreline consistently with the individual Bruun model (Equation 3.1). This suggests that introducing dY_{PF} (PF model) into the ESM, the consequent disequilibrium increase ($dE_{eq,SLR}$), which reproduces the dY_{WR} , explains the Bruun model's results (Figure 3.7b). As SLR is applied to (Y09 + PF)* at each time step, the relative passive flood dY_{PF} and the resulting wave reshaping (dY_{WR}) are infinitesimal compared to the sole wave-driven shoreline change. The latter is such that the difference between the (Y09 + PF)* and (Y09 + B) results is minimal (Figure 3.7a,b and Table 3.2). However, the difference between the two model results (Figure 3.7c) shows seasonal fluctuations, with larger magnitudes in the summer (low wave energy) and smaller magnitudes in the winters (high energy). In fact, in the (Y09 + PF)* model the wave reshaping (dY_{WR}) produced in response to SLR occurs at a slower rate during low energy periods (summer) and a higher rate during high energy periods (winters) (see Section 3.2.2, Figure 3.3c) compared to the average rate produced by the Bruun Rule (Appendix B1). Such seasonal behaviour highlights the role of wave energy trends (in this case seasonal) on the magnitude of the modelled wave reshaping component (dY_{WR}). Recall that this is a theoretical scenario, in which all Bruun's assumptions are satisfied. In reality, such conditions are not granted, and other processes, such as variability in wave climate, may dominate the evolution of the beach when combined with SLR (Banno and Kuriyama, 2020). Applications of the (Y09 + PF)* to these cases are expected to capture interactions between waves and SLR and produce results that diverge from the Bruun model application.

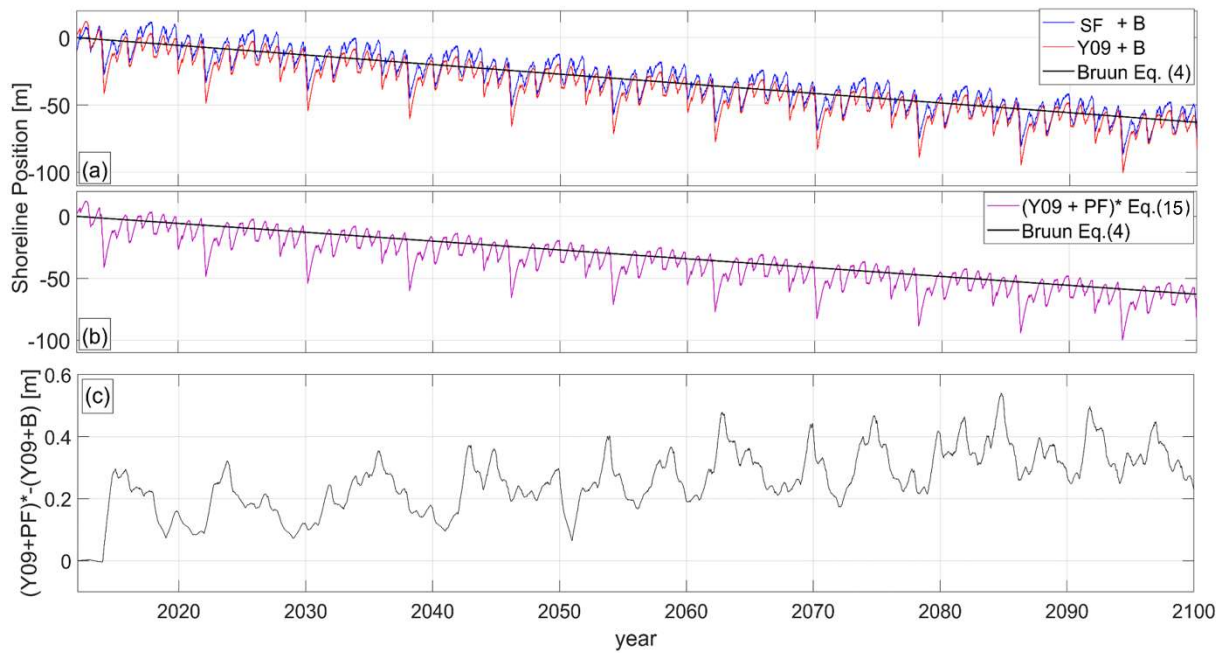


Figure 3.7. (a) Model Results for the Y09 and SF approaches integrated with the Bruun model with no feedback (red and blue curve, respectively), using Equations 3.9 and 3.12, respectively, and the sole Bruun model (black curve); (b) Model results for the Y09 approach integrated with the PF with feedback (red curve), using Equation 3.15, and the sole Bruun model (black curve); (c) difference between the (Y09 + PF)* and (Y09 + B) model results. The negative and positive dS correspond to erosion and accretion, respectively.

Table 3.2. Eight-year averaged shoreline position at 2100, and minimum, maximum and standard deviation of the shoreline position over the last 8 simulated years, for (Y09 + PF)*, (Y09 + B) and the Bruun Rule.

Shoreline position			
Model	8-Year Mean from at 2100 [m]	[min; Max] Over Last 8-Years [m]	σ Over Last 8-Years [m]
(Y09 + PF)*	-58	[-41; -100]	8.7
(Y09 + B)	-58.5	[-41; -100]	8.7
Bruun	-55	[-55; -55]	0

3.5. Discussion

3.5.1. Bruun Rule Interpretation

The idealized model applications suggest that when the Bruun Rule's assumptions are satisfied, the results obtained with (Y09 + PF)* and the Bruun Rule are consistent. This indicates that under these specific conditions the physics of the Bruun model can be explained by our proposed interpretation (*i.e.* $dY_{PF} + dY_{WR}$). The latter does not aim to validate or encourage the use of the Bruun model, but highlights that, in a geomorphology context where the Bruun's assumptions are tenable, our proposed mechanism provides a physical explanation for the magnitudes and time scales of the Bruun Rule's shoreline recession. When the conditions for the application of the Bruun model are not met (*i.e.* short

time scale, long-term variability of wave climate, presence of sources or sinks of sediment, limited accommodation space, etc.), the Bruun Rule is expected to fail (Cooper et al., 2020; Cooper and Pilkey, 2004; SCOR Working group 89, 1991), while, as long as the dY_{WR} component is resolved at the time scale of wave events, the physical mechanism proposed here remains valid.

For instance, current rates of SLR are in the order of mm/year and can increase to cm/year by mid-century (SROCC projections, Oppenheimer et al., 2019). Therefore, SLR can be considered as a quasi-static process when analysing shoreline change by tide- and wave-induced processes. However, our concept can potentially be applied to any time scale, down to a single wave event (hours), as it captures the contribution to dY_{WR} of each wave event in response to changes in MSL. Although on time scales shorter than years the recession due to SLR (*i.e.* dY_{PF} and dY_{WR}) is infinitesimal compared to the wave-driven shoreline change, other irregular processes acting on these time scales (*e.g.* wave climate variability, longshore sediment transport, etc.) and/or short-term sea-level changes (*e.g.* storm surges) may affect the beach equilibrium state and, in turn, the instantaneous dY_{PF} and cumulative dY_{WR} .

Resolving the passive flooding effects on the time scale of wave events (hours) also allows us to model the shoreline response to the lowering sea level, accounting for the varying efficiency of erosion and accretion processes. In fact, lowering sea level would reduce the flooded area (inducing a first seaward shoreline migration), while the lowered MSL associates a reduced slope across the profile (that appears more eroded), which is more balanced with high energy waves and less balanced with low energy waves (Wright and Short, 1984). Thus, the lowering sea level drives the “beach–wave climate” system into a disequilibrium state where the wave-driven-erosion efficiency is reduced. Instead, although the Bruun model can be applied in such case, the underlying physical assumptions are not designed for lowering sea levels (Bruun, 1988, 1983).

3.5.2. Integrating ESMs and SLR-Driven Shoreline Models

Based on the proposed physical interpretation of the SLR-driven shoreline response, our analytical discussion identifies multiple generalized approaches to integrate SLR effects into ESMs where passive flooding and the wave reshaping effect are explicitly resolved. The analysis shows that two approaches can be adopted to include the shoreline relaxation that follows passive flooding (Figure 3.3c, Sections 3.2.2 and 3.2.4) into ESMs. If the ESM disequilibrium condition is based on wave history (*e.g.* Equation 3.7), the integration of

dY_{PF} does not alter the disequilibrium, so that the term dY_{WR} should be computed separately and added. Instead, ESMs relying on the shoreline position to define the disequilibrium condition may require or not the additional dY_{WR} term, depending on whether feedbacks between model equations are enabled or not. In the first two instances (ESMs based on wave history or shoreline position with no feedback) a specific function that quantifies dY_{WR} in response to SLR is required. Instead, when feedback is allowed within ESMs based on previous shoreline positions (Equation 3.15, the model produces dY_{WR} , provided that a relationship between dY_{PF} (or SLR) and $dE_{eq,SLR}$ is assigned. Here, particular attention must be paid to the potential role of wave energy trends in the modelling of dY_{WR} .

It must be noted that using the Bruun model with ESMs (Antolínez et al., 2019; Robinet et al., 2020; Vitousek et al., 2017b) assumes a constant active profile, which implicitly assumes a stationary wave climate. Therefore, applications to regions subject to statistically significant wave climate changes must be performed with care. The available global studies (0.5° to 1.5° spatial resolution) indicate significant changes in wave climate offshore (~200 m depth) of ~50% of the world's coastline over the next century (COWCLIP, Morim et al., 2019), suggesting that significant nearshore wave changes may be expected in some localized areas. In addition, when addressing future shoreline variability (rather than overall trends), changes in the seasonal and interannual variability of the wave climate as well as storminess could modify the shoreline behaviour (Ibaceta et al., 2020; Splinter et al., 2017), and should be accounted. Coupling SLR and ESM models with feedback resolves all SLR-induced shoreline change components on the same short time scale, reproducing the wave-event by wave-event response of the shoreline to passive flooding and capturing the joint effects of SLR with possible changes in the wave energy distribution.

3.5.3. Applications of Integrated Shoreline Models and Uncertainties

While ESMs are generally applicable to cross-shore-transport-dominated open beaches, the quantity, frequency and accuracy of the available shoreline data at a given site are a potential source of model uncertainty (see Chapters 4, 5 and 6, Ibaceta et al., 2020; and Splinter et al., 2013). In real case applications of ESMs (with or without SLR-driven erosion component), such uncertainties can be empirically quantified and introduced in the frame of probabilistic shoreline predictions (see Chapter 4, Kroon et al., 2020; and Ruessink, 2005; Simmons et al., 2017). Here, however, we performed an idealized model application to compare the behaviour of different model combinations, and the evaluation of model

uncertainty, as well as a full validation of the wave-driven models, is outside the scope of this work.

Our idealized model application is forced using a synthetic wave time series obtained by replicating 8 years of wave hindcast data. Although this is a simplistic approach, such wave series ensures that the Bruun's assumption of steady wave climate is satisfied. In real case applications, where the Bruun's assumptions are not necessarily satisfied, the model should be forced with realistic wave time series. Given the key role of short- and long-term variability of the incident wave energy in equilibrium-based models (integrated or not), uncertainties on the inherent variability of the wave climate should be considered (Vitousek et al., 2021). The latter can be addressed by performing ensemble simulations using a large number of different plausible wave series generated, for instance, with statistical methods (Cagigal et al., 2020; Pringle and Stretch, 2021; Vitousek et al., 2021). However, in this proof-of-concept study we aim to analyse the behaviour of integrated models in an idealized context where Bruun's assumptions are satisfied, and the construction of a more realistic synthetic wave time series is beyond our scope.

The SLR-induced shoreline change component is very sensitive to the slope used into the SLR impact model ($\tan(\beta)$ and $\tan(\alpha)$). The Bruun model slope ($\tan(\beta)$) is determined by the limits of the active beach profile. Local scale bathymetric surveys are scarce on most sandy coasts and do not allow for a reliable validation of the seaward limit of the active beach profile. The available global wave and topo-bathymetric merged datasets and local scale bathymetric surveys currently allow for estimates of $\tan(\beta)$ (Athanasidou et al., 2019). However, the accuracy of such data is limited owing to the spatiotemporal variability of the available merged data, merging procedures and estimation of the depth of closure (Athanasidou et al., 2020, 2019). Therefore, the Bruun slope $\tan(\beta)$ is typically associated to large uncertainties (Le Cozannet et al., 2016; Nicholls, 1998; Ranasinghe et al., 2012). The foreshore beach slope, which is adopted in the current model, does not require the estimation of active beach boundaries and can be extracted from topographic profiles (regular enough to account for potential temporal and spatial variability) that can be more easily surveyed by various means at a low cost. Further, recently developed satellite-remote sensing techniques to derive foreshore beach slopes over large scales (Vos et al., 2020) may represent a promising complement to the model developed here. Thus, the ESMs combined with SLR-driven recession (including feedbacks) may result in reduced uncertainty in long-term shoreline change and a potential of application to a much wider range of coasts compared to the models based on the linear sum of the Bruun and ESM projections.

3.5.4. Beyond the Bruun Rule

The conceptualization of SLR-driven erosion provided in this chapter identifies the wave-reshaping process as a key component of this mechanism. The derivation of the wave-efficiency change requires an assumption on the complex interaction between the waves and the changing sea level, which amplifies the impact of the waves on the shoreline position. In this chapter, the SLR-induced disequilibrium that drives wave-reshaping erosion is quantified based on the assumption that such disequilibrium corresponds to the effect of passive flooding on the shoreline. Future research efforts may aim at providing a generalized physics-based expression of this disequilibrium, for instance by investigating wave energy dissipation change in response to the changing bottom slope. For instance, Davidson (2021) recently proposed a model where the influence of the changing sea level and bottom slope on wave energy dissipation is accounted.

It is to be noted that the aim of this chapter is to present a proof of concept, and the next challenges include a validation of the concept against observations. Such validation would require a long-term (*e.g.* decadal) time series of accurate shoreline position (for calibration purposes) with persistent low-energy incident waves (*e.g.* $<1\text{m}$), a fast-changing relative sea level (of the order of centimetres per year) and a relatively stable sediment budget to depict SLR impact at a given field site. To the best of the authors' knowledge, such dataset does not exist. Another avenue is to address the impact of sea-level anomalies of the order of tenths of centimetres on time scales of weeks to months, as observed off the coast of Japan (Banno et al., 2020) or in El Niño Southern Oscillation (Barnard et al., 2017), associated with frequent shoreline measurements. Alternatively, laboratory data produced during reduced scale studies assessing the effects of SLR (Atkinson et al., 2018; Bayle et al., 2020) may be used for the validation of the present framework.

3.6. Conclusions

The Bruun Rule is increasingly used in current coastal impact models, whether standalone (regional to global scale) or coupled to ESMs (local scale), often without full consideration of its underlying physics. This chapter introduces a new interpretation of the SLR-driven shoreline response mechanism based on equilibrium beach theory, identifying two main contributing processes: passive flooding and wave reshaping. It is shown that, when Bruun's assumptions are satisfied, the proposed conceptualization provides a physics-

based background to the Bruun model. Our concept also provides support to the integration of SLR impact into ESMs for future studies, and new ground for the development of more generalized shoreline models. We also showed that ESMs can be used to explicitly compute the portion of sea-level-driven shoreline change induced by the change in wave-erosion efficiency. In particular, using a disequilibrium condition based on the current shoreline position can be efficiently coupled (with feedback) with the SLR-induced passive flooding. Such modelling does not require the knowledge of the active profile (Bruun) slope but, instead, the foreshore slope, which can be easily measured and is typically associated with less uncertainties than the Bruun slope. This can ultimately avoid bias in long-term shoreline projection considering climate change and the sea-level rise.

We addressed the coupling of SLR-driven erosion with ESMs, for cross-shore-transport-dominated coasts. However, our analysis also holds for the new generation of hybrid models that couple ESM with other transport processes (*e.g.* longshore transport), local geology and/or the backing coastal dunes (*e.g.* Antolínez et al., 2019; Robinet et al., 2020; Tran & Barthélemy, 2020; Vitousek et al., 2017b), and to ESMs that continuously adapt the shoreline response to the non-stationary wave climate through time-varying model parameters (Ibaceta et al., 2020). In such models, not only SLR but also other processes can affect shoreline position and, in turn, the equilibrium profile conditions. We therefore anticipate that our findings will help future studies addressing the long-term evolution of wave-dominated sandy coasts as sea level rises.

The findings of this work support the linear combination ESMs with the Bruun Rule (*i.e.* no feedbacks between the models) when addressing long-term shoreline change at Truc Vert beach. This methodological choice is undertaken in the following chapters.

Chapter 4

4. Impact of model free parameters and sea-level rise uncertainties on a 20-year shoreline hindcast

This chapter addresses the uncertainties on a 20-year shoreline hindcast at Truc Vert beach, including uncertainties on model free parameters, depth of closure and sea-level rise, in order to approach the research questions *Q2* and *Q3* C recalled here:

“**Q2.** *How do the relative contributions of uncertain model parameters and physical forcing to modelled shoreline uncertainties evolve over time?*”

Q3. *How do the uncertainties on model parameters and equilibrium approaches relate to the wave climate forcing?”*

The results and discussion of this analysis are based on the following research work:

D’Anna, M., Castelle, B., Idier, D., Le Cozannet, G., Rohmer, J. & Robinet, A. (2020). Impact of model free parameters and sea-level rise uncertainties on 20-years shoreline hindcast: the case of Truc Vert beach (SW France). *Earth Surface Processes and Landforms* 45(8), 1895-1907. [doi:10.1002/esp.4854](https://doi.org/10.1002/esp.4854).

4.1. Introduction

Between 24% and 70% of sandy coasts are estimated to be already under chronic erosion (Luijendijk et al., 2018), increasing the pressure on the development of coastal adaptation measures and the need of long-term shoreline predictions. However, the process of shoreline change modelling inherits uncertainties of driving processes (*e.g.* sea-level rise) as well as uncertainties related to modelling assumptions. Most studies addressing uncertainties of shoreline behaviour at decadal timescales rely on data-driven approaches, based on extrapolated observations or empirical models calibrated with measured data (Allenbach et al., 2015; Casas-Prat et al., 2016; Le Cozannet et al., 2016, 2019; Toimil et al., 2017). Reduced-complexity models (RCMs) have been proposed as a way forward to increase the reliability of long-term shoreline modelling (Castelle et al., 2014; Davidson et al., 2013;

Hallin et al., 2019; Robinet et al., 2018; Splinter et al., 2014b; Vitousek et al., 2017b; Yates et al., 2009). RCMs typically consider general principles, such as semi-empirical and behaviour rules. On cross-shore transport dominated sites, RCMs that address shoreline change from the timescales of hours (storm) to years and decades are often based on the disequilibrium concept (Section 2.2.1), with equilibrium conditions defined in terms of shoreline position (Yates et al., 2009) or wave history (Davidson et al., 2013). This generation of RCMs has been applied successfully at many sites where longshore processes have little influence on shoreline variability (*e.g.* Castelle et al., 2014; Dodet et al., 2019; Ludka et al., 2015; Lemos et al., 2018; Montaña et al. 2020; Robinet et al., 2020; Splinter et al., 2014b). However, these models rely heavily on a data-driven approach to search for the best free parameters. Duration and quality of shoreline data, for which minimum requirements have been subject to debate, are important with model skill increasing with increasing calibration data period and frequency (Splinter et al., 2013). More recently, it has been shown that a subtle changes in the seasonality of storms can have a profound impact on the shoreline mode of variability, for instance from a seasonally-dominated mode (annual cycle) to a storm-dominated (~monthly) mode at Narrabeen, SE Australia (Splinter et al., 2017). This shows that changes in the intra-annual and interannual distribution of wave energy, resulting from natural modes of climate variability or from climate change, is critical to the shoreline mode of response and, in turn, the free parameters of RCMs, although this is still poorly understood.

In this chapter, we analyse the effect of uncertainties in sea-level rise (SLR) rate, depth of closure (DoC) and shoreline model free parameters on a 20-year shoreline hindcast at Truc Vert beach (described in Section 2.1). The analysis is carried out using a state-of-the-art shoreline change model, LX-Shore (Robinet et al., 2018), and performing a variance-based Global Sensitivity Analysis (see Section 2.3.2). The variance-based Global Sensitivity Analysis (GSA) allows assessing the respective contributions of uncertain physical inputs and empirical parameters to the uncertainty in the shoreline hindcast and analysing their variation in time in response to changes in the inter- and intra-annual distribution of wave energy. This chapter proceeds as follows. Section 4.2 briefly recalls the datasets and the GSA methodology, and provides a description of LX-Shore. Section 4.3 describes the design of the probability distributions for each uncertain input variable, and describes the modelling setup used for this study. In Section 4.4, we present the application of the methodology to Truc Vert beach showing the probabilistic modelling results and the corresponding evolution of the sensitivity indices for all variables. Finally, in Section 4.5

we discuss the implications from the perspectives of model calibration and potential forecast application in the frame of a changing climate, as well as the limitations of the present work.

4.2. Data, models and method

4.2.1. Shoreline, wave and sea level data

For this application, we exploited the alongshore averaged shoreline position data derived from monthly and bimonthly topographic surveys (Section 2.1.2.1) and wave hindcast data (Section 2.1.2.2) up to December 2017 to calibrate and force the shoreline model. In order to address SLR-driven shoreline recession, we used the yearly time series of reconstructed relative mean sea level (Section 2.1.2.3) from 1998 to 2018, and the topobathymetry and digital elevation model (Section 2.1.2.1) to assess the main characteristics of the cross-shore beach profile.

4.2.2. Shoreline evolution model

In this study, we used the LX-Shore shoreline evolution model (Robinet et al., 2018, 2020). In LX-Shore, shoreline change is primarily driven by the gradients in total longshore sediment transport and by the cross-shore transport owing to variability in incident wave energy. Herein, LX-Shore was used in a simple configuration with (i) the longshore sand transport module switched off given that Truc Vert is known to be a cross-shore transport dominated site (Castelle et al., 2014; Splinter et al., 2014b), and (ii) breaking wave conditions directly computed from offshore wave conditions using the Larson et al. (2010) formula. In addition to the model presented in Robinet et al. (2018), we included a module accounting for shoreline retreat through the model of Bruun (1962). The study period covered 20 years (from January 1998 to December 2017).

The LX-Shore cross-shore module is the adaptation of the *ShoreFor* (SF) model described in Section 2.2.1.1, which defines the shoreline displacement as a function of the nearshore wave power ($P(W)$) and a disequilibrium condition based on recent past offshore wave conditions. We remind here the governing equation of the SF model adopting the notation from Splinter et al. (2014b):

$$\frac{dY}{dt} = c^{+/-} P^{0.5} \frac{\Delta\Omega(\Phi)}{\sigma_{\Delta\Omega}} + b \quad (4.1)$$

where $c^{+/-}$ ($\text{m}^{1.5}\text{s}^{-1}\text{W}^{-0.5}$) is the response rate parameter (corresponding to $k_s^{+/-}$ in Equation 2.1), and b (m/s) a linear component that accounts for longer-term processes that are not explicitly included in the model, and Φ is the beach memory parameter. The coefficients c^+ ,

b and Φ are the three model free parameters that require site-specific calibration against shoreline data. Hereafter we drop the superscript of c^+ and denote the response rate parameter simply as c .

The contribution of SLR to multi-annual shoreline retreat (dY_{SLR}/dt) is computed in LX-Shore by the means of the Bruun Rule (Section 2.2.2). The Bruun model computes SLR-driven shoreline recession as the ratio between SLR rate (SLR_{rate}) and the average slope of the active beach profile ($\tan(\beta)$), here extending from the dune crest down to the depth of closure (DoC). We estimated a $\tan(\beta) = 0.0235$ (Section 2.2.2).

In LX-Shore, the cross-shore and SLR modules are run separately and then combined linearly. This approach was shown to be suitable to represent the integrated short- and long-term processes at Truc Vert beach (see Chapter 3).

4.2.3. Method (Global Sensitivity Analysis)

When predicting or hindcasting shoreline change, the uncertainties associated to the input variables cascade through the model producing uncertain results. A way to understand how stochastic input variables affect the uncertainty of the prediction is by conducting a sensitivity analysis. In this study, we used the variance-based GSA described in Section 2.3.2 of this thesis. The GSA aims to unravel the uncertainties on the results of a given calculation (model) by decomposing the variance into fractions that are attributed to the uncertain input variables (or sets of input variables). These fractions are used to estimate *first-order Sobol' indices* (S_i), defined by Equation 2.10, which we recall here:

$$S_i = \frac{\text{Var}(E(Y|X_i))}{\text{Var}(Y)} \quad (4.2)$$

where E is the expectation operator, Y is the modelled shoreline, and X_i represents the i -th uncertain variable. We remind that S_i only expresses the primary impact of the variable X_i on the model results uncertainty (Section 2.3.2).

It is worth noticing that during periods when the model results are affected by a large variance, the S_i variations are expected to be small compared to those observed in periods with smaller variance. This effect owes to the nature of the S_i calculation (Equation 4.2) that is inversely proportional to the unconditional model variance. For the present application, we focus on the time varying relative impact of the uncertainty associated to SLR rate, DoC and the cross-shore module free parameters (c , b and Φ) on the resulting modelled shoreline (Y). The effects of SLR induced uncertainties on model results could be analysed by observing the S_i of the ratio $SLR_{rate}/\tan(\beta)$. However, due to the different nature of their

respective uncertainties, we address the relative impacts of SLR rate and DoC separately. The nature of the LX-Shore cross-shore module is such that its uncertain input parameters (c , b , and Φ) are correlated one to the other. To account for this dependence in the computation of the S_i , we relied on the sampling-based algorithm by Li and Mahadevan (2016). We remind here that when using (even slightly) correlated variables, the S_i of a particular variable contributes to the S_i of the correlated variables. Hence, the sum of the S_i s may exceed 1 when using correlated variables. Here, our goal was to conduct a 'Factors' Prioritization' (as defined by Saltelli et al. 2008). At a given time, the Factors' Prioritization identifies the main driver of model results uncertainty (associating the largest S_i), that is, the uncertain input variable that would most reduce the output's variance when fixed to its true value. Figure 4.1 illustrates the generic and case specific methodology developed in the present work. The following section describes the design of the site-specific input probability distributions used in the present study.

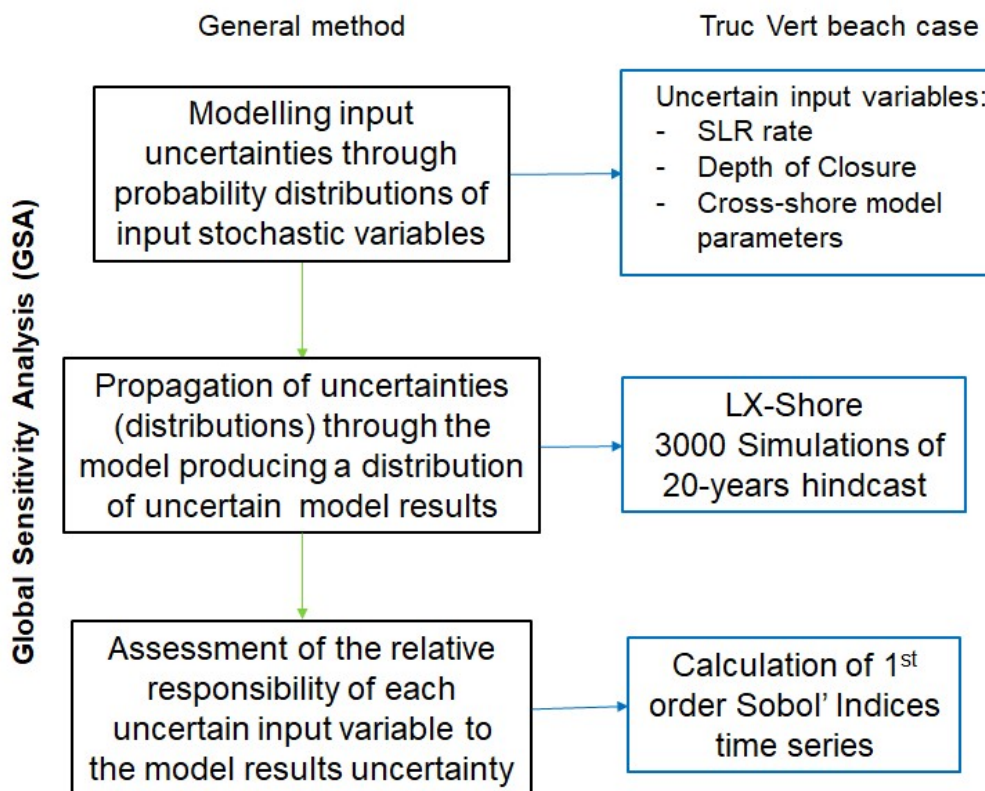


Figure 4.1 Flowchart of the method applied herein, summarized for a general case (black boxes), and for the Truc Vert shoreline hindcast application (blue boxes).

4.3. Input probability distributions

4.3.1. Mean sea-level changes

The uncertainties affecting the reconstructed mean sea-level change account for measurement errors affecting mean sea level in the Bay of Biscay and local vertical ground motions in Lèges-Cap-Ferret. These uncertainties follow Normal distributions due to the methods used in both cases (Rohmer & Le Cozannet, 2019; Santamaría-Gómez et al., 2017), as usually assumed in reconstructions of past sea-level change (Meysignac et al., 2012). Residual uncertainties that cannot be quantified include the possibility that Truc Vert beach is not affected by the same subsidence rate as the Lèges Cap-Ferret GPS station, as they are separated by 8 km. Hence, over the period 1998-2018 the relative SLR rate is approximately constant, and follows a Normal probability distribution with a mean value $\mu_{SLRrate} = 3.31$ mm/year and $\sigma_{SLRrate} = 0.67$ mm/year standard deviation (Figure 4.2b).

4.3.2. Depth of closure

Assuming the Bruun Rule, the uncertainties associated to the impact of past SLR on the shoreline are mostly due to the definition of the equivalent slope used in the formula. The dune crest level is known to have been quite stable over the past 20 years at the Truc Vert because it is part of the mechanically reprofiled dune in the 70s. Hence, the DoC primarily depends on the wave climate. The most common approach relating DoC to the yearly wave climate is using the Hallermeier (1978) formula. Therefore, we calculated the DoC over several portions of the wave climate using a 1-year moving window at a 30-day step. The resulting population of DoC is well fitted by a Gaussian probability density curve with a mean value $\mu_{DoC} = 14.28$ m, and a standard deviation $\sigma_{DoC} = 1.05$ m (Figure 4.2a).

4.3.3. Model free parameters

As numerical models are by definition an approximation of the reality, they are affected by uncertainty. LX-Shore cross-shore module has an empirical nature and required the calibration of three model free parameters (c , b and Φ). The main source of uncertainty in the calibration process lies in the criteria used to assess the optimal combination of model free parameters. We optimized the parameters by minimizing the RMSE (root-mean-square error) between the modelled and the observed shoreline positions over the period 2011-2018 using the Simulated Annealing algorithm (Bertsimas & Tsitsiklis, 1993). Shoreline data estimated from surveys prior to 2011 were not included in the calibration process due to the

scarce confidence associated with the limited longshore coverage of the surveys (see Section 2.1.2.1). The uncertainties related to the quality and limited amount of observations make reasonable to think that other combinations of c , b and Φ producing a RMSE higher than the optimal over the period 2011-2018 may perform better over the actual simulated period. For this reason, we accepted all combinations of parameters producing a RMSE lower than 10 m during the iterations of the Simulated Annealing, in comparison to the minimum RMSE of 7.3 m obtained using the optimised parameters over the 2011-2018 period. The RMSE limit of 10 m was selected based on complementary calibration tests, which showed that optimizing the model parameters over shorter time window (3-year sliding window) between 2011 and 2018 and validating the model over the whole period 2011-2018, produced RMSE ranging between 9.3 m and 13 m. During the calibration procedure the LX-Shore SLR module was activated, so that the effect of SLR is explicitly expressed and segregated from the long-term parameter b . This procedure resulted in a population of quasi-randomly generated parameter combinations to which we fitted an empirical tri-variate probability distribution using a multivariate Gaussian Kernel density estimation (Silverman, 1998; Figure 4.2c-e). The result of this procedure led to the possible ranges of c , b and Φ reported in Table 4.1, which are in line with the ones obtained in Splinter et al. (2014b).

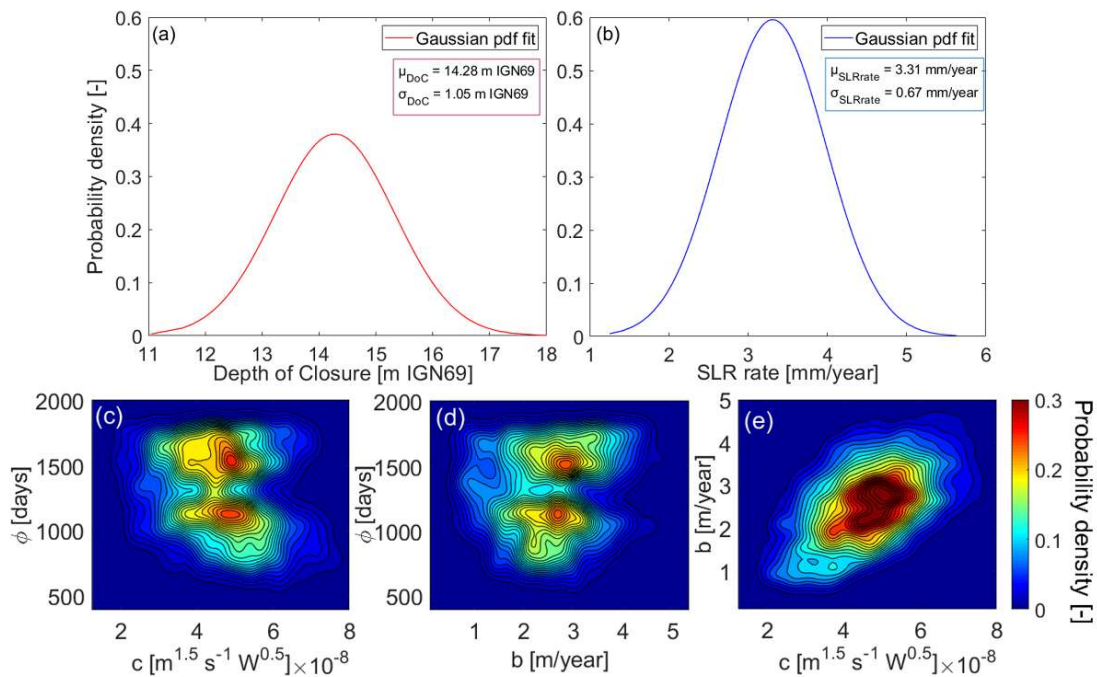


Figure 4.2. Probability density functions of: (a) DoC; (b) SLR rate; (c), (d) and (e) (c, Φ) , (b, Φ) and (c, b) cross-shore module parameters, respectively.

Table 4.1 Best fit parameters from Simulated Annealing, variation range of the cross-shore model free parameters used in the Simulated Annealing process and in the probability distribution

Model parameter	Optimised value	Distribution range	Simulated annealing range
c [$\text{m}^{1.5} \text{s}^{-1} \text{W}^{0.5}$]	4.5217×10^{-8}	$[1.3586; 7.7691] \times 10^{-8}$	$[0.5; 10] \times 10^{-8}$
b [m/year]	2.7479	[0.2158; 4.9678]	[-6; 6]
Φ [days]	1638	[474; 1988]	[400; 2000]

4.3.4. Shoreline modelling setup

An ensemble of modelled shoreline over the past 20 years (1998-2018) was produced by simulating the Truc Vert shoreline evolution for 3000 different combinations of the uncertain input parameters SLR rate, DoC, and (c , b , and Φ). We generated the combinations of input parameters sampling 3000 values from their respective probability functions. Model outputs were stored at intervals of 7-days (Dt) over the simulated period to build the shoreline position time series. To compare the 3000 modelled shoreline trajectories, a position at a certain reference time (t_0) had to be defined. The starting date of the calibration period (5th January 2011) was chosen both to fit with observations during the calibration procedure and because uncertainties in the model results increase towards the past, where shoreline measurements are less reliable or not available (Figure 4.3b).

4.4. Results

4.4.1. Shoreline evolution

Shoreline change computed with all 3000 combinations of uncertain parameters showed similar behaviours with only notable differences in long-term trends, and amplitude in seasonal and interannual variability (Figure 4.3b,c). Results show a 4-year accretion phase from 2001 to 2005 in response to a series of low-energy winters (Figure 4.3a), which is consistent with the observed trend at Porsmilin beach in Brittany, exposed to a similar wave climate as Truc Vert (Dodet et al., 2019). In contrast, large erosion was systematically modelled during the outstanding high-energy winter of 2013-2014. Model results are also in line with the ranges of possible shoreline positions estimated from data prior to 2011, which was not used for the calibration, but are still believed to provide a realistic indication on shoreline variability.

4.4.2. Global Sensitivity Analysis

The reference position at the reference time t_0 represents the point from which all modelled shorelines are projected (backwards and/or forward) in time. Therefore, there is

no uncertainty (variance) of model results at t_0 , and the selection of t_0 affects the evolution of the results variance over the simulated period and the corresponding Sobol' indices. The following analysis of the results is carried out using firstly the observed position at the calibration starting date as reference (t_0) for the modelled shoreline time series (Figure 4.3b), such that the variance equals 0 at the beginning of the 2011 year (Figure 4.3c).

The S_i time series corresponding to each uncertain input variable are shown in Figure 4.3d-h. The uncertainties in the 20-year shoreline hindcast are dominated by the variations of the cross-shore model free parameters (c , b and Φ). For the parameters b , c and Φ (Figure 4.3d-f), S_i evolves more or less gradually with some seasonal variability during the farther past period (1998-2006) when the variance of the model results is relatively large (Figure 4.3c). Subsequently (2006-2018) much larger seasonal and interannual variabilities are observed, associated with smaller model variance, suggesting that model sensitivity strongly depends on wave conditions. In contrast, the S_i curves of SLR rate and DoC remain roughly constant below 1% during the entire simulated period ($S_{i,SLRrate} \in [0; 0.1]$; $S_{i,DoC} \in [0.001; 0.1]$) implying that on these timescales shoreline change is not sensitive to SLR. Such low impact of SLR on the model uncertainty was expected: it is due to the limited uncertainty associated with both DoC and SLR rates relative to the other variables during the analysed period. This becomes evident when comparing the mean and 99th percentiles of long-term SLR-induced erosion (2.7 m, and 3.8 m) with the effects of b (51.3 m, and 88.3 m) over the 20-year simulated period.

We observe that during 1998-2006 the variation of parameter b is responsible for most of the variance in modelled shoreline, with S_i regularly increasing towards the past from 61% to 94%, and a notable step during the 2000-2001 high-energy winter. The regularity of the b 's trend in this period is due to its linear nature (in the model, b represents the long-term shoreline trend, see Equation 2.1, and is not dependent on wave conditions). Over this 1998-2006 period, the sensitivity of the model results to parameter c also slightly increases (towards the past) with substantial seasonal variations, with S_i maximised at 63% during the 2000-2001 high-energy winter. From 2006 onwards, when model variance is lower, the model sensitivity to c shows large inter- and intra-annual variability exceeding 90% during the high-energy winters (2013-2014 and 2015-2016) and lowering to approximately 5% during milder conditions between some winters. Over the same period, b 's S_i shows a somewhat mirrored behaviour to c 's S_i . The influence of beach memory parameter Φ on the results' uncertainties gradually increases from 10% in 1998 to 52% in 2006, and oscillates between 10% and 82% afterwards, and is sometimes in phase or out-of-phase of b and c S_i s.

In Table 4.2 we provide the average S_i values for c , b , and Φ over the periods from January 1998 to December 2005, from January 2006 to December 2017 and the outstanding winter December 2013 to March 2014 (as an example of short term period).

To examine the influence of t_0 on the time evolution of the Sobol' indices, Figure 4.4a-c show S_i time series for the full spectrum of possible reference times t_0 (for which the modelled shoreline equals 0) within the simulated period, for b , c and Φ . On these plots, a diagonal intersecting the horizontal axis ($Dt=0$) at a certain t_0 represents the time series of S_i s computed observing the results in reference to t_0 . Consequently, a horizontal section of the plots in Figure 4.4a-c ($Dt = \text{constant}$) represents the time series of S_i s calculated on progressive variations of the model variance (over a time Dt) rather than the total variance. Results show that the sensitivity of the modelled shoreline to c (Figure 4.4a) increases in the short-term (see the horizontal sections with Dt approaching 0), and both seasonal and interannual variability are striking along the diagonals. The variation of b 's S_i (Figure 4.4b) appears once again mirrored in respect to c 's S_i , providing weak contribution to the uncertainties in the short term and growing (backwards and forward) in the long-term, showing that the uncertainties associated to b become dominant only on the long-term for each given t_0 . Figure 4.4c shows that Φ 's S_i is mostly low with consistent seasonal variability, and that it only becomes dominant when b and c are both small. All plots show evident break-lines in S_i , corresponding to 2000-2001, 2006-2007 and 2013-2014 and 2015-2016 high-energy winters, highlighting the importance of outstanding winters on modulating model sensitivity to the different free parameters.

Figure 4.5 shows the time series of progressive S_i , calculated on the variation of modelled shoreline (dY) at each output time step Dt (*i.e.* horizontal section at $Dt = 1$ week in Figure 4.4a-c), to disregard the cumulative effect of the variance over time. It is observed that parameter c controls the response rate of the shoreline to the incident wave power (P , see Equation 2.1), driving shoreline changes at the time scales of storms (days). This illustrates how the variability of the c parameter over a time Dt is responsible for almost the entire model variance, although we also observe occasional drops in c 's S_i corresponding to low-energy periods following high-energy events (Figure 4.3a). On this one-week time scale, the effect of the linear term b is negligible, and the variations of its S_i is only related to the effect of the two other uncertain parameters (c and Φ). This is better observed in Figure 4.6, which shows a 90 days average of the relative S_i s between 2013 and 2014.

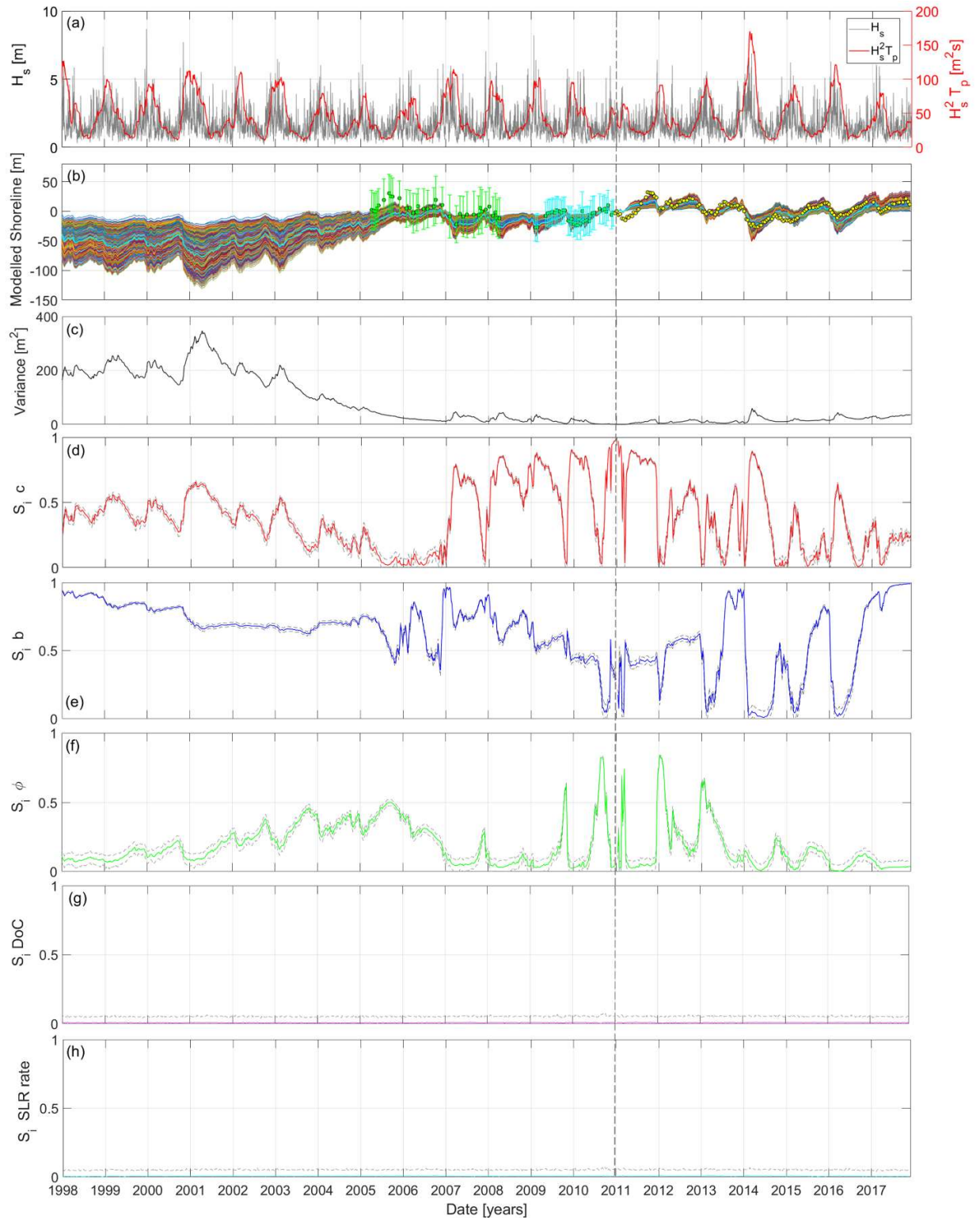


Figure 4.3. (a) Simulated offshore wave conditions synthesized in the average value $H_{s,o}^2 T_p$; (b) Envelope of 3000 simulated shoreline over the period 1998-2018 (coloured lines), and observed average shoreline positions between 2005 and 2017 (green before 2011 and yellow dots after 2011) with bars indicating the estimated maximum possible range of variability due to longshore variability of the shoreline, corrected to account for limited size of the survey coverage ($\pm 28\text{m}$ in the period 2005-2008, green bars, and $\pm 18\text{m}$ in the period 2008-2011, cyan lines); (c) model variance time series; (d) to (h) 1st order Sobol' index time series for the uncertain input variables with 3%-97% confidence interval derived from a bootstrap-based approach with 200 bootstraps (grey dash lines). $dY/dt > 0$ and $dY/dt < 0$ indicate accretion and erosion, respectively. The vertical dash line indicates the t_0 .

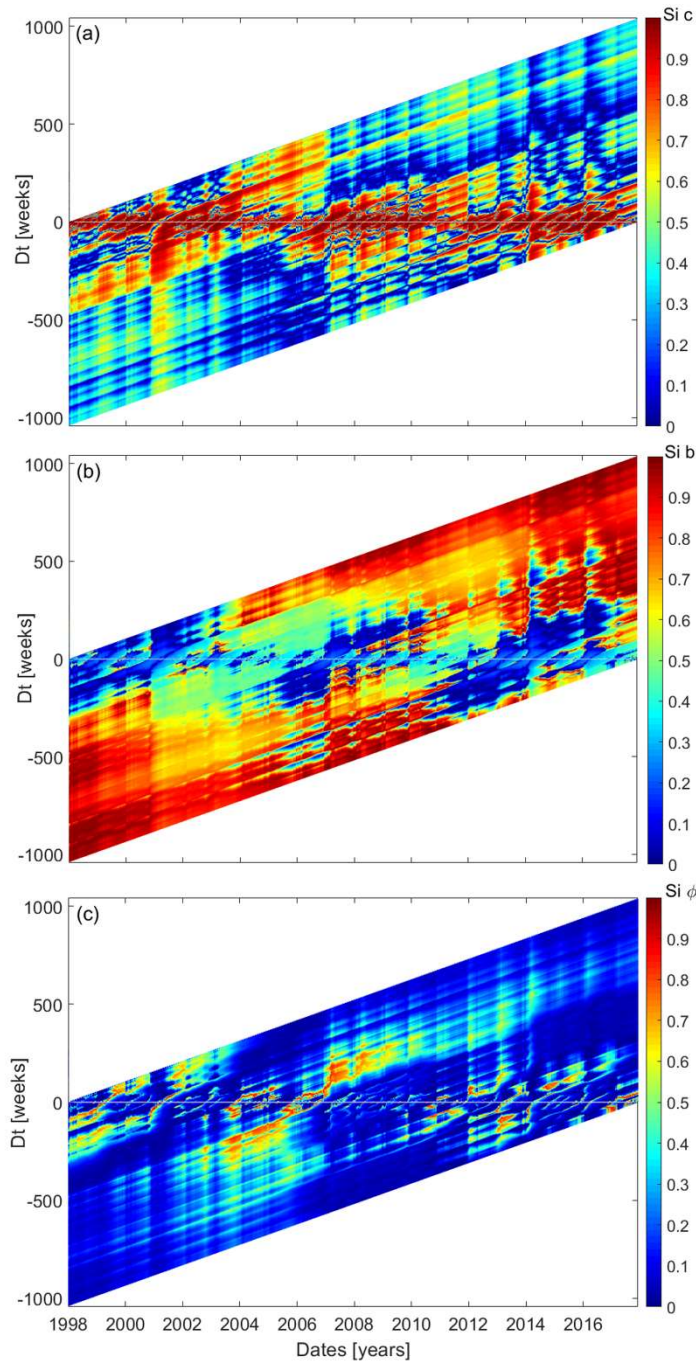


Figure 4.4. Full spectrum of 1st order Sobol' indices time series calculated for (a) c ; (b) b ; and (c) Φ parameters, where diagonals represent time series corresponding to each possible reference starting time.

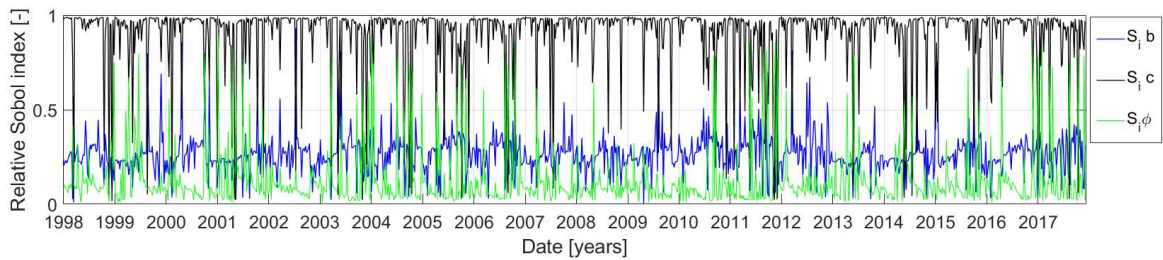


Figure 4.5. Progressive ($Dt = 1$ week) 1st order Sobol' index time series for c , b , and Φ , corresponding to the horizontal section for $Dt=1$ week of the plots showed in Figure 3.4a-c.

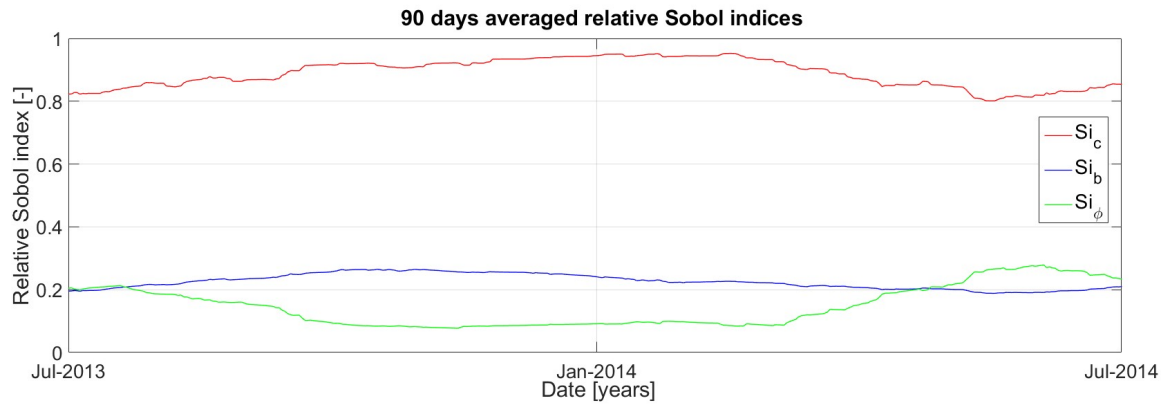


Figure 4.6. Time series of 90 days average relative Sobol' indices, over the period 2013-2014 for c , b and Φ .

Table 4.2. Mean 1st Sobol' indices for c , b and Φ , and mean model variance over selected periods of simulation.

Period	Mean $S_i c$ [-]	Mean $S_i b$ [-]	Mean $S_i \Phi$ [-]	Mean Model Variance [m ²]
1998- 2005	0.35	0.74	0.23	165.14
2006-2017	0.42	0.54	0.15	16.57
2013-2014	0.53	0.29	0.10	24.73

4.5. Discussion and conclusions

4.5.1. Sea-level rise

The GSA performed on the 20-year shoreline hindcast at Truc Vert beach indicates that the uncertainties of shoreline evolutions are primarily controlled by the uncertainties of the free parameters of the wave-driven (cross-shore) model. This means that the contribution of the uncertainties associated to the past SLR rate and DoC, which influence SLR-driven chronic erosion, are negligible comparing to the uncertainties affecting the wave-driven model parameters on these timescales. This is not surprising given that SLR acts on long timescales and that uncertainties of SLR estimates over the period of interest. For instance, previous work showed that uncertainties of future shoreline change, as sea level rises, are primarily related to interannual variability of storm events during the next decades (Le Cozannet et al., 2016). The effects of SLR uncertainties may only emerge from natural shoreline change variability during the second half of the 21st century (Le Cozannet et al., 2016), together with uncertainties related to future emission gas scenario and validity of SLR-driven erosion model (Le Cozannet et al., 2019). It is however important to note that current sea-level projections may underestimate future SLR as they may slightly underestimate future ice-sheets melting (Jevrejeva et al., 2019), thus reducing the timescales of emergence of widespread SLR-induced sandy shoreline retreat. Therefore, a relevant

research avenue is to account for wave-driven shoreline uncertainties that were addressed here together with updated SLR projections (Toimil et al., 2020). Building on state-of-the-art RCMs of shoreline change such as LX-Shore and others (*e.g.* Antolínez et al., 2019; Robinet et al., 2018; Vitousek et al., 2017b) will also allow addressing the natural variability of uncertainty contributions, as the respective contributions of the processes driving shoreline change (*e.g.* longshore and cross-shore processes, sediment supply from nearby rivers) and their related uncertainties are essentially site specific.

4.5.2. Wave-driven model uncertainties and implications for model calibration and shoreline projections

Our results show that the respective contributions of the wave-driven model free parameters to shoreline change uncertainties are strongly variable in time. The response rate parameter c which represents a measure of the rate at which the shoreline responds to incident wave conditions and the beach memory parameter Φ reflecting the impact of antecedent wave conditions (Splinter et al., 2014b) both show a strong and mirrored seasonality of their impact on the modelled shoreline. The linear parameter b , which accounts for the effects of long-term processes that are not included in the model, shows complex patterns. In fact, despite the simplicity of b 's role in the governing equations (Equation 2.1) and the consequent long-term effects of its variability on the model variance, its impact relative to the other uncertain variables (S_i) is not obvious. The parameter b dominates the shoreline variance during extended low-energy periods, and its S_i dramatically drops during high-energy winters. This large time variation of the free parameter uncertainties explains why the calibration period is critical to shoreline model skill when performing shoreline hindcast (Splinter et al., 2013). Given that b is expected to account for other processes that are not taken into account in the model, the growing sensitivity of the model results on b towards the past (and future) also suggests that improving wave-driven shoreline change models may significantly reduce the uncertainties affecting the modelled shoreline positions at the timescales of years to decades. Such improvement would limit and delay the long-term effects of b overwhelming the effects of other variables contributing to the model uncertainties, allowing to address the model sensitivity to other processes at large time scales. A better understanding of short-term processes would reduce uncertainties on the c parameter, significantly reducing the uncertainties at seasonal scale. The generally low sensitivity of modelled shoreline to Φ , in spite of its large variability (Figure 4.2c-d), is consistent with the findings from Splinter et

al. (2014b) for high-energy beaches and large values of Φ . A complementary analysis of Φ 's S_i evolution, where we only addressed the model sensitivity using $\Phi < 1000$ days, showed only an increase in model sensitivity to Φ during extended low-energy periods (*i.e.* 2001-2006) with no other substantial change comparing to Figure 4.3d-f, once again supporting Splinter et al. (2014b) results.

Our result show that the intra-annual and interannual distribution of wave energy is critical for the model free parameter uncertainties, which also explain why even subtle changes in wave energy distribution can dramatically change the mode of shoreline response as observed by Splinter et al. (2017). To further investigate the role of interannual wave energy variability on parameter uncertainties we simulated two idealized cases preserving the model setup used for the real case and using the same distributions of uncertain model inputs, but using different distribution of wave energy. In the case of shoreline change forced by a seasonal wave climate extracted from the real wave time series (including winter 1998-1999) in the absence of interannual energy variability (Figure 4.7a-c), the S_i s are quasi-steady with only little seasonal variability, once again with mirrored behaviours of b 's and c 's S_i . In addition, consistently with the above discussion, Figure 4.7b,c shows that an increase (decrease) in offshore wave energy results in higher (lower) model sensitivity to c , and *vice versa* to b . A second idealized case was run to address the effects of interannual distribution of wave energy alternating high-energy and low-energy winters every four years (Figure 4.8). In this case, the winter 2002-2003 was extracted from the real wave climate to represent a low-energy winter, and the same conditions were amplified by 40% in significant wave height and 20% in peak wave period to generate a high-energy winter. In addition to the effects observed in the previous idealized case, large interannual variations of the S_i s are observed. We also observe the cumulative effect of b , which gradually overwhelms those of c on the long-term.

The dependence of the model sensitivity to the wave energy variability also has implications for shoreline change projections in the frame of climate change, which are regionally variable. In some regions the wave climate is expected to be only slightly affected by climate change, such as in the Bay of Biscay where Truc Vert beach is located (Charles et al., 2012a; Perez et al., 2015). In these regions, efforts to predict future shoreline change on open coasts should be put into improving wave-driven models and in particular better accounting for other long-term processes that are implicitly accounted through b . In contrast, in some regions of the world, climate change will have a profound impact on wave climate and extremes and, in turn, on the uncertainties associated to the model free

parameters related to the wave energy (e.g. c and Φ in the LX-Shore model), introducing an additional component of uncertainty to the projection.

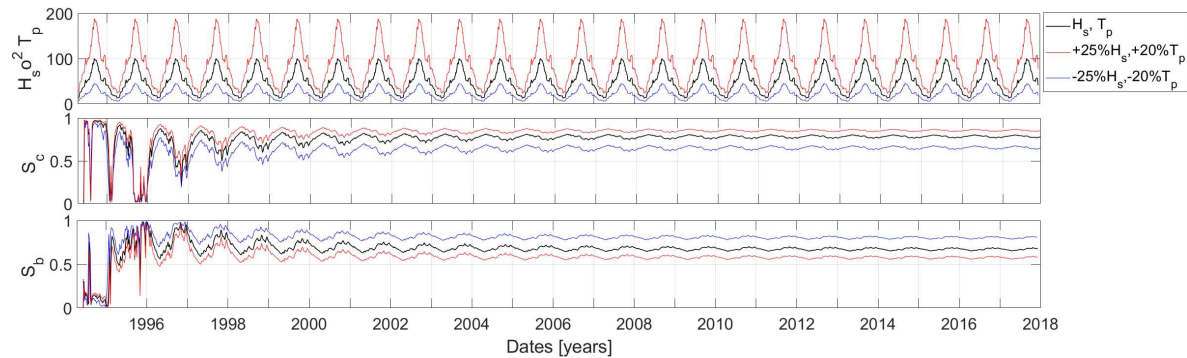


Figure 4.7. Idealized seasonal wave climate, with increased (red curves) and decreased (blue curves) intensity. (a) Simulated seasonal wave conditions; (b) and (c) Sobol' indices of the free parameters c and b , respectively.

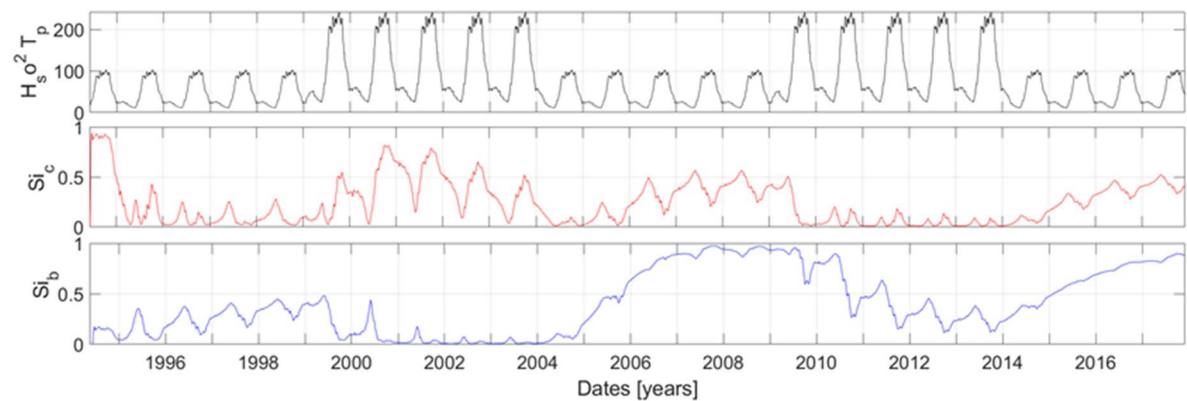


Figure 4.8. Idealized alternate low-energy and high-energy winters every 4 years. (a) Simulated seasonal wave conditions; (b) and (c) Sobol' indices of the free parameters c and b , respectively.

4.5.3. Assumptions and limitations

The LX-Shore cross-shore module used herein is based on disequilibrium conditions determined by the recent history of dimensionless fall velocity at the site (Equation 2.3) *i.e.* on antecedent wave conditions, regardless of the previous shoreline position. In contrast, other existing equilibrium models assume that the disequilibrium is determined by current shoreline position (Yates et al., 2009). Hence, although these two models show similar skill and shoreline change patterns at Truc Vert (Castelle et al., 2014), there is an additional source of uncertainty related to the choice of the approach for defining the disequilibrium state. The application of the method proposed in this chapter using a different disequilibrium approach would allow assessing the results sensitivity to the choice of the model, similarly to the analysis carried out by Le Cozannet et al. (2019) and Montañó et al. (2020). However, this belongs to future research.

Here, we only addressed the first-order order Sobol' indices for the uncertain inputs, and combined effects of variables uncertainties (higher-order Sobol' indices as well as total effect indices) were not evaluated. An assessment of higher-order effects would require a larger number of model results to calculate the conditional variances. Estimating the minimum amount of simulations required for a reliable evaluation of second-order Sobol' indices would need a convergence analysis, consistently with the analysis performed by Benaichouche and Rohmer (2016) on several test cases, which may result in a prohibitive number of simulations. The first-order Sobol' index is still an informed choice to rank the importance of correlated model inputs, when defined by using average local variances instead of specifically located variances (Li and Mahadevan, 2016; Saltelli and Tarantola, 2002). However, addressing higher-order Sobol' indices may confirm the low-impact character of certain variables (such as Φ) within a factor fixing setting as described in Saltelli et al. (2008). The possibility to address second-order Sobol' indices can be explored in future research works. A second limitation of the present work is that the results reported here apply to a given high-energy open beach, which is known both to be cross-shore transport dominated and to respond predominantly at the seasonal scale (Splinter et al., 2014b). Other beaches, such as Narrabeen (SE Australia) may respond at the scale of single storms and be more sensitive to variations of the model parameter Φ (Splinter et al., 2014b), resulting in very different probability distributions of model free parameters or be affected by other processes such as longshore sand transport (Harley et al., 2011). Further research work is required to understand the uncertainties on different types of coastal setting.

4.6. Conclusions

A Global Sensitivity Analysis was performed on a 20-year shoreline hindcast at Truc Vert beach. We computed the first-order order Sobol' index time series for all the identified uncertain input variables, namely sea-level rise rate, closure depth and wave-driven model free parameters (c , b and Φ). We found that, on this 20-year time span, shoreline change uncertainties are primarily the result of uncertainties on the wave-driven free parameters, with the influence of SLR and DoC uncertainties being negligible. However, the respective contributions of the uncertainties related to each model free parameter are strongly variable in time, in response to the intra-annual and interannual distribution of incident wave energy. This means that such shoreline change models need to be trained with long-term time series comprising a substantial number of representative high-energy and low-energy storm

seasons. In addition, our results have strong implications from the perspective of shoreline projections in the frame of climate change. In some regions of the world, climate change may largely affect wave climate and extremes, which in turn challenges the validity of calibration parameters in the future and, ultimately, the validity of projections. The approach developed herein is applicable at other sites worldwide using any fast running shoreline model. Therefore, application of this methodology to coastlines controlled by different driving processes is encouraged to address the genericity of our results.

Despite the negligible impact of SLR uncertainties on the results obtained here for the past evolution of Truc Vert shoreline, the large uncertainties associated with future SLR may play an important role on long-term shoreline projections. However, particular attention must be paid to the response of equilibrium shoreline models and their uncertainties to wave climate variability, which is addressed in the subsequent chapter.

Chapter 5

5. Uncertainties on future shoreline projections to 2100

This chapter presents an analysis of the uncertainties associated with future shoreline evolution at Truc Vert beach over the 21st century in the frame of climate change, where wave-driven shoreline change is resolved using two different equilibrium approaches. This analysis provides elements to answer the research questions *Q2*, approached in Chapter 4, *Q3* and *Q4* (Section 1.2) recalled below.

“Q2. How do the relative contributions of uncertain model parameters and physical forcing to modelled shoreline uncertainties evolve over time?”

Q3. How do the uncertainties on model parameters and equilibrium approaches relate to the wave climate forcing?”

Q4. On which time scale the uncertainties on SLR become the primary driver of the uncertainties on modelled shoreline?”

This part of the manuscript is based on the following research paper:

D’Anna, M., Castelle, B., Idier, D., Rohmer, J., Le Cozannet, G., Thiéblemont, R., and Bricheno, L. (2021). Uncertainties in shoreline projections to 2100 at Truc Vert beach (France): Role of sea-level rise and equilibrium model assumptions. *J. Geophys. Res. Earth Surf.*, 126, e2021JF006160, <https://doi.org/10.1029/2021JF006160>

5.1. Introduction

In a context of changing climate predictions of long-term (decadal to centennial) shoreline change are increasingly sought. When addressing long-term shoreline projections, limits in our understanding and modelling capacity of the primary processes driving shoreline change, together with the uncertainties associated to the future climate (*e.g.* carbon emission scenario, sea-level rise, storminess, etc.), undermine the confidence in future shoreline estimates proportionally to the time scale of application (Ranasinghe, 2020; Toimil et al., 2020). While probabilistic frameworks are rapidly replacing deterministic

approaches for shoreline projections, most applications focused primarily on future sea-level rise (SLR) (e.g. Le Cozannet et al., 2016,2019; Vousdoukas et al., 2020) and changes in frequency/intensity of storms (e.g. Allenbach et al., 2015; Casas-Prat et al., 2016) and their uncertainties, and did not resolve wave-driven shoreline change explicitly. However, short- and long-term variability in wave energy, as well as the chronology of storm events, can strongly affect future shoreline patterns (Cagigal et al., 2020; Coco et al., 2014; Dissanayake et al., 2015; Vitousek et al., 2021). Recently, Cagigal et al. (2020) developed and used a stochastic climate-based wave emulator to generate ensembles of wave time series at several beaches, and addressed shoreline response to different wave chronologies. Based on the same emulator, Vitousek et al. (2021) analytically investigated the uncertainties in shoreline predictions associated to the inherent variability of the wave climate in the context of equilibrium shoreline modelling. Kroon et al. (2020) showed the significant effects of wave-climate variability and model uncertainty on the short-term (1 year) probabilistic assessment of coastline change at the Sand Engine (Netherlands). The authors used a one-line model, *i.e.* resolving wave-driven longshore sediment transport gradients and resulting shoreline evolution, as this stretch of coast is longshore transport dominated.

Currently, there are no studies addressing the time evolution of the effects that uncertainties in future SLR and model parameters have on shoreline projections to the end of the 21st century while explicitly resolving wave-driven shoreline response. The recent development of equilibrium shoreline models opened the way to skillful simulation of wave-driven shoreline response on cross-shore transport dominated sites, which are ubiquitous worldwide, on time scales from hours (storm events) to decades, with low computational cost (Antolínez et al., 2019; Davidson et al., 2013; Lemos et al., 2018; Robinet et al., 2018; Splinter et al., 2014b; Vitousek et al., 2017; Yates et al., 2009). Equilibrium shoreline models are based on the principle that the shoreline dynamically moves towards a time-varying equilibrium condition (Wright & Short, 1984), which can be expressed as a function of the current shoreline position (Yates et al., 2009) or antecedent wave conditions (Davidson et al. 2013). While the two latter equilibrium formulations show similar skill against shoreline observations on a multi-year timescale (Castelle et al., 2014; Montaña et al., 2020), the accuracy of one approach over the other in different wave forcing scenarios is unclear, particularly on long timescales (multi-decadal). In addition, in this type of models, sediment transport processes are described by semi-empirical relationships that require site-specific calibration against observed shoreline data, introducing further

uncertainty (see Splinter et al., 2013 and Chapter 4). Implementations of cross-shore equilibrium models into probabilistic frameworks recently showed that uncertainties in the calibration of model free parameters (see Chapter 4) and in future wave conditions (Vitousek et al., 2021) have a significant impact on model predictions. In addition, recent studies found an inherent connection between the seasonality of wave climate and shoreline model parameters that defines the frequency of shoreline response, for several beaches along the Australian coast (Ibaceta et al., 2020; Splinter et al., 2017).

SLR-driven shoreline retreat is often estimated using the Bruun (1962) model. This model relates the rate of shoreline erosion to the SLR rate and the average slope of the active beach profile, defined between the seaward and landward limits of cross-shore sediment exchange. The seaward limit of the active beach profile is commonly identified by the depth of closure (Hallermaier, 1978). As local scale bathymetric surveys are scarce and the estimation of the depth of closure is essentially empirical, the active beach profile slope is typically associated with large uncertainties (Nicholls, 1998; Ranasinghe et al., 2012).

In this work, we aim at deepening our understanding in the role and impact of different uncertainties in shoreline projections. We perform a Global Sensitivity Analysis (GSA) (Saltelli et al., 2008) to unravel the respective contributions of SLR, depth of closure, and shoreline model free parameters uncertainties. The framework is applied to the cross-shore dominated Truc Vert beach (SW France) using two different wave-driven shoreline models, the Bruun model, and recent SLR and wave projections for two future Representative Concentration Pathways (RCP) scenarios. The likely range provided along with median SLR estimates in IPCC reports does not cover the full uncertainty range of mean sea level projections. Hence, there remains a probability of up to 33% that sea-level rise exceeds the likely range. Therefore, we also assess shoreline projections in the deterministic high-end SLR scenario, which remains unlikely but plausible and is associated with large impacts (Stammer et al., 2019). The remainder of this chapter includes: an outline of Truc Vert beach, the data, the shoreline models, and the method (Section 5.2); a description of the GSA input variables' probability distributions and the numerical modelling setup (Section 5.3); and the presentation of the results (Section 5.4). Discussion and conclusions are provided in Section 5.5 and 5.6, respectively.

5.2. Material and method

5.2.1. Waves and sea level data

In this study, the shoreline projections are assessed at Truc Vert beach, described in Section 2.1. The alongshore averaged shoreline position data from topographic surveys described in Section 2.1.2.1 are used to calibrate the wave-driven shoreline models. Wave hindcast data (Section 2.1.2.2) is also needed in order to: (1) run the shoreline models on the past period and estimate the distribution of the model parameters; and (2) support the correction of the wave projection dataset. In order to address SLR-driven shoreline recession over the models calibration period, we used the time series of reconstructed relative mean sea level (Section 2.1.2.3). The main characteristics of the cross-shore beach profile are assessed using the topo-bathymetry merged with the UAV-derived digital elevation model of the upper beach and dune (Section 2.1.2.1). The wave projections modelled by Bricheno and Wolf (2018) (hereon denoted as BW18) and the relative MSL based on SROCC projections (Section 2.1.3) from 2020 to 2100 are used to force the wave- and SLR-driven shoreline models, respectively, for the RCP4.5 and 8.5 scenarios.

5.2.2. Shoreline models

We assessed wave-driven shoreline response using the two equilibrium-based models described in Section 2.2.1: the Yates et al. (2009) model, and the adapted *ShoreFor* model. Breaking wave conditions were computed directly from offshore wave conditions using the Larson et al. (2010) formula and chronic shoreline retreat induced by SLR is estimated using the Bruun (1962) model (Section 2.2.2). Herein, the wave-driven shoreline models (short-term) and the Bruun Rule (long-term) were run individually and then linearly combined, so that no feedback mechanisms occur between the models, in line with previous applications (see Vitousek et al., 2017b and Chapter 3). In this section, we briefly recall the main assumptions and the governing equations of the two wave-driven models.

The *ShoreFor* model (SF) disequilibrium approach is based on the present and past wave conditions. SF estimates the rate of shoreline change as a function of the current breaking wave power (P (W)), the disequilibrium of dimensionless fall velocity ($\Delta\Omega$) and three site-specific parameters $k_s^{+/-}$ ($\text{m s}^{-1}\text{W}^{-0.5}$), Φ (days) and b (m/s) (Equation 2.1). The $k_s^{+/-}$ parameter is a shoreline response rate that assumes different values for accretion and erosion conditions, Φ is the beach memory of past wave conditions, and b is a linear term that encapsulates the effect of slow processes, other than wave-driven equilibrium based, which

may drive chronic shoreline change. The values of the $k_s^{+/-}$ parameter for accretion and erosion conditions are assumed to be linearly related by a coefficient r ($k_s^- = rk_s^+$). The r value is determined so that no trend in wave forcing results in no trend in the modelled shoreline position (Equation 2.4).

We note here that, while accounting for the effects of slow processes using a constant linear trend (*i.e.* b) can improve the model skill for simulated periods within the decade, the application of such trend over longer time scales (decades to centuries) becomes increasingly inaccurate (see Chapter 4). Therefore, given the long time scale of our application and the absence of secondary processes (*e.g.* longshore gradients in sediment transport) that may drive long-term shoreline trends at Truc Vert, we set $b=0$. Hence, Equation 2.1 becomes:

$$\frac{dY}{dt} = k_s^{+/-} P^{0.5} \frac{\Delta\Omega}{\sigma_{\Delta\Omega}} \quad (5.1)$$

In the Yates et al. (2009) model (Y09) the disequilibrium condition is expressed in terms of incident wave energy (ΔE), and the equilibrium state E_{eq} is defined as a linear function of the current shoreline position Y , through the empirical parameters a_1 (m^2/m) and a_2 (m^2). Y09 calculates the rate of shoreline change as the product of the incident wave energy (E (m^2)), the disequilibrium ΔE (m^2), and the shoreline response rate $k_y^{+/-}$ ($m^2 s^{-1}/m$) (Equation 2.6). Reminding Equation 2.6 and 2.7, the model reads:

$$\frac{dY}{dt} = k_y^{+/-} E^{0.5} (E_{eq}(Y) - E) \quad (2.6)$$

$$E_{eq}(Y) = a_1 Y + a_2 \quad (2.7)$$

In Y09, the values for a_1 , a_2 , k_y^+ , and k_y^- are specific to the site of application, and need calibration against wave and shoreline observations. The $k_y^{+/-}$ parameter is analogous to $k_s^{+/-}$ of SF in that it represents the efficiency rate of the incident wave forcing to shoreline change. Contrarily to SF, here the equilibrium state formulation (Equation 2.7) does not depend on recent wave conditions, making this model insensitive to wave-climate variability on timescales longer than the calibration period. Instead, Equation 2.6 depends on the current shoreline position (Y), introducing the potential for feedbacks between Y09 and shoreline change induced by other cross-shore processes (*e.g.* SLR) (see Chapter 3).

Recently, Vitousek et al. (2021) showed that a rearrangement of Y09 free parameters results in combined terms that can be interpreted as local equilibrium time and spatial scale factors. However, here Y09 was implemented in its original form, where a_1 and a_2 are treated as empirical parameters.

5.2.3. Global Sensitivity Analysis

Numerical modelling of shoreline change inherits the uncertainties associated to input variables and their complex interactions, affecting the robustness of the shoreline projections. While numerical modelling provides a ‘key-hole’ to observe the explicit interactions among defined sets of variables, sensitivity analysis provides a way to understand the role of input variables uncertainties in shoreline predictions. Here, we use the variance-based Global Sensitivity Analysis (GSA) described in Section 2.3.2. and illustrated in Chapter 5 to address the relative impact of uncertainties in SLR, DoC and of model free parameters on shoreline projections (Y) over time for the SF and Y09 modelling approaches. Identifying the main source of model results uncertainties through time is a fundamental step towards improving the reliability of long-term shoreline projections. Seemingly to Chapter 4, we computed first-order Sobol’ indices (S_i s) using the modularized sample-based approach by Li and Mahadevan (2016), which allows to account for the statistical dependence among model free parameters, and we estimate S_i s for the purpose of Factors’ Prioritization, *i.e.* identifying the factor that one should fix to minimize output uncertainty. Figure 5.1 synthesizes the generalized method and details for the Truc Vert probabilistic applications (excluding the additional high-end SLR deterministic scenario).

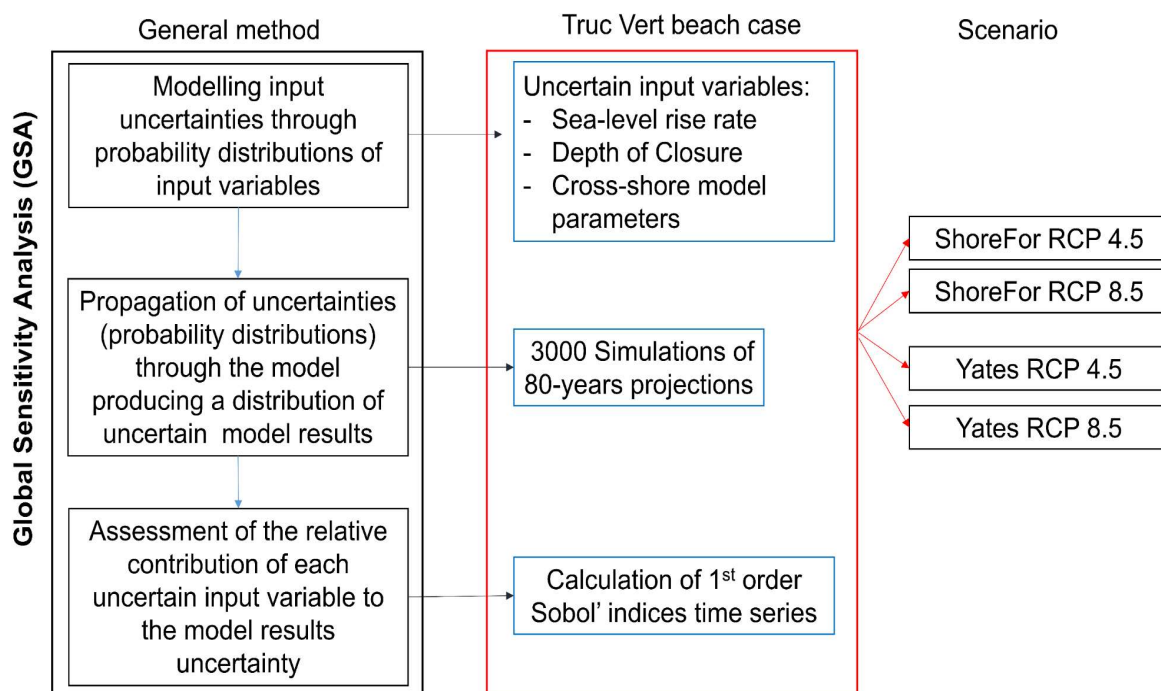


Figure 5.1. Flowchart of the method applied herein, summarized for a general case (black box), and for the Truc Vert application (red box) in the four application scenarios.

5.3. Input probability distributions for future projections

5.3.1. Probabilistic sea-level rise

Sea-level projections inherit uncertainties associated with physical unknowns and modelling of the contributing processes. While many efforts were dedicated to assess such uncertainties, there is no single approach to define MSL probability distributions yet (Jackson and Jevrejeva, 2016; Jevrejeva et al., 2019; Kopp et al., 2014). We produced probabilistic relative MSL projections, conditional to the RCP8.5 and 4.5 scenarios, defining time varying normal probability distributions characterized by the yearly median and standard deviations obtained in Section 2.1.3.1 (Figure 5.2a,b), following Hunter et al. (2013). In the high-emission scenario (RCP8.5), the large uncertainty associated with Antarctic ice sheet dynamics generates a skewness of the distributions in the second half of the 21st century, enhancing the amount of possible extreme SLR (Grinsted et al., 2015; Jackson and Jevrejeva, 2016; Kopp et al., 2014). The upper tail of the skewed probability distribution is very much debated (Jevrejeva et al., 2019) and is not represented by the Gaussian distributions. Therefore, in addition to the Gaussian distribution reflecting the SROCC assessment (Oppenheimer et al., 2019), we consider a high-impact, low probability

high-end sea level scenario that might take place for high greenhouse gas emissions (RCP8.5; black line in Figure 5.2b) following the same assumptions as Thiéblemont et al. (2019) (see Appendix C2 for details). The possibility that the subsidence rate revealed by the Cap-Ferret GPS station is not representative of the Truc Vert area (located at 8 km distance) constitutes a residual uncertainty that cannot be quantified, and is not accounted in this study due to the lack of quantitative information supporting an alternative scenario for residual vertical ground motions.

5.3.2. Depth of closure

The active beach profile slope is critical to SLR-driven erosion rate (Section 2.2.2), and strongly depends on the depth of closure (DoC). The DoC was calculated from the wave climate using the Hallermeier (1978) formula. Given that DoC depends on the period of time over which the Hallermeier formula is applied (Nicholls, 1998), we iteratively applied the Hallermeier formula over a 1-year moving window of the future wave climate with a 30-days step. For both RCP8.5 and RCP4.5 scenarios, the latter procedure generated an ensemble of possible DoC values well fitted by a Gaussian distribution (Figure 5.2c). The DoC probability distribution shows higher median and standard deviation values in the RCP4.5 ($\mu = 17.2$ m; $\sigma = 1.75$ m) than in the RCP8.5 ($\mu = 16.3$ m; $\sigma = 0.95$ m). This results from the more frequent occurrence and larger wave heights associated to isolated extreme events in the RCP4.5 scenario, compared to the RCP8.5 scenario.

5.3.3. Model parameters

Numerical models are associated with uncertainties owing to the choice of modelling approach and to the estimation of model free parameters. We accounted for the uncertainty conditional to the choice of modelling approach assessing the shoreline projections using the Y09 and the SF models described in Section 2.2.1, in two separated scenarios. Both models rely on shoreline observations to calibrate the respective free parameters, and inherit uncertainties due to the quality and amount of available data (Splinter et al., 2013), to possible non-stationarity of the parameters in respect to the wave climate (Ibaceta et al., 2020), and to the optimization method. Uncertainties affecting model free parameters of the Y09 model ($k_y^{+/-}$, a_1 , a_2) and the SF model (k_s^+ , Φ) are synthesized by their associated joined probability distribution. We follow the approach developed in Chapter 4, who calibrated the SF model free parameters using the Simulated Annealing algorithm (Bertsimas & Tsitsiklis,

1993), and determined their joint probability distribution by fitting an empirical multivariate distribution (multivariate kernel function) on an ensemble of model parameters combinations. The authors built the latter ensemble selecting all parameters combinations that produced a RMSE < 10 m against observed shoreline data during the optimization process. Unlike Chapter 4, here we calibrated the models between January 2012 and December 2019, where no long-term trend in shoreline position is observed, in line with the assumption of the SF parameter $b=0$ (see Section 2.2.1.1). In addition, we used the Nash and Sutcliffe (1970) efficiency score (NS) instead of the RMSE to determine the models' performance (as for instance in Kroon et al., 2020). The NS measures the model skill in comparison to the 'mean model' (defined as the observed mean shoreline position), based on the error's variance, and it is calculated as follows:

$$NS = 1 - \frac{\sum_{n=1}^N (Y_m^n - Y_o^n)^2}{\sum_{n=1}^N (\bar{Y}_o - Y_o^n)^2} \quad (5.2)$$

where N is the number of observations, Y_m^n and Y_o^n are the n-th modelled and observed shoreline positions, respectively, and \bar{Y}_o is the mean of the observed shoreline positions. The NS coefficient can range between $-\infty$ and 1, where $NS = 1$ corresponds to a model perfectly reproducing the observations, $NS = 0$ to a model with skill comparable to the 'mean model', and $NS < 0$ corresponds to models less skilful than the 'mean model'. We obtained the probability distribution using combinations of parameters that resulted in a $NS \geq 0.25$ (compared to the maximum $NS = 0.63$), which corresponds to a max RMSE of ~ 10 m consistently with Chapter 4. We defined the latter threshold with the iterative procedure described in Appendix C3. This procedure results in the probability distributions of $k_y^{+/-}$, a_1 , and a_2 for Y09, and k_s^+ and Φ for SF shown in Figure 5.2d,e, with the range of possible parameters values reported in Table 5.1.

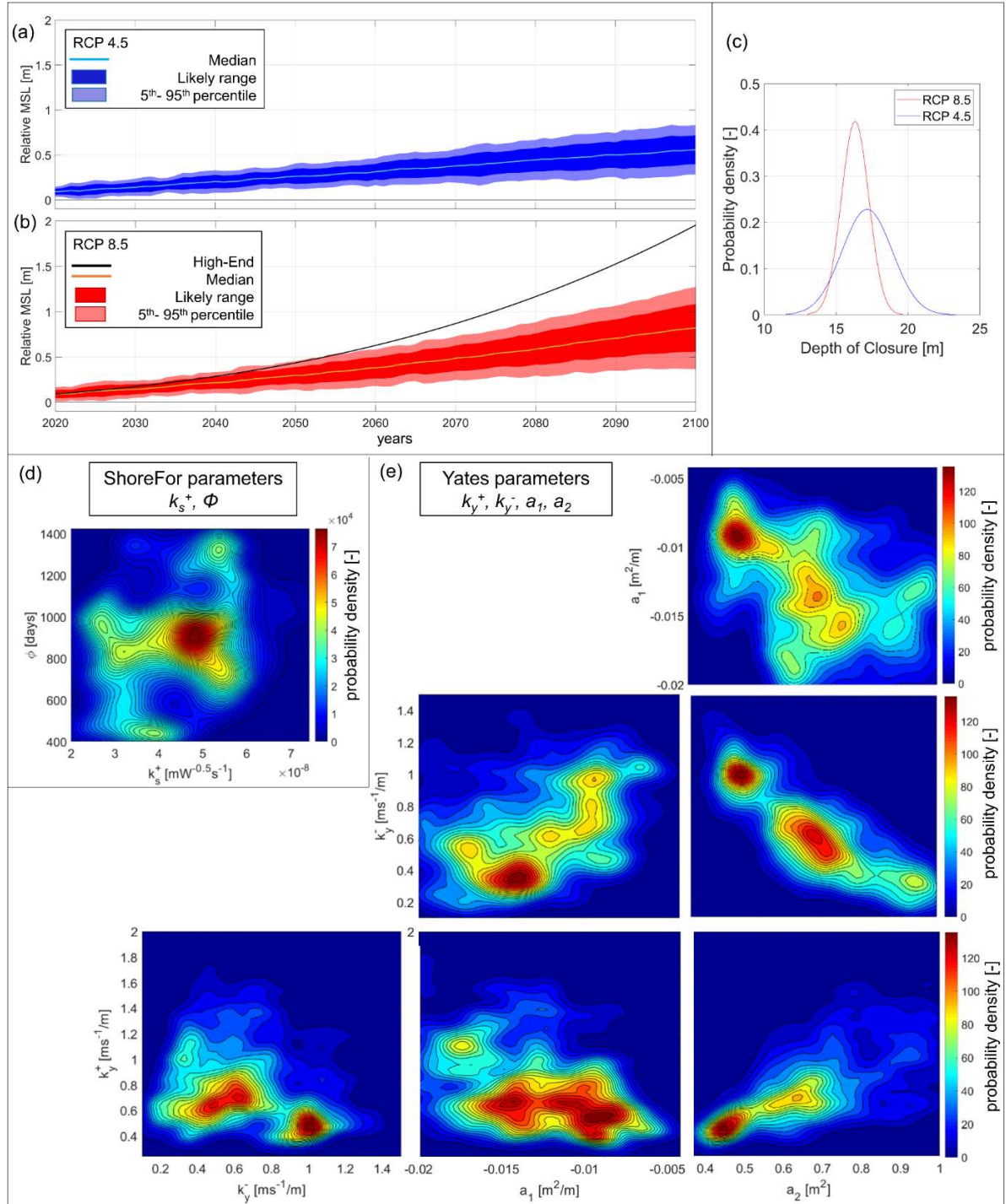


Figure 5.2. Probability distributions of: relative mean sea level over the period 2020-2100, including the likely (dark shaded areas) and 5th to 95th percentile (light shaded areas) ranges, for (a) RCP4.5 and (b) RCP8.5 scenarios, with deterministic high-end sea-level projections based on 2100 high-end ‘highest-modelled’ estimates following Thiéblemont et al. (2019) (black line); (c) Gaussian distributions of depth of closure values calculated over the 2020-2100 wave time series for RCP4.5 (blue curve) and RCP8.5 (red curve) scenarios; and empirical joint probability distributions of (d) *ShoreFor* [k_s^+ , Φ] parameters, and (e) Yates [$k_y^{+/-}$, a_1 , a_2] parameters, obtained fitting a kernel density function (with bandwidths estimated from the marginal kernel density function for each variable) on 6000 combinations of model parameters producing NS > 0.25 against shoreline data.

Table 5.1. Optimised combinations of cross-shore model free parameters, and respective range of variation in the probability distributions.

Model	Model parameter	Optimised value	Distribution range
<i>ShoreFor</i>	$k_s^+ [\text{m}^{1.5} \text{s}^{-1} \text{W}^{0.5}]$	4.4×10^{-8}	$[2; 7.4] \times 10^{-8}$
	Φ [days]	1193	[400; 1423]
<i>Yates</i>	$k_y^+ [\text{m}^2 \text{s}^{-1} / \text{m}]$	0.87	[0.24 ; 2]
	$k_y^- [\text{m}^2 \text{s}^{-1} / \text{m}]$	0.5	[0.1 ; 1.5]
	$a_1 [\text{m}^2/\text{m}]$	-0.008	[-0.02 ; -0.004]
	$a_2 [\text{m}^2]$	0.49	[0.33 ; 1]

5.3.4. Model setup of shoreline projections

Four ensembles of 3000 possible shoreline trajectories from 2020 to 2100 were generated using the SF and Y09 shoreline change models, and the Bruun Rule, for the two RCP8.5 and RCP4.5 scenarios (Table 5.2). For each model and RCP scenario, 3000 simulations were run with different combinations of model free parameters, DoC and SLR time series, sampled from the respective probability distributions. Shoreline change was computed with a 3-hour time step from the 1st January 2020 to the 31st December 2099 starting from the same shoreline position ($Y_0=0$), and model outputs were recorded with a 2-weeks resolution. As the characteristics of the MSL probability distribution are time-dependent, we randomly sampled percentile values and extracted the corresponding MSL at each year. The ensemble projections character was synthesized by the *likely range*, defined here at each time step as the variance, and the *envelope* (min and max) of modelled shoreline positions, acknowledging that the latter is dependent on the number of simulations and the tails of the probability distributions. The impact of individual winters on shoreline projections is qualitatively discussed observing the distributions of shoreline positions corresponding to the most seaward and landward median shoreline position within each simulated annual cycle (1st September to 31th August). We analysed the decadal shoreline trends by filtering the modelled shoreline time series with a 5-year running mean. In addition, for RCP8.5 scenario, a deterministic high-end-SLR simulation was run with both shoreline models using the optimized model parameters (Table 5.1) and the median DoC. It is to be noted that the GSA results (*i.e.* S_f s) are calculated on the likely range (variance) of the model results, regardless of the envelope of modelled shoreline positions.

Table 5.2 Probabilistic future scenarios for two Representative Concentration Pathways (RCP) and two different wave-driven modelling approaches, using the Bruun Rule and 3000 different combinations of model parameters, SLR percentile and DoC.

Future scenario	SLR-driven shoreline change	Wave-driven shoreline change	# Combinations of uncertain variables
RCP 4.5	Bruun Rule	<i>ShoreFor</i> (SF)	3000
		<i>Yates</i> (Y09)	3000
RCP 8.5	Bruun Rule	<i>ShoreFor</i> (SF)	3000
		<i>Yates</i> (Y09)	3000

5.4. Results

5.4.1. Shoreline projections

The four future scenarios in Table 5.2 resulted each one in 3000 shoreline evolution simulations spanning 2020-2100 (Figure 5.3 and Figure 5.4). Figure 5.3c,d and Figure 5.4c,d represent the distribution of 3000 modelled shoreline positions at each recorded output time. All scenarios show a net erosion by 2100, mostly driven by SLR (Table 5.3). All model ensembles also show large interannual variability that is essentially enforced by the interannual variability in incident winter-mean wave height (Figure 5.3a,b and Figure 5.4a,b). In the RCP8.5 (RCP4.5) scenario we observe a long-term shoreline change pattern responding to alternating sequences of high- and low-energy winters with a period of ~20 years (~10 years) and even longer (Figure 5.3a,e,f and Figure 5.4a,e,f).

Figure 5.3c,d (Figure 5.4c,d) show several episodes of rapid erosion driven by isolated extreme energy winters, for instance for the RCP8.5 (RCP4.5) scenario in winter 2030, 2076, and 2086 (2068, 2073 and 2085). The two wave-driven shoreline models (Y09 and SF) produce consistent short- and long-term shoreline cycles, with larger tendency to accretion in SF than in Y09 during extended periods of low energy winters, for instance during 2050-2055 for RCP4.5 and 2060-2070 for RCP8.5 (Figure 5.3c,d and Figure 5.4c,d).

In the RCP4.5 emission scenario, the modelled 2020-2100 Truc Vert shoreline trend leads to a likely (envelope) retreat of 15 to 33 m (4 to 75 m) with Y09, and 10 to 23 m (6 to 65 m) with SF. On a yearly time scale, the shoreline position is likely (envelope) to be farther landward from the initial position, by 76 m (123 m) with Y09, and 43 m (74 m) with SF (Figure 5.3c,d, Table 5.3). Indeed, the occurrence of extreme winters can produce significant landward shifts of the envelope of shoreline positions, as observed during the 2084-2085 winter (Figure 5.3c,d).

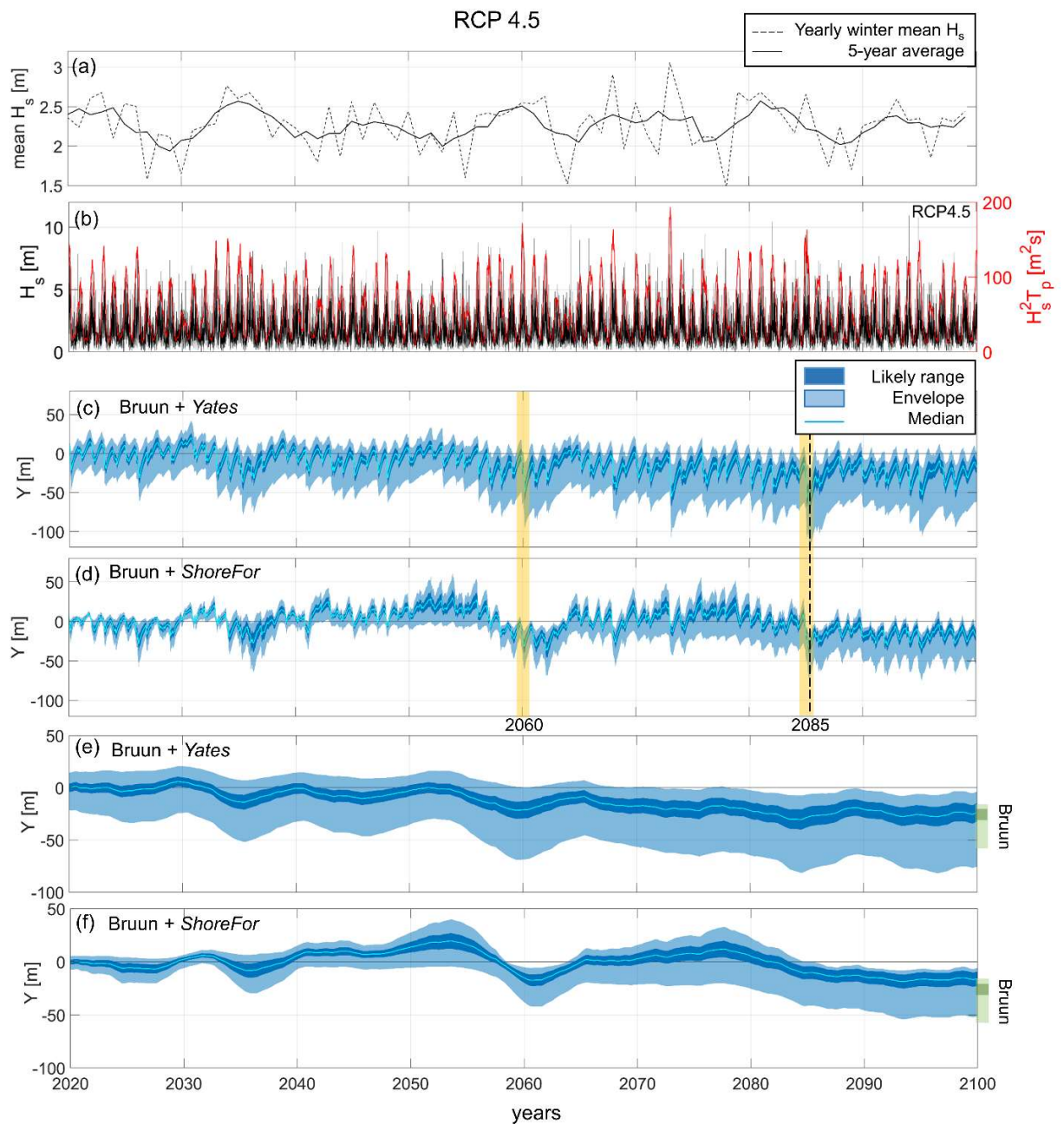


Figure 5.3. (a) Time series of winter mean wave height of the BW18 RCP4.5 projections (dashed line) with corresponding 5-year average (solid line); (b) BW18 RCP4.5 wave height time series (black line), and 3-month average $H_s^2 T_p$ time series (red line); RCP4.5 scenario 2020-2100 shoreline projections at 14-days resolution obtained using (c) Y09 and (d) SF; and 5-year running mean shoreline projections modelled with (e) Y09, (f) SF, and the standalone Bruun Rule (green bars). Dark (light) blue shaded areas indicate the likely (envelope) range, *i.e.* variance (min-max), of shoreline position, and solid light line median shoreline position. The dashed vertical line indicates the most landward shoreline position over the simulated period. Yellow shaded areas indicate examples of years including high-energy winters.

When forced with RCP8.5 scenario's wave and MSL projections, from 2020 to 2100 simulations indicate an average likely (envelope) erosion of 27 to 48 m (16 to 83 m) using Y09, and 14 to 33 m (2 to 67 m) using SF (Figure 5.4d,e). In this scenario, over the simulated

period the likely (envelope) most landward shoreline position reaches up to 70 m (108 m) from the initial shoreline position with Y09 model, and 48 m (76 m) with SF (Figure 5.4c,d, Table 5.3). Similarly to the RCP4.5, here we observe for both models some important shifts in shoreline position distribution owing to extreme winters such as 2086's winter (Figure 5.4c,d).

In the high-end SLR scenario, both models predict a shoreline position within the envelope of probabilistic projections until 2090, before the shoreline moves further inland during the last decade (Figure 5.4d,e). The modelled 5-year averaged shoreline position in 2100 is of 88 and 74 m for Y09 and SF, respectively (Table 5.3). The most landward shoreline position observed throughout the simulation is 107 m with Y09, and 86 m with SF (black dashed line in Figure 5.4c,d).

The likely (envelope) ranges erosion produced by the combined Y09+Bruun models at the end of the simulated period are comparable (larger) to the standalone application of the Bruun Rule (Table 5.3, and in Figure 5.3, Figure 5.4,e,f with Bruun model predictions in green). With the combined SF+Bruun models, the likely (envelope) ranges of shoreline positions obtained show ~10 m (~15 m) less erosion than the Bruun Rule.

5.4.2. Global Sensitivity Analysis

In both RCP8.5 and 4.5 scenarios and for both shoreline model applications, the GSA shows that over the first 30 years of simulation the variance of modelled shoreline projections is driven primarily by the uncertainties in model free parameters, while the effects of SLR uncertainties on shoreline position become increasingly significant after 2050 (Figure 5.5 and Figure 5.6). The S_i s of the Y09 and SF response rate parameters ($k_y^{+/-}$ and k_s^+ , respectively) and the SF beach memory parameter (Φ) show seasonal (6 months) and decadal modulation with a decreasing trend as shoreline projections become more sensitive to SLR (Figure 5.5c,d and Figure 5.6c,d). Variations in $k_y^{+/-}$ and k_s^+ are the primary source of shoreline projection uncertainties during accretion periods. However, the response rate parameters' uncertainties have a stronger impact on seasonal scale when using the Y09 model (Figure 5.5c), and a larger impact on interannual scale when using the SF model (Figure 5.6c), due to the different response of the models to incident wave energy variability. Seasonal modulation is also observed for the S_i s of the Y09 empirical parameters (a_1 and a_2), although the correlation between the variability in incident wave conditions and the parameters' S_i s, (both filtered of their seasonal signal with a 1-year running mean) is negligible ($R^2 \sim 0.06$ for a_1 , and $R^2 \sim 0.03$ for a_2).

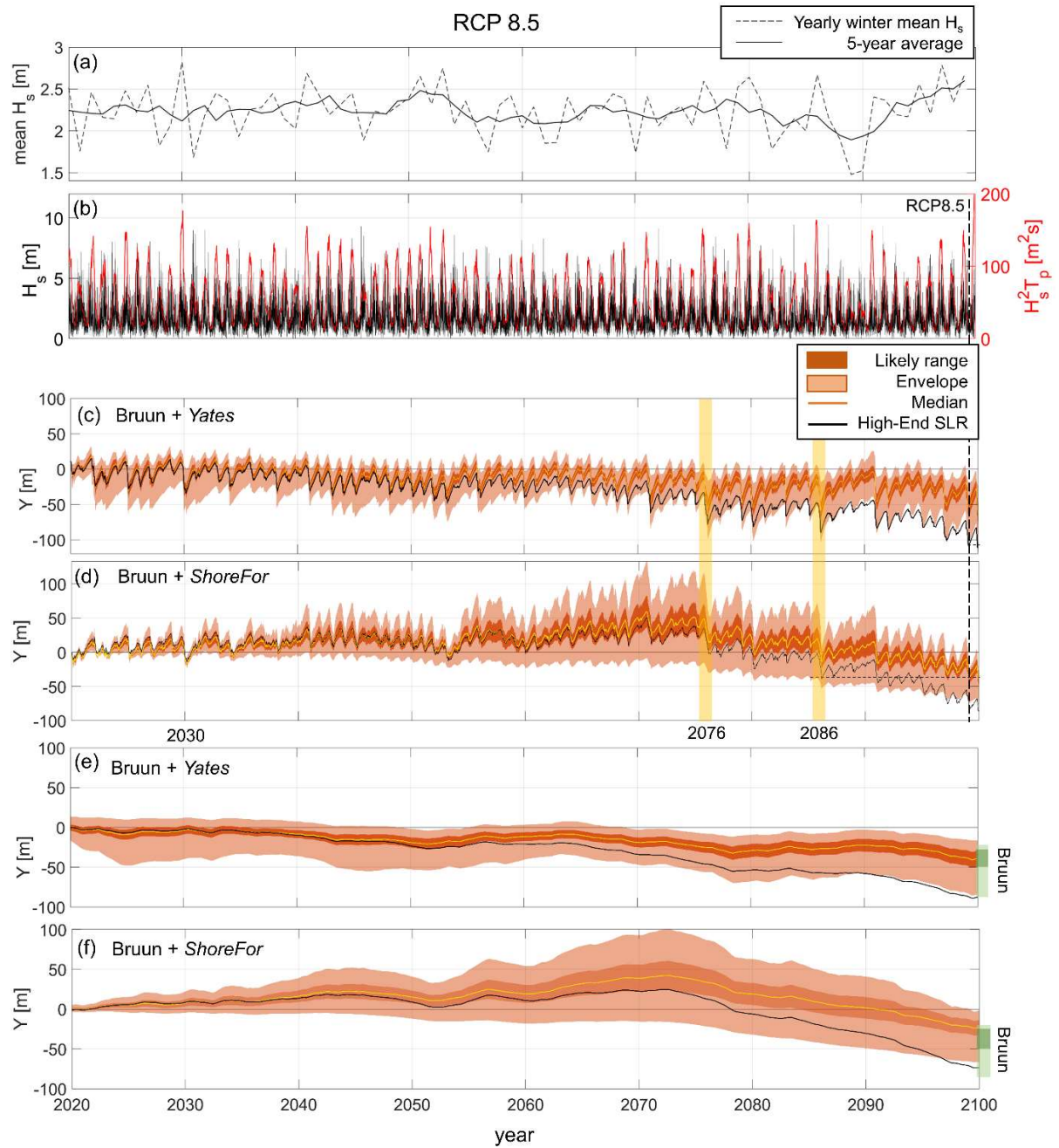


Figure 5.4. (a) Time series of winter mean wave height of the BW18 RCP8.5 projections (dashed line) with corresponding 5-year average (solid line); (b) BW18 RCP8.5 wave height time series (black line), and 3-month average $H_s^2 T_p$ time series (red line); RCP8.5 scenario 2020-2100 shoreline projections at 14-days resolution obtained using (c) Y09 and (d) SF; and 5-year running mean shoreline projections modelled with (e) Y09, (f) SF, and the standalone Bruun Rule (green bars). Dark (light) shaded areas indicate the likely (envelope) range, *i.e.* variance (min-max), of shoreline position. Black solid lines indicate shoreline projections in the RCP8.5 high-end SLR scenario. The dashed vertical line indicates the most landward shoreline position over the simulated period. Yellow shaded areas indicate examples of years including high-energy winters.

Table 5.3. Likely (modelled shoreline variance) and envelope (min-max) values of the 5-year averaged projected shoreline position in 2100, and 2020-2100 most landward shoreline position, obtained using the standalone Bruun Rule (B), and the combined B with Y09 and SF equilibrium shoreline models, for the RCP4.5 and RCP8.5 probabilistic scenarios, and the deterministic high-end SLR scenario.

Scenario		2100 5-year averaged shoreline position		Most landward shoreline position	
		<i>likely range</i> (m)	<i>envelope</i> (m)	<i>likely</i> (m)	<i>envelope</i> (m)
RCP 4.5	Y09+B	-15 – -33	-4 – -75	-76	-123
	SF+B	-10 – -23	-6 – -52	-43	-74
	B	-21 – -33	-17 – -60	-33	-60
RCP 8.5	Y09+B	-27 – -48	-16 – -83	-70	-108
	SF+B	-14 – -33	-2 – -65	-48	-76
	B	-28 – -49	-21 – -86	-49	-86
Deterministic scenario		2100 5-year averaged shoreline position (m)		Most landward shoreline position (m)	
High-end RCP 8.5	Y09+B	-95		-111	
	SF+B	-74		-84	
	B	-81		-81	

However, the estimated a_1 's and a_2 's S_i s remain below 20% during most of the simulated period with occasional peaks up to 45% (Figure 5.5e,f). The primary effects of SLR uncertainties emerge at different times, which depend both on the RCP scenario and on the shoreline model. When using Y09, a positive trend in SLR's S_i emerges in the 2050-2060 period, with SLR's S_i exceeding those of model parameters since approximately 2060-2070, for both RCP scenarios (Figure 5.5g). Instead, with SF in the RCP8.5 (RCP4.5) scenario, such quasi-monotonic trend appears later, approximately during the 2070s' (2060s') and only exceeds the model parameters' S_i s after 2085 (2080) (Figure 5.6e). For all scenarios, DoC's S_i slowly increases, with similar trends as SLR's S_i , and reaches approximately 5% and 10%, in the RCP8.5 and 4.5 scenarios, respectively. This difference is probably due to the larger uncertainties of SLR in the RCP8.5 scenario (Figure 5.2b), and to the larger variance of the DoC probability distribution obtained for the RCP4.5 scenario (Figure 5.2c).

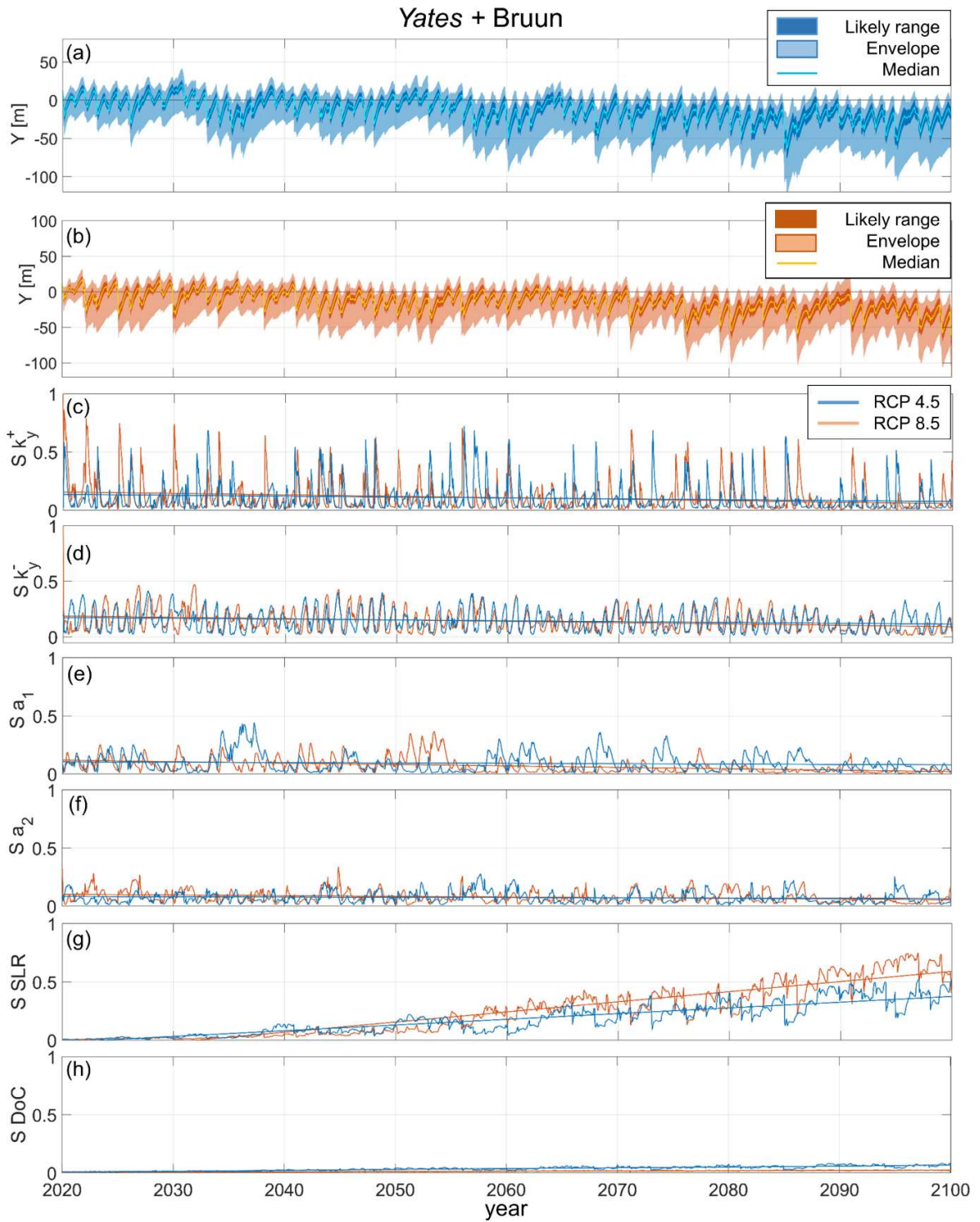


Figure 5.5. Global Sensitivity Analysis results over the period 2020-2100 using the Yates model in the RCP4.5 (blue lines) and RCP8.5 (orange lines) scenarios. (a) RCP4.5 and (b) RCP8.5 Ensemble shoreline projections (shaded areas) over 2020-2100; First-order Sobol' index time series for (c) k_y^+ , (d) k_y^- , (e) a_1 , (f) a_2 , (g) sea-level rise, and (h) depth of closure, with respective linear fit (solid straight lines).

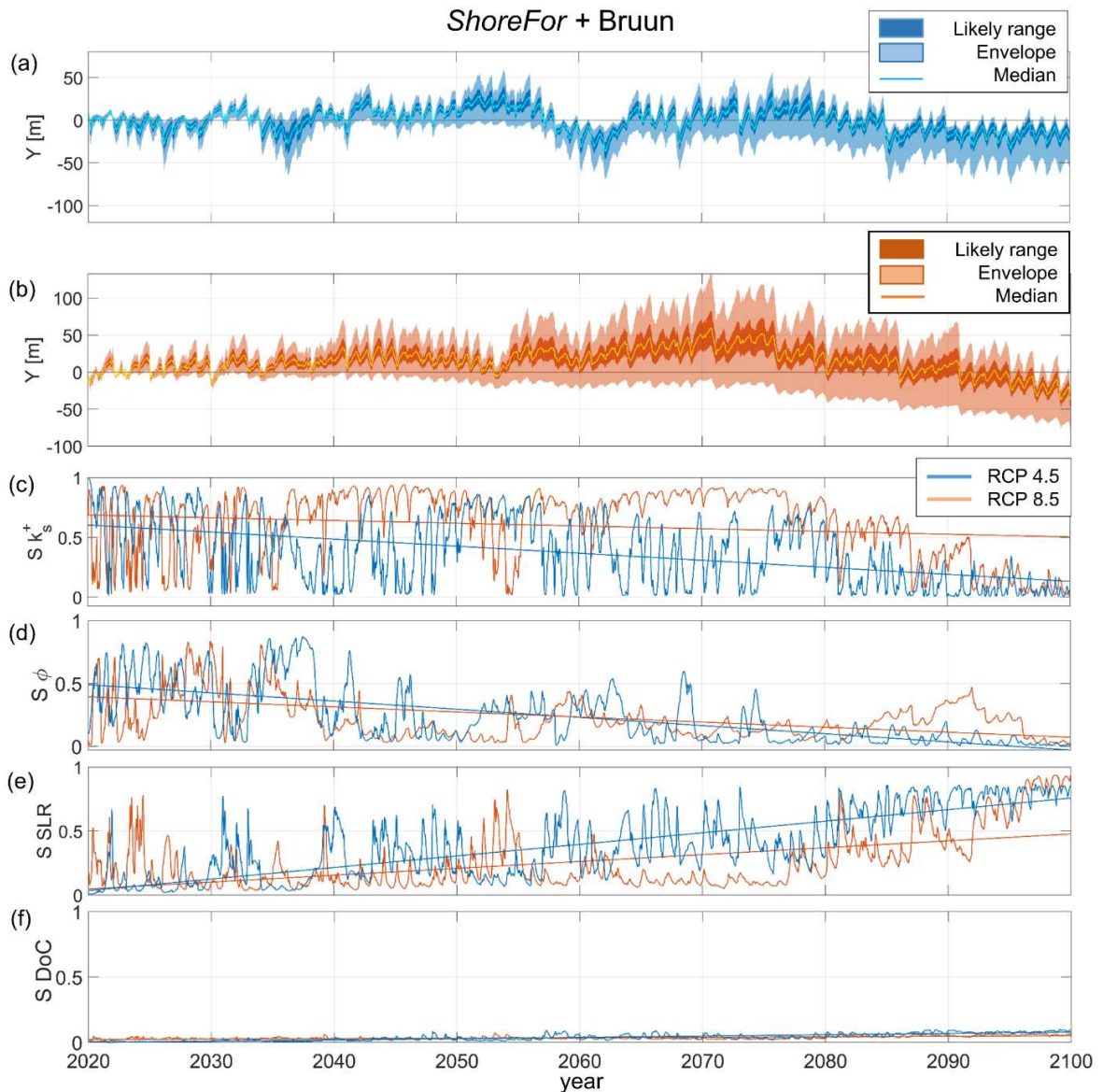


Figure 5.6. Global Sensitivity Analysis results over the period 2020-2100 using the ShoreFor model in the RCP4.5 (blue lines) and RCP8.5 (orange lines) scenarios. (a) RCP4.5 and (b) RCP8.5 Ensemble shoreline projections (shaded areas) over 2020-2100; First-order Sobol' index time series for (c) k_s^+ , (d) Φ , (e) sea-level rise, and (f) depth of closure, with respective linear fit (solid straight lines).

5.5. Discussion

5.5.1. Sea-level rise

While observed shoreline erosion in Aquitaine is not yet attributed to SLR, sooner or later a SLR-driven signal will emerge from the current shoreline change variability, as sea levels are committed to rise by meters over the coming centuries (Anderson et al., 2015; Oppenheimer et al., 2019). Our results suggest that these times of emergence of a SLR-driven erosive trend could be visible during the 2nd half of the 21st century, possibly by 2070. This is consistent with the fact that uncertainty (17th – 83rd percentiles) in future sea level

grows from roughly 15 cm by the mid 21st century to 30 cm (RCP4.5) and 50 cm (RCP8.5) in 2100. Yet, this result relies on our modelling assumptions, including the Bruun Rule and the *Yates* or *ShoreFor* models.

The GSA applications to four simulated scenarios indicate that uncertainties in the modelled 2020-2100 shoreline projections at Truc Vert are primarily caused by uncertainties in model free parameters between the present day and 2050. The effects SLR uncertainties always emerge as a significant contribution to the shoreline change uncertainties in the second half of the century. We also observed that the time evolution of S_t s and the onset of SLR uncertainties effects are conditional to the RCP scenario (in agreement with Le Cozannet et al., 2019), the choice of shoreline model, and the variability of forcing wave climate.

The shoreline trajectory obtained in the deterministic high-end SLR scenario exceeds the envelope of probabilistic projections in the last simulated decade. Truc Vert beach is remote and backed by a high (~20 m) and wide (~250 m) dune system, so that shoreline retreat is not limited by non-erodible geological outcrops or coastal structure. While such large erosion does not threaten any human assets close to Truc Vert beach, such scenario, though unlikely, questions adaptation planning in other eroding urbanised coastal areas with limited accommodation space in southwest France.

5.5.2. Shoreline models

While the SF and Y09 models are both based on the equilibrium beach concept, the respective model structures and parameters associate different physical interpretations and shoreline behaviours (Section 2.2.1). Therefore, the uncertainty associated with the choice of the equilibrium modelling approach cannot be measured by direct confrontation of the S_t s obtained with the two models, but requires consideration of the different model responses to the forcing conditions.

The results obtained for the two disequilibrium approaches (Y09 and SF) show similar seasonal and interannual shoreline cycles, although with notably different amplitudes. Such behaviours are rooted in the different expressions of the equilibrium physics adopted in the two wave-driven models (*i.e.* the mechanism that would drive the shoreline to an equilibrium position under constant wave conditions). Vitousek et al. (2021) analytically show that the type of equilibrium condition is critical for the short- and long-term response of the shoreline model. On one hand, Y09's equilibrium condition depends on the current shoreline position, and is not influenced by storm events that occurred prior

to a given time scale that is implicitly defined by the model calibration (see ‘Appendix A’ of Vitousek et al., 2021). On the other hand, SF’s equilibrium state is determined by the (time varying) past wave conditions with an explicit ‘beach memory’ function, and evolves in time accordingly. This means that, in absence of other processes, the Y09 modelled shoreline oscillates persistently around the same position regardless of the temporal variability of wave energy. Instead, SF can only achieve such a stable mean shoreline trend when forced with a periodic long-term wave climate (Vitousek et al., 2021). Hence, in presence of long-term trends of wave energy, Y09 emphasizes the short-term shoreline erosion/accretion in order to re-establish the equilibrium shoreline position, while SF adapts to the wave climate pattern. The latter results in larger amplitudes of seasonal fluctuations and in attenuation of long-term fluctuations, compared to SF.

The combined Y09 and Bruun models simulated shoreline ranges at 2100 are overall comparable to the ranges of the standalone Bruun Rule, indicating that in this scenario the net erosion modelled by 2100 is essentially driven by SLR. In fact, Y09 constrains the shoreline response to long-term wave climate shifts to a limited range (as described above) while the linearly added contribution of the Bruun model determines the shoreline trend. Instead, SF can produce wave-driven long-term shoreline trends that are combined with the Bruun retreat. This effect is observed in both RCP4.5 and 8.5 scenarios, where the decreasing wave energy trend (Figure 2.5d,e) is translated by SF into shoreline accretion trends, resulting in less erosion than the Bruun model alone (Table 5.3).

Such properties of the two model behaviours highlight the different model sensitivities to long-term variability of the wave climate, which can have implications on the uncertainties in shoreline projections. Including the uncertainty of long-term wave climate variability in the ensemble projections would allow investigating the uncertainties related to the different behaviours of the shoreline models.

5.5.3. Model free parameters

Resolving process-based shoreline response to time-varying incident wave energy revealed that uncertainties in model parameters have the largest impact over the first simulated 30 years, regardless of the cross-shore shoreline model choice. Over this period, Y09 and SF uncertainties in response rate parameters ($k_y^{+/-}$ and k_s^+ , respectively) are responsible for most of the results uncertainties, which increases during low energy winters (on seasonal scale), and is particularly emphasized for SF in correspondence of extended low energy periods. This suggests that the assumption of a linear relationship between SF’s

response rate parameters ($k_s^- = r k_s^+$) may not hold in the context of long-term simulations, as it might depend on the evolution of waves properties (Ibaceta et al., 2020). In fact, Ibaceta et al. (2020) found that, such relation is not necessarily linear, indicating that the value of r may vary dynamically with changes in wave regimes. While the S_i s of the remaining model parameters (Φ for SF; a_1 and a_2 for Y09) show a definite seasonality, their variability on longer time scales is unclear. However, Φ 's S_i , which exhibit relatively high values (up to 90%) at the beginning of the simulation, shows an overall decaying trend for both RCP scenarios applications. The a_1 and a_2 's S_i s remain weak, though not negligible, (<20%) over all the simulated period.

The behaviour of the model free parameters' S_i s highlights, once again, the importance of wave energy variability in determining the impact of the parameters uncertainties on shoreline projections. This was also observed in previous studies, which showed that changes in wave regime can alter the model parameters and the functional relations between them (Ibaceta et al., 2020; Splinter et al., 2017). As a perspective of future work, one way to reduce the effects of model free parameters' uncertainties on modelled shoreline may be to employ non-stationary parameters that can adjust to changes in wave-climate regimes (Ibaceta et al., 2020). The use of non-stationary parameters would also imply a dynamic value of the r parameter, reducing uncertainties associated to the assumption of a linear relationship, between SF's response rate parameters. In addition, rearranging the Y09 parameters so that the new parameters have a similar order of magnitudes may increase the efficiency of model calibration, reducing model parameters uncertainties (Vitousek et al., 2021).

5.5.4. The role of wave time series

Our results indicate that the shoreline erosion is not only associated with large winter energy, but also depends on the trends of past winter wave energy and the internal variability of high-energy events within the season. For instance, in the RCP4.5 scenario the winters 2084-2085 and 2059-2060 show similar 3-month averaged $H_s^2 T_p$ peak (164 m²s and 172 m²s, respectively), but they are preceded by several years of negative and positive winter energy trend, respectively (2.1.3.2b). This results in the winter 2084-2085 producing a rapid landward shift of shoreline position distribution, and the winter 2059-2060 driving more moderate annual changes while contributing to a long-term erosive trend (Figure 5.3c,d). We also observe that the interannual patterns of shoreline evolution are clearly correlated to those of winter wave energy. These behaviours underline the critical role of high/low energy

winters interannual cycles, as well as storms sequencing, in wave-driven shoreline response, in line with previous studies (Dissanayake et al., 2015; Dodet et al., 2019). In addition, the temporal variability of wave climate (*e.g.* seasonal distribution of storm events) has been observed to affect the frequency (or ‘mode’) of shoreline response (Splinter et al., 2017; Ibaceta et al., 2020).

Therefore, we further investigated the potential role of future waves uncertainties in shoreline projections performing the GSA on an additional ensemble of 3000 simulations forcing the Y09 and SF models with 100 different wave time series. We generated 100 random synthetic wave series using the method proposed by Davidson et al. (2017), which consists in building continuous series of wave conditions by sampling 1-month portions from a reference dataset of existing wave data (*e.g.* historic wave data) at a given location. The method generates synthetic wave time series with random, though realistic, chronology of wave events, while maintaining the seasonal and yearly character of the wave climate. However, this assumes a long-term stationarity of the generated wave time series. We used the BW18 projections for the RCP8.5 scenario as reference wave data. We individually applied the Davidson et al. (2017) method over 8 windows of 10 years from 2020 to 2100 in order to preserve the long-term (>10 years) characteristics of the reference time series while providing enough sampling reference data (Figure 5.7a). For instance, all the synthetic events from 2030 to 2040 were generated using monthly samples from the 2030-2040 reference dataset.

When using the latter approach to generate ensemble waves the SF model shows some limitations. Therefore, here we exploit only the test results obtained with Y09. The results of the SF test application and the aforementioned limitations are illustrated in Appendix C4.

The GSA shows that introducing uncertainties in the temporal distribution of wave events (Figure 5.7a) has a large impact on the variance of model results (Figure 5.7b) and, in turn, on the relative contributions of the remaining uncertain input parameters (Figure 5.7c-h). In fact, accounting for uncertainty in wave events chronology (though in a simplistic way) increases the overall model variance throughout the entire simulated period (Figure 5.3c and Figure 5.7b), and associates a dominating S_i (up to 0.3) over the first half of the simulated period (Figure 5.7i). However, SLR’s S_i still emerges after 2060 and dominate shoreline projections uncertainties over the last two simulated decades. We also observe that the inclusion of wave chronology uncertainty attenuates the interannual variability of all S_i s while preserving the seasonal and 10-year signals (Figure 5.7c-h).

Yates + Bruun RCP 8.5 (ensemble waves)

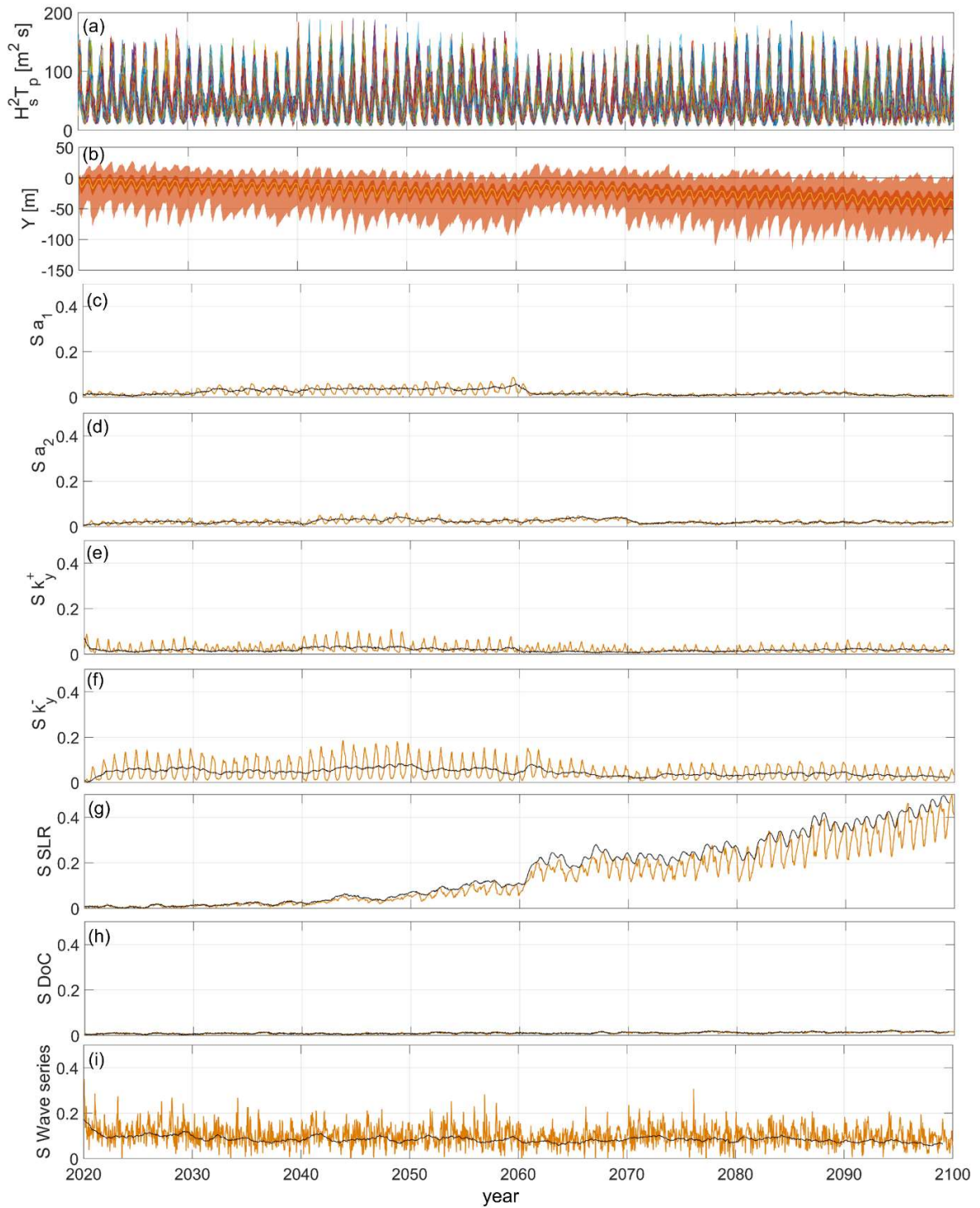


Figure 5.7. Ensemble of 3000 Yates simulations forced using (a) 3-month average energy ($H_s^2 T_p$) of 100 random wave time series from 2020 to 2100 generated with the Davidson et al. (2017) method based on the BW18 wave projections for the RCP8.5 scenario; (b) Ensemble shoreline projections over the analysed period (dark/light shaded areas indicate the likely/envelope range, *i.e.* variance (min-max), of shoreline position); First-order Sobol' index time series for (c) k_y^+ , (d) k_y^- , (e) a_1 , (f) a_2 , (g) sea-level rise, (h) depth of closure, and (i) wave energy, with respective time series calculated on the 1-year running average of model results (black lines).

This is a natural consequence of the method used to generate the wave series ensemble. In fact, the Davidson et al. (2017) method is designed to preserve the seasonal variability, while its application to fixed time windows of the reference time series constrains the ensemble members to maintain the 10-year variability. The black lines in Figure 5.6c-i show the time evolution of S_i s obtained removing the seasonal signal from the model results with a 1-year running average. When the seasonal variability of the results is removed, the SLR's S_i compensates the fluctuations of the model parameter's S_i s, resulting in an increased trend.

The test application illustrated above suggests that including uncertainties in short-term wave chronology can significantly impact the uncertainties of shoreline projections and the relative contributions of the remaining uncertain input variables. Further, introducing uncertainties on long-term non-stationarity of wave conditions would overcome the SF limitations occurring in this specific application, and may unveil new implications of the different Y09 and SF equilibrium approaches in the context of probabilistic long-term shoreline projections.

5.5.5. Assumptions and limitations

Wave projections are affected by uncertainties owing to the choice of the Global Climate Model (Morim et al., 2020) and random variability of wave events. Although our results are based on deterministic BW18's wave projections, in the northeast Atlantic region the estimated future wave statistics have been observed to be mostly sensitive to the RCP scenario (Morim et al., 2020). Yet, the use of deterministic wave projections hides a potentially large impact of the uncertain wave-climate variability on both shoreline predictions uncertainty and behaviour of the shoreline models.

In addition, accounting for uncertainties in wave projections may also increase the uncertainties in DoC, which were based on one deterministic wave time series in the present study. However, to the authors' knowledge there is no other dataset of continuous 2020-2100 wave projections, over the north Atlantic area, with a sufficient spatial resolution to resolve the site-specific regional scale processes. This underlines the need of continuous wave time series (obtained with different wave models of fine enough spatial resolution, different climate models, for different RCP scenarios), as well as tools allowing generating continuous realistic future wave time series, such as climate based stochastic wave emulators (Anderson et al., 2019; Cagigal et al., 2020).

In the current work, we assumed that MSL 2020-2100 projections are normally distributed. However, the MSL distribution may be skewed towards higher values due to

additional uncertainty related to Antarctic ice-sheet melting in the RCP8.5 scenario. We simulated a deterministic RCP8.5 high-end SLR scenario to define a low-probability/high-impact scenario for projected shoreline erosion. Yet, our high-end SLR scenario is based on a particular combination of high-end contributions to sea-level rise, which makes no consensus in the scientific community (Bamber et al., 2019; Edwards et al., 2021; Stammer et al., 2019). While this is not included in the GSA, the use of a skewed probability distribution may lead to an earlier onset of SLR uncertainties in shoreline projections.

The Bruun Rule, used in our application to estimate SLR-driven shoreline recession, builds on several strong assumptions that reduce the applicability of this model to a limited range of beaches (Cooper et al., 2020). As the Truc Vert is an uninterrupted natural cross-shore transport dominated beach, with large sediment availability, most underlying assumption of the Bruun model are satisfied. However, alternative models to address beach response to SLR, such as *ShoreTrans* (McCarroll et al., 2021), can be implemented in this framework.

Coupling the Bruun Rule with Y09 and SF allows accounting for long-term effects of SLR while resolving short-term shoreline response to the wave climate. The Y09 and SF models do not explicitly resolve sediment exchange between the different beach compartments (*e.g.* upper beach and dune), and may fail reproducing episodic shoreline changes such as short-term accretion following to dune erosion events. However, if such events occur during the model calibration period, as in our applications (*i.e.* winter 2013-2014), their influence on the bulk shoreline response is partially accounted.

Here, we investigated the main effect of the uncertainties in input variables (S_i s). While the estimated S_i of the DoC remains relatively low over the simulated period, in all simulated scenarios, the interaction of DoC and SLR uncertainties (*i.e.* second-order Sobol' index) may have a larger impact. However, estimating robust interaction terms would require a larger ensemble of simulations (several tens of thousands). Furthermore, in order to rigorously conclude on the negligible character of some uncertainties, GSA should be conducted within the factors' fixing setting (*i.e.*, investigating the 'total effect' of uncertain variables, Saltelli et al., 2008). In the presence of dependence among the inputs, more advanced GSA indices should be used for this purpose. In particular, a method that employs the so-called *Shapley effects* has recently been proposed and showed very promising results (Iooss & Prieur, 2019). While the direct application of this method requires computational cost of several order of magnitudes larger than the Sobol' indices (see Iooss & Prieur, 2019), Broto et al. (2020) successfully implemented a more

computationally efficient sampling-based method for GSA using Shapley indices. This may be an interesting perspective for future works.

5.6. Conclusions

We performed a Global Sensitivity Analysis on probabilistic 2020-2100 shoreline projections at the cross-shore transport dominated Truc Vert beach in southwest France. Time varying first-order Sobol' indices were calculated for sea-level rise, depth of closure, and model free parameters for two different cross-shore shoreline models (*Yates* and *ShoreFor*) and two RCP scenarios (RCP4.5 and RCP8.5). We show that uncertainties in shoreline projections are initially driven by uncertainties in model free parameters, with the effects of SLR uncertainties only emerging in the second half of the 21st century. However, the relative effects of SLR and model parameters uncertainties on shoreline projections do not only depend on the shoreline modelling approach and RCP scenarios, but their time evolution is also related to the forcing wave-climate variability. We also emphasize the importance of accounting for uncertainties related to the temporal distribution of wave energy, and therefore the need of ensembles of synthetic wave time series that account for the inherent variability of the wave climate, which is addressed in the following chapter.

Chapter 6

6. Effects of stochastic wave forcing on probabilistic equilibrium shoreline response across the 21st century including SLR

This chapter analyses the effects of the inherent variability of the wave climate on the behaviour and the uncertainties of shoreline change modelled with different equilibrium modelling approaches. By accounting for uncertainties on the chronology of wave events, this part of the manuscript tackles the research question *Q5* (Section 1.2) while providing new elements to the understanding of the relative impact that several sources of uncertainties have on shoreline predictions (*Q2*, *Q3*, and *Q4* of Section 1.2).

“Q2. How do the relative contributions of uncertain model parameters and physical forcing to modelled shoreline uncertainties evolve over time?”

Q3. How do the uncertainties on model parameters and equilibrium approaches relate to the wave climate forcing?”

Q4. On which time scale the uncertainties on SLR become the primary driver of the uncertainties on modelled shoreline?”

Q5. What is the role of uncertain wave climate variability on modelled shoreline?”

The investigation presented in this chapter stems from ongoing research, currently under peer review process:

D’Anna, M., Idier, D., Castelle, B., Cagigal, L., Rohmer, J., and Mendez, F.J.. Effects of Stochastic Wave Forcing on Equilibrium Shoreline Modelling Across the 21st Century Including Sea-Level Rise. *Coastal Engineering Journal*. (Under review)

6.1. Introduction

The input parameters and variables of (statistical or numerical) shoreline models include uncertainties that derive from simplifications and limited knowledge of some physical processes (model assumptions) or from the inherent variability of a model forcing (climate

unpredictability). Regardless of their nature, these uncertainties cascade through the model and result in uncertain model predictions (Toimil et al., 2021). Thus, current practices for coastal impact assessments are moving towards probabilistic frameworks for a robust risk-informed decision-making (Hinkel et al., 2019; Wainwright et al., 2015). Probabilistic, mostly ensemble-based, approaches have become increasingly popular to study the impact several sources of uncertainties on shoreline predictions. However, most studies focused on the impact of uncertainties in future SLR on shoreline predictions while including probabilistic wave-driven shoreline trends by extrapolation from past shoreline observations (Athanasίου et al., 2020; Le Cozannet et al., 2016; Thiéblemont et al., 2021, 2019; Vousdoukas et al., 2020), or resolving ~hourly shoreline response to deterministic realizations of future wave climate (Chapters 4 and 5), and did not include the inherent variability of wave climate.

The natural variability of the wave conditions introduces an unavoidable component of uncertainty to wave projections, which makes the intra-seasonal and intra-storm chronology of wave events hardly predictable (Mankin et al., 2020). Even when associating a comparable cumulative wave energy, different storm sequences can result in very different shoreline responses (Baldock et al., 2021; Coco et al., 2014; Eicientopf et al., 2020; Splinter et al., 2014a). Thus, the intrinsic uncertainty associated with the variability of wave conditions can have a significant impact on the confidence in modelled shoreline projections (Toimil et al., 2021; Vitousek et al., 2021). As the limited predictability of the future climate (and waves) introduces a certain uncertainty (Deser, 2020) to shoreline predictions, the use of large ensembles is advocated to quantify its contribution to the uncertainty in model results (Mankin et al., 2020). Davidson et al. (2017) developed a method to generate ensembles of annual wave time series by sampling and shuffling monthly wave sequences from a pool of historical wave data. Although this method preserves the seasonal variability of the wave climate, it does not ensure a realistic variability on longer time scales. The recent development of stochastic climate-based wave emulators enabled the efficient generation of large ensembles of indefinitely long wave series that are characterized by different chronologies of events while obeying to realistic climate patterns (Anderson et al., 2019; Antolínez et al., 2016; Cagigal et al., 2020; Pringle and Stretch, 2019; Rueda et al., 2016).

Resolving long-term wave-driven shoreline change in ensemble settings requires high computational efficiency. In this context, equilibrium shoreline models are particularly convenient tools (Montaño et al., 2020) as they simulate cross-shore shoreline response to

wave-driven sediment transport processes on time scales from hours to decades with low computational effort (Alvarez-Cuesta et al., 2021a; Davidson, 2021; Davidson et al., 2013; Jaramillo et al., 2020; Lemos et al., 2018; Robinet et al., 2018; Splinter et al., 2014b; Toimil et al., 2017; Yates et al., 2009). These models are based on the concept that changes in incident wave energy drive the shoreline towards a time-varying equilibrium position (Wright and Short, 1984) that is typically formulated as a function of either the current shoreline position (Miller and Dean, 2004; Yates et al., 2009) or the past wave conditions (Davidson et al., 2013; Splinter et al., 2014b). Although both equilibrium approaches have shown good skill in simulating multi-year shoreline change (Castelle et al., 2014; Montaña et al., 2020), their different responses to wave energy variability (see Chapter 5 and Vitousek et al., 2021) motivate further considerations on the respective skills in reproducing shoreline change under different wave forcing scenarios, particularly on multi-decadal timescales. Further, equilibrium shoreline models rely on the parametrization of some physical processes that require site-specific calibration against shoreline observations, of which the quality and availability introduce uncertainties in the model parameters (Splinter et al., 2013) that can significantly affect model predictions Chapter 4.

To date, few studies investigated the influence of uncertainties associated with short- and long-term variability of wave conditions on shoreline modelling. Cagigal et al. (2020) applied a stochastic wave emulator to force ensemble long-term shoreline predictions to several sites dominated by cross-shore sediment transport processes to replicate shoreline return periods observed in the past. Kroon et al. (2020) and Vitousek et al. (2021) quantified the relative contributions of the uncertainties associated with the inherent wave variability and model parameters to longshore (1 year) and cross-shore (8 years) shoreline projections, respectively. Alvarez-Cuesta et al. (2021b) examined short- and long-term drivers of the mean shoreline change at two longshore transport dominated sites using a wave ensemble and three percentiles of future SLR for two future climate scenarios. Toimil et al. (2021) produced multi-ensemble 2081-2100 projections to quantify the uncertainties associated with the individual steps of the modelling process, including uncertainties on SLR, waves, storm surges, and future climate scenario for two shoreline models. The works mentioned above resolved cross-shore wave-driven shoreline change using disequilibrium approach of the same kind, that is, where the beach equilibrium state is defined by the current shoreline position (Miller and Dean, 2004; Yates et al., 2009).

Many efforts have been dedicated to quantify the impact of intrinsic uncertainty on shoreline predictions. However, the role of the inherent wave conditions variability on

ensemble shoreline predictions in relation to uncertain SLR and model free parameters, and how substantially different modelling approaches respond to this type of uncertainties, has not been investigated. In addition, as observed in Chapters 4 and 5 the wave-driven parameters uncertainties are strongly connected to the wave forcing variability (Ibaceta et al., 2020; Splinter et al., 2017, 2014b; Vitousek et al., 2021), and the effects of possible interactions and correlations between the stochastic wave forcing and other uncertain model inputs have not yet been investigated.

In this chapter, we investigate the response of two different wave-driven equilibrium shoreline models to wave-forcing ensembles, and analyse how stochastic wave forcing affects the respective long-term shoreline predictions in relation to other uncertain factors (e.g. SLR) while accounting for possible interactions among them. New tools for Global Sensitivity Analysis (GSA, Saltelli et al., 2008) that account for correlated inputs are used to perform factor prioritization (by quantifying the relative importance of the uncertainties) and factor fixing (by identifying the uncertainties of negligible influence). The GSA estimates the model sensitivity ‘globally’ by exploring all the range of plausible values for the uncertain inputs while accounting for all possible interactions and statistical dependence between them. While previous studies addressed some of the elements investigated herein, this work includes the combined effects of these components, providing a more comprehensive analysis. The analysis is carried out on the cross-shore transport dominated Truc Vert beach (France) accounting for uncertainties in free model parameters, variability of wave conditions and SLR projections for two future representative greenhouse-gas concentration pathway (RCP) scenarios, under the assumption that future wave climate maintains the properties observed over the past decades. We investigate an additional scenario over the past 23.5 years, where only wave chronology and model free parameters are considered as uncertain input variables.

The remainder of the chapter provides a description of the data, the shoreline models and the method used herein (Section 6.2); the assessment of the probability distributions associated to the uncertain model inputs, required for the GSA, and the ensemble modelling setup (Section 6.3). The results are presented and discussed in Section 6.4 and 6.5, respectively, followed by the conclusions (Section 6.6).

6.2. Material and Methods

6.2.1. Waves and sea-level data

Historical wave data was required for calibration of the shoreline models and for generating the wave ensemble used in this work to force the probabilistic past and future shoreline projections. Information on past and future relative mean sea level (MSL) at Truc Vert beach was needed to account for SLR-driven shoreline erosion during model calibration and simulations. Here, we used the same datasets of past wave conditions, past MSL, and future SLR projections described in Section 2.1. This section briefly describes these datasets, which are all extended here to June 2021.

Historical incident wave conditions at Truc Vert beach was obtained from the NORGAS-UG regional wave hindcast (Section 2.1.2). We adopted a constant rate of historical relative SLR of 3.3 ± 0.7 mm/year (median $\pm \sigma$), obtained in Chapter 4 from the combination of geocentric MSL change and vertical land motion at Truc Vert beach. Future relative MSL at Truc Vert beach was estimated from the global SROCC projections SLR projections until 2100 and the respective likely ranges (17th – 83rd percentiles) described in Chapter 5, for the RCP4.5 and RCP8.5 scenarios.

6.2.2. Shoreline models

Similarly to Chapter 5 cross-shore shoreline response to the incident wave climate was resolved using the *ShoreFor* (Davidson et al., 2013; Splinter et al., 2014b) and the Yates et al. (2009) equilibrium shoreline models. Breaking wave conditions, which are required to force the above models, were estimated with the Larson et al. (2010) empirical formula. Long-term shoreline retreat induced by SLR was modelled using the Bruun (1962) Rule. The wave-driven models and the Bruun Rule were run separately and then linearly combined in order to avoid feedback mechanisms between the models (Chapter 3), in line with previous works (Vitousek et al., 2017b).

Here, we briefly describe the shoreline models used in this chapter. The *ShoreFor* model (SF) computes the rate based on the forcing wave power (P (W)) and disequilibrium of dimensionless fall velocity ($\Delta\Omega$). The model includes three site-specific parameters: the shoreline response rate $k_s^{+/-}$ ($\text{m s}^{-1}\text{W}^{-0.5}$), the beach memory Φ (days) and the linear trend b (m/s) (Equation 2.1). The values of the $k_s^{+/-}$ parameter for accretion and erosion conditions are assumed proportional through the coefficient r ($k_s^- = rk_s^+$), where r is estimated from the

forcing wave time series and is such that no trend in wave forcing results in no trend in the modelled shoreline position as described by Equation 2.4:

$$r = \left| \frac{\sum_{i=1}^N \langle F^+ \rangle}{\sum_{i=1}^N \langle F^- \rangle} \right| \quad (2.4)$$

Here, following Chapter 5, we set $b=0$, reducing the model to Equation 5.1 that we recall here:

$$\frac{dY}{dt} = k_s^{+/-} P^{0.5} \frac{\Delta\Omega}{\sigma_{\Delta\Omega}} \quad (5.1)$$

In the Yates et al. (2009) model (Y09) the rate of shoreline change is determined as a function of the incident wave energy (E (m^2)) and the wave energy disequilibrium (ΔE (m^2)). The equilibrium state E_{eq} is defined as an empirical function of the current shoreline position Y , through the site-specific parameters a_1 (m^2/m) and a_2 (m^2) (Equation 2.7). Y09 also includes a site-specific shoreline response rate parameter $k_y^{+/-}$ ($\text{m}^2 \text{ s}^{-1}/\text{m}$) (Equation 2.6). Reminding Equations 2.6 and 2.7, the model reads:

$$\frac{dY}{dt} = k_y^{+/-} E^{0.5} (E_{eq}(Y) - E) \quad (2.6)$$

$$E_{eq}(Y) = a_1 Y + a_2 \quad (2.7)$$

As discussed in Chapter 4, Y09's equilibrium state does not depend on recent wave conditions, limiting the model sensitivity to wave-climate variability on timescales longer than the calibration period. Vitousek et al. (2021) showed that a rearrangement of Y09 free parameters results in combined terms that can be interpreted as local equilibrium time and spatial scale factors. However, in this application we retained the original form of Y09, interpreting a_1 and a_2 as empirical parameters.

6.2.3. Multivariate stochastic climate-based wave emulator

Equilibrium shoreline models require continuous time series of incident wave conditions with a time resolution of the order of hours. In this study, we produced an ensemble of synthetic wave forcing conditions using the climate-based stochastic wave emulator developed by Cagigal et al. (2020). For a given location, the emulator exploits broad spatial scale sea level pressure fields and synoptic patterns, together with local historical wave data, to generate ensembles of unique continuous realistic wave time series. The wave series are generated through: (i) a statistical downscaling of climate forcing relying on annual and daily synoptic patterns; (ii) an intra-seasonal chronology model based on autoregressive logistic regression (Anderson et al., 2019); and (iii) a 'stretching and

shuffling’ of intra-storm historical wave properties using Gaussian copulas. This method ensures that the modelled wave time series present different chronologies of events while preserving intra-storm to interannual statistical properties consistent with the historical data. The latter means that the generated time series are also characterized by the same long-term trend observed over the historical wave data, therefore assuming an unchanged future wave climate. The wave emulator has already been applied to produce ensembles of wave time series for probabilistic shoreline modelling at several sites based on the respective records of historical wave conditions, and showed good skill in reproducing observed shoreline erosion statistics (Cagigal et al., 2020; Vitousek et al., 2021). For a more detailed outline of the underlying methodology see Cagigal et al. (2020).

We used the wave emulator to model 200 hourly time series of wave conditions (H_s , T_p , D_m) from January 1994 to December 2099, based on 26-year (1994-2020) of wave hindcast data offshore Truc Vert beach (Section 2.2) and sea level pressure fields from the Climate Forecast System Reanalysis (Saha et al., 2010). Figure 6.1b shows the mean (orange line), standard deviation (yellow area), and the min-max envelope (red area) of the emulated H_s series, which attains extreme values of same order of magnitude as observed during the hindcast period ($H_s \sim 8-10$ m). Figure 6.1c illustrates the standard deviation (yellow area) and envelope (red area) of the 3-month averaged $H_s^2 T_p$ ensemble, along with an example of individual time series (black line). The statistical properties of the generated ensemble showed good agreement with the historical wave data. Figure 6.1d,e show a *quantile-quantile* comparison of H_s between the reference hindcast data (1994-2020) and each member of the wave ensemble (1994-2099) for the full time series and their seasonal repartition, respectively. Here, seasons were defined as follows: Winter (December-January-February), Spring (March-April-May), Summer (June-July-August) and Autumn (September-October-November). The comparisons of T_p and D_m are shown in the Appendix D1. While the H_s quantiles estimated on the entire time series show a near-perfect consistency (Figure 6.1c), the seasonal plots show some discrepancies (Figure 6.1d). However, these differences are not expected to affect the analyses carried out in this work (as discussed in Section 6.5.4). Consistently with the historical wave series, the winter mean wave heights of the emulated time series show no significant trend between present day (2021) and the end of the 21st century (Figure D.2). Finally, the emulated wave time series well reproduce the historical weather type probabilities for large scale predictors such as annual weather types (AWT) and Madden-Julian Oscillation (MJO) (Appendix D1, Figure D.3).

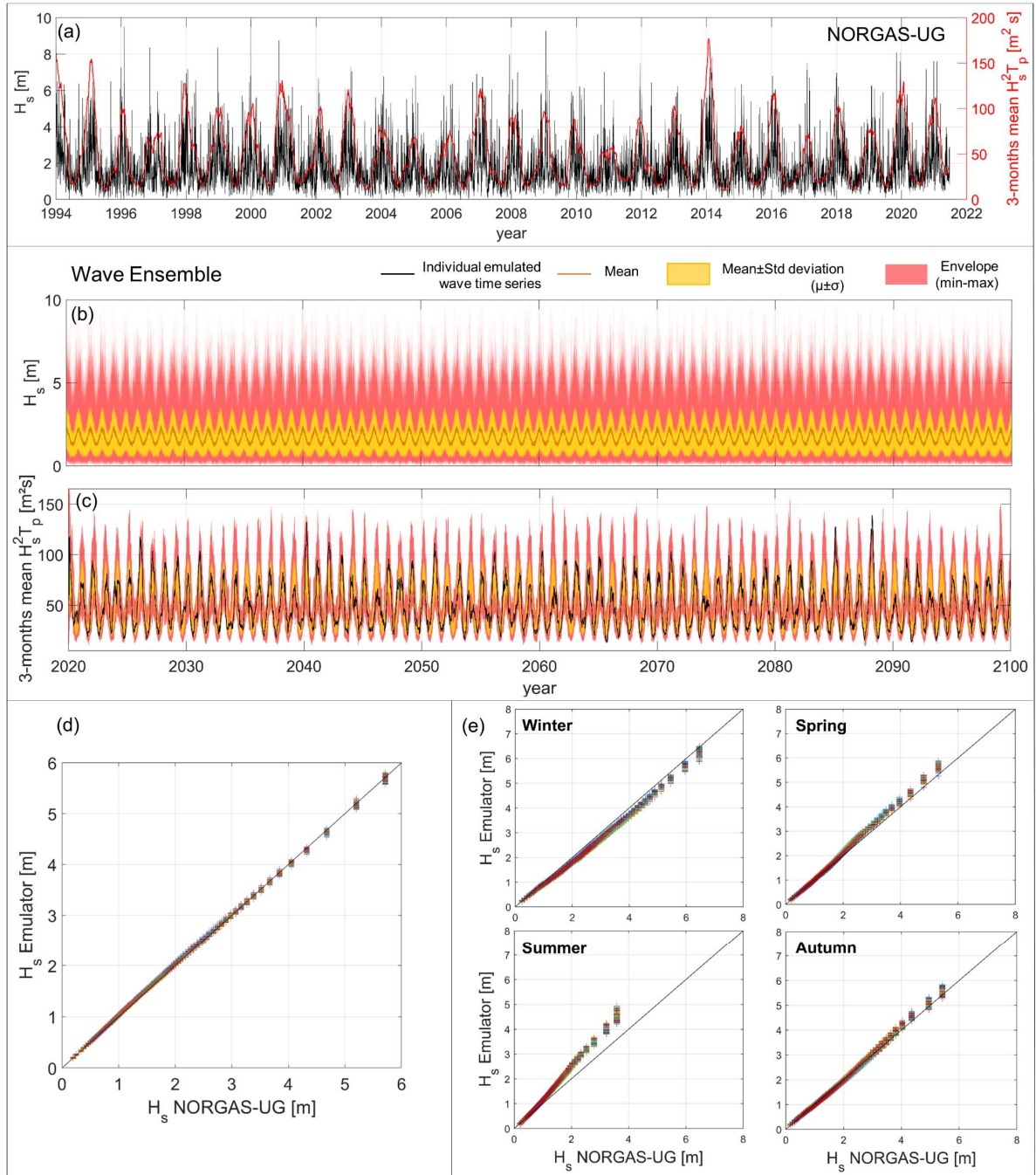


Figure 6.1. (a) Time series of H_s (black line) and 3-month averaged $H_s^2T_p$ (red line) from 1994 to 2021 from NORGAS-UG hindcast model; Envelope (min. and max.) (red area) and mean $\pm \sigma$ interval (yellow area) of the 200 (b) H_s and (c) 3-month averaged $H_s^2T_p$ time series from 2021 to 2100, generated using the wave emulator, with mean H_s (orange line) and the 3-month averaged $H_s^2T_p$ of an individual time series; quantile-quantile comparison between the H_s of hindcast data and each member of the wave ensemble for (d) the full time series, and (e) their seasonal repartition.

6.2.4. Global Sensitivity Analysis

We quantified the different contributions to the uncertainties on modelled shoreline change at Truc Vert beach by performing the variance-based GSA (Saltelli et al., 2008) described in Section 2.3.2. The variance-based GSA divides the uncertainties (represented

by the variance) of probabilistic model results into several portions, each one attributed to an uncertain model input. For each uncertain input X_i , the normalized main effect of X_i uncertainties on the model results can be synthesized by first-order Sobol' indices (S_i) (Sobol', 2001). S_i quantifies the percentage of the model results variance that can be attributed to the uncertainties on the variable X_i alone. However, possible interactions among uncertain inputs within the model can increase the impact of each interacting variable on the results uncertainties. The latter increase is included in the higher-order (or interaction) effects. Higher-order terms describe the effects of the simultaneous variation of multiple uncertain inputs on the results variance. The GSA based on Sobol' indices assumes that all the uncertain input variables are statistically independent from one to another. If two or more uncertain inputs are statistically dependent, say X_i and X_j , such correlations can significantly influence the uncertainties of model results, and the S_i includes some information that is also included in S_j , regardless of the possible interactions between the two variables (Do and Razavi, 2020; Iooss and Prieur, 2019). This is the case, for instance, of calibrated model parameters, which can associate up to more than 70% correlation coefficient (see Section 6.3.1).

The *Shapley Effects* (Sh 's) have been proposed based on the *Shapley values* (Shapley, 1953) to overcome the difficulties in the interpretation and use of the *Sobol' indices* in presence of statistical dependence and interaction among inputs (Iooss and Prieur, 2019; Owen, 2014; Song et al., 2016). The *Shapley values* were originally introduced in game theory to evaluate the "fair share" of team players after a game based on their individual contributions and their interactions with other players. In the context of the GSA the 'players' are the uncertain model inputs, and the model results variance is the 'value' to share. The Sh_i quantifies the percentage of output variance ($0 \leq Sh_i \leq 1$) associated to the input variable X_i , including the main effect, an equitable share of all its interaction terms with other variables, and the contributions of possible statistical dependence (correlation) among the uncertain inputs, and is expressed as follows:

$$Sh_i = \frac{1}{k} \sum_{A \subseteq K \setminus \{i\}} \binom{k-1}{|A|}^{-1} (S_{A \cup \{i\}} - S_A) \quad (6.1)$$

$$S_A = \frac{\text{Var}(E(Y|X_A))}{\text{Var}(Y)} \quad (6.2)$$

where k is the number of uncertain input variables, $K \setminus \{i\}$ is the set of input indices $(1, \dots, k)$ excluding i , A is a subset of $K \setminus \{i\}$, and $|A|$ is the cardinality number of the subset A (see Appendix A2 for details). For a given input X_i , $Sh_i=1$ indicates that the uncertainties on X_i

are accountable for the entirety of the results uncertainties, while for $Sh_i=0$ the model results are essentially insensitive to X_i , and the sum of all Sh 's equals 1. While Sh 's include the first- and higher-order terms and the shared effects of inputs correlations to the model results, they do not provide these contributions separately.

We analyse the time-varying effects of uncertainties associated to model free parameters, SLR, and wave chronology on the modelled Truc Vert shoreline change. In addition, we assess the impact of the shoreline modelling approach choice by repeating the application for each of the two wave-driven models (SF and Y09). The framework described above requires the definition of a probability distribution for each uncertain input variable, a large number of realizations based on a Monte-Carlo procedure (accounting for statistical dependence among the variables), and the computation of Shapley effects at each analysed time step (Figure 6.2).

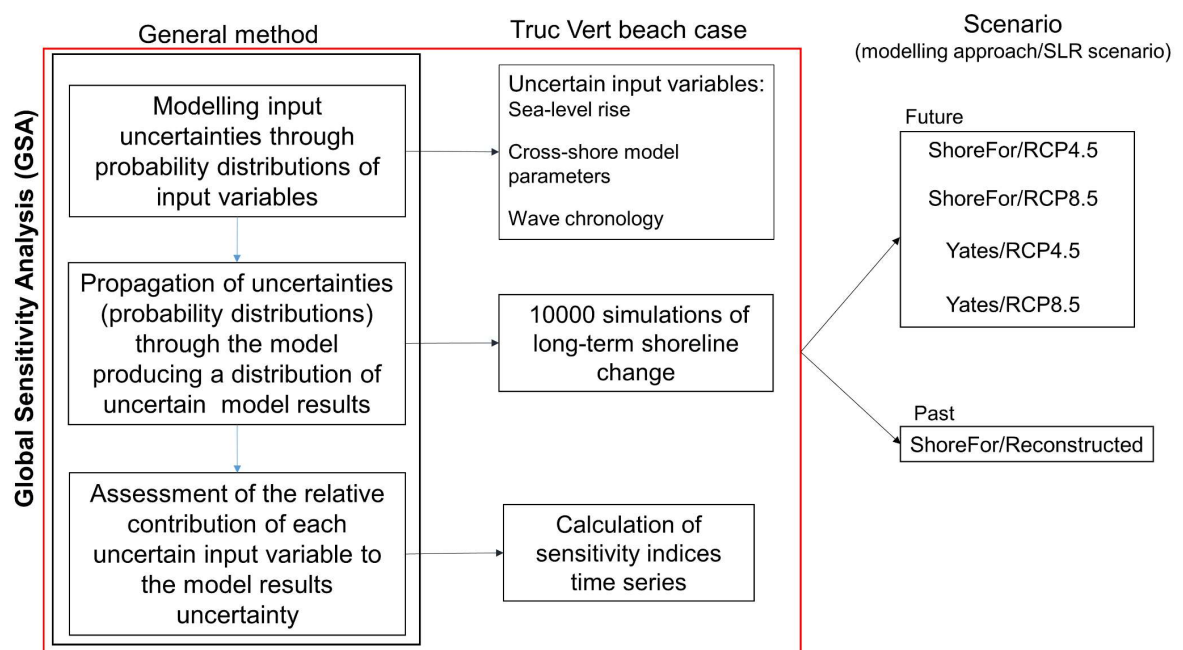


Figure 6.2. Method outline of a generalized case (black box) and the Truc Vert beach applications (red box) for past and future different sea-level rise and shoreline modelling scenarios.

6.3. Input uncertainties and models setup

6.3.1. Model free parameters

Equilibrium shoreline models are affected by uncertainties related to the underlying physical assumptions as well as their data-driven nature. We accounted for the former by running and comparing the GSA for different scenarios using the disequilibrium approaches of the SF and Y09 models (Section 2.2.1). These models require the calibration of free

parameters that associate uncertainties depending on the extent, density and quality of the available shoreline datasets (Splinter et al., 2013). The uncertainties on the calibration of SF (k_s^+ , Φ) and Y09 ($k_y^{+/-}$, a_1 , a_2) model free parameters are represented by the respective joined probability distributions, defined using the approach adopted in Chapter 5. In this approach, the shoreline models are calibrated using the Simulated Annealing algorithm (Bertsimas and Tsitsiklis, 1993), which generates a large number of model parameters combinations before converging to a set of best-fit parameters. The parameters combinations that produce a model performance higher than a predefined threshold are selected and used to fit an empirical multivariate probability distribution (multivariate kernel function). The model performance is measured in terms of Nash and Sutcliffe (1970) score (NS). The minimum threshold used to fit the free parameters probability distribution is set to $NS \geq 0.25$, which is an appropriate value for SF and Y09 applications at Truc Vert beach (see Chapter 5). Here, we calibrated the models over the period March 2012 – September 2019, which show no long-term shoreline trend supporting the assumption that $b=0$ in the SF model. Further available shoreline observations up to June 2021 (Figure 2.1e) are exploited for the validation of the ensemble simulations. Shoreline data prior to 2012 is discarded from the calibration procedure due to the lower confidence deriving from the limited alongshore coverage of their associated topographic survey (see Section 2.1.2.1). Over the calibration period, the Y09 and SF models produce a Root-Mean-Square-Error (RMSE) of 5.1 m and 7.2 m, respectively, and a coefficient of determination R^2 of 0.80 and 0.65, respectively. The resulting probability distributions of Y09 and SF model free parameters are shown in Figure 6.3c,d together with the respective Pearson correlation coefficients (denoted ρ) indicating several levels of correlation among the model parameters. The ranges of possible parameters values are reported in Table 6.1.

6.3.2. Sea-Level Rise

Information on past relative MSL associates uncertainties related with measurement errors of the geocentric MSL and the vertical land motion. This kind of uncertainties are very small compared to the uncertainties on the free parameters of shoreline models, and have been shown to have a negligible impact on the uncertainties of shoreline change at Truc Vert over the past 20 years (Chapter 4). Therefore, here the uncertainties on past SLR were not included in the GSA.

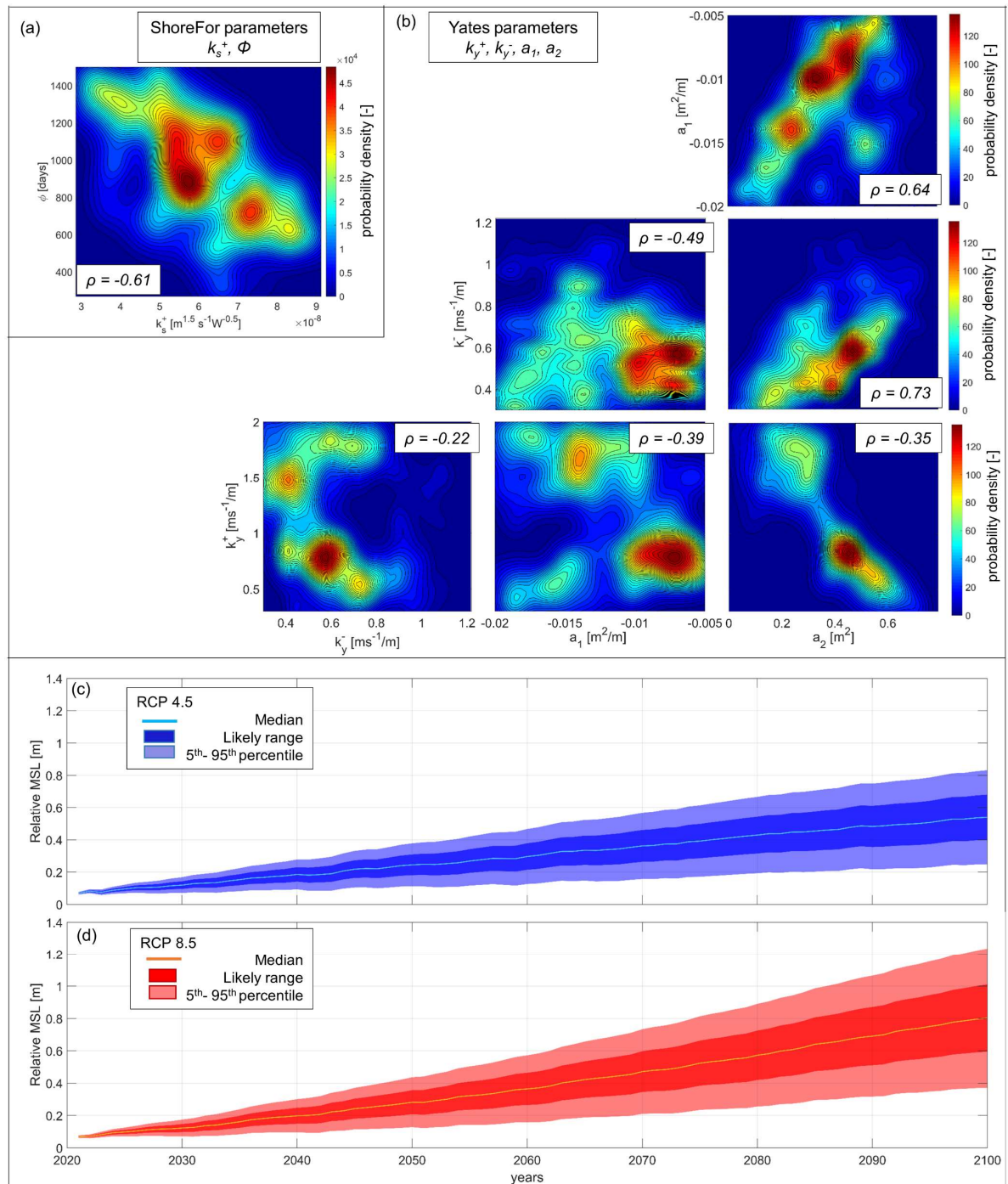


Figure 6.3. Joint distributions of (a) the ShoreFor (k_s^+ , Φ) and (b) Yates ($k_y^{+/-}$, a_1 , a_2) free parameters with the corresponding Pearson correlation coefficients ρ ; and probability distributions of 2021-2100 sea-level rise projections for (c) the RCP4.5 and (d) RCP8.5 scenarios, with the respective 66% confidence interval (dark-shaded areas) and 5th-95th percentile range (light-shaded area).

Table 6.1. Optimised combinations of cross-shore model free parameters, and respective range of variation in the probability distributions.

Model	Model parameter	Optimised value	Distribution range
ShoreFor (SF)	$k_s^+ [m^{1.5} s^{-1} W^{-0.5}]$	5.0×10^{-8}	$[1.6; 9.8] \times 10^{-8}$
	φ [days]	1127	[106; 1729]
Yates (Y09)	$k_y^+ [m^2 s^{-1} /m]$	0.71	[0.15 ; 2.41]
	$k_y^- [m^2 s^{-1} /m]$	0.56	[0.10 ; 1.32]
	$a_1 [m^2/m]$	-0.01	[-0.02 ; -0.003]
	$a_2 [m^2]$	0.46	[0.01 ; 0.79]

Uncertainties on future SLR estimates essentially derive from unknowns on the future climate scenario and modelling of the different contributing processes. These sources of uncertainty were accounted through the likely range of the SROCC projections. Following Chapter 4, we produced probabilistic MSL projections assuming a Gaussian distribution (in line with Hunter et al., 2013), with median and standard deviation corresponding to the yearly median and likely range SROCC estimates for the RCP4.5 and RCP8.5 scenarios (Figure 6.3c,d). As the SROCC projections refer to the year 2007, we re-fitted the projections between 2021 and 2100, conditioning the MSL median and likely range to the corresponding values observed in 2021. See Appendix D2 for more details on this correction. As the characteristics of the future MSL probability distribution are time-dependent, in the following applications MSL time series were defined for a given percentile (p) by extracting the sea level corresponding to p at each year.

6.3.3. Waves chronology

The stochastic nature of wave conditions provides a portion of uncertainties to the modelled shoreline change, which responds differently to different chronologies of wave events. In order to account for the uncertainties on wave chronology, we define an indicator variable (i.e. categorical variable) that takes up discrete values between 1 and 200, each value being associated to a given time series described in Section 2.4.1 (index 1 for time series N°1, index 2 for time series N°2, etc.). Then, we randomly and uniformly sample the values of the indicator variable to select the time series used to force the shoreline modelling realizations within the GSA. In the following, the influence of the wave chronology is analysed by assessing the Shapley Effect of the defined indicator variable. This differs from the analysis of uncertain model free parameters (parameters values) and future SLR (values

of 5th to 95th SLR percentile) in that the indicator variable is not a quantitative value but a categorical number (index 1 to 200). This approach, has been applied by Rohmer (2014) for spatially varying uncertain inputs, allows accounting for the bulk effect of stochastic time-varying wave forcing on the uncertainties of modelled shoreline positions.

6.3.4. Model setup

Ensembles of simulated shoreline time series were generated for one ‘past scenario’ and four ‘future scenarios’ at Truc Vert beach. All scenarios covered the calibration period (March 2012 – September 2019) and a validation period (September 2019 – June 2021). In the ‘past scenario’, shoreline evolution was simulated from January 1998 to June 2021 using SF and the Bruun model. To perform such ensemble computation, we need to select a reference time with a known shoreline position. Here, we select the first observation of the calibration period (March 2012). From this date, the ensemble modelling is classically done forward (from 2012 to 2021). To perform backward ensemble simulations, the SF and Bruun models are inverted to estimate the shoreline position at time step $i-1$ using shoreline position and wave forcing conditions at time step i and the $(SLR_{i-1} - SLR_i)$ quantity (see Appendix). As the Y09 computation of shoreline change at a given time is dependent on the previous shoreline position, the model does not allow propagating the uncertainties on modelled shoreline towards the past. Therefore, the Y09 model application to the ‘past scenario’ was not included in the main analysis, as discussed in Section 6.5.1. Although wave data is available on the ‘past scenario’ simulated period, here we considered random wave conditions characterized by the same statistical properties as the hindcast wave data, *i.e.* wave data generated with the stochastic climate-based wave emulator (Section 6.2.3). In the ‘future scenarios’, the shoreline position was modelled over March 2012 – December 2099 using Y09 and SF with the Bruun model for the RCP4.5 and 8.5 SLR scenarios. The models were forced using MSL time series corresponding to percentiles randomly sampled between the 5th and 95th, and the randomly selected wave time series (Section 6.3.3) characterized by the same properties as the past wave climate (unchanged future wave climate).

For each ensemble, several thousands of shoreline trajectories were simulated using different combinations of model free parameters, sea level percentiles and wave time series sampled from the respective probability distributions. One exception is the ‘past scenario’, where local SLR is considered deterministic with a constant rate of 3.31 mm/year, while only the model free parameters and forcing wave series were sampled for each model run.

Over the calibration and validation periods, the models were forced using the observed (deterministic) wave and sea-level time series. The starting time of both past and future shoreline simulations was set to the starting date of the models calibration (23rd May 2012), so that the modelled shoreline trajectories fit the shoreline data as observed during the calibration and the uncertainties on simulated past shoreline change propagate towards the past. All simulations are run with a 3-hour time step and outputs were stored with a 2-weeks frequency. The ensembles of model results were analysed through the *envelope* (min-max) and the *likely range*, defined here as the standard deviation interval ($\mu \pm \sigma$), of the simulated shoreline positions. The former is an indicator of the shoreline response to extreme wave events, while the latter is proportional to the results variance (σ^2) used to perform the GSA. Herein, positive (negative) variations of the shoreline position $dY/dt > 0$ ($dY/dt < 0$) indicate shoreline accretion (erosion).

The *Shapley Effects* (Section 6.2.4) were computed for each stored model output excluding the calibration and validation periods (i.e. excluding March 2012 – June 2021) by post-processing the inputs and the results of the ensemble model realizations with a nearest-neighbour search technique (Broto et al., 2020), using the 15 nearest neighbours. Before the *Sh*'s computation, the uncertain input values were rescaled with a whitening procedure in order to achieve a homogeneous scale, and the wave time series were treated as a categorical input, i.e. they are identified as the *i*-th, ... , *j*-th, time series. For each GSA application, we estimated 90% confidence bounds applying a 100-iteration bootstrapping at three different times of the simulated period for the ‘future scenarios’ (1st Jan. 2030, 2060 and 2090) and two for the ‘past scenario’ (1st Jan. 2000 and 2010). Confidence intervals were estimated by sampling without replacement with a proportion of the total sample size of 0.80, drawn uniformly (following the implementation in R *sensitivity* package).

Table 6.2. Past and future simulated ensembles based on 10000 different combinations of model parameters, SLR percentile and wave time series, for two future Representative Concentration Pathways (RCP) and two different wave-driven modelling approaches with the Bruun Rule. Over the period 2012-2021, the models are forced with deterministic wave and sea level conditions, and 10000 combinations of model free parameters.

Scenario	SLR scenario	SLR-driven shoreline model	Wave-driven shoreline model	Dataset name	Combinations	Simulated period
Past	Reconstructed	Bruun Rule	<i>ShoreFor</i> (SF)	SF+B/Past	10000	1998-2021
Future	RCP 4.5	Bruun Rule	<i>ShoreFor</i> (SF)	SF+B/RCP4.5	10000	2012-2100
			<i>Yates</i> (Y09)	Y09+B/RCP4.5	10000	
	RCP 8.5	Bruun Rule	<i>ShoreFor</i> (SF)	SF+B/RCP8.5	10000	
			<i>Yates</i> (Y09)	Y09+B/RCP8.5	10000	

6.4. Results

The modelling setup described in Section 3.4 (Table 6.2) produced five ensembles of simulated shoreline position time series: one covering the past 23.5 years (Figure 6.4a), and four spanning from present day to 2100 (Figure 6.4b-e). Figure 6.4a-c and Figure 6.4d,e show the envelopes (min-max) and likely ranges ($\mu \pm \sigma$) of shoreline trajectories obtained using the SF and Y09 approaches, respectively, for the different scenarios. All modelled ensembles consistently fit the shoreline data over the calibration period (2012-2019) and well reproduce the large erosion associated with the particularly energetic winter of 2013-2014. The models also reproduce the shoreline variations observed during the validation period (2019-2021), with a mean determination coefficient $R^2=0.73$ and a mean RMSE=10.65 m. Over the validation period, the modelled shoreline ensembles capture the erosive trend associated with the increasing interannual winter wave energy in 2019-2021 (Figure 6.4), with shoreline data falling within the range of the modelled ensembles (Figure 6.4). Compared to the ‘future scenarios’, the SF+B application to the past scenario shows slightly larger ranges of modelled shoreline over the calibration and validation periods (Figure 6.4a). This is due to the influence of the ensemble forcing wave conditions prior to 2012 on the SF shoreline change computed over the following period.

In the ‘past scenario’ (Figure 6.4a), the likely range (envelope) of shoreline position varies from [-29 m; -7.6 m] ([-59.2 m; 46.9 m]) in 1998 to [-8.3 m; -1 m] ([-15.1 m; 6.3 m]) in 2012. The application of ensemble wave forcing (1998-2012) results in a ‘richer’ envelope of possible shoreline trajectories and visibly larger model variance compared to the calibration and validation period (2012-2021) where a deterministic wave time series was applied (Figure 6.4a). The ensemble results also capture the shoreline data prior to 2012, which was discarded from the model calibration but provides a realistic reference of shoreline variability.

Figure 6.4b-e show the ‘future scenarios’ of ensemble shoreline projections modelled combining the Bruun model with SF and Y09, respectively, for two SLR scenarios (RCP4.5 and 8.5). All models were forced with the same random selection of wave time series, and no feedbacks were allowed between the wave- and SLR-driven models. Therefore, any long-term shoreline trend induced by each wave series of the ensemble is reproduced identically for the RCP4.5 and 8.5. Hence, the results obtained for the different RCP scenarios only differ in the magnitudes of the SLR-driven erosional trends. Indeed, using either SF or Y09, the RCP8.5 scenario produces a more eroded shoreline position in 2100

and a larger variance compared to the RCP4.5 scenario. Likely ranges and envelope values of the 2100 simulated shoreline position are summarized in Table 6.3 for each ‘future scenario’, including the corresponding ranges resulting from the application of the Bruun Rule alone.

The application of ensemble wave forcing series (from 2021 to 2100) results in different, though realistic, interannual and multiannual shoreline patterns for the two wave-driven shoreline models (SF and Y09), with uncertainties increasing over time. In particular, SF+B produces possible large interannual accretional trends of shoreline position (Figure 6.4b,c) of the same order (~50s of meters) as the interannual cycles observed over the past decades (Figure 2.1e). Contrarily, Y09+B results in permanently erosional trends. In the two SF future scenarios (Figure 6.4b,c), the ensemble projections show an initial period of overall accretion of (2021-2030). Over the remaining part of the projection period (2030-2100), the likely range of shoreline position maintains a seasonal character with a stable long-term erosive trend. Instead, the envelopes of simulated shoreline trajectories show inter- and multi-annual fluctuations of both the most accreted (max) and eroded (min) modelled shoreline position, highlighting the SF ability to respond to long-term variability of the wave conditions. This is also illustrated by the two individual modelled shoreline trajectories extracted from the ensembles (yellow and green lines in Figure 6.4b,c). The width of both likely range and envelope of shoreline position increases progressively from 2021 to ~2030 as the memory of (deterministic) wave conditions prior to 2021 decays. After 2030, the likely ranges gradually grow until ~2070 before narrowing until 2100 (as discussed in Section 6.5.1), while the envelope range follows the same trends with superposed interannual variations, once again, associated to the temporal patterns of the forcing wave series (Figure 6.4b,c). However, while characterized by different chronologies, the members of the wave ensemble used here preserve consistent seasonal to multiannual statistics, which somehow constrain the SF envelope of shoreline ensemble to a fixed possible range.

When wave-driven shoreline change is modelled with the Y09 model (Figure 6.4d,e), both likely range and envelope of simulated shoreline positions show a clear seasonal signal with a regular erosive trend throughout the entire projection period (2021-2100), regardless of the RCP scenario. Here, the individual shoreline trajectories (yellow and green lines in Figure 6.4d,e), forced with the same wave series as the individual realization selected for the SF model, evolve with no long-term variations. In these two scenarios, the width of likely ranges and envelopes grows gradually, and the lower bound of the envelope exhibits some interannual variability.

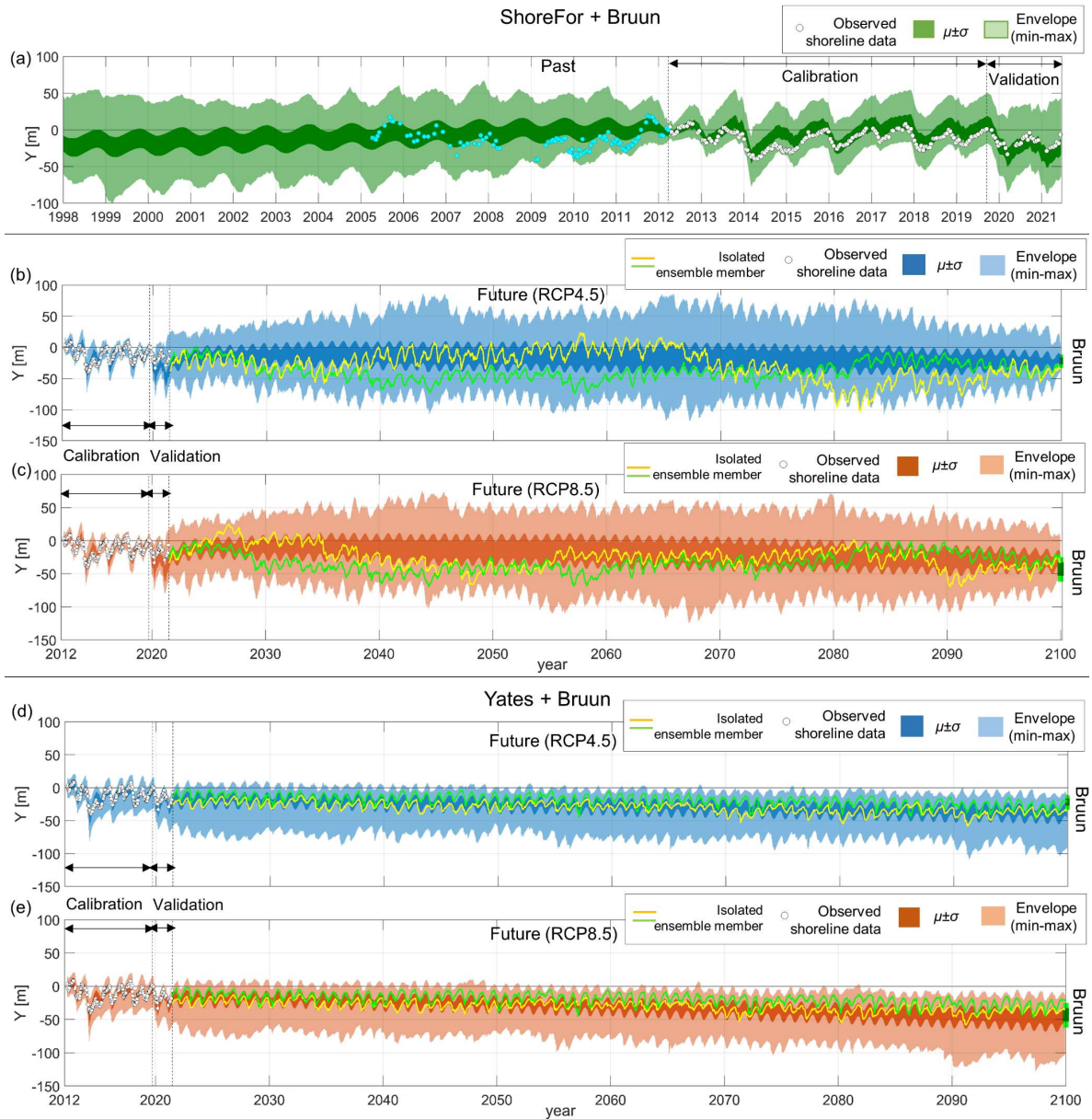


Figure 6.4. Ensemble shoreline evolution simulated using the (a-c) *ShoreFor* and (d,e) *Yates*, combined with Bruun models, including the envelope (light-shaded areas) and the standard deviation intervals ($\mu \pm \sigma$) (dark-shaded areas) of the 10000 simulated shoreline trajectories, respectively, over (a) the 1998-2021 period ('past scenario'), and from 2012 to 2100 ('future scenarios') for the (b,d) RCP4.5 and (c,e) RCP8.5 future sea-level rise scenarios. Yellow and green lines (b-e) are individual model realizations within the ensemble. Black dashed lines delimit the calibration and validation periods, including shoreline observations (white circles). Cyan-coloured circles (a) indicate shoreline data prior to March 2012.

Table 6.3. Model results at 2090 and 2100 obtained for the four ‘future scenarios’ and the applications of the Bruun Rule alone, including the likely range ($\mu \pm \sigma$) and envelope (min-max) of simulated shoreline position, and the mean of 1-year averaged shoreline trajectories.

Future scenario	2090 modelled shoreline position		2100 modelled shoreline position	
	Likely range ($\mu \pm \sigma$)	Envelope (min-max)	Likely range ($\mu \pm \sigma$)	Envelope (min-max)
(SF+B)/RCP4.5	[-39 m; -7 m]	[-88 m; 44 m]	[-27 m; -12 m]	[-40.5 m; -0.7 m]
(SF+B)/RCP8.5	[-47 m; -12 m]	[-96 m; 40 m]	[-41 m; -19 m]	[-57 m; -3 m]
(Y09+B)/RCP4.5	[-47 m; -29 m]	[-79 m; -10 m]	[-48 m; -29 m]	[-93 m; -13 m]
(Y09+B)/RCP8.5	[-58 m; -35 m]	[-105 m; -15 m]	[-61 m; -36 m]	[-101 m; -15 m]
Bruun/RCP4.5	[-25 m; -15 m]	[-31 m; -11 m]	[-37 m; -28 m]	[-43 m; -22 m]
Bruun/RCP8.5	[-37 m; -21 m]	[-45 m; -13 m]	[-53 m; -33 m]	[-62 m; -25 m]

6.4.1. Global Sensitivity Analysis

For each model output time-step, the GSA decomposed the variances (i.e. uncertainties) of the simulated shoreline ensembles into a set of *Shapley Effects* corresponding to the uncertain model inputs. The GSA for the ‘past scenario’ results in roughly stable *Sh*’s of the model free parameters and the wave chronology over time, with mild long-term trends. As the model variance reduces from 1998 to 2012, the *Sh* values of the SF parameters k_s^+ and Φ first decrease from 15% to 5% and 13% to 5% (~2006), respectively, then increase to 40% and to 39%, respectively by 2012. The wave chronology’s *Sh* gradually increases from 78% to 85% (~2006) before decaying to 21% (Figure 6.5b-d). The 90% confidence bounds were estimated to be within $\pm 1\%$ for all the variables. All *Sh*’s show a mild seasonal, where the *Sh*’s of free parameters increase during accretion (low wave energy) periods, contrary to wave chronology’s *Sh*.

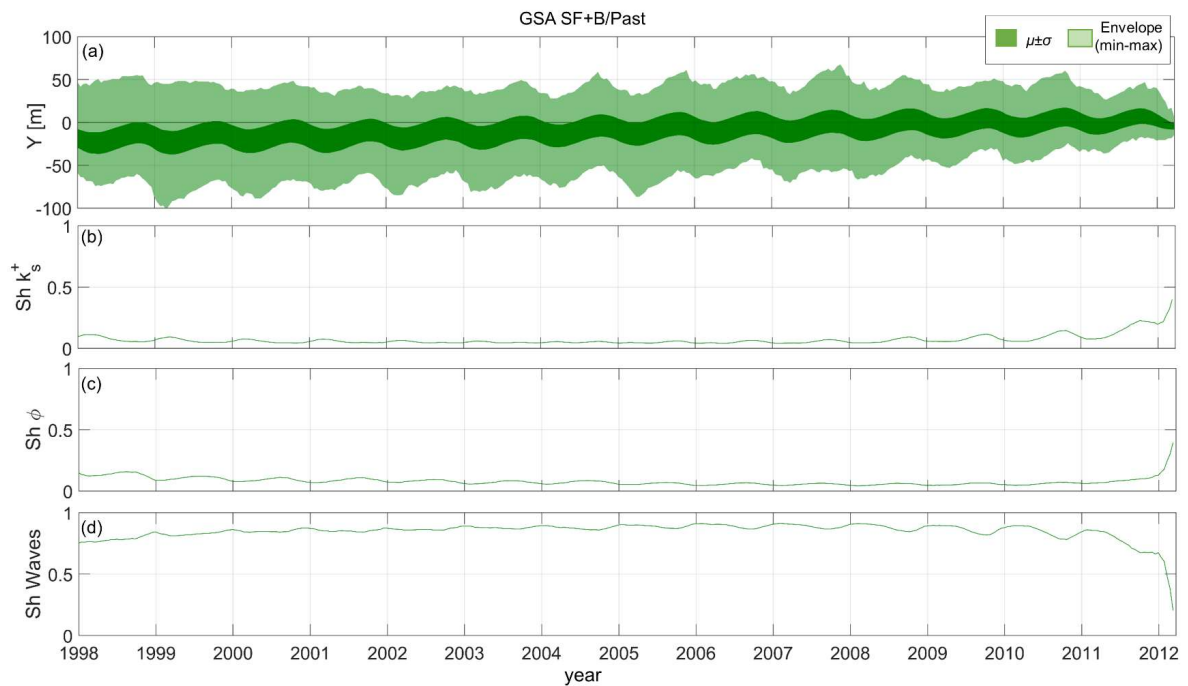


Figure 6.5. Global Sensitivity Analysis results for the ‘past scenario’, including time series of: (a) the ensemble simulated shoreline positions from 1998 to 2012; and *Shapley Effects* of the *ShoreFor* parameters (b) k_s^+ and (c) Φ , and (d) wave chronology.

Figure 6.6 and Figure 6.7 show the GSA results for the ‘future scenarios’ where wave-driven shoreline change is simulated using the SF and Y09 models, respectively. For both modelling approaches, the *Sh*’s show a similar behaviour between the RCP4.5 and RCP8.5 scenarios, with notable differences only in the second half of the 21st century, where the two SLR uncertainties diverge significantly.

In the SF scenarios, the model free parameters k_s^+ and Φ control the initial model variance of the projection period, with *Sh*’s attaining 32% and 48%, respectively, before exponentially decaying to 6% and 5% by 2030 (Figure 6.6b,c). Starting from 2030, both *Sh*’s of k_s^+ and Φ gradually increase up to 10% by 2095, and further up to ~18% by 2100. The SLR *Sh* rapidly drops from 20% to 5% between 2021 and 2025, then grows gently back to ~20% by 2080 and dramatically up to 80% by 2100 in the RCP8.5 scenario (Figure 6.6d). In the RCP4.5 scenario, the model sensitivity to SLR remains below 10% until 2097 before increasing up to 23% by 2100 (Figure 6.6d). The impact of the uncertain wave chronology raises up to ~83% from 2021 to 2025, and then decreases progressively mirroring the behaviour of SLR *Sh* (Figure 6.6). In the RCP8.5 (RCP4.5) scenario, the wave chronology *Sh* decays down to ~70% (~80%) by 2080, and accelerates down to 0% (~30%) at the end of the simulated period.

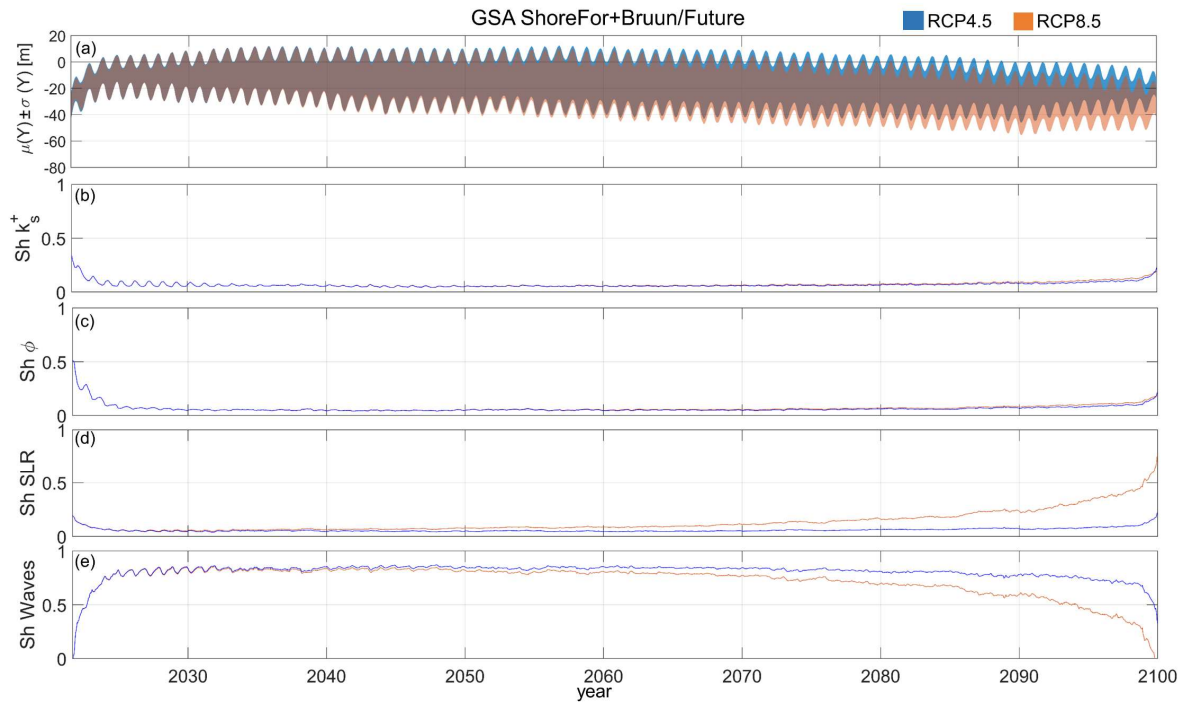


Figure 6.6. Global Sensitivity Analysis results for ‘future scenarios’ simulated using *ShoreFor* for the RCP4.5 (blue) and RCP8.5 (orange) SLR scenario. Time series of (a) standard deviation of simulated 2021-2100 shoreline positions, and *Shapley Effects* of model parameters (b) k_s^+ and (c) Φ , (d) sea-level rise rate, and (e) wave chronology.

When using the Y09 approach, the GSA produces the series *Sh* shown in Figure 6.7. The *Sh*'s of the empirical Y09 parameters a_1 and a_2 decrease regularly from the initial values of 23% and 14%, respectively, to 10% by 2100 (Figure 6.7b,c). Over the projection period, the *Sh* of k_y^+ (k_y^-) decreases from 23% to 10% (10% to 8%), and associates a well-defined (weak) seasonal signal with higher values during the summer (winter) (Figure 6.7d,e). SLR's *Sh* increases regularly from ~5% in 2021 to 20% in 2050, and up to 58% and 32% in the RCP8.5 and RCP4.5 scenarios, respectively (Figure 6.7f). The wave chronology's *Sh* shows a decreasing long-term trend mirroring the behaviour of SLR's *Sh* and a marked seasonality. In both RCP scenarios, the latter *Sh* ranges between 45% and 18% over the first decade (2021- 2030), and between 17% and 1% (23% and 1%) over 2090-2100 for the RCP8.5 (RCP4.5) scenario (Figure 6.7e).

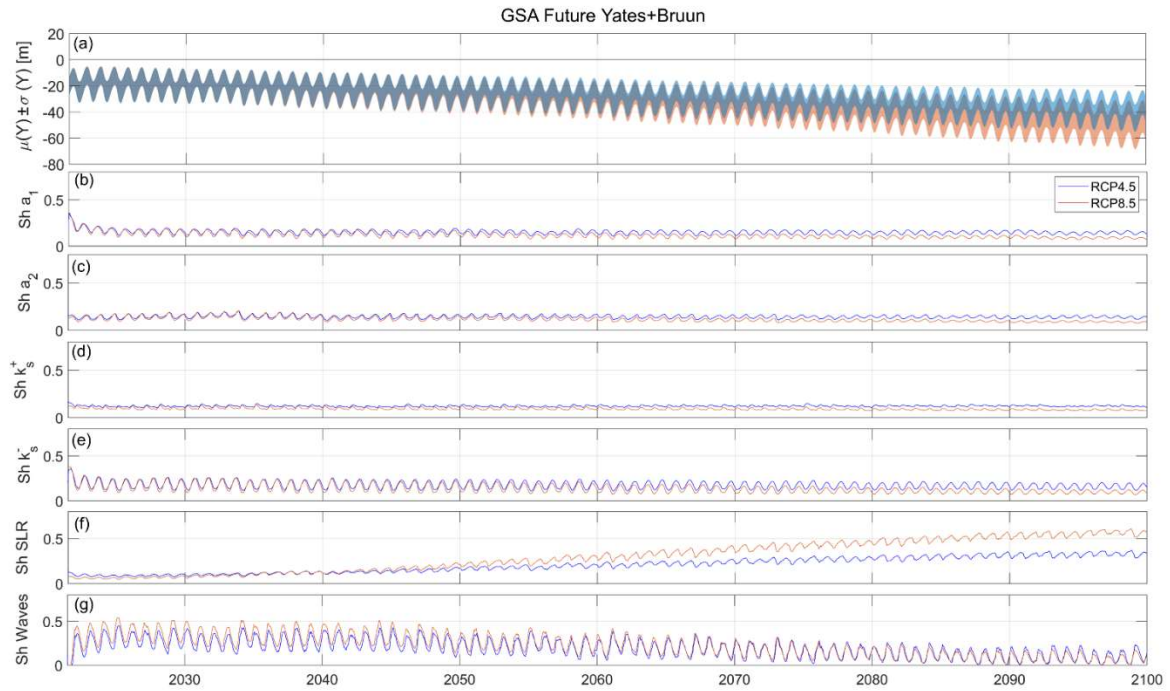


Figure 6.7. Global Sensitivity Analysis results for ‘future scenarios’ simulated using Yates’ model for the RCP4.5 (blue) and RCP8.5 (orange) SLR scenario. Time series of (a) standard deviation of simulated 2021-2100 shoreline positions, and *Shapley Effects* of model parameters (b) a_1 (c) a_2 , (d) k_y^+ , (e) k_y^- , (f) sea-level rise rate, and (g) wave chronology.

6.5. Discussion

6.5.1. Effects of stochastic wave chronology

Past scenario

In the ‘past scenario’, shoreline change is simulated from 1998 to 2021 using SF and the Bruun model and uncertainties on SLR are omitted (Section 6.4.1, Figure 6.4a). Despite the availability of wave hindcast data, we forced the ‘past scenario’ simulations using ensemble (stochastic) wave conditions. This choice is motivated by two reasons: (i) since the wave forcing ensemble is based on the aforementioned hindcast data, existing observations and shoreline hindcasts support an indirect validation for the emulated wave time series; and (ii) including stochastic wave chronologies in the ‘past scenario’ allows to analyse the relative impact of the intrinsic uncertainties of waves and the epistemic uncertainties of model free parameters on simulated shorelines. In the following discussion we refer to the period 1998-2012, excluding the calibration and validation periods (2012-2021). For this scenario, the modelled shoreline trajectories are consistent with shoreline observations between 2005 and 2012 and show an overall accreting trend from 1998 to 2012. This is consistent with the ensemble shoreline reconstruction obtained Chapter 4 over

the same period at Truc Vert beach, which produced similar shoreline trends and 1998 envelope of shoreline positions. While in Chapter 4 we used deterministic wave forcing conditions and a different modelling setup, the comparison still provides a qualitative validation of the wave ensemble used here.

In this scenario, the GSA identified the inherent wave forcing variability as the dominant driver of the modelled shoreline variance, with the estimated Sh 's value of the wave chronology more than doubling the cumulated effects of the k_s^+ and Φ parameters over the simulated period (Figure 6.6b,c,e). All Sh 's time series exhibit a very mild seasonal signal between 2005 and 2012, associated with higher model sensitivity to the k_s^+ and Φ parameters during low-energy periods (summers), and stabilize over time as the model variance increases (Figure 6.6b,c). Compared to previous GSAs where only model free parameters governed the modelled shoreline variance Chapter 4, the effects of uncertainties in wave forcing variability override and buffer the complex seasonal patterns of the model sensitivity to model free parameters. Our findings are also in line with the analytical results of Vitousek et al. (2021), who showed that the intrinsic uncertainties on wave chronology can more than double the contribution of the epistemic uncertainty on calibrated model parameters to the shoreline ensemble variance.

Although the Y09 model does not allow to propagate the uncertainties on modelled shoreline towards the past, for the sake of completeness of this analysis, we repeated the 'past scenario' GSA using the Y09 model instead of SF, where the initial condition was set to the mean shoreline position obtained during the model calibration (2012-2019) (Appendix D3). Unlike the SF 'past scenario' application, the use of Y09 results in no long-term trend of the shoreline ensemble, with seasonal fluctuations around a stable position equal to the mean shoreline position observed during the calibration (2012-2019) (Figure D.5). The GSA results show that, on average, the uncertainties in modelled shoreline trajectories are driven by the stochastic wave chronology for 44% while the remaining 56% of shoreline uncertainty is partitioned among the model free parameters (Figure D.6).

Future scenarios

The differences in ranges of shoreline projections observed for the Y09+B and SF+B applications reflect the different representations of the physical mechanisms and assumptions underlying the respective disequilibrium formulations. These behaviours were also observed and analysed in previous studies that described the different model responses to short- and long-term variations in the wave forcing (Chapter 5 and Vitousek et al., 2021). The SF equilibrium condition is defined by past wave conditions over a fixed time

proportional to the beach memory (Φ), so that the equilibrium state of the beach adapts dynamically to the wave climate and its temporal variations. Instead, the Y09 equilibrium condition is defined by the previous shoreline position and the fixed equilibrium energy function ($E_{eq}=a_1Y+a_2$), which does not respond to past wave forcing variations beyond a time scale implicitly determined by the fixed value of the a_1 and a_2 parameters. The different responses to multiannual variations in wave conditions are clearly illustrated by the individual model realizations reported in Figure 6.4b-e (yellow and green lines). The variance of modelled shoreline trajectories is constrained within a limited bound when using the Y09 model, while this is not necessarily the case for SF, consistently with the analysis of Vitousek et al.'s (2021). For this reason, the shoreline trajectories modelled with SF exhibit rapidly increasing uncertainties over time, particularly beyond the time scale of years. The Y09+B and SF+B ensemble shoreline projections also show notable differences in the trends and the ranges of modelled shoreline positions over the initial projection period. In fact, SF equilibrium state over the initial projection period is influenced by the deterministic wave conditions prior to 2021 and the current (random) wave conditions, until the deterministic conditions are 'forgotten'. Given that the two years prior to 2021 are characterized by high-energy winters, the equilibrium condition over the initial projection period is more likely to result in a constructive (accretive) disequilibrium. Over this same period, the Y09 equilibrium condition is only affected by the current (random) wave energy, resulting in an immediate spread of model results and possible trajectories. The narrowing of ensemble ranges observed over the last years of the SF+B projections derives from the assumption that the SF parameter r (Section 6.2.2/Equation 2.4), which defines the ratio between k_s^+ and k_s^- , is such that the trend in modelled shoreline is conditioned to the trend of the wave forcing (Splinter et al., 2014b). Therefore, given that all the wave time series are constrained to the same long-term trend, SF will tend to reproduce the same trend by the end of the simulated period for any selected wave time series. The latter model limitation suggests that the assumption of a fixed linear relationship between erosion/accretion response rates may not be valid on such long time scales where, instead, the values of model free parameters are likely to be non-stationary (Ibaceta et al., 2020). The SF assumption on the r parameter has also implications on the GSA, as it drives the SLR's and waves' Sh 's to diverge rapidly towards high and low values, respectively (Figure 6.7d,e), once again, questioning the validity of r 's formulation in the context of long-term simulations.

The GSAs for the 'future scenarios' suggest that the uncertainties on wave chronology steadily dominate the variance of shoreline projections until the effects of SLR start

concurring to shoreline uncertainties. The estimated Sh 's show that for the simulated scenarios the uncertain future SLR always becomes the primary driver of modelled shoreline variance after 2060. Compared to previous GSA applications based on deterministic wave time series (Chapter 5), the inclusion of ensemble wave forcing in future shoreline projections postponed the onset of the SLR dominance on the uncertainties of the model results by ~ 10 years.

6.5.2. Waves uncertainties, interactions and correlation effects

Given the connection between model free parameters and wave forcing in the Y09 and SF models formulations (Splinter et al., 2014b; Vitousek et al., 2021), the interaction of these variables and the respective uncertainties within the model may drive higher-order effects contributing to the results uncertainties. Moreover, the correlations among the model parameters of both shoreline models (Figure 6.3a,b) may further influence the decomposition of the results variance. While a full decomposition of the model results variance that allow discriminating main and interaction terms, and correlation effects is still a matter of ongoing research (Mara and Becker, 2021), here we investigate the presence of interaction and correlation effects by comparing the Sh 's with the corresponding individual main effects estimated with first-order Sobol' indices (S_i 's) (Equation 2.10, Section 2.3.2).

The difference between Sh_i and S_i associated to the variable X_i provides an indication of the presence of the cumulated effects of the cumulated terms of correlations and interactions between X_i with the other uncertain inputs. The comparison between Sh 's and S_i 's for the 'past scenario' (Figure 6.8) suggests the presence of such correlation and interaction effects, between the free model parameters and the wave conditions, on modelled shoreline uncertainties when using the SF model. Indeed, for this scenario the cumulated differences between Sh 's and S_i 's of all the uncertain variables make up $\sim 15\%$ of the total results variance on average, and up to $\sim 75\%$ (near 2012). The latter highlights the risk of underestimating the influence of the model inputs uncertainties on the results uncertainties, and suggests the potential occurrence of contributing waves-parameters interactions. Interestingly, we observe that the seasonal signal of the model sensitivity to the free parameters (higher sensitivity during low-energy periods) is associated to the first-order effects (Figure 6.8), which is in line with previous assessments of main effects on the modelled shoreline (D'Anna et al., 2020).

We acknowledge however that the afore-described comparison analysis should only be considered a qualitative indication of the joint impact of interactions and correlations, which

might be larger than the differences observed here. This is related to the effects of correlation among uncertain inputs that are partitioned among the correlated variables in the Shapley effects (by construction), but may be accounted redundantly in the Sobol' indices of the correlated variables (Section 2.3.2), causing a possible overestimation of first-order Sobol' indices, hence introducing some biases in the differences $Sh_i - S_i$.

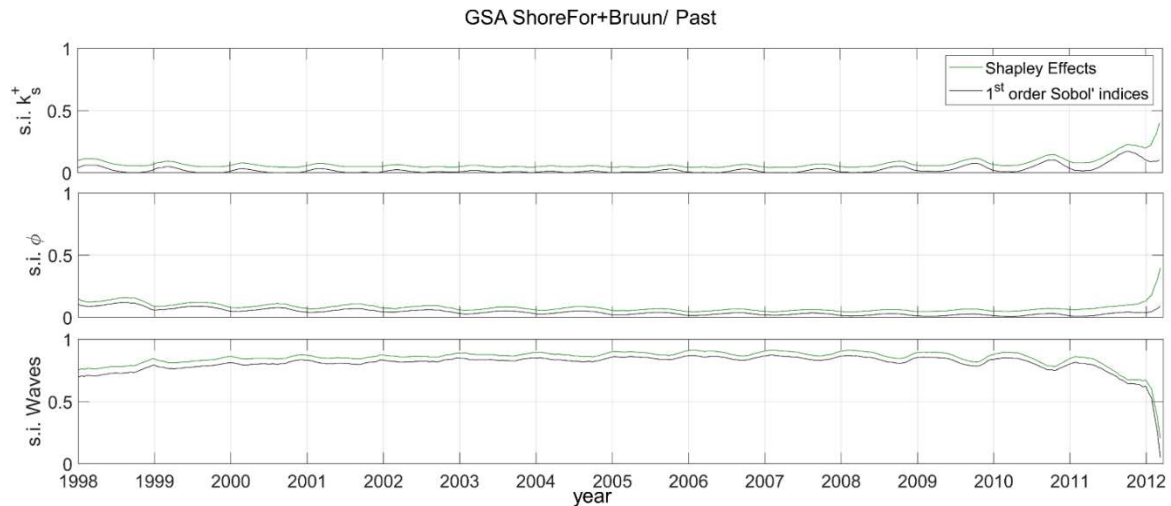


Figure 6.8. Comparison of *Shapley Effects* (green lines) and *1st order Sobol'* (black lines) sensitivity indices (s.i.) of the *ShoreFor* free parameters (a) k_s^+ , (b) Φ , and (c) wave chronology, for the 'past scenario' ensemble.

6.5.3. Dynamic model free parameters

The analysis in Section 6.5.1 highlighted some shortcomings of both the SF and Y09 approaches: the Y09's limits in reproducing large interannual shoreline patterns, and the SF long-term trend imposed by the fixed r parameter. The respective limitations can be attributed, at least partially, to the assumption of stationary model parameters. Indeed, the SF's free parameters values have been observed to be dependent on time variations of the wave forcing (Ibaceta et al., 2020; Splinter et al., 2017), while Y09's parameters prevent the equilibrium condition from adapting to shifts in the wave forcing (Vitousek et al., 2021), as discussed in Section 6.5.1. Therefore, we make a further step to explore the potential impact of the assumption of stationary model free parameters on long-term shoreline projections and run two more sets of 10000 simulations using dynamic values for some of the Y09 and SF parameters for the 'future scenario' RCP8.5.

Vitousek et al. (2021) proposed a physical interpretation of the Y09 free parameters, where the a_2 parameter in Equation 2.7 is identified as fixed background wave energy ($a_2 = \hat{E}$) that contributes to define the site-specific equilibrium time scale and range of shoreline excursion. Based on site-specific calibration of the model, the optimized value of $\sqrt{a_2}$ was

found to approximate that of the average significant wave height ($\overline{H_s}$) over the observed period, so that Equation 7 becomes:

$$E_{eq}(Y) = a_1Y + a_2 \approx a_1Y + \overline{H_s^2} \quad (6.3)$$

We run an ensemble of simulations using a modified and calibrated Y09 model (hereon Y09*) based on Equation 6.3, and we define the background wave energy at a given time as the average significant wave height over the past n years ($\overline{H_s} = \overline{H_s}(t)$). This assumption not only provides a dynamic character to Y09's equilibrium condition, but also brings Y09 conceptually closer to SF in that the time-window ' n ' is analogue to SF's 'beach memory' Φ . For this application, we set $n=5$ years, which correspond roughly to the upper limit of SF's Φ values (Table 6.1). The Y09* model achieves slightly improved skill than Y09 (Section 3.1), with RMSE=4.95 m and $R^2=0.82$ on over the calibration. Over the validation period the Y09* model produces an ensemble mean (minimum) RMSE of 8.1 m (3.2 m) and a mean (max) R^2 of 0.89 (0.92), showing a net improvement compared to the Y09 ensemble (Section 6.3.1). The individual shoreline trajectories (yellow and green lines in Figure 6.9) show how Y09* produces interannual fluctuations that were not visible in the Y09 results (Figure 6.4e). The use of a time-varying a_2 parameter produces a more irregular envelope of simulated shoreline positions compared to the results obtained with stationary parameters, with larger amplitudes of the shoreline positions envelope (Figure 6.9a). It is to be noted that since a_2 is fully defined as a function of H_s and the n value is fixed, a_2 is no longer an uncertain model parameter and Y09* has less uncertain inputs than Y09.

In the SF model, the ratio of erosion/accretion shoreline response rate (r) is calculated as a function of the trend in wave forcing over the full extent of the simulated period (Equation 2.4). Here, we relate r to the forcing wave climate dynamically and generate a time series of r values by applying Equation 2.4 over a progressive time window instead of the full simulation period. At a given time step (t), $r(t)$ is calculated based on the previous n years ($n < \text{simulation period}$) of wave forcing, as follows:

$$r(t) = \left| \frac{\sum_{t-n}^t \langle F^+ \rangle}{\sum_{t-n}^t \langle F^- \rangle} \right| \quad (6.4)$$

Such formulation preserves the original SF concept that links the trends of shoreline change and wave climate but allows different multi-decadal wave climate patterns to result in different shoreline positions by the end of the simulated period. We calibrated a modified SF (hereon SF*) model based on Equation 6.4 with $n= 5$ years and used it to run a new ensemble of simulations. The SF* model produces an RMSE=6.8 m and a $R^2=0.71$ on the simulated period, showing some improvement compared to SF (Section 6.3.1). The model

skill also improved over the validation period, with a mean (min) RMSE of 8.62 m (3.05 m) and a mean (max) R^2 of 0.85 (0.93) (Section 6.3.1). The use of non-stationary values for the r parameter results in a progressive increase of the modelled shoreline variance, due to the increasing number of possible sequences of high- and low- energy winters (Figure 6.9). The values of erosion/accretion rate r computed with Equation 6.4 occasionally attains values above 10 and near 0. This is likely to cause the σ (envelope) ranges of the modelled shoreline to spread over time up to roughly [-10 m; -110 m] ([150 m; -250 m]). However, while the SF* tested here is based on some arbitrary assumptions (i.e. $n=5$, no limits in the range of r variability), the model produces different long-term trends in response to the different wave forcing time series, and do not converge to the same final shoreline position at the end of the simulated period.

The latter applications show that accounting for the effects of waves in the Y09 and SF models parameterizations can significantly affect the modelled shoreline response to the wave climate variability and potentially improve the models performances. This encourages future research efforts towards unravelling the inherent relationship between the temporal variability of free parameters and wave climate, and move towards more comprehensive shoreline models. However, these simulations are based on some arbitrary assumptions and are not to be interpreted as an improved assessment of shoreline projections.

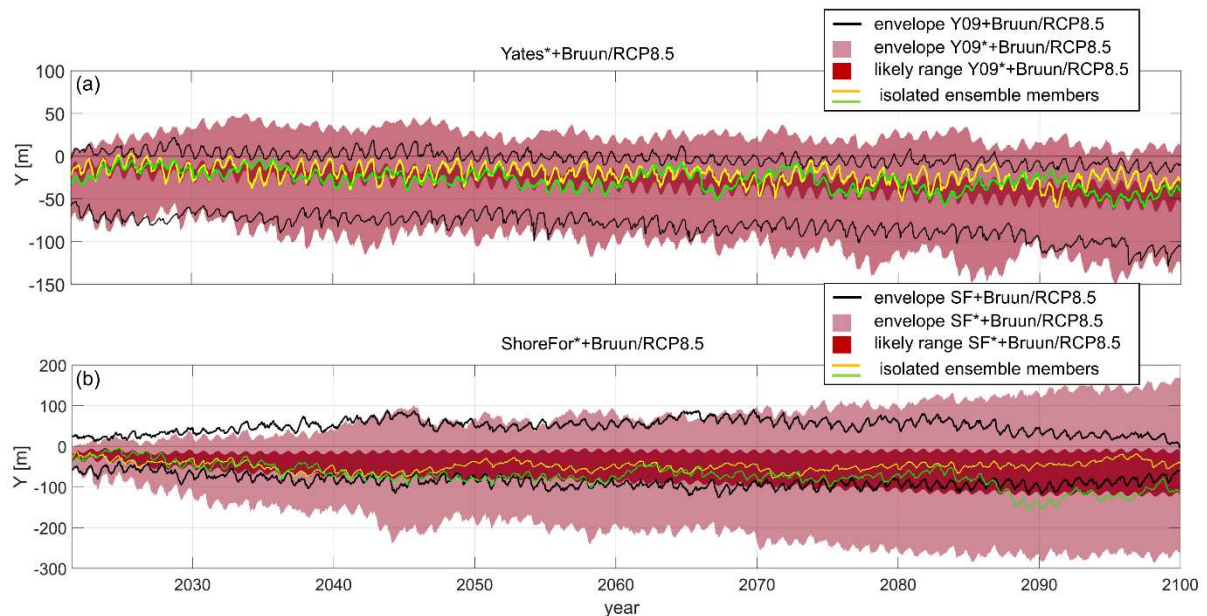


Figure 6.9. Ensemble of simulated shoreline trajectories from 2021 to 2100 for the RCP8.5 future sea-level rise scenario using the Bruun Rule with the modified (a) Yates et al. (2009) and (b) ShoreFor models, including: the envelope (light-shaded areas) and the standard deviation intervals ($\mu \pm \sigma$) (dark-shaded areas); two individual model realizations (yellow and green lines). Black solid lines indicate the limits of the envelope of the corresponding simulations obtained using the original Yates et al. (2009) and ShoreFor models.

6.5.4. Assumptions and limitations

One of the main assumptions of this work is that the current wave climate remains unchanged in the future. In fact, the wave ensemble used here assumes that all the simulated wave time series maintain the same seasonal to multiannual statistics observed in the past wave data, and accounts only for the intrinsic uncertainty associated with the short-term variability of wave conditions. However, climate change could alter the future wave climate in some regions of the world (Morim et al., 2020), potentially affecting the evolution of sandy shorelines. On one hand, the wave climate over the northeast Atlantic region is not expected to change significantly over the 21st century (Bricheno and Wolf, 2018; Morim et al., 2019), with dynamically downscaled projections estimating a ~ 2 mm/year decrease of winter mean H_s in the Truc Vert area (Charles et al., 2012 and Chapter 5). On the other hand, the limited extent of the hindcast wave data used to generate the wave ensemble (26 years) hinders the inclusion of uncertainties on wave forcing variability on time scales longer than a few decades. In addition, changes in the temporal distribution of extreme events may affect the long-term wave climate cycles (Lobeto et al., 2021), and in turn the multi-annual shoreline variability. The inclusion of uncertain future waves in shoreline projections requires wave ensembles accounting for different realistic climate-driven wave climate patterns, such as multi-model ensembles (e.g. Toimil et al, 2021) or emulated ensembles based on future climate.

While the ensemble of wave time series generated with the wave emulator capture the overall characteristics of the reference past 26-year wave series, the comparison of seasonal wave energy distribution shows some differences (Section 6.2.3). Indeed, the emulator slightly underestimates extreme H_s in the winter, and overestimates them in the remaining seasons. These differences are likely due to a smoothing effect of the seasonality produced by the emulator, together with the strong seasonal variability of the wave climate observed at Truc Vert. However, these differences tend to compensate throughout the different seasons, preserving the overall yearly properties of the wave climate (Figure 6.1d), so that the simulations are only expected to underestimate seasonal excursions of the modelled shoreline.

The GSA applications indicate that uncertainties on modelled shoreline position at Truc Vert are mostly driven by the stochastic character of wave conditions over the first half of the century. However, it is to be noted that Truc Vert beach shows large seasonal and interannual variability enforced by the incident wave climate, and the current results may not apply to other sites under less variable wave conditions.

While the applications of different wave-driven equilibrium shoreline models (SF and Y09) produced realistic ranges of shoreline positions, the model results become increasingly uncertain over time, questioning the reliability of these models beyond decadal time scale. Such uncertainties could be reduced by exploiting new available shoreline data over time, e.g. applying data assimilation techniques and recalibrating the models periodically over time. However, the aim of this paper is to analyse such uncertainties in order to identify their primary drivers over time, and detailed shoreline projections are secondary to the scope of the work.

In this work, we estimated the future local relative MSL based on SROCC projections. Recently, the *IPCC 6th Assessment Report (AR6)* provided updated SLR projections to 2150 (Magnan et al., 2019), including new considerations on the Antarctic Ice-sheet dynamic contribution to SLR, and based on combined Shared Socio-economic Pathways (SSP) (Riahi et al., 2017) and RCP scenarios. However, our sea level projections (2021-2100) remain close to the medium confidence projections published in *AR6 Working Group I - Chapter 9* (within the order of 1 cm difference).

Finally, we modelled SLR-driven shoreline recession using the Bruun model, which builds on a number of assumptions that limit its applicability to a reduced selection of beaches (Cooper et al., 2020). As Truc Vert beach is a cross-shore transport dominated, uninterrupted beach with large accommodation space most of the Bruun model assumptions are satisfied. However, alternative rule-based approaches (McCarroll et al., 2021), or dynamically coupled wave-driven and sea-level equilibrium approaches (Chapter 3)(D'Anna et al., 2021b) could be implemented for applications of this framework to a wider range of sites. In addition, here the Bruun Rule combined linearly with Y09 and SF with no feedbacks between wave- and SLR-driven modelled processes, preventing any interaction between wave forcing and SLR uncertainties. Approaches that combine wave- and sea-level-driven processes in a coupled fashion (i.e. with feedback between the models), may reveal further contributions of the wave forcing uncertainties to modelled shoreline change.

6.6. Conclusions

We applied a Global Sensitivity Analysis to long-term shoreline evolution modelling at the cross-shore transport dominated Truc Vert beach (France) including the intrinsic uncertainties associated with unknown wave chronology and using two different equilibrium shoreline models. Our results suggest that uncertainties in wave chronology

play an exceedingly important role in probabilistic shoreline modelling. When modelling shoreline change with no uncertainties on SLR (e.g. ‘past scenario’ and near-future projections), the uncertain wave chronology is responsible for up to 83% of the modelled shoreline variance at this site. We also find that the interactions between the uncertain wave chronology and model parameters within the models and the correlation among the model parameters can significantly influence shoreline predictions uncertainties, highlighting the interplay between intrinsic and epistemic uncertainties. The future shoreline projections suggest that the onset of the SLR dominance on the uncertainties of the model results can be expected to start from 2060, with strong implications for future research priorities and decision-making in climate change adaptation planning where coastal settings are similar to Truc Vert beach. While the two equilibrium modelling approaches compared in our applications (*ShoreFor* and *Yates*) show different responses to wave climate variability and its uncertainties, the main conclusions drawn above are valid for both approaches. We also found that applying non-stationary model free parameters by linking them to the wave climate variability can significantly alter the model behaviour, and further research efforts in this direction could improve the understanding of model uncertainties.

Chapter 7

7. Conclusions and perspectives

7.1. Conclusions

Overall, this work provided new insight into long-term shoreline modelling of sandy beaches and the related uncertainties based on the joint use of integrated shoreline recession driven by sea-level-rise (SLR) and equilibrium shoreline models (ESMs) and a flexible probabilistic framework for uncertainty and sensitivity analysis of long-term shoreline predictions. Firstly, we introduced a new interpretation of the SLR-driven shoreline response mechanism in the context of equilibrium beach theory with the respective implications for integrated wave- and sea-level-driven equilibrium shoreline modelling. Then, Global Sensitivity Analyses (GSA) have been performed on past and future ensemble shoreline projections at the cross-shore transport dominated Truc Vert beach for different climate scenarios and equilibrium modelling approaches to analyse the role that uncertain model parameters, and hydrodynamic forcing play on the modelled shoreline variance. The work gathered in this manuscript contributes to answer to the five research questions introduced in Section 1.2, as illustrated below.

“Q1. How can the effects of short- and long-term drivers (i.e. wave action and SLR) be combined in the context of equilibrium shoreline modelling?”

The interpretation of the SLR-driven shoreline response mechanism presented in Chapter 3 identifies two main contributing processes: passive flooding and wave reshaping. Based on this concept, the analysis of the integration of SLR-driven recession into equilibrium shoreline models and the application to an idealized test case suggest that the proposed conceptualization provides a physics-based background to the Bruun model when Bruun’s assumptions are satisfied.

“Q2. On which time scale the uncertainties on SLR become the primary driver of the uncertainties on modelled shoreline?”

The GSA applications showed that, compared to other uncertain input variables, the uncertainties associated with SLR over the past 20 years have a negligible impact on the predicted shoreline variance (Chapter 4), and that the effects of SLR uncertainties only emerge in the second half of the 21st century (Chapter 5). The inclusion of ensemble wave forcing in future shoreline projections significantly postpones the onset of the SLR dominance on the uncertainties of the model results by 10 to 20 years (Chapter 6). It is also observed that these times of emergence of SLR uncertainties on shoreline projections depend on the shoreline modelling approach and the RCP scenarios (Chapters 5 and 6).

“Q3. How do the relative contributions of uncertain model parameters and physical forcing to modelled shoreline uncertainties evolve over time?”

When using deterministic wave forcing conditions, the uncertainties related to model free parameters resulted to be the main driver of modelled shoreline variance up to 2050, while the impact of SLR uncertainties always dominates shoreline uncertainties after 2070 (Chapters 4 and 5).

“Q4. How do the uncertainties on model parameters and equilibrium approaches relate to the wave climate forcing?”

Model sensitivity to free parameters showed a strong variability in time, revealing a clear interplay with the intra-annual and interannual distribution of incident wave energy (Chapters 4 and 5). When using ensemble wave forcing and analysing the Shapley Effects, we found that interactions between the uncertain wave chronology and model parameters and the correlation among the model parameters can strongly influence shoreline predictions uncertainties. This reveals a connection between intrinsic and epistemic uncertainties within the applied modelling framework (Chapter 6).

“Q5. What is the role of uncertain wave climate variability on modelled shoreline?”

The results discussed in Chapter 6 suggest that including uncertainties in wave chronology is crucial for comprehensive probabilistic shoreline modelling. When modelling shoreline change with no uncertainties on SLR (e.g. ‘past scenario’ and near-future projections), the uncertain wave chronology is responsible for up to 83% of the modelled shoreline variance. The equilibrium modelling approaches compared in our applications (*ShoreFor* and *Yates*) show different responses to wave climate variability and its uncertainties, questioning the skill of one model over the other on long-term simulations, under different wave conditions (Chapters 5 and 6).

7.2. Research perspectives

The findings obtained throughout this work bring forward several research perspectives.

R1. *Exploring uncertainties on other types of beaches*

The analyses and applications throughout this thesis apply to open cross-shore transport dominated sandy beaches, such as Truc Vert, and to the equilibrium shoreline models used here. GSA applications to sites affected by other processes (*e.g.* longshore sand transport) and using different shoreline models (*e.g.* hybrid models), may reveal different sensitivity patterns of modelled shoreline change to model forcing, assumptions and free parameters. Further research efforts are required to explore uncertainties on a wider range of different coastal settings and driving processes, and address the genericity of the current results.

R2. *Accounting for uncertain climate-driven changes of future wave fields*

The ensemble modelling and GSA applications performed here are based on deterministic wave time series (Chapters 4 and 5) or wave forcing ensemble characterized by the same seasonal to multiannual statistics observed in the past (Chapter 6), and do not account for uncertainties in climate-driven changes of future wave fields. Future studies could fill this gap by incorporating uncertain long-term variability of the future wave forcing in probabilistic shoreline projections, for instance using multi-model wave ensembles or emulated ensembles based on future climate (as in Toimil et al., 2021). Alternatively, one could analyse the effects of uncertainty in future extreme wave events by using ensembles of wave series where the energy of extreme events is increased or decreased following predefined patterns and/or trends (*e.g.* yearly $H_{90\%}$ linearly increasing by 1% to 5% over the simulated period). While the latter approach would include arbitrary assumptions on the future wave climate, it would relevant insight into the models response to the uncertain long-term wave forcing variability.

R3. *Reducing uncertainties by improving wave-driven shoreline modelling...*

Although it is understood that the different shoreline behaviours observed for the *ShoreFor* and *Yates'* models derive from the responses of the respective disequilibrium conditions to the short- and long-term wave forcing variability, the skill of one approach over the other in simulating long-term shoreline trajectories is still unclear. This encourages conceptual efforts to address the different model responses to forcing acting on different time scales (*e.g.* Montaña et al., 2021; Schepper et al., 2021). Further research on

determining the intrinsic link between wave climate variability and the model free parameters (*e.g.* building on the work of Ibaceta et al., 2020) will also help to improve our understanding of the different models behaviour, potentially reduce uncertainties on the predictions, and move towards generalized equilibrium shoreline modelling approaches.

R4. ... and Sea-level-driven shoreline modelling

Uncertainties on the SLR-driven shoreline change component could be reduced by implementing alternative methods to the Bruun Rule. For instance, ESMs based on the current shoreline position can be efficiently coupled (with feedback) with the SLR-induced passive flooding based on the knowledge of the foreshore slope, which typically associates lower uncertainty than the Bruun slope. In addition, within probabilistic applications, approaches that combine wave- and SLR-driven processes with feedback between the models would enable to investigate the interaction effects of wave forcing uncertainties and SLR uncertainties on modelled shoreline change. In addition, our methodological analysis also holds for the new generation of hybrid equilibrium-based models (*e.g.* Alvarez-Cuesta et al., 2021; Antolinez et al., 2019; Robinet et al., 2018, 2020; Tran & Barthelemy, 2020; Vitousek et al., 2017), and shoreface translation models (*e.g.* *ShoreTrans*, McCarroll et al., 2021), setting new ground for the development of more generalized integrated shoreline models.

R5. Improving variance decomposition

The implementation of Shapley Effects instead of first-order Sobol' indices identified the Shapley-based GSA as a promising approach for future probabilistic shoreline modelling studies, where calibrated parameters are statistically dependent from each other and are often interacting with wave forcing variability. However, the Shapley Effects do not allow to quantify the separated contributions of the interaction terms and the shared effects of inputs correlations to the model results. Approaches that separate these contributions (Mara and Becker, 2021) would further improve the GSA and provide a deeper understanding of the uncertainties drivers.

The research perspectives and possible improvements outlined above share the underlying need for large datasets of shoreline position. This encourages the systematic combination of long-term, sustainable, monitoring program and hybrid models in future

research, such as satellite-derived data (*e.g.* Vos et al., 2020), to develop well-balanced data-driven/process-based approaches for multi-decadal shoreline projections.

Publications and presentations

Research articles

- **D’Anna, M.**, Castelle, B., Idier, D., Le Cozannet, G., Rohmer, J. & Robinet, A. (2020). Impact of model free parameters and sea-level rise uncertainties on 20-years shoreline hindcast: the case of Truc Vert beach (SW France). *Earth Surface Processes and Landforms* 45(8), 1895-1907. <https://doi.org/10.1002/esp.4854>
- **D’Anna, M.**, Castelle, B., Idier, D., Rohmer, J., Le Cozannet, G., Thieblemont, R., and Bricheno, L. (2021). Uncertainties in shoreline projections to 2100 at Truc Vert beach (France): Role of sea-level rise and equilibrium model assumptions. *J. Geophys. Res. Earth Surf.*, 126, e2021JF006160. <https://doi.org/10.1029/2021JF006160>
- **D’Anna, M.**, Idier, D., Castelle, B., Vitousek, S., & Le Cozannet, G. (2021). Reinterpreting the Bruun Rule in the context of equilibrium shoreline models. *Journal of Marine Science and Engineering*, 9(9). <https://doi.org/10.3390/jmse9090974>
- **D’Anna, M.**, Idier, D., Castelle, B., Rohmer, J., Cagigal, L., and Mendez, F.J. (Under Review). Effects of Stochastic Wave Forcing on Equilibrium Shoreline Modelling Across the 21st Century Including Sea-Level Rise. *Coastal Engineering*.
- Robinet, A., Castelle, B., Idier, D., **D’Anna, M.**, and Le Cozannet, G. (2020). Simulating the impact of sea-level rise and offshore bathymetry on embayment shoreline changes. *J. Coast. Res.*, 95, 1263–1267. [doi:10.2112/SI95-244.1](https://doi.org/10.2112/SI95-244.1)
- Castelle, B., Robinet, A., Idier, D., **D’Anna, M.** (2020). Modelling of embayed beach equilibrium planform and rotation signal. *Geomorphology*, 369, 107367. [doi:10.1016/j.geomorph.2020.107367](https://doi.org/10.1016/j.geomorph.2020.107367)

Conference presentations

- D’Anna, M., Castelle, B., Idier, D., Le Cozannet, G., Rohmer, J. & Robinet, A. (2020). Impact of model free parameters and sea-level rise uncertainties on 20-years shoreline hindcast: the case of Truc Vert beach (SW France). *International Conference on Coastal Engineering* October-2020. **Oral (virtual) presentation**

- D'Anna, M., Castelle, B., Idier, D., Rohmer, J., Le Cozannet, G., Thieblemont, R., and Bricheno, L. (2021). Uncertainties in shoreline projections to 2100 at Truc Vert beach (France): Role of sea-level rise and equilibrium model assumptions. *EGU21, Natural Hazards*, April-2021. **Oral (virtual) presentation**

- D'Anna, M., Castelle, B., Idier, D., Rohmer, J., Le Cozannet, G., Thieblemont, R., and Bricheno, L. (2021). Uncertainties in shoreline projections to 2100 at Truc Vert beach (France): Role of sea-level rise and equilibrium model assumptions. *Coastal Dynamics, Delft, Netherlands*, June-2021. **Oral (virtual) presentation**

References

- Allenbach, K., Garonna, I., Herold, C., Monioudi, I., Giuliani, G., Lehmann, A., Velegrakis, A.F., 2015. Black Sea beaches vulnerability to sea level rise. *Environ. Sci. Policy* 46, 95–109. <https://doi.org/10.1016/j.envsci.2014.07.014>
- Alvarez-Cuesta, M., Toimil, A., Losada, I.J., 2021a. Modelling long-term shoreline evolution in highly anthropized coastal areas. Part 1: Model description and validation. *Coast. Eng.* 169, 103960. <https://doi.org/10.1016/j.coastaleng.2021.103960>
- Alvarez-Cuesta, M., Toimil, A., Losada, I.J., 2021b. Reprint of: Modelling long-term shoreline evolution in highly anthropized coastal areas. Part 2: Assessing the response to climate change. *Coast. Eng.* 169, 103985. <https://doi.org/10.1016/j.coastaleng.2021.103985>
- Anderson, D.L., Rueda, A., Cagigal, L., Antolinez, J.A.A., Mendez, F.J., Ruggiero, P., 2019. Time-Varying Emulator for Short and Long-Term Analysis of Coastal Flood Hazard Potential. *J. Geophys. Res. Ocean.* 124, 9209–9234. <https://doi.org/10.1029/2019JC015312>
- Anderson, T.R., Fletcher, C.H., Barbee, M.M., Frazer, L.N., Romine, B.M., 2015. Doubling of coastal erosion under rising sea level by mid-century in Hawaii. *Nat. Hazards* 78, 75–103. <https://doi.org/10.1007/s11069-015-1698-6>
- Anderson, T.R., Fletcher, C.H., Barbee, M.M., Romine, B.M., Lemmo, S., Delevaux, J.M.S., 2018. Modeling multiple sea level rise stresses reveals up to twice the land at risk compared to strictly passive flooding methods. *Sci. Rep.* 8. <https://doi.org/10.1038/s41598-018-32658-x>
- Antolínez, J.A.A., Méndez, F.J., Anderson, D.L., Ruggiero, P., Kaminsky, G.M., 2019. Predicting Climate-Driven Coastlines With a Simple and Efficient Multiscale Model. *J. Geophys. Res. Earth Surf.* 124. <https://doi.org/10.1029/2018JF004790>
- Antolínez, J.A.A., Méndez, F.J., Camus, P., Vitousek, S., González, E.M., Ruggiero, P., Barnard, P., 2016. A multiscale climate emulator for long-term morphodynamics (MUSCLE-morpho). *J. Geophys. Res. Ocean.* 121, 775–791. <https://doi.org/10.1002/2015JC011107>
- Athanasiou, P., van Dongeren, A., Giardino, A., Vousdoukas, M.I., Gaytan-Aguilar, S., Ranasinghe, R., 2019. Global distribution of nearshore slopes with implications for coastal retreat. *Earth Syst. Sci. Data* 11. <https://doi.org/10.5194/essd-11-1515-2019>
- Athanasiou, P., van Dongeren, A., Giardino, A., Vousdoukas, M.I., Ranasinghe, R., Kwadijk, J., 2020. Uncertainties in projections of sandy beach erosion due to sea level rise: an analysis at the European scale. *Sci. Rep.* 10. <https://doi.org/10.1038/s41598-020-68576-0>
- Atkinson, A.L., Baldock, T.E., Birrien, F., Callaghan, D.P., Nielsen, P., Beuzen, T., Turner, I.L., Blenkinsopp, C.E., Ranasinghe, R., 2018. Laboratory investigation of the Bruun Rule and beach response to sea level rise. *Coast. Eng.* 136. <https://doi.org/10.1016/j.coastaleng.2018.03.003>
- Baldock, T.E., Gravois, U., Callaghan, D.P., Davies, G., Nichol, S., 2021. Methodology for estimating return intervals for storm demand and dune recession by clustered and non-clustered morphological events. *Coast. Eng.* 168, 103924. <https://doi.org/10.1016/j.coastaleng.2021.103924>
- Bamber, J.L., Oppenheimer, M., Kopp, R.E., Aspinall, W.P., Cooke, R.M., 2019. Ice sheet contributions to future sea-level rise from structured expert judgment. *Proc. Natl. Acad. Sci.* 116, 11195–11200. <https://doi.org/10.1073/pnas.1817205116>
- Banno, M., Kuriyama, Y., 2020. Supermoon Drives Beach Morphological Changes in the Swash Zone. *Geophys. Res. Lett.* 47. <https://doi.org/10.1029/2020GL089745>
- Banno, M., Kuriyama, Y., Hashimoto, N., 2015. Equilibrium-Based Foreshore Beach Profile Change Model for Long-Term Data, in: *Coastal Sediments*. World Scientific. https://doi.org/10.1142/9789814689977_0235
- Banno, M., Nakamura, S., Kosako, T., Nakagawa, Y., Yanagishima, S., Kuriyama, Y., 2020. Long-

- Term Observations of Beach Variability at Hasaki, Japan. *J. Mar. Sci. Eng.* 8. <https://doi.org/10.3390/jmse8110871>
- Barnard, P.L., Hoover, D., Hubbard, D.M., Snyder, A., Ludka, B.C., Allan, J., Kaminsky, G.M., Ruggiero, P., Gallien, T.W., Gabel, L., McCandless, D., Weiner, H.M., Cohn, N., Anderson, D.L., Serafin, K.A., 2017. Extreme oceanographic forcing and coastal response due to the 2015–2016 El Niño. *Nat. Commun.* 8. <https://doi.org/10.1038/ncomms14365>
- Bayle, P.M., Beuzen, T., Blenkinsopp, C.E., Baldock, T.E., Turner, I.L., 2020. Beach Profile Changes under Sea Level Rise in Laboratory Flume Experiments at Different Scale. *J. Coast. Res.* 95. <https://doi.org/10.2112/SI95-038.1>
- Benaichouche, A., Rohmer, J., 2016. Sobol' indices and variance reduction diagram estimation from samples used for uncertainty propagation, in: VIII International Conference on Sensitivity Analysis of Model Output. Tampon, Réunion.
- Bertsimas, D., Tsitsiklis, J., 1993. Simulated Annealing. *Stat. Sci.* 8. <https://doi.org/10.1214/ss/1177011077>
- Boak, E.H., Turner, I.L., 2005. Shoreline Definition and Detection : A Review Shoreline Definition and Detection : A Review 21, 688–703. <https://doi.org/10.2112/03-0071.1>
- Bricheno, L.M., Wolf, J., 2018. Future Wave Conditions of Europe, in Response to High-End Climate Change Scenarios. *J. Geophys. Res. Ocean.* 123, 8762–8791. <https://doi.org/10.1029/2018JC013866>
- Broto, B., Bachoc, F., Depecker, M., 2020. Variance Reduction for Estimation of Shapley Effects and Adaptation to Unknown Input Distribution. *SIAM/ASA J. Uncertain. Quantif.* 8, 693–716. <https://doi.org/10.1137/18M1234631>
- Bruun, P., 1988. The Bruun Rule of Erosion by Sea-Level Rise: A Discussion on Large-Scale Two- and Three-Dimensional Usages. *J. Coast. Res.* 4, 627–648.
- Bruun, P., 1983. Review of conditions for uses of the Bruun Rule of erosion. *Coast. Eng.* 7, 77–89.
- Bruun, P., 1962. Sea-level rise as a cause of shore erosion. *J. Waterw. Harb. Div.*
- Burningham, H., Fernandez-Nunez, M., 2020. Shoreline change analysis, in: *Sandy Beach Morphodynamics*. Elsevier, pp. 439–460. <https://doi.org/10.1016/B978-0-08-102927-5.00019-9>
- Cagigal, L., Rueda, A., Anderson, D.L., Ruggiero, P., Merrifield, M.A., Montaña, J., Coco, G., Méndez, F.J., 2020. A multivariate, stochastic, climate-based wave emulator for shoreline change modelling. *Ocean Model.* 154. <https://doi.org/10.1016/j.ocemod.2020.101695>
- Casas-Prat, M., McInnes, K.L., Hemer, M.A., Sierra, J.P., 2016. Future wave-driven coastal sediment transport along the Catalan coast (NW Mediterranean). *Reg. Environ. Chang.* 16, 1739–1750. <https://doi.org/10.1007/s10113-015-0923-x>
- Castelle, B., Bonneton, P., Dupuis, H., Sénéchal, N., 2007. Double bar beach dynamics on the high-energy meso-macrotidal French Aquitanian Coast: A review. *Mar. Geol.* 245, 141–159. <https://doi.org/10.1016/j.margeo.2007.06.001>
- Castelle, B., Bujan, S., Marieu, V., Ferreira, S., 2020. 16 years of topographic surveys of rip-channelled high-energy meso-macrotidal sandy beach. *Sci. Data* 7. <https://doi.org/10.1038/s41597-020-00750-5>
- Castelle, B., Dodet, G., Masselink, G., Scott, T., 2018a. Increased Winter-Mean Wave Height, Variability, and Periodicity in the Northeast Atlantic Over 1949-2017. *Geophys. Res. Lett.* 45. <https://doi.org/10.1002/2017GL076884>
- Castelle, B., Dodet, G., Masselink, G., Scott, T., 2017. A new climate index controlling winter wave activity along the Atlantic coast of Europe: The West Europe Pressure Anomaly. *Geophys. Res. Lett.* 44. <https://doi.org/10.1002/2016GL072379>
- Castelle, B., Guillot, B., Marieu, V., Chaumillon, E., Hanquiez, V., Bujan, S., Popeschi, C., 2018b. Spatial and temporal patterns of shoreline change of a 280-km high-energy disrupted sandy coast

- from 1950 to 2014: SW France. *Estuar. Coast. Shelf Sci.* 200, 212–223. <https://doi.org/10.1016/j.ecss.2017.11.005>
- Castelle, B., Marieu, V., Bujan, S., Ferreira, S., Parisot, J.-P., Capo, S., Sénéchal, N., Chouzenoux, T., 2014. Equilibrium shoreline modelling of a high-energy meso-macrotidal multiple-barred beach. *Mar. Geol.* 347. <https://doi.org/10.1016/j.margeo.2013.11.003>
- Castelle, B., Marieu, V., Bujan, S., Splinter, K.D., Robinet, A., Sénéchal, N., Ferreira, S., 2015. Impact of the winter 2013–2014 series of severe Western Europe storms on a double-barred sandy coast: Beach and dune erosion and megacusp embayments. *Geomorphology* 238. <https://doi.org/10.1016/j.geomorph.2015.03.006>
- Charles, E., Idier, D., Delecluse, P., Déqué, M., Le Cozannet, G., 2012a. Climate change impact on waves in the Bay of Biscay, France. *Ocean Dyn.* 62. <https://doi.org/10.1007/s10236-012-0534-8>
- Charles, E., Idier, D., Thiébot, J., Le Cozannet, G., Pedreros, R., Arduin, F., Planton, S., 2012b. Present Wave Climate in the Bay of Biscay: Spatiotemporal Variability and Trends from 1958 to 2001. *J. Clim.* 25. <https://doi.org/10.1175/JCLI-D-11-00086.1>
- Coco, G., Sénéchal, N., Rejas, A., Bryan, K.R., Capo, S., Parisot, J.-P., Brown, J.A., MacMahan, J.H.M., 2014. Beach response to a sequence of extreme storms. *Geomorphology* 204, 493–501. <https://doi.org/10.1016/j.geomorph.2013.08.028>
- Cooper, J.A.G., Masselink, G., Coco, G., Short, A.D., Castelle, B., Rogers, K., Anthony, E., Green, A.N., Kelley, J.T., Pilkey, O.H., Jackson, D.W.T., 2020. Sandy beaches can survive sea-level rise. *Nat. Clim. Chang.* 10. <https://doi.org/10.1038/s41558-020-00934-2>
- Cooper, J.A.G., Pilkey, O.H., 2004. Sea-level rise and shoreline retreat: time to abandon the Bruun Rule. *Glob. Planet. Change* 43. <https://doi.org/10.1016/j.gloplacha.2004.07.001>
- D’Anna, M., Castelle, B., Idier, D., Rohmer, J., Le Cozannet, G., Thieblemont, R., Bricheno, L., 2021a. Uncertainties in Shoreline Projections to 2100 at Truc Vert Beach (France): Role of Sea-Level Rise and Equilibrium Model Assumptions. *J. Geophys. Res. Earth Surf.* 126, 1–26. <https://doi.org/10.1029/2021JF006160>
- D’Anna, M., Idier, D., Castelle, B., Le Cozannet, G., Rohmer, J., Robinet, A., 2020. Impact of model free parameters and sea-level rise uncertainties on 20-years shoreline hindcast: the case of Truc Vert beach (SW France). *Earth Surf. Process. Landforms* 45, 1895–1907. <https://doi.org/10.1002/esp.4854>
- D’Anna, M., Idier, D., Castelle, B., Vitousek, S., Le Cozannet, G., 2021b. Reinterpreting the bruun rule in the context of equilibrium shoreline models. *J. Mar. Sci. Eng.* 9. <https://doi.org/10.3390/jmse9090974>
- Da Veiga, S., Wahl, F., Gamboa, F., 2009. Local Polynomial Estimation for Sensitivity Analysis on Models With Correlated Inputs. *Technometrics* 51, 452–463. <https://doi.org/10.1198/TECH.2009.08124>
- Davidson-Arnott, R.G.D., 2005. Conceptual Model of the Effects of Sea Level Rise on Sandy Coasts. *J. Coast. Res.* 216. <https://doi.org/10.2112/03-0051.1>
- Davidson, M.A., 2021. Forecasting coastal evolution on time-scales of days to decades. *Coast. Eng.* 168. <https://doi.org/10.1016/j.coastaleng.2021.103928>
- Davidson, M.A., Splinter, K.D., Turner, I.L., 2013. A simple equilibrium model for predicting shoreline change. *Coast. Eng.* 73, 191–202. <https://doi.org/10.1016/j.coastaleng.2012.11.002>
- Davidson, M.A., Turner, I.L., Splinter, K.D., Harley, M.D., 2017. Annual prediction of shoreline erosion and subsequent recovery. *Coast. Eng.* 130, 14–25. <https://doi.org/10.1016/j.coastaleng.2017.09.008>
- Dean, R.G., 1991. Equilibrium beach profiles: characteristics and applications. *J. Coast. Res.* 7, 53–84.
- Dean, R.G., Houston, J.R., 2016. Determining shoreline response to sea level rise. *Coast. Eng.* 114. <https://doi.org/10.1016/j.coastaleng.2016.03.009>

- Deser, C., 2020. "Certain Uncertainty: The Role of Internal Climate Variability in Projections of Regional Climate Change and Risk Management." *Earth's Futur.* 8. <https://doi.org/10.1029/2020EF001854>
- Dissanayake, P., Brown, J., Wisse, P., Karunarathna, H., 2015. Comparison of storm cluster vs isolated event impacts on beach/dune morphodynamics. *Estuar. Coast. Shelf Sci.* 164, 301–312. <https://doi.org/10.1016/j.ecss.2015.07.040>
- Do, N.C., Razavi, S., 2020. Correlation Effects? A Major but Often Neglected Component in Sensitivity and Uncertainty Analysis. *Water Resour. Res.* 56. <https://doi.org/10.1029/2019WR025436>
- Dodet, G., Castelle, B., Masselink, G., Scott, T., Davidson, M.A., Floch, F., Jackson, D., Suarez, S., 2019. Beach recovery from extreme storm activity during the 2013–14 winter along the Atlantic coast of Europe. *Earth Surf. Process. Landforms* 44, 393–401. <https://doi.org/10.1002/esp.4500>
- Edwards, T.L., Brandon, M.A., Durand, G., Edwards, N.R., Golledge, N.R., Holden, P.B., Nias, I.J., Payne, A.J., Ritz, C., Wernecke, A., 2019. Revisiting Antarctic ice loss due to marine ice-cliff instability. *Nature* 566, 58–64. <https://doi.org/https://doi.org/10.1038/s41586-019-0901-4>
- Edwards, T.L., Nowicki, S., Marzeion, B., Hock, R., Goelzer, H., Seroussi, H., Jourdain, N.C., Slater, D.A., Turner, F.E., Smith, C.J., McKenna, C.M., Simon, E., Abe-Ouchi, A., Gregory, J.M., Larour, E., Lipscomb, W.H., Payne, A.J., Shepherd, A., Agosta, C., Alexander, P., Albrecht, T., Anderson, B., Asay-Davis, X., Aschwanden, A., Barthel, A., Bliss, A., Calov, R., Chambers, C., Champollion, N., Choi, Y., Cullather, R., Cuzzone, J., Dumas, C., Felikson, D., Fettweis, X., Fujita, K., Galton-Fenzi, B.K., Gladstone, R., Golledge, N.R., Greve, R., Hattermann, T., Hoffman, M.J., Humbert, A., Huss, M., Huybrechts, P., Immerzeel, W., Kleiner, T., Kraaijenbrink, P., Le clec'h, S., Lee, V., Leguy, G.R., Little, C.M., Lowry, D.P., Malles, J.-H., Martin, D.F., Maussion, F., Morlighem, M., O'Neill, J.F., Nias, I., Pattyn, F., Pelle, T., Price, S.F., Quiquet, A., Radić, V., Reese, R., Rounce, D.R., Rückamp, M., Sakai, A., Shafer, C., Schlegel, N.-J., Shannon, S., Smith, R.S., Straneo, F., Sun, S., Tarasov, L., Trusel, L.D., Van Breedam, J., van de Wal, R., van den Broeke, M., Winkelmann, R., Zekollari, H., Zhao, C., Zhang, T., Zwinger, T., 2021. Projected land ice contributions to twenty-first-century sea level rise. *Nature* 593, 74–82. <https://doi.org/10.1038/s41586-021-03302-y>
- Eichentopf, S., van der Zanden, J., Cáceres, I., Baldock, T.E., Alsina, J.M., 2020. Influence of storm sequencing on breaker bar and shoreline evolution in large-scale experiments. *Coast. Eng.* 157, 103659. <https://doi.org/10.1016/j.coastaleng.2020.103659>
- Falqués, A., Garnier, R., Ojeda, E., Ribas, F., Guillen, J., 2007. Q2D-morfo: a medium to long term model for beach morphodynamics. *Coast. Estuar. Morphodynamics* 1, 71–78.
- Frederikse, T., Landerer, F., Caron, L., Adhikari, S., Parkes, D., Humphrey, V.W., Dangendorf, S., Hogarth, P., Zanna, L., Cheng, L., Wu, Y.-H., 2020. The causes of sea-level rise since 1900. *Nature* 584, 393–397. <https://doi.org/10.1038/s41586-020-2591-3>
- Gallagher, E.L., MacMahan, J., Reniers, A.J.H.M., Brown, J., Thornton, E.B., 2011. Grain size variability on a rip-channeled beach. *Mar. Geol.* 287, 43–53. <https://doi.org/10.1016/j.margeo.2011.06.010>
- Ghermandi, A., Nunes, P.A.L.D., 2013. A global map of coastal recreation values: Results from a spatially explicit meta-analysis. *Ecol. Econ.* 86, 1–15. <https://doi.org/10.1016/j.ecolecon.2012.11.006>
- Grinsted, A., Jevrejeva, S., Riva, R., Dahl-Jensen, D., 2015. Sea level rise projections for northern Europe under RCP8.5. *Clim. Res.* 64, 15–23. <https://doi.org/10.3354/cr01309>
- Hallermeier, R.J., 1978. Uses for a calculated limit depth to beach erosion, in: *The 16th Coastal Engineering Conference*. ASCE, New York, pp. 1493–1512.
- Harley, M.D., Turner, I.L., Short, A.D., Ranasinghe, R., 2011. A reevaluation of coastal embayment rotation: The dominance of cross-shore versus alongshore sediment transport processes, Collaroy-Narrabeen Beach, southeast Australia. *J. Geophys. Res.* 116, F04033. <https://doi.org/10.1029/2011JF001989>

- Hazeleger, W., Wang, X., Severijns, C., Ștefănescu, S., Bintanja, R., Sterl, A., Wyser, K., Semmler, T., Yang, S., van den Hurk, B., van Noije, T., van der Linden, E., van der Wiel, K., 2012. EC-Earth V2.2: description and validation of a new seamless earth system prediction model. *Clim. Dyn.* 39, 2611–2629. <https://doi.org/10.1007/s00382-011-1228-5>
- Hinkel, J., Church, J.A., Gregory, J.M., Lambert, E., Le Cozannet, G., Lowe, J., McInnes, K.L., Nicholls, R.J., Pol, T.D., Wal, R., 2019. Meeting User Needs for Sea Level Rise Information: A Decision Analysis Perspective. *Earth's Futur.* 7, 320–337. <https://doi.org/10.1029/2018EF001071>
- Ibaceta, R., Splinter, K.D., Harley, M.D., Turner, I.L., 2020. Enhanced Coastal Shoreline Modeling Using an Ensemble Kalman Filter to Include Nonstationarity in Future Wave Climates. *Geophys. Res. Lett.* 47. <https://doi.org/10.1029/2020GL090724>
- Idier, D., Castelle, B., Charles, E., Mallet, C., 2013. Longshore sediment flux hindcast: spatio-temporal variability along the SW Atlantic coast of France. *J. Coast. Res.* 165, 1785–1790. <https://doi.org/10.2112/SI65-302.1>
- Iooss, B., Prieur, C., 2019. Shapley effects for sensitivity analysis with correlated inputs: Comparisons with sobol' indices, numerical estimation and applications. *Int. J. Uncertain. Quantif.* 9, 493–514. <https://doi.org/10.1615/Int.J.UncertaintyQuantification.2019028372>
- Jackson, L.P., Jevrejeva, S., 2016. A probabilistic approach to 21st century regional sea-level projections using RCP and High-end scenarios. *Glob. Planet. Change* 146, 179–189. <https://doi.org/10.1016/j.gloplacha.2016.10.006>
- Jara, M.S., González, M., Medina, R., 2015. Shoreline evolution model from a dynamic equilibrium beach profile. *Coast. Eng.* 99. <https://doi.org/10.1016/j.coastaleng.2015.02.006>
- Jaramillo, C., Jara, M.S., González, M., Medina, R., 2020. A shoreline evolution model considering the temporal variability of the beach profile sediment volume (sediment gain / loss). *Coast. Eng.* 156. <https://doi.org/10.1016/j.coastaleng.2019.103612>
- Jevrejeva, S., Frederikse, T., Kopp, R.E., Le Cozannet, G., Jackson, L.P., van de Wal, R.S.W., 2019. Probabilistic Sea Level Projections at the Coast by 2100. *Surv. Geophys.* <https://doi.org/10.1007/s10712-019-09550-y>
- Klingebiel, A., Legigan, P., 1992. Carte Géologique et structure du Bassin de la Leyre. *Bull. l'Institut Geol. du Bassin d'Aquitaine* 51–52, 7–20.
- Kopp, R.E., Horton, R.M., Little, C.M., Mitrovica, J.X., Oppenheimer, M., Rasmussen, D.J., Strauss, B.H., Tebaldi, C., 2014. Probabilistic 21st and 22nd century sea-level projections at a global network of tide-gauge sites. *Earth's Futur.* 2, 383–406. <https://doi.org/10.1002/2014EF000239>
- Kroon, A., de Schipper, M.A., van Gelder, P.H.A.J.M., Aarninkhof, S.G.J., 2020. Ranking uncertainty: Wave climate variability versus model uncertainty in probabilistic assessment of coastline change. *Coast. Eng.* 158. <https://doi.org/10.1016/j.coastaleng.2020.103673>
- Laporte-Fauret, Q., Marieu, V., Castelle, B., Michalet, R., Bujan, S., Rosebery, D., 2019. Low-Cost UAV for High-Resolution and Large-Scale Coastal Dune Change Monitoring Using Photogrammetry. *J. Mar. Sci. Eng.* 7, 63. <https://doi.org/10.3390/jmse7030063>
- Larson, M., Hoan, L.X., Hanson, H., 2010. Direct Formula to Compute Wave Height and Angle at Incipient Breaking. *J. Waterw. Port, Coastal, Ocean Eng.* 136. [https://doi.org/10.1061/\(ASCE\)WW.1943-5460.0000030](https://doi.org/10.1061/(ASCE)WW.1943-5460.0000030)
- Le Cozannet, G., Bulteau, T., Castelle, B., Ranasinghe, R., Wöppelmann, G., Rohmer, J., Bernon, N., Idier, D., Louisor, J., Salas-y-Méla, D., 2019. Quantifying uncertainties of sandy shoreline change projections as sea level rises. *Sci. Rep.* 9, 42. <https://doi.org/10.1038/s41598-018-37017-4>
- Le Cozannet, G., Oliveros, C., Castelle, B., Garcin, M., Idier, D., Pedreros, R., Rohmer, J., 2016. Uncertainties in Sandy Shorelines Evolution under the Bruun Rule Assumption. *Front. Mar. Sci.* 3. <https://doi.org/10.3389/fmars.2016.00049>
- Lemos, C., Floc'h, F., Yates, M.L., Le Dantec, N., Marieu, V., Hamon, K., Cuq, V., Suanez, S., Delacourt, C., 2018. Equilibrium modeling of the beach profile on a macrotidal embayed low tide

- terrace beach. *Ocean Dyn.* 68. <https://doi.org/10.1007/s10236-018-1185-1>
- Li, C., Mahadevan, S., 2016. An efficient modularized sample-based method to estimate the first-order Sobol' index. *Reliab. Eng. Syst. Saf.* 153, 110–121. <https://doi.org/10.1016/j.ress.2016.04.012>
- Lobeto, H., Menendez, M., Losada, I.J., 2021. Future behavior of wind wave extremes due to climate change. *Sci. Rep.* 11, 7869. <https://doi.org/10.1038/s41598-021-86524-4>
- Ludka, B.C., Guza, R.T., O'Reilly, W.C., Yates, M.L., 2015. Field evidence of beach profile evolution toward equilibrium. *J. Geophys. Res. Ocean.* 120. <https://doi.org/10.1002/2015JC010893>
- Luijendijk, A., Hagenaars, G., Ranasinghe, R., Baart, F., Donchyts, G., Aarninkhof, S.G.J., 2018. The State of the World's Beaches. *Sci. Rep.* 8, 6641. <https://doi.org/10.1038/s41598-018-24630-6>
- Magnan, A.K., Garschagen, M., Gattuso, J.-P., Hay, J.E., Hilmi, N., Holland, E., Isla, F., Kofinas, G., Losada, I.J., Petzold, J., Ratter, B., Schuur, T., Tabe, T., van de Wal, R.S.W., 2019. Cross-Chapter Box 9: Integrative Cross-Chapter Box on Low-Lying Islands and Coasts. In: IPCC Special Report on the Ocean and Cryosphere in a Changing Climate.
- Mankin, J.S., Lehner, F., Coats, S., McKinnon, K.A., 2020. The Value of Initial Condition Large Ensembles to Robust Adaptation Decision-Making. *Earth's Futur.* 8. <https://doi.org/10.1029/2020EF001610>
- Mara, T.A., Becker, W.E., 2021. Polynomial chaos expansion for sensitivity analysis of model output with dependent inputs. *Reliab. Eng. Syst. Saf.* 214, 107795. <https://doi.org/10.1016/j.ress.2021.107795>
- Masselink, G., Castelle, B., Scott, T., Dodet, G., Suarez, S., Jackson, D., Floc'h, F., 2016. Extreme wave activity during 2013/2014 winter and morphological impacts along the Atlantic coast of Europe. *Geophys. Res. Lett.* 43. <https://doi.org/10.1002/2015GL067492>
- McCarroll, R.J., Masselink, G., Valiente, N.G., Scott, T., Wiggins, M., Kirby, J.-A., Davidson, M.A., 2021. A rules-based shoreface translation and sediment budgeting tool for estimating coastal change: ShoreTrans. *Mar. Geol.* 435, 106466. <https://doi.org/10.1016/j.margeo.2021.106466>
- Merkens, J.-L., Reimann, L., Hinkel, J., Vafeidis, A.T., 2016. Gridded population projections for the coastal zone under the Shared Socioeconomic Pathways. *Glob. Planet. Change* 145, 57–66. <https://doi.org/10.1016/j.gloplacha.2016.08.009>
- Michaud, H., Pasquet, A., Lecker, F., Baraille, R., Dalphinnet, A., Aouf, L., 2016. Improvements of the new French coastal wave forecasting system and application to a wave-current interaction study, in: 14th International Workshop on Wave Hindcasting and Forecasting & 5th Coastal Hazard Symposium SHOM & Meteo France. Venice. <https://doi.org/10.13140/RG.2.2.13218.02243>
- Miller, J.K., Dean, R.G., 2004. A simple new shoreline change model. *Coast. Eng.* 51. <https://doi.org/10.1016/j.coastaleng.2004.05.006>
- Montaño, J., Coco, G., Antolínez, J.A.A., Beuzen, T., Bryan, K.R., Cagigal, L., Castelle, B., Davidson, M.A., Goldstein, E.B., Ibaceta, R., Idier, D., Ludka, B.C., Masoud-Ansari, S., Méndez, F.J., Murray, A.B., Plant, N.G., Ratliff, K.M., Robinet, A., Rueda, A., Sénéchal, N., Simmons, J.A., Splinter, K.D., Stephens, S., Townend, I., Vitousek, S., Vos, K., 2020. Blind testing of shoreline evolution models. *Sci. Rep.* 10, 2137. <https://doi.org/10.1038/s41598-020-59018-y>
- Montaño, J., Coco, G., Cagigal, L., Mendez, F., Rueda, A., Bryan, K.R., Harley, M.D., 2021. A Multiscale Approach to Shoreline Prediction. *Geophys. Res. Lett.* 48. <https://doi.org/10.1029/2020GL090587>
- Morim, J., Hemer, M., Wang, X.L., Cartwright, N., Trenham, C., Semedo, A., Young, I., Bricheno, L., Camus, P., Casas-Prat, M., Erikson, L., Mentaschi, L., Mori, N., Shimura, T., Timmermans, B., Aarnes, O., Breivik, Ø., Behrens, A., Dobrynin, M., Menendez, M., Staneva, J., Wehner, M., Wolf, J., Kamranzad, B., Webb, A., Stopa, J., Andutta, F., 2019. Robustness and uncertainties in global multivariate wind-wave climate projections. *Nat. Clim. Chang.* 9. <https://doi.org/10.1038/s41558-019-0542-5>
- Morim, J., Trenham, C., Hemer, M., Wang, X.L., Mori, N., Casas-Prat, M., Semedo, A., Shimura, T.,

- Timmermans, B., Camus, P., Bricheno, L., Mentaschi, L., Dobrynin, M., Feng, Y., Erikson, L., 2020. A global ensemble of ocean wave climate projections from CMIP5-driven models. *Sci. Data* 7, 105. <https://doi.org/10.1038/s41597-020-0446-2>
- Nash, J.E., Sutcliffe, J.V., 1970. River flow forecasting through conceptual models part I — A discussion of principles. *J. Hydrol.* 10, 282–290. [https://doi.org/10.1016/0022-1694\(70\)90255-6](https://doi.org/10.1016/0022-1694(70)90255-6)
- Nicholls, R.J., 1998. Assessing erosion of sandy beaches due to sea-level rise. *Geol. Soc. London, Eng. Geol. Spec. Publ.* 15. <https://doi.org/10.1144/GSL.ENG.1998.015.01.08>
- Oppenheimer, M.B., Glavovic, J., Hinkel, R., Magnan, A.K. et al, 2019. Sea Level Rise and Implications for Low-Lying Islands, Coasts and Communities. In: IPCC Special Report on the Ocean and Cryosphere in a Changing Climate, IPCC Special Report on the Ocean and Cryosphere in a Changing Climate.
- Owen, A.B., 2014. Sobol' Indices and Shapley Value. *SIAM/ASA J. Uncertain. Quantif.* 2, 245–251. <https://doi.org/10.1137/130936233>
- Parisot, J.-P., Capo, S., Castelle, B., Bujan, S., Moreau, J., Gervais, M., Réjas, A., Hanquiez, V., Almar, R., Marieu, V., Gaunet, J., Gluard, L., George, I., Nahon, A., Dehouck, A., Certain, R., Barthe, P., Le Gall, F., Bernardi, P.J., Le Roy, R., Pedreros, R., Delattre, M., Brillet, J., Sénéchal, N., 2009. Treatment of topographic and bathymetric data acquired at the Truc-Vert Beach during the ECORS Field Experiment. *J. Coast. Res.* 1786–1790.
- Perez, J., Menendez, M., Camus, P., Mendez, F.J., Losada, I.J., 2015. Statistical multi-model climate projections of surface ocean waves in Europe. *Ocean Model.* 96, 161–170. <https://doi.org/10.1016/j.ocemod.2015.06.001>
- Pringle, J., Stretch, D.D., 2021. On a new statistical wave generator based on atmospheric circulation patterns and its applications to coastal shoreline evolution. *Comput. Geosci.* 149. <https://doi.org/10.1016/j.cageo.2021.104707>
- Pringle, J., Stretch, D.D., 2019. A New Approach for the Stochastic Simulation of Regional Wave Climates Conditioned on Synoptic-Scale Meteorology. *J. Coast. Res.* 35, 1331. <https://doi.org/10.2112/JCOASTRES-D-18-00158.1>
- Ranasinghe, R., 2020. On the need for a new generation of coastal change models for the 21st century. *Sci. Rep.* 10, 2010. <https://doi.org/10.1038/s41598-020-58376-x>
- Ranasinghe, R., 2016. Assessing climate change impacts on open sandy coasts: A review. *Earth-Science Rev.* 160. <https://doi.org/10.1016/j.earscirev.2016.07.011>
- Ranasinghe, R., Callaghan, D.P., Stive, M.J.F., 2012. Estimating coastal recession due to sea level rise: beyond the Bruun rule. *Clim. Change* 110. <https://doi.org/10.1007/s10584-011-0107-8>
- Riahi, K., van Vuuren, D.P., Kriegler, E., Edmonds, J., O'Neill, B.C., Fujimori, S., Bauer, N., Calvin, K., Dellink, R., Fricko, O., Lutz, W., Popp, A., Cuaresma, J.C., KC, S., Leimbach, M., Jiang, L., Kram, T., Rao, S., Emmerling, J., Ebi, K., Hasegawa, T., Havlik, P., Humpenöder, F., Da Silva, L.A., Smith, S., Stehfest, E., Bosetti, V., Eom, J., Gernaat, D., Masui, T., Rogelj, J., Strefler, J., Drouet, L., Krey, V., Luderer, G., Harmsen, M., Takahashi, K., Baumstark, L., Doelman, J.C., Kainuma, M., Klimont, Z., Marangoni, G., Lotze-Campen, H., Obersteiner, M., Tabeau, A., Tavoni, M., 2017. The Shared Socioeconomic Pathways and their energy, land use, and greenhouse gas emissions implications: An overview. *Glob. Environ. Chang.* 42, 153–168. <https://doi.org/10.1016/j.gloenvcha.2016.05.009>
- Robin, N., Billy, J., Castelle, B., Hesp, P., Nicolae Lerma, A., Laporte-Fauret, Q., Marieu, V., Rosebery, D., Bujan, S., Destribats, B., Michalet, R., 2021. 150 years of foredune initiation and evolution driven by human and natural processes. *Geomorphology* 374. <https://doi.org/10.1016/j.geomorph.2020.107516>
- Robinet, A., Castelle, B., Idier, D., D'Anna, M., Le Cozannet, G., 2020. Simulating the Impact of Sea-level Rise and Offshore Bathymetry on Embayment Shoreline Changes. *J. Coast. Res.* 95. <https://doi.org/10.2112/SI95-244.1>

- Robinet, A., Castelle, B., Idier, D., Le Cozannet, G., Déqué, M., Charles, E., 2016. Statistical modeling of interannual shoreline change driven by North Atlantic climate variability spanning 2000–2014 in the Bay of Biscay. *Geo-Marine Lett.* 36. <https://doi.org/10.1007/s00367-016-0460-8>
- Robinet, A., Idier, D., Castelle, B., Marieu, V., 2018. A reduced-complexity shoreline change model combining longshore and cross-shore processes: The LX-Shore model. *Environ. Model. Softw.* 109. <https://doi.org/10.1016/j.envsoft.2018.08.010>
- Rohmer, J., 2014. Combining meta-modeling and categorical indicators for global sensitivity analysis of long-running flow simulators with spatially dependent inputs. *Comput. Geosci.* 18, 171–183. <https://doi.org/10.1007/s10596-013-9391-x>
- Rohmer, J., Le Cozannet, G., 2019. Dominance of the mean sea level in the high-percentile sea levels time evolution with respect to large-scale climate variability: a Bayesian statistical approach. *Environ. Res. Lett.* 14, 014008. <https://doi.org/10.1088/1748-9326/aaf0cd>
- Rosati, J.D., Dean, R.G., Walton, T.L., 2013. The modified Bruun Rule extended for landward transport. *Mar. Geol.* 340. <https://doi.org/10.1016/j.margeo.2013.04.018>
- Rueda, A., Camus, P., Tomás, A., Vitousek, S., Méndez, F.J., 2016. A multivariate extreme wave and storm surge climate emulator based on weather patterns. *Ocean Model.* 104, 242–251. <https://doi.org/10.1016/j.ocemod.2016.06.008>
- Ruessink, G., 2005. Predictive uncertainty of a nearshore bed evolution model. *Cont. Shelf Res.* 25. <https://doi.org/10.1016/j.csr.2004.12.007>
- Saha, S., Moorthi, S., Pan, H.-L., Wu, X., Wang, Jiande, Nadiga, S., Tripp, P., Kistler, R., Woollen, J., Behringer, D., Liu, H., Stokes, D., Grumbine, R., Gayno, G., Wang, Jun, Hou, Y.-T., Chuang, H., Juang, H.-M.H., Sela, J., Iredell, M., Treadon, R., Kleist, D., Van Delst, P., Keyser, D., Derber, J., Ek, M., Meng, J., Wei, H., Yang, R., Lord, S., van den Dool, H., Kumar, A., Wang, W., Long, C., Chelliah, M., Xue, Y., Huang, B., Schemm, J.-K., Ebisuzaki, W., Lin, R., Xie, P., Chen, M., Zhou, S., Higgins, W., Zou, C.-Z., Liu, Q., Chen, Y., Han, Y., Cucurull, L., Reynolds, R.W., Rutledge, G., Goldberg, M., 2010. The NCEP Climate Forecast System Reanalysis. *Bull. Am. Meteorol. Soc.* 91, 1015–1058. <https://doi.org/10.1175/2010BAMS3001.1>
- Saltelli, A., Ratto, M., Andres, T., Campolongo, F., Cariboni, J., Gatelli, D., Saisana, M., Tarantola, S., 2008. *Global sensitivity analysis: The premier*. Chichester West Sussex PO19 8SQ, England.
- Saltelli, A., Tarantola, S., 2002. On the Relative Importance of Input Factors in Mathematical Models. *J. Am. Stat. Assoc.* 97, 702–709. <https://doi.org/10.1198/016214502388618447>
- Santamaría-Gómez, A., Gravelle, M., Dangendorf, S., Marcos, M., Spada, G., Wöppelmann, G., 2017. Uncertainty of the 20th century sea-level rise due to vertical land motion errors. *Earth Planet. Sci. Lett.* 473, 24–32. <https://doi.org/10.1016/j.epsl.2017.05.038>
- Schepper, R., Almar, R., Bergsma, E., de Vries, S., Reniers, A., Davidson, M., Splinter, K., 2021. Modelling Cross-Shore Shoreline Change on Multiple Timescales and Their Interactions. *J. Mar. Sci. Eng.* 9, 582. <https://doi.org/10.3390/jmse9060582>
- SCOR Working group 89, 1991. The Response of Beaches to Sea-Level Changes: A Review of Predictive Models. *J. Coast. Res.* 7, 895–921.
- Sénéchal, N., Abadie, S., Gallagher, E., MacMahan, J., Masselink, G., Michallet, H., Reniers, A., Ruessink, G., Russell, P., Sous, D., Turner, I.L., Arduin, F., Bonneton, P., Bujan, S., Capo, S., Certain, R., Pedreros, R., Garlan, T., 2011. The ECORS-Truc Vert'08 nearshore field experiment: presentation of a three-dimensional morphologic system in a macro-tidal environment during consecutive extreme storm conditions. *Ocean Dyn.* 61, 2073–2098. <https://doi.org/10.1007/s10236-011-0472-x>
- Sénéchal, N., Gouriou, T., Castelle, B., Parisot, J.-P., Capo, S., Bujan, S., Howa, H., 2009. Morphodynamic response of a meso- to macro-tidal intermediate beach based on a long-term data set. *Geomorphology* 107, 263–274. <https://doi.org/10.1016/j.geomorph.2008.12.016>
- Shapley, L.S., 1953. A Value for n-Person Games, in: *Contributions to the Theory of Games (AM-28)*,

- Volume II. Princeton University Press, pp. 307–318. <https://doi.org/10.1515/9781400881970-018>
- Simmons, J.A., Harley, M.D., Marshall, L.A., Turner, I.L., Splinter, K.D., Cox, R.J., 2017. Calibrating and assessing uncertainty in coastal numerical models. *Coast. Eng.* 125. <https://doi.org/10.1016/j.coastaleng.2017.04.005>
- Slangen, A.B.A., Carson, M., Katsman, C.A., van de Wal, R.S.W., Köhl, A., Vermeersen, L.L.A., Stammer, D., 2014. Projecting twenty-first century regional sea-level changes. *Clim. Change* 124, 317–332. <https://doi.org/10.1007/s10584-014-1080-9>
- Sobol', I., 2001. Global sensitivity indices for nonlinear mathematical models and their Monte Carlo estimates. *Math. Comput. Simul.* 55, 271–280. [https://doi.org/10.1016/S0378-4754\(00\)00270-6](https://doi.org/10.1016/S0378-4754(00)00270-6)
- Song, E., Nelson, B.L., Staum, J., 2016. Shapley Effects for Global Sensitivity Analysis: Theory and Computation. *SIAM/ASA J. Uncertain. Quantif.* 4, 1060–1083. <https://doi.org/10.1137/15M1048070>
- Splinter, K.D., Carley, J.T., Golshani, A., Tomlinson, R., 2014a. A relationship to describe the cumulative impact of storm clusters on beach erosion. *Coast. Eng.* 83, 49–55. <https://doi.org/10.1016/j.coastaleng.2013.10.001>
- Splinter, K.D., Turner, I.L., Davidson, M.A., 2013. How much data is enough? The importance of morphological sampling interval and duration for calibration of empirical shoreline models. *Coast. Eng.* 77. <https://doi.org/10.1016/j.coastaleng.2013.02.009>
- Splinter, K.D., Turner, I.L., Davidson, M.A., Barnard, P.L., Castelle, B., Oltman-Shay, J., 2014b. A generalized equilibrium model for predicting daily to interannual shoreline response. *J. Geophys. Res. Earth Surf.* 119. <https://doi.org/10.1002/2014JF003106>
- Splinter, K.D., Turner, I.L., Reinhardt, M., Ruessink, G., 2017. Rapid adjustment of shoreline behavior to changing seasonality of storms: observations and modelling at an open-coast beach. *Earth Surf. Process. Landforms* 42. <https://doi.org/10.1002/esp.4088>
- Stammer, D., Wal, R.S.W., Nicholls, R.J., Church, J.A., Le Cozannet, G., Lowe, J.A., Horton, B.P., White, K., Behar, D., Hinkel, J., 2019. Framework for High-End Estimates of Sea Level Rise for Stakeholder Applications. *Earth's Futur.* 7, 923–938. <https://doi.org/10.1029/2019EF001163>
- Stive, M.J., Aarninkhof, S.G.J., Hamm, L., Hanson, H., Larson, M., Wijnberg, K.M., Nicholls, R.J., Capobianco, M., 2002. Variability of shore and shoreline evolution. *Coast. Eng.* 47, 211–235. [https://doi.org/10.1016/S0378-3839\(02\)00126-6](https://doi.org/10.1016/S0378-3839(02)00126-6)
- Taylor, K.E., Stouffer, R.J., Meehl, G.A., 2012. An Overview of CMIP5 and the Experiment Design. *Bull. Am. Meteorol. Soc.* 93, 485–498. <https://doi.org/10.1175/BAMS-D-11-00094.1>
- Thiéblemont, R., Le Cozannet, G., Rohmer, J., Toimil, A., Álvarez-Cuesta, M., Losada, I.J., 2021. Deep uncertainties in shoreline change projections: an extra-probabilistic approach applied to sandy beaches. *Nat. Hazards Earth Syst. Sci.* 21, 2257–2276. <https://doi.org/10.5194/nhess-21-2257-2021>
- Thiéblemont, R., Le Cozannet, G., Toimil, A., Meyssignac, B., Losada, I.J., 2019. Likely and High-End Impacts of Regional Sea-Level Rise on the Shoreline Change of European Sandy Coasts Under a High Greenhouse Gas Emissions Scenario. *Water* 11. <https://doi.org/10.3390/w11122607>
- Toimil, A., Camus, P., Losada, I.J., Alvarez-Cuesta, M., 2021. Visualising the Uncertainty Cascade in Multi-Ensemble Probabilistic Coastal Erosion Projections. *Front. Mar. Sci.* 8. <https://doi.org/10.3389/fmars.2021.683535>
- Toimil, A., Camus, P., Losada, I.J., Le Cozannet, G., Nicholls, R.J., Idier, D., Maspataud, A., 2020a. Climate change-driven coastal erosion modelling in temperate sandy beaches: Methods and uncertainty treatment. *Earth-Science Rev.* 202. <https://doi.org/10.1016/j.earscirev.2020.103110>
- Toimil, A., Losada, I.J., Camus, P., Díaz-Simal, P., 2017. Managing coastal erosion under climate change at the regional scale. *Coast. Eng.* 128. <https://doi.org/10.1016/j.coastaleng.2017.08.004>
- Toimil, A., Losada, I.J., Nicholls, R.J., Dalrymple, R.A., Stive, M.J.F., 2020b. Addressing the

- challenges of climate change risks and adaptation in coastal areas: A review. *Coast. Eng.* 156, 103611. <https://doi.org/10.1016/j.coastaleng.2019.103611>
- Tolman, H.L., 2009. User manual and system documentation of WAVEWATCH-III version 3.14. Tech. note 220.
- Tran, Y.H., Barthélemy, E., 2020. Combined longshore and cross-shore shoreline model for closed embayed beaches. *Coast. Eng.* 158. <https://doi.org/10.1016/j.coastaleng.2020.103692>
- Vitousek, S., Barnard, P.L., Limber, P., 2017a. Can beaches survive climate change? *J. Geophys. Res. Earth Surf.* 122. <https://doi.org/10.1002/2017JF004308>
- Vitousek, S., Barnard, P.L., Limber, P., Erikson, L., Cole, B., 2017b. A model integrating longshore and cross-shore processes for predicting long-term shoreline response to climate change. *J. Geophys. Res. Earth Surf.* 122. <https://doi.org/10.1002/2016JF004065>
- Vitousek, S., Cagigal, L., Montaño, J., Rueda, A., Méndez, F.J., Coco, G., Barnard, P.L., 2021. The Application of Ensemble Wave Forcing to Quantify Uncertainty of Shoreline Change Predictions. *J. Geophys. Res. Earth Surf.* 126. <https://doi.org/10.1029/2019JF005506>
- Vos, K., Harley, M.D., Splinter, K.D., Walker, A., Turner, I.L., 2020. Beach Slopes From Satellite-Derived Shorelines. *Geophys. Res. Lett.* 47. <https://doi.org/10.1029/2020GL088365>
- Vousdoukas, M.I., Ranasinghe, R., Mentaschi, L., Plomaritis, T.A., Athanasiou, P., Luijendijk, A., Feyen, L., 2020. Sandy coastlines under threat of erosion. *Nat. Clim. Chang.* 10, 260–263. <https://doi.org/10.1038/s41558-020-0697-0>
- Wainwright, D.J., Ranasinghe, R., Callaghan, D.P., Woodroffe, C.D., Jongejan, R., Dougherty, A.J., Rogers, K., Cowell, P.J., 2015. Moving from deterministic towards probabilistic coastal hazard and risk assessment: Development of a modelling framework and application to Narrabeen Beach, New South Wales, Australia. *Coast. Eng.* 96, 92–99. <https://doi.org/10.1016/j.coastaleng.2014.11.009>
- Wolinsky, M.A., Murray, A.B., 2009. A unifying framework for shoreline migration: 2. Application to wave-dominated coasts. *J. Geophys. Res.* 114. <https://doi.org/10.1029/2007JF000856>
- Wong, P.P., Losada, I.J., Gattuso, J.-P., Hinkel, J., Khattabi, A., McInnes, K.L., Saito, Y., Sallenger, A., 2014. Coastal Systems and Low-Lying Areas, in: Field, C.B., Barros, V.R., Dokken, D.J., Mach, K.J., Mastrandrea, M.D. (Eds.), *Climate Change 2014 Impacts, Adaptation, and Vulnerability*. Cambridge University Press, Cambridge, pp. 361–410. <https://doi.org/10.1017/CBO9781107415379.010>
- Wright, L., Short, A.D., 1984. Morphodynamic variability of surf zones and beaches: A synthesis. *Mar. Geol.* 56. [https://doi.org/10.1016/0025-3227\(84\)90008-2](https://doi.org/10.1016/0025-3227(84)90008-2)
- Yates, M.L., Guza, R.T., O'Reilly, W.C., 2009. Equilibrium shoreline response: Observations and modeling. *J. Geophys. Res.* 114. <https://doi.org/10.1029/2009JC005359>
- Yates, M.L., Guza, R.T., O'Reilly, W.C., Hansen, J.E., Barnard, P.L., 2011. Equilibrium shoreline response of a high wave energy beach. *J. Geophys. Res.* 116. <https://doi.org/10.1029/2010JC006681>

Appendix A Methodology

A1. Direct formulation for wave refraction and breaking

Throughout this manuscript, the breaking wave height and angle are estimated using the direct approach proposed by Larson et al. (2010). The approach consists in solving the energy flux conservation iteratively, assuming the validity of Snell's law. For an arbitrary water depth d , the equations read:

$$H_{s,d}^2 C_{g,d} \cos(\theta_d) = H_{s,b}^2 C_{g,b} \cos(\theta_b) \quad (\text{A1})$$

$$\frac{\sin(\theta_d)}{C_d} = \frac{\sin(\theta_b)}{C_b} \quad (\text{A2})$$

where H_s is the significant wave height, θ is the angle of wave incidence, C and C_g are the wave and wave-group celerity, respectively, and the subscript b denotes wave breaking conditions. Introducing $\lambda = gh_b/C_d^2$ and manipulating Equations A1 and A2, under the assumption of shallow-water wave theory the following formulation is obtained:

$$\lambda^{5/2} \left(\frac{C_d}{\sqrt{gH_{s,d}}} \right)^4 \frac{C_d}{C_{g,d}} \frac{\gamma_b^2}{\cos(\theta_d)} \sqrt{1 - \sin^2(\theta_d)} \lambda = 1 \quad (\text{A3})$$

where γ_b is the wave breaking index ($H_{s,b}/h_b$). Assuming a small breaking wave angle, Equation A3 can be simplified as follows, providing an approximate solution (λ_a):

$$\lambda_a = \left[\left(\frac{C_d}{\sqrt{gH_{s,d}}} \right)^4 \frac{C_d}{C_{g,d}} \frac{\gamma_b^2}{\cos(\theta_d)} \right]^{-2/5} \quad (\text{A4})$$

Equation A4 can be used to compute the approximate λ_a , which is then corrected using an empirical function obtained from input wave data (see Larson et al. 2010, for more detail).

A2. Global Sensitivity Analysis

The variance-based Global Sensitivity Analysis (GSA) (Saltelli et al., 2008) aims to unravel the uncertainties on the results of a given calculation (model) by decomposing the variance into several fractions, each one attributed to the uncertain input variables (or combinations of input variables). As a first step, the GSA explores the entire variability range of the uncertain inputs by sampling different values from the respective probability distributions and performing an ensemble of model realizations, each one with a different

combination of sampled model inputs. This ultimately produces a comprehensive ensemble of model results that is confronted to each uncertain input X_i , and the relative (normalized) contribution of the uncertainties on X_i to the model results are estimated with sensitivity measures.

Sobol' indices

A well established sensitivity measure are the so-called *Sobol' indices* (Sobol', 2001) (S_i s). At their first order, S_i s are estimated as follows:

$$S_i = \frac{\text{Var}(E(Y|X_i))}{\text{Var}(Y)} \quad (\text{A5})$$

where S_i is the first-order *Sobol' index* of the i -th uncertain input, Y is the model prediction, $E(Y|X_i)$ is the expected value of Y conditional to X_i , and $\text{Var}(E(Y|X_i))$ is the variance of the $E(Y|X_i)$ s obtained for all the possible values of X_i . S_i (0, 1) quantifies the percentage of the model results variance that can be attributed to the uncertainties on the variable X_i alone. For example, consider an ensemble of model results (Y) resulting from the application of two uncertain input variables (X_1 and X_2) over a certain time interval, as shown in Figure A.1a. The estimated time varying S_i associated with X_1 and X_2 (Figure A.1b and A.1c, respectively) show that initially (t_1) the main effects of uncertainties on the variable X_2 are the major driver of Y 's uncertainties ($S_{X_2} \gg S_{X_1}$) while on a second time (t_2) these are dominated by the main effects of X_1 's uncertainties ($S_{X_2} \ll S_{X_1}$).

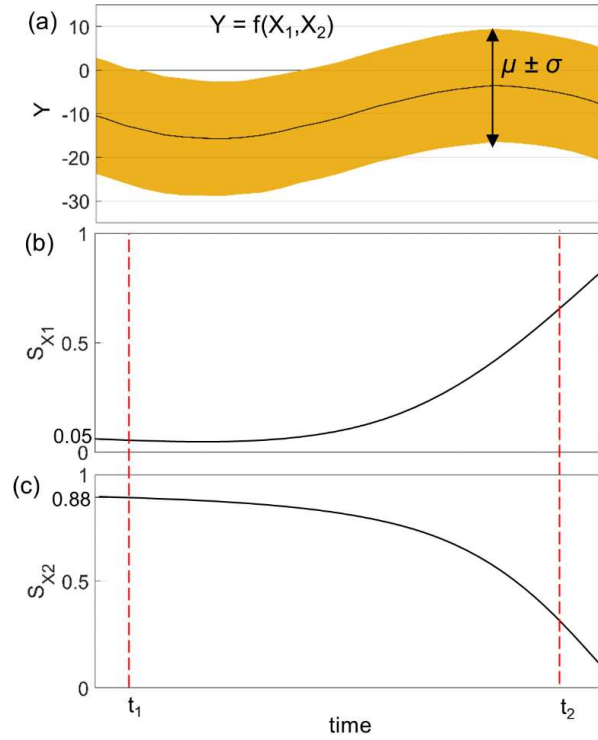


Figure A.1 Example of time series of (a) probabilistic model results Y obtained from the uncertain inputs X_1 and X_2 , at corresponding first-order Sobol' indices associated with (b) X_1 and (c) X_2 . Vertical red dashed lines indicate two different time steps t_1 and t_2 .

If an interaction exists between X_i and X_j , the relative contribution of X_i and X_j to the variance of model results is larger than $S_i + S_j$ and can be estimated by calculating second-order *Sobol' indices* as follows:

$$S_i + S_j + S''_{i,j} = \frac{\text{Var}\left(\text{E}(Y | X_i, X_j)\right)}{\text{Var}(Y)} \quad \text{with } i \neq j \quad (\text{A6})$$

where $S''_{i,j}$ is the interaction term between the i -th and j -th uncertain variable. More generally, higher-order terms including all possible main effects and interactions (of any order) among the uncertain inputs can be estimated as follows:

$$\sum_i S_i + \sum_i \sum_{j>i} S''_{i,j} + \dots + S^k_{1,2,3,\dots,k} = \frac{\text{Var}\left(\text{E}(Y | X_i, \dots, X_k)\right)}{\text{Var}(Y)} \quad \text{with } i < j < \dots < k \quad (\text{A7})$$

where k is the order of interaction investigated.

If the input variables are statistically independent and k is the number of uncertain input variables, Equation A7 describes the full decomposition of the output variance ($\text{Var}(Y)$) into all the possible main effects and interactions (of any order k) among the uncertain inputs and the right-hand term of the equation is equal to 1. Hence, the sum of the main effects

(S_i s) must be ≤ 1 , and the difference between 1 and the sum of the main effects can be used as an indicator of the presence of interactions.

If the input variables are statistically dependent (due to the presence of correlations among uncertain input variables) the variance decomposition can significantly be impacted as discussed by (Do & Razavi, 2020; Iooss & Prieur, 2019), and the afore-described interpretation of the terms in Equation A7 for sensitivity analysis no longer valid. If two or more uncertain inputs are statistically dependent (correlated), say X_i and X_j , the S_i includes some information that is also included in S_j , regardless of the possible interactions between the two variables. In this case, the sum of S_i s may exceed 1. We note here, that in the case of statistically dependent inputs, the S_i s still are a useful tool for ‘Factor Prioritization’ (as defined by Saltelli et al., 2008), that is the identification of the variable that would most reduce the variance of the results if fixed to its true value. However, in settings where correlations and potential interactions occur among the uncertain input variables (such as in the current work), overlooking their effects on the results uncertainties may significantly compromise the interpretation of the GSA outcome.

Appendix B Supporting information for Chapter 3

B1. Passive Flooding, Wave Reshaping and the Bruun Rule

In this Appendix, we show how expressing the Bruun Rule as the long-term cumulated effects of passive flooding and wave reshaping implies constant mean rates of these two contributions over time. The physical mechanism proposed in Section 3.2.2 indicates that SLR induces a shoreline change driven by the cumulated effects of passive flooding (Y_{PF}) and wave reshaping (Y_{WR}) over a time T :

$$Y_{PF} + Y_{WR} = \int_T dY_{PF}dt + \int_T dY_{WR}dt \quad (B1)$$

When the Bruun Rule assumptions (Section 3.2.1) are satisfied, namely the assumption of stationary long-term wave climate and constant SLR rate, over periods associating no trends in wave climate (*e.g.* $dT \geq O(\text{year})$), the mean rates of passive flooding and wave reshaping effects are constant over time:

$$\overline{dY_{PF}} + \overline{dY_{WR}} = \frac{1}{dT} \int_{dT} dY_{PF}dt + \frac{1}{dT} \int_{dT} dY_{WR}dt = c_1 + c_2 \quad (B2)$$

Hence, over a time $\Delta T = n dT$ (with n positive integer), Equation (B1) becomes:

$$Y_{PF} + Y_{WR} = \int_{\Delta T} dY_{PF}dt + \int_{\Delta T} dY_{WR}dt = \overline{dY_{PF}}\Delta T + \overline{dY_{WR}}\Delta T \quad (B3)$$

Therefore, under these specific conditions, on the time scale of dT (years or longer), the Bruun Rule can be expressed in terms of cumulated passive flooding and wave reshaping effects, as follows:

$$Y_{Bruun} = \frac{SLR}{\tan(\alpha)} = Y_{PF} + Y_{WR} = \overline{dY_{PF}}\Delta T + \overline{dY_{WR}}\Delta T \quad (B4)$$

B2. Integrating SLR-Driven Disequilibrium into ESMs with Feedback

In this Appendix, we provide a more detailed description of the approach introduced in Section 3.3.2, where SLR-driven erosion and an ESM based on the current shoreline position are integrated, enabling feedback between SLR effects and the disequilibrium condition. Then, we further analyse the assumption used to quantify the disequilibrium

induced by sea-level rise (SLR), and we analytically show that such assumption is consistent with the Bruun model structure.

Given an ESM based on the current shoreline position, if the equilibrium energy in Equation 3.5 ($E_{eq} = E_{eq}(Y)$) is expressed by a linear relationship between incident wave energy (E) and current shoreline cross-shore distance from a given reference (Y) (*i.e.* $E_{eq} = aY + b$, after Yates et al., 2009), the instantaneous disequilibrium state can be represented on the Y-E Cartesian plane (Figure B.1). In Figure B.1a, a given shoreline position is associated with an equilibrium wave energy (E_{eq}) that would not produce a shoreline change (black solid line), while positions located above and below the equilibrium line are associated with erosion ($dY/dt < 0$, red points) and accretion ($dY/dt > 0$, blue points), respectively. An increase in MSL (dMSL) induces passive flooding (dY_{PF}), corresponding to a landward shift of the reference shoreline (Figure 3.3b of the main text), *i.e.* a smaller Y value. Recall that this shift represents only a translation of the reference system with no morphologic changes to the beach profile. Therefore, the effect of passive flooding is projected on the Y-E plane as a landward shift of the equilibrium shoreline position (red arrows and red point in (Figure B.1b)). The second consequence of dMSL (observed in Figure 3.3b of the main text) is a general increase in the bottom slope relative to the local wave climate propagating over the new MSL. In morphologic terms, in respect to a given equilibrium profile, a generally steeper beach profile is closer to equilibrium with low-energy wave conditions and farther from high-energy wave conditions (Wright and Short, 1984), resulting in an overall (erosive) disequilibrium of the beach–wave climate system (Figure 3.3c of the main text). As the equilibrium condition is defined in terms of wave energy (E), the SLR-induced disequilibrium is projected on the Y-E plane as a downward shift of the equilibrium line ($dE_{eq,SLR}$ and dashed black line in Figure B.1b), indicating that for a given shoreline position (Y) less wave energy is required to erode the beach and restore the equilibrium. Or, alternatively, for a given wave climate, the efficiency of erosion is increased, which can result from an increased depth and bottom slope across the beach profile due to SLR and wave breaking tending to occur closer to the shore.

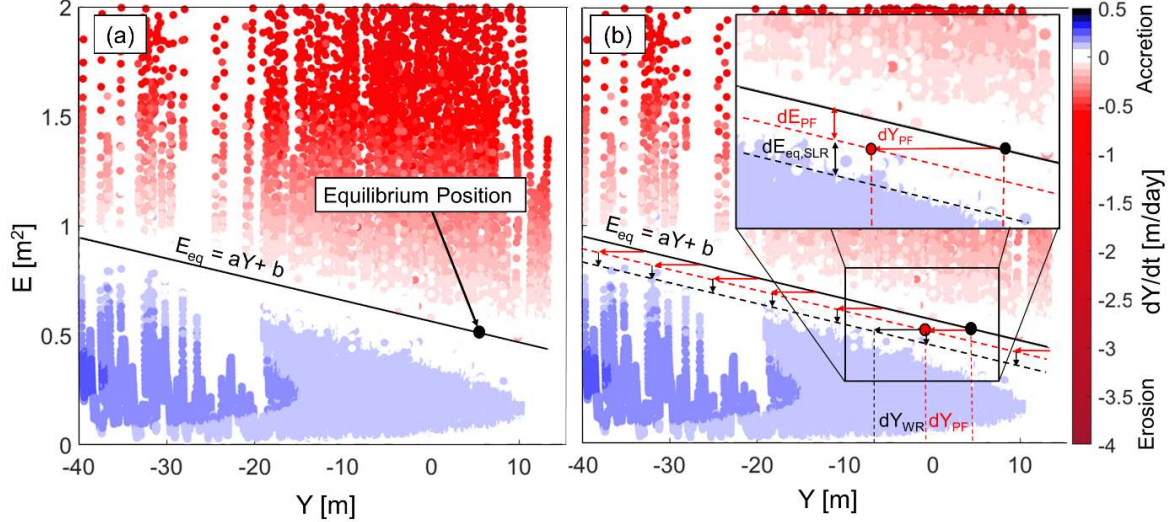


Figure B.1. Example of shoreline position (Y) vs. incident wave energy density ($E = 1/16 H_s^2$, where H_s is the significant wave height) Cartesian plane, with the linear equilibrium beach-wave condition following Yates et al. (2009) (solid black line). The colour bar indicates the magnitude of potential erosion (red) and accretion (blue). Red arrows indicate the geometric shift due to Passive Flooding (dY_{PF}); vertical black arrows indicate the disequilibrium change ($dE_{eq,SLR}$) corresponding to the change in the bottom slope relative to MSL; and the horizontal black arrow indicates the potential Wave Reshaping effect (dY_{WR}) that would re-establish the equilibrium state. The black dash line indicates the new equilibrium beach-wave condition post-SLR. The data used for this example refer to Truc Vert beach.

Quantifying $dE_{eq,SLR}$ is not straightforward. To our knowledge, the literature does not provide a physical expression of the increase in wave-driven erosion efficiency as a function of SLR. Therefore, to go one step further in the quantification of this complex interaction, we make the reasonable (though approximate) assumption that the increase in wave efficiency ($dE_{eq,SLR}$) has the same magnitude as the apparent wave-energy increase associated with the passive flooding shift on the Y - E plane ($dE_{PF} = -a dY_{PF}$ in (Figure B.1b)). Hence, for a given wave energy, additional erosion must occur and, consequently, the magnitude of this wave-efficiency-driven erosion (dY_{WR}) is the same as dY_{PF} . The latter implication is consistent with the Bruun Rule's structure, as demonstrated below.

Given that $E_{eq} = aY + b$, the increase in disequilibrium ($dE_{eq,SLR}$) that results in dY_{WR} is:

$$dE_{eq,SLR} = -a dY_{WR} \quad (B5)$$

The Bruun Rule can be expressed in terms of passive flooding and wave reshaping, as follows:

$$Y_{Bruun} = \frac{SLR}{\tan(\beta)} = Y_{PF} + Y_{WR} \quad (B6)$$

As described in Section 3.2.2, the passive flooding contribution can be computed as:

$$Y_{PF} = \frac{SLR}{\tan(\alpha)} \quad (B7)$$

where $\tan(\alpha)$ is the slope of the beach foreshore.

In order for the combined recession to be consistent with the Bruun Rule recession (Eq. B6), Y_{WR} can be expressed as:

$$Y_{WR} = cY_{PF} = c \frac{SLR}{\tan(\alpha)} \quad (\text{B8})$$

and substituted into Equation B6 to give

$$\frac{SLR}{\tan(\beta)} = \frac{SLR}{\tan(\alpha)} + c \frac{SLR}{\tan(\alpha)} \quad (\text{B9})$$

$$\frac{SLR}{\tan(\beta)} = \frac{SLR}{\tan(\alpha)}(1 + c) \quad (\text{B10})$$

$$c = \frac{\tan(\alpha)}{\tan(\beta)} - 1 \quad (\text{B11})$$

Thus, expressing Equation B8 in incremental terms (dY_{WR} and dY_{PF}), substituting the result into Equation B5, we obtain:

$$dE_{eq,SLR} = -a dY_{WR} = -a c dY_{PF} \quad (\text{B12})$$

and, assuming $c = 1$ (hence, $(\tan(\alpha))/(\tan(\beta)) = 2$), we obtain

$$dE_{eq,SLR} = -a dY_{PF} = dE_{PF} \quad (\text{B13})$$

Recall that, while realistic, the assumption described herein (Equation B13) is only used to provide an approximate quantification of $dE_{eq,SLR}$. Here, we adopt Equation B13 in order to analyse the behaviour of an ESM where feedbacks between the modelled processes are enabled, but it may not be applicable in the generality of cases in practice.

In Section 3.3.2 of the main text, we proposed an approach for integrating SLR-driven recession into ESMs based on the current shoreline position, where feedbacks between modelled processes are allowed. In particular, we focused on ESMs where the equilibrium condition is expressed as $E_{eq} = aY + b$.

For this case, if SLR is applied at a given time step, the consequent dY_{PF} is added on the short-term to the ESM, accounting for the shoreline reference retreat induced by passive flooding. This first (geometric) effect of passive flooding is accounted in the equilibrium condition as a landward shift of the reference shoreline position (Figure B.1). The second effect of SLR (and thus passive flooding) is a disequilibrium increase due to the apparent increase in the beach profile slope, which ultimately results in dY_{WR} . Therefore, the new equilibrium condition (E^*_{eq}) can be rewritten as:

$$E^*_{eq} = a \left(Y - \sum dY_{PF} \right) + b + \sum dE_{eq,SLR} \quad (\text{B14})$$

where the term “ ΣdY_{PF} ” represents the cumulative landward shift of the reference shoreline position, while the term “ $\Sigma dE_{eq,SLR}$ ” quantifies the cumulative disequilibrium change induced by SLR.

Under the assumption described above, the disequilibrium increase ($dE_{eq,SLR}$) can be expressed by Equation B5 and can be injected in Equation B14, giving:

$$E^*_{eq} = a \left(Y - 2 \sum dY_{PF} \right) + b \quad (B15)$$

Recall that although the additional SLR-induced disequilibrium is expressed as a function of dY_{PF} , the dY_{WR} resulting from it is of a different nature (Section 3.2.2). In response to the altered disequilibrium, the model captures the contribution of waves at each modelled time step to profile reshaping (dY_{WR}). In this approach, the effect of SLR is included correctly by adding the sole dY_{PF} term to the ESM and using the equilibrium condition in Equation B13:

$$dS = k^{+/-F} \left\{ \left[a \left(Y - 2 \sum dY_{PF} \right) + b \right] - E \right\} dt + dY_{PF} \quad (B16)$$

The presence of the dY_{PF} term in Equation B16 is so that the shoreline adjusts instantly to the passive flooding and evolves over time due to wave reshaping, consistently with the conceptual model.

We note that the magnitude of dY_{WR} at each time step is quantified in Equation B16 as a function of the sea-level-driven disequilibrium change and the instantaneous wave intensity, as follows:

$$dY_{WR} = k^{+/-F} dE_{eq,SLR} dt \quad (B17)$$

Appendix C Supporting information for Chapter 5

C1. Wave projections correction

The future wave projections issued by Bricheno and Wolf (2018) (hereafter BW18) are the product of a wave model forced with one downscaled Global Climate Model (GCM) outputs. Therefore, the wave projections inherit systematic errors associated with simplified representation of physical processes in the GCM, and/or numerical parametrization within the GCM and the wave model. We perform a seasonal *quantile-quantile* (q-q) comparison between the NORGAS-UG and BW18 wave *historic* time series over the period 1994-2004, and derive a coefficient for each quantile to reduce biases in the BW18 modelled time series. For each season, we compare 101 quantiles (from 1st to 99th with 1% step, plus 0.5th and 99.5th) of H_s , T_p and D_m (Figure C.1), and we estimate correction coefficients as follows:

$$C_X^{qi} = X_N^{qi} - X_{BW}^{qi} \quad (C1)$$

where X is the analysed variable (H_s , T_p or D_m), qi is the i -th quantile, and C is the corresponding correction coefficient. N and BW indicate the NORGAS-UG (reference) and BW18 (to correct) datasets, respectively. At each time step, the values of BW18 H_s , T_p and D_m are corrected using the coefficient corresponding to the nearest quantile of the variable:

$$X_{BW}^{*qi} = X_{BW}^{qi} + C_X^{qi} \quad (C2)$$

where X_{BW}^* is the corrected BW18 variable. The q-q plot of corrected seasonal BW18 time series are shown in Figure C.2.

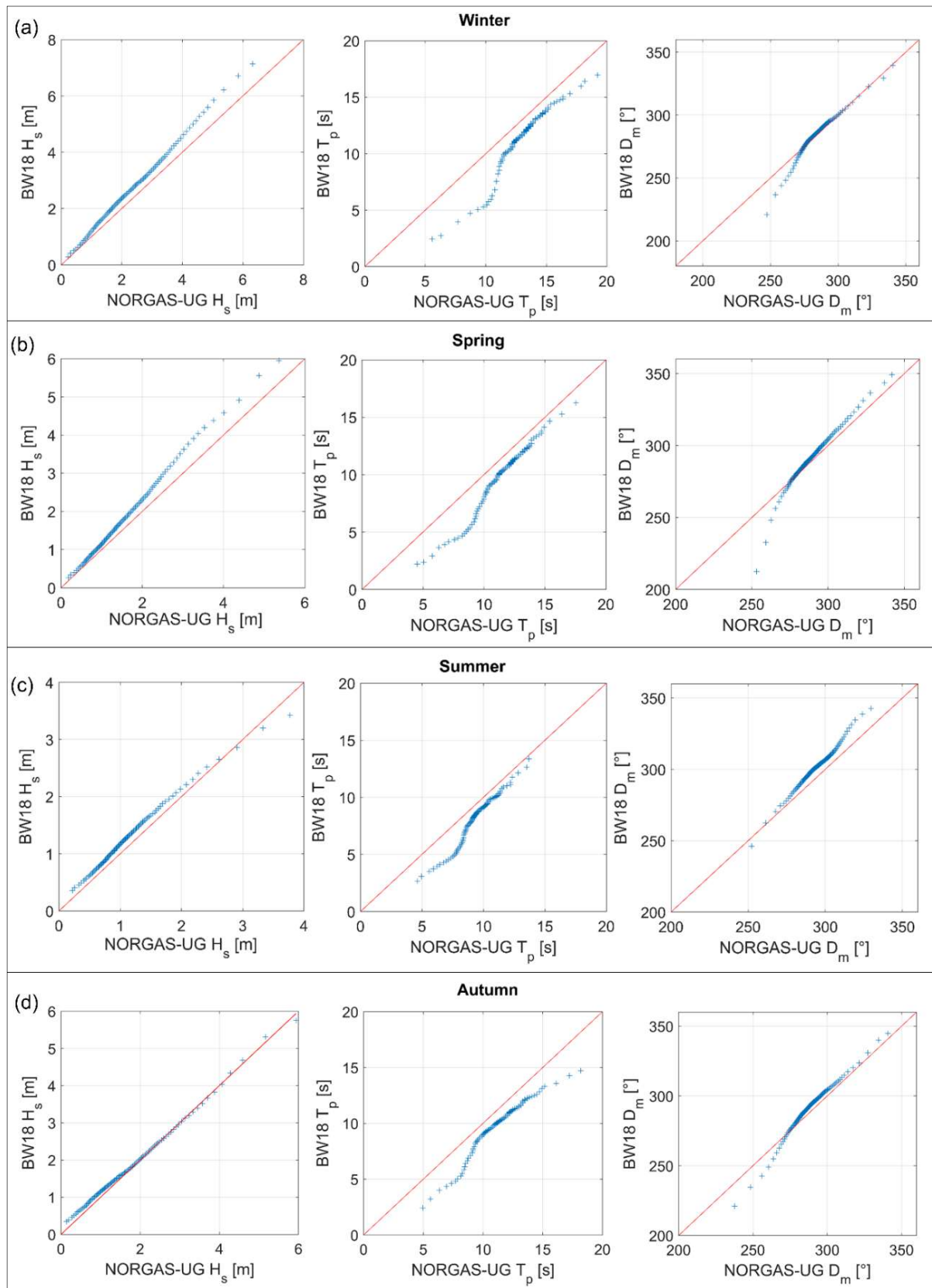


Figure C.1. Comparison between NORGAS-UG and Bricheno and Wolf (2018) hindcasts from 2006 to 2020. Quantile-quantile plots of H_s , T_p and D_m time series assessed for (a) winter, (b) spring, (c) summer, and (d) autumn.

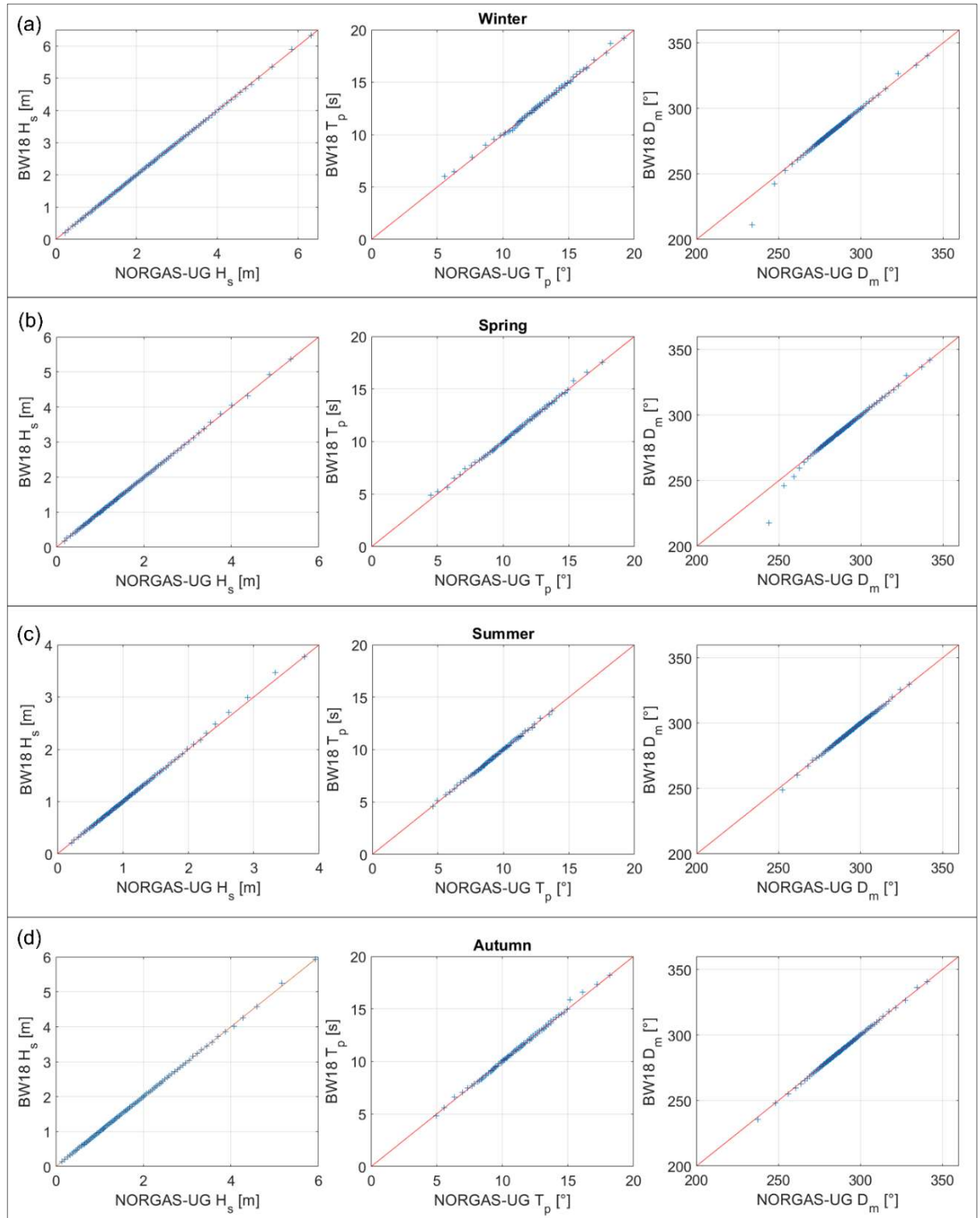


Figure C.2. Comparison between NORGAS-UG and the corrected Bricheno and Wolf (2018) hindcasts from 2006 to 2020. Quantile-quantile plots of H_s , T_p and D_m time series assessed for (a) winter, (b) spring, (c) summer, and (d) autumn.

C2. Construction of the high-end sea level scenario

The Gauss-distributed sea-level projections described in Section 5.3.1 do not include the skewness occurring in the second half of the 21st century associated with uncertainty on dynamic processes in Antarctica. Therefore, we consider the low probability high-end sea level scenario to provide an upper bound of SLR projections over the second half of the 21st century.

We assessed the high-end sea level as the sum of the contributing processes based on Thiéblemont et al. (2019). Thiéblemont et al. (2019) designed the high-end scenario considering the value of each contribution to sea-level rise (SLR) corresponding to the highest physics-based global model estimate (*i.e.* high-end scenario B in Table 2 of Thiéblemont et al., 2019) and added an additional contribution from Antarctica from Marine Ice Cliffs instabilities, which is a low confidence process that could raise the contribution of ice melting in Antarctica to 0.8m (Edwards et al., 2019). These estimates were, then, downscaled to regional scale using barystatic-fingerprints. High-end annual estimates of each contribution are provided only for 2100 and therefore an interpolation is required between 2020 and 2100. In order to better constrain the interpolation we also used SROCC estimates from 2007.

We applied a spline interpolation for each contribution to SLR except for the Antarctic surface mass balance, where we used a linear interpolation, and glacial isostatic adjustment, where the median is used. The spline interpolations (except for the sterodynamic contribution) were performed over the median SROCC values from 2007 to 2020 and the 2100 high-end estimates (Table 2 of Thiéblemont et al., 2019). For the sterodynamic contribution, the spline was fitted on worst-model estimate directly obtained from CMIP5 (Coupled Model Intercomparison Project – Phase 5, Taylor et al., 2012) results for 2007, 2020, 2050, and 2100.

C3. Model free parameters probability distribution

In the present work, we determined the joined probability distribution of model parameters by fitting an empirical multivariate distribution on an ensemble of model parameters combinations that produced sufficient model skill against observed shoreline data.

We determined the shoreline change models' performance using the Nash-Sutcliffe (Nash and Sutcliffe, 1970) efficiency score (*NS*), calculated as follows:

$$NS = 1 - \frac{\sum_{n=1}^N (Y_m^n - Y_o^n)^2}{\sum_{n=1}^N (\bar{Y}_o - Y_o^n)^2} \quad (C3)$$

where N is the number of observations, Y_m^n and Y_o^n are the n -th modelled and observed shoreline positions, respectively, and \bar{Y}_o is the mean of the observed shoreline positions. The maximum NS s obtained using the optimized model parameters are 0.63 and 0.83 step for SF and Y09, respectively. For the two shoreline models, we investigate different values of the NS lower limit (NS_{min}), and we analyse the resulting empirical probability distributions of model parameters with the corresponding behaviour of modelled shoreline. We started by setting NS_{min} to 0.60 and 0.80 for SF and Y09, respectively, then we iteratively reduced NS_{min} with a 0.05 step. We assumed that the NS_{min} decrease is no longer acceptable when this causes abrupt changes in the probability distributions of the model parameters (e.g. emergence of isolated peaks) that associate unrealistic modelled shoreline evolution patterns. For SF, the procedure resulted in an $NS_{min} = 0.25$, with lower values producing a new isolated peak in the parameters distribution (Figure C.3) that associated a near-flat modelled shoreline trend. Variations of NS_{min} down to $NS_{min} = 0.25$ did not show abrupt changes to the Y09 parameters distribution, and the modelled shoreline evolution remained realistic. Thus, we assessed the parameter distributions of both shoreline models by selecting the combinations of parameters producing $NS \geq 0.25$.

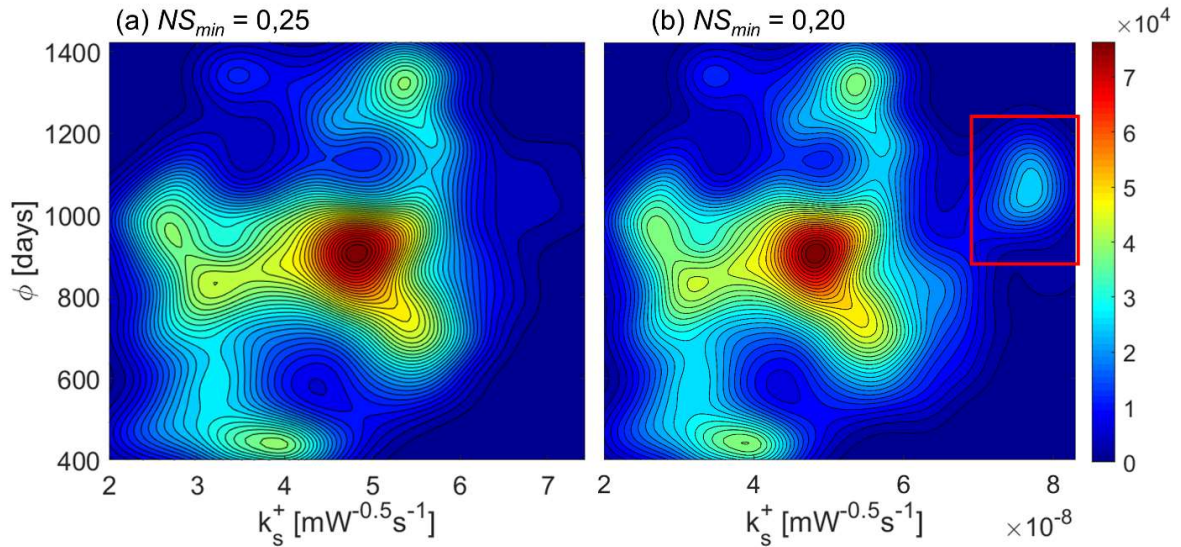


Figure C.3. Comparison of ShoreFor model parameters probability distributions obtained using combinations of model parameters producing (a) $NS \geq 0.25$, and (b) $NS \geq 0.20$ where a peak emerges (red box).

C4. Ensemble waves test with ShoreFor

Here, we analyse the results of the Global Sensitivity Analysis (GSA) on shoreline projections obtained using the SF model in the test application described in Section 5.5.3 of the main text (i.e. including ensemble wave time series).

The GSA results show that the introduction of uncertainties in the chronology of wave events (Figure C.4a) has a large impact on the variance of model results (Figure C.4b) and, in turn, on the relative contributions of the remaining uncertain input parameters (Figure C.4c-f). However, we note that the wave forcing's S_i decays rapidly over the last 5 simulated years (Figure C.4g) causing the SLR's S_i to compensate the responsibility to model variance growing rather unnaturally (Figure C.4e). This behaviour is likely to be non-physical. Indeed, it is due to the nature of the SF model and the approach used to create the synthetic wave time series. In particular, the r parameter in SF (Equation C4), which defines the ratio between k_s^+ and k_s^- , is such that the trend in modelled shoreline is conditioned to the trend in wave forcing (Splinter et al., 2014b). Therefore, given that all the synthetic wave time series are constrained by the same long-term trend of the reference BW18 time series, the r parameter will tend to reproduce the same trend by the end of the simulated period. Thus, the 3000 modelled shoreline trajectories tend to converge when approaching the end of the simulation.

$$r = \left| \frac{\sum_{i=1}^N \langle F^+ \rangle}{\sum_{i=1}^N \langle F^- \rangle} \right| \quad (\text{C4})$$

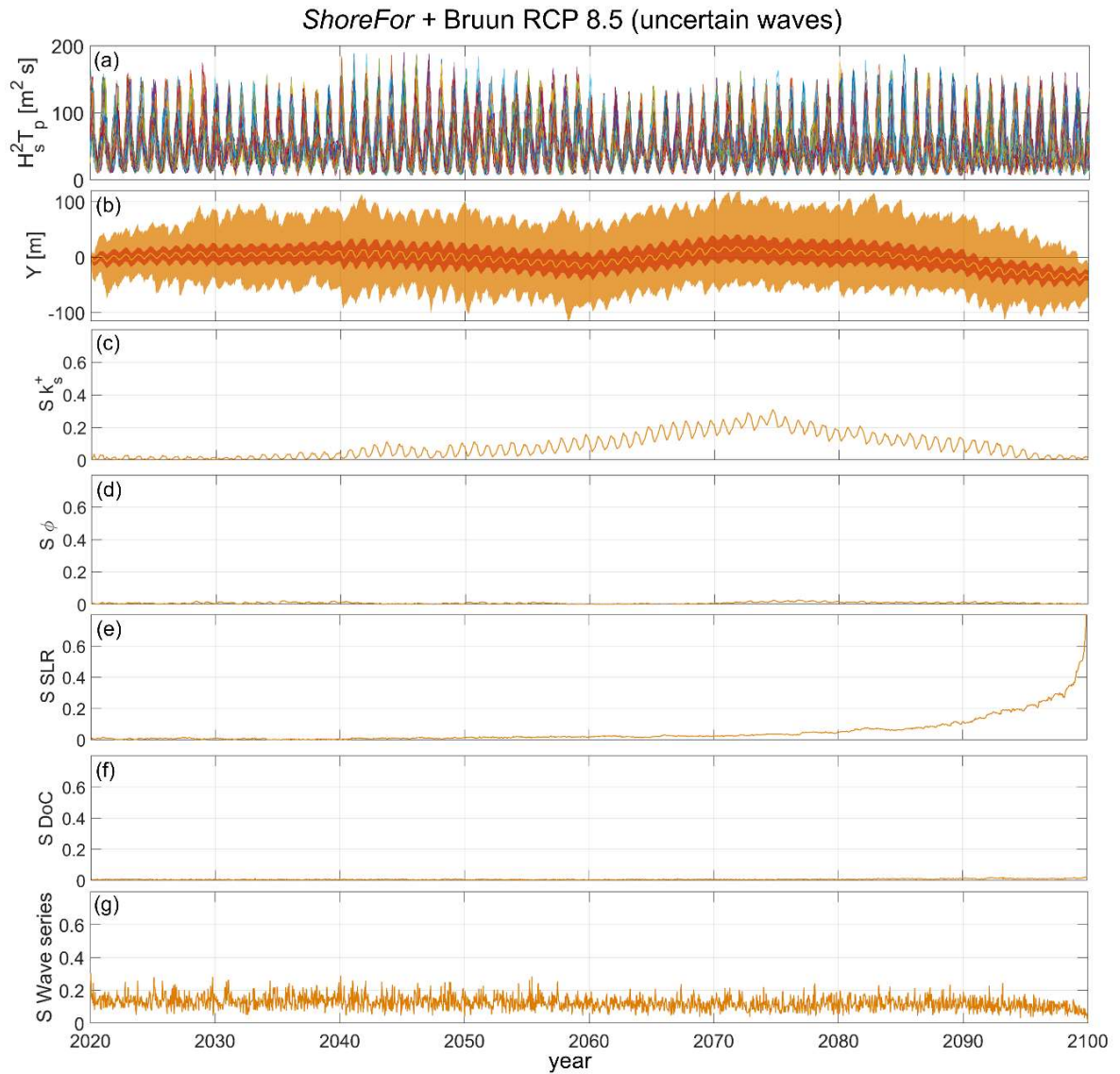


Figure C.4. Ensemble of 3000 *ShoreFor* simulations forced using (a) 100 synthetic wave time series from 2020 to 2100 generated with the Davidson et al. (2017) method based on BW18 wave projections for the RCP8.5 scenario; (b) Ensemble shoreline projections over the analysed period; first-order Sobol' index time series for (c) k_s^+ , (d) Φ , (e) sea-level rise, (f) depth of closure, and (g) wave energy.

Appendix D Supporting information for Chapter 6

D1. Wave ensemble and hindcast wave data comparison

The statistical properties of the generated wave ensemble described in Section 6.2.3 showed good agreement with the historical wave data. Figure D.1 shows the quantile-quantile comparison of T_p and D_m between the reference hindcast data (1994-2020) and each member of the wave ensemble (1994-2099) for the full time series and their seasonal repartition, respectively. Figure D.2 shows that the winter mean wave heights of the emulated time series associate no significant trend between present day (2021) and the end of the 21st century, with trends ranging between -2 and +2 mm/year.

The wave emulator described in Section 2.4.1 of the main text relies on an autoregressive logistic regression (Anderson et al., 2019) to model realistic chronologies of wave events based on large scale predictors such as Annual Weather Types (AWT, yearly time scale) and Madden-Julian Oscillation (MJO, monthly-seasonal time scale). Here, we show that the probabilities of AWT and MJO of the current wave climate are well maintained in the emulated wave time series.

Figure S3 shows the probabilities of historical and emulated AWTs and MJOs, including: a direct comparison of historical and simulated probabilities (Figures S3a and S3d); and historical (Figures S3b and S3e) and emulated weather types transition probabilities (Figures S3c and S3f). In the above plots the rainbow-coloured bars and points indicate different weather types while the white-blue shaded colour bars indicate the probability.

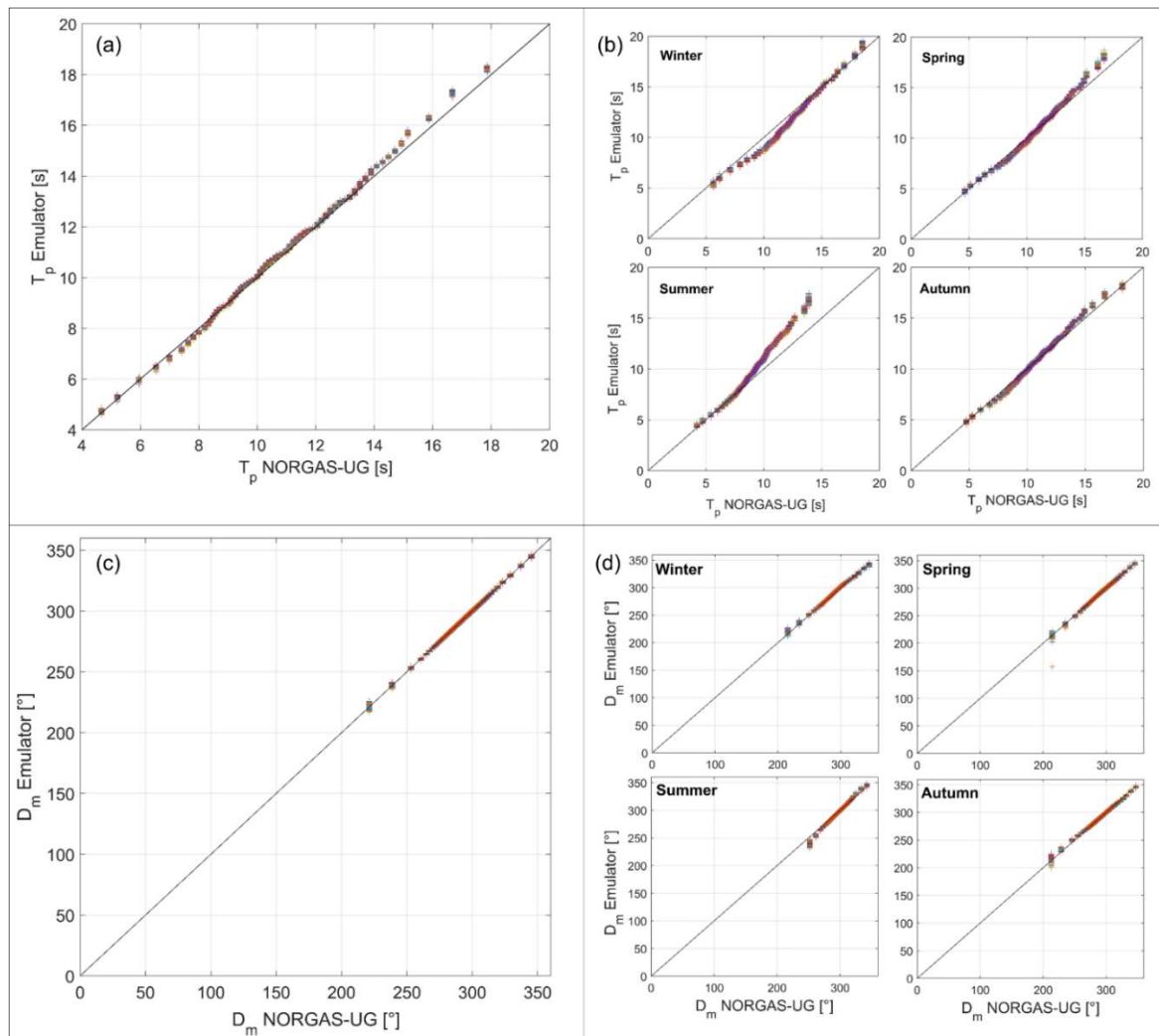


Figure D.1. Quantile-quantile comparisons of T_p (a,b) and D_m (c,d) between wave hindcast data and each of the 200 time series generated using the wave emulator for the (a,c) full time series and (b,d) their respective seasonal repartition.

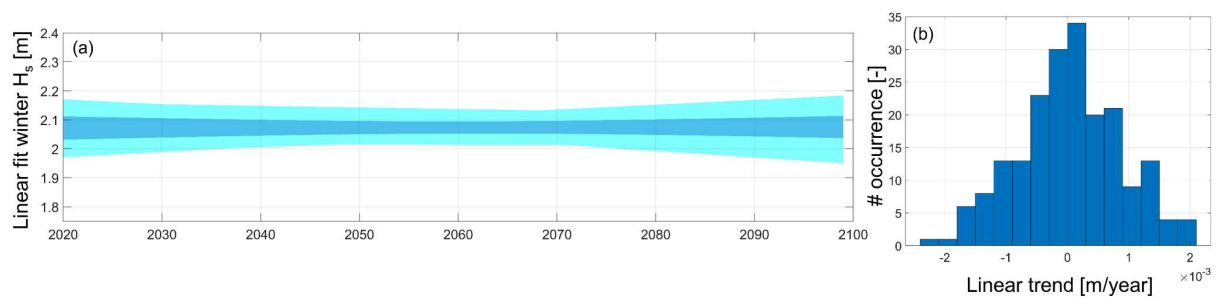


Figure D.2. (a) Time series and (b) histogram of the linear trend in winter-mean H_s associated with the 200 wave time series generated with the wave emulator.

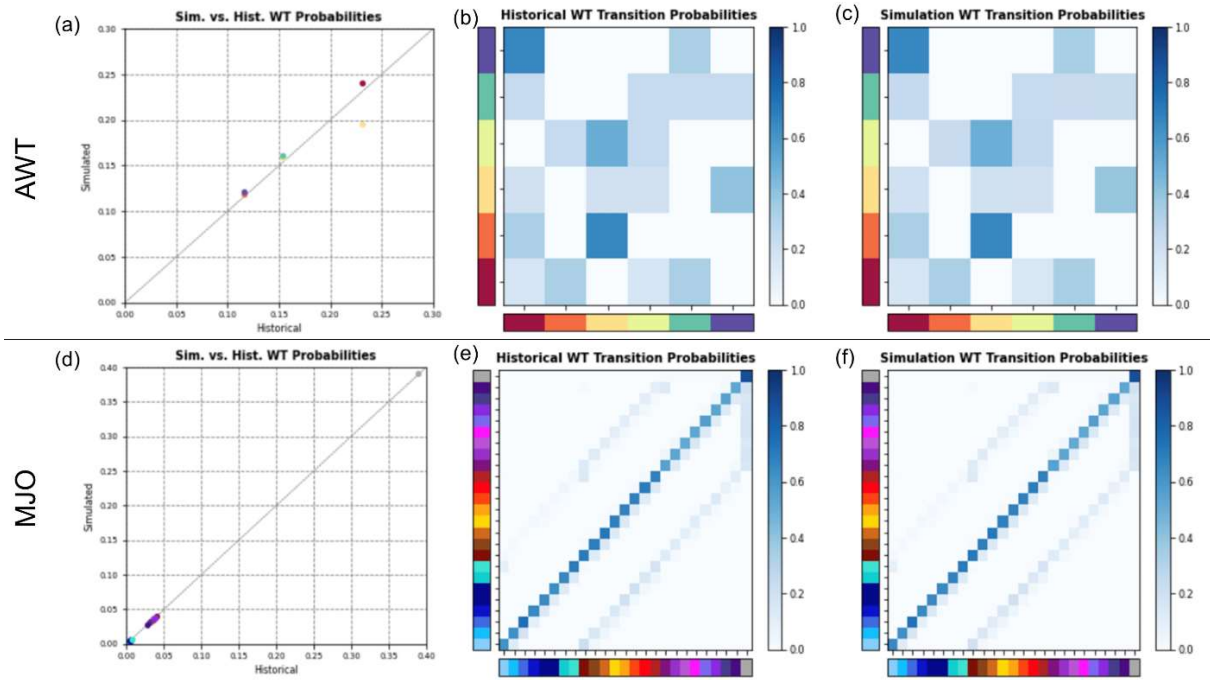


Figure D.3. Weather type probabilities for (a-c) annual weather type (AWT), and (d-f) Madden-Julian Oscillation (MJO), including: (a,d) comparison between emulated and historical probabilities; (b,e) historical weather type transition probabilities; and (c,f) emulated weather type transition probabilities. Rainbow-coloured bars indicate the different weather types and blue-shaded bars indicate the probability of occurrence.

D2. Sea-Level Rise

In this work, we adopt a constant rate of historical relative SLR of 3.3 ± 0.7 mm/year (median $\pm \sigma$), obtained in Chapter 4 from the combination of geocentric MSL change and vertical land motion at Truc Vert beach. Geocentric MSL change was reconstructed from 1994 to 2021 using a Kalman filter assimilation and tidal gauge data available in the Bay of Biscay (Rohmer & Le Cozannet, 2019), while vertical land motion at Truc Vert (1.2 ± 0.6 mm/yr) was estimated from the nearby Lège-Cap-Ferret GNSS station records available from the SONEL database (Santamaría-Gómez et al., 2017). Mean sea level (MSL) data up to present day (2021) derives from measured observations. As such, the range of uncertainties associated to the 2021 measure MSL is mostly due to measurement errors, which are relatively smaller than the uncertainties on MSL projections, especially for high-emission socioeconomic pathways scenarios (*e.g.* RCP4.5 and 8.5). The SROCC provides median and likely range projections of SLR in reference to the rates observed in the year 2007. The latter results in two issues for the present application: (i) different RCP scenarios may associate different present-day (2021) estimates of MSL; and (ii) the estimated 2021 likely range may not be representative of the uncertainties associated with current

observations. Consequently, the projected likely ranges of MSL may significantly overestimate the uncertainties over the first half of the century.

We corrected the trend of MSL projections at Truc Vert beach for both RCP4.5 and RCP8.5 scenarios, by re-interpolating the relative MSL time series using the reconstructed 2021 median and likely range described in Section 2.1.2.3 of the main text. In order to ensure the consistency with the SROCC projections over the second half of the century, a second-degree polynomial curve was conditioned with the median and likely range of relative MSL in 2021 from reconstructed MSL time series, and 2050, 2090 and 2100 from the original SROCC projections. The latter procedure produced nearly unchanged median relative MSL time series, with likely ranges significantly reduced in 2021 that gradually join the original SROCC values in 2050 (Figure D.4).

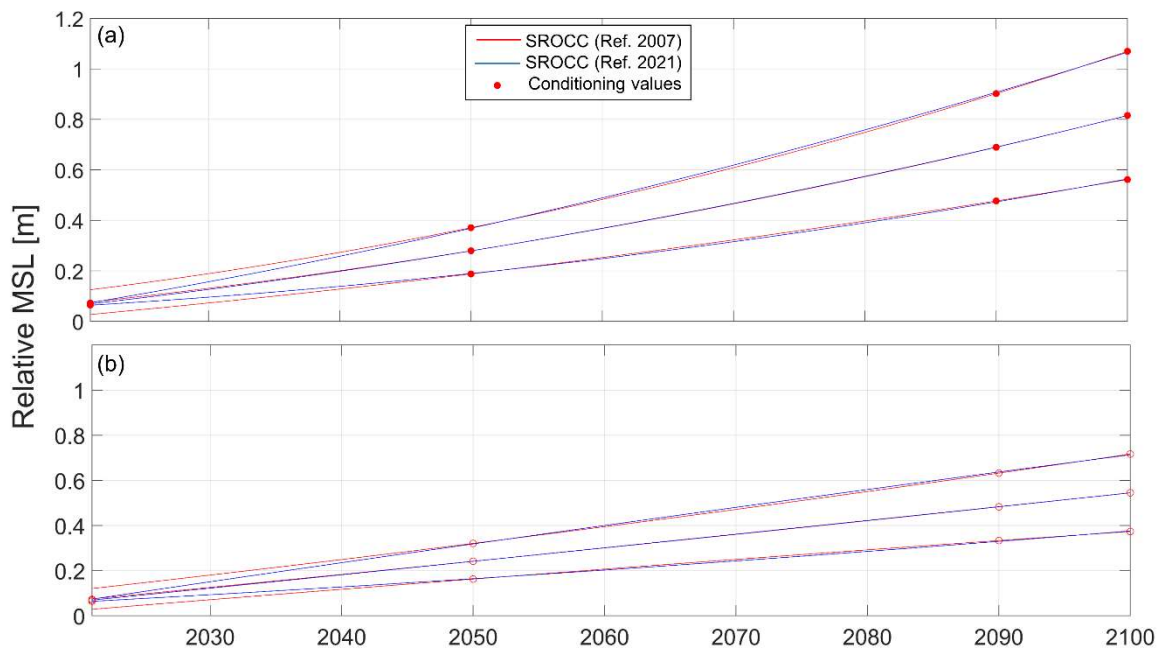


Figure D.4. Median and likely range of relative MSL projections (second-degree polynomial trends) at Truc Vert beach over the 21st century, derived from SROCC projections with reference MSL in 2007 (red lines) and 2021 (blue lines) for the (a) RCP8.5 and (b) RCP4.5 scenarios. The red circles indicate the MSL values used to constrain the new polynomial fit with reference to 2021, which correspond to the original SROCC projections for 2050, 2090, and 2100 and to the observed data in 2021.

D3. Past scenario simulation with the ShoreFor and Yates models

ShoreFor application

The SF model computes the rate of shoreline change (dY/dt) at a given time independently of the current shoreline position, and therefore the calculated rate does not depend on the initial condition provided (i.e. initial shoreline position). In the ‘past scenario’ application, we simulated shoreline evolution over the past 20 years using the combined SF and

Bruun models by imposing the shoreline position at the calibration starting time (March 2012) and resolving the inverted SF's governing equation:

$$Y_{i-1} = Y_i - \left(k_s^{+/-} P_i^{0.5} \frac{\Delta\Omega}{\sigma_{\Delta\Omega}} \right) (t_i - t_{i-1}) - \frac{SLR_i - SLR_{i-1}}{\tan\beta} \quad (D1)$$

where $i-1$ and i represent two following positions in time separated by one time step.

In this setup, the shoreline position imposed at the calibration start (March 2012) can be interpreted as the initial shoreline position for the application of the inverted SF model (Y_i in Equation D1). As the simulation progresses backwards in time, the results uncertainties propagate towards the past from the calibration start.

Yates model application

When addressing the probabilistic reconstruction of shoreline evolution over the past years ('past scenario'), the uncertainties on model inputs and modelled shoreline propagate from present day, where waves and shoreline observation are available, towards the past. The SF+B models compute shoreline change in response to forcing waves and sea level conditions (dY/dt) at each time step regardless of the current shoreline position. Thus, the estimated shoreline change (dY/dt) is independent from the initial shoreline position. Therefore, if the present-day shoreline position is enforced, the initial shoreline position is univocally determined by the simulated dY/dt .

Instead, the application of the Y09+B models over past periods has some conceptual limitations owing to the dependence between Y09's disequilibrium condition and the past shoreline position. Indeed, Y09's disequilibrium formulation (Equation D2), which depends on the past shoreline position (Y), determines the direction of the shoreline change and the respective response rate value $k_y^{+/-}$.

$$E_{eq}(Y) - E = a_1 Y + a_2 - E \quad (D2)$$

At a given time t^* , the shoreline position at the time t^*-dt cannot be univocally determined, as the problem has one solution for each of the $k_y^{+/-}$ values. Therefore, Y09 does not allow fixing the shoreline position at the starting date of the calibration period (23-Mar-2012) and determine the initial condition (Y_0). However, here we carry out the 'past scenario' GSA application with the Y09+B models for demonstrational purposes.

The simulated ensemble shoreline positions fit well the shoreline observations over the calibration and validation periods. The limited SLR-driven erosion over this the simulated period (~0.5 m) and the character of Y09's disequilibrium condition (described in Section 6.5.1 of the main text) result in a roughly stable shoreline position over the 1998-2012 period

(Figure D.5), contrary to the accreting trend observed in the SF ‘past scenario’ application. The introduction of ensemble wave forcing increases the envelope and likely range of shoreline position compared with the calibration and validation period (Figure D.5).

Similarly to the SF application, the GSA shows rather stable Sh 's, with a persistent seasonal modulation, with the uncertainties of wave chronology dominating the simulated shoreline ensemble (Figure D.6). The Sh of wave chronology is seasonally modulated around an average of roughly 43%, with winter peaks up to ~60% and summer lows of ~30% (Figure D.6a). The Sh values of the a_1 and a_2 parameters fluctuate around 12% and 18%, respectively, while k_y^+ and k_y^- Sh 's settle on an average value of 14% and 13%, respectively (Figure D.6a-d). We note that the total contribution of uncertainties on model free parameters reaches 53%, exceeding the one the uncertainties on the stochastic wave variability, although the contributions of wave-parameters interactions and parameters correlations may play an important role in this decomposition.

The estimated first-order *Sobol' indices* (S_i) of each uncertain input indicates the likely existence of a significant contribution of interaction and correlation effects. Indeed, the cumulated differences between Sh 's and S_i 's approximates 48%. The Sh of wave chronology is seasonally modulated around an average of roughly 43%, with winter peaks up to ~60% and summer lows of ~30% (Figure D.6).

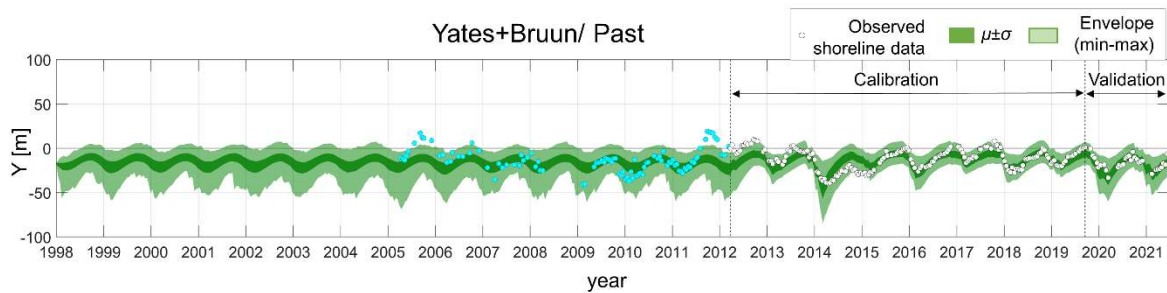


Figure D.5. Ensemble shoreline evolution simulated using the combined Yates and Bruun models, including the envelope (light-shaded areas) and the standard deviation intervals ($\mu \pm \sigma$) (dark-shaded areas) of the 10000 simulated shoreline trajectories, respectively, over the 1998-2021 period (‘past scenario’). Black dashed lines delimit the calibration and validation periods, including shoreline observations (white circles). Cyan circles indicate shoreline data prior to March 2012.

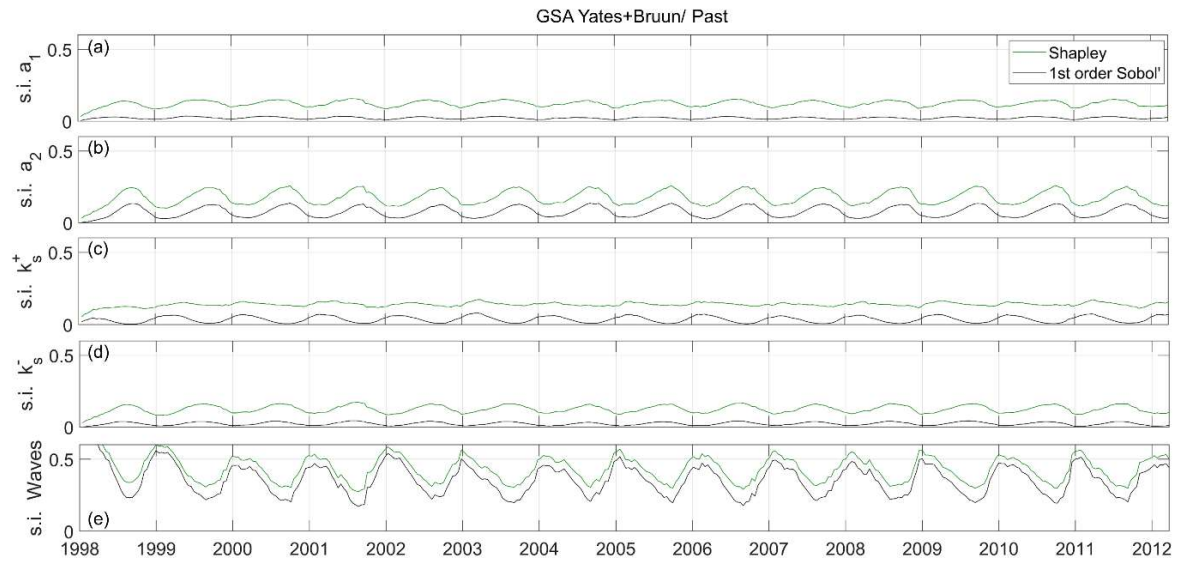


Figure D.6. Sensitivity indices (s.i.) obtained for the ‘past scenario’ Y09+B ensemble. Comparison of *Shapley Effects* (green lines) and first-order *Sobol’ indices* (black lines) of the *Yates* model free parameters (a) a_1 , (b) a_2 , (c) k_y^- , (d) k_y^+ , and (e) wave chronology.